Final Report

DSE08 Spring 2019

RAMSES: RAM Satellite for Earth Sensing

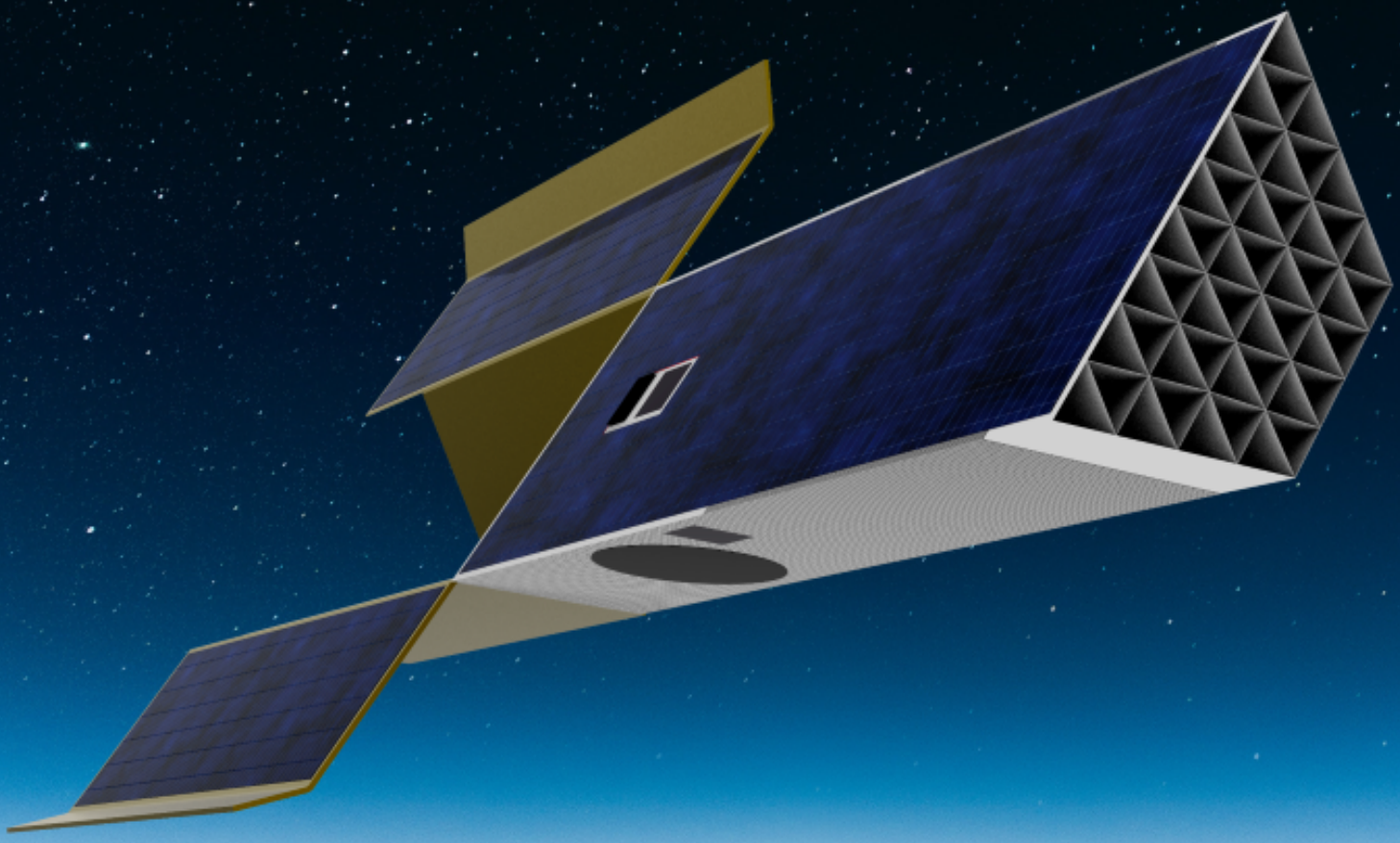

TU Delft

Final Report

RAMSES: RAM Satellite for Earth Sensing

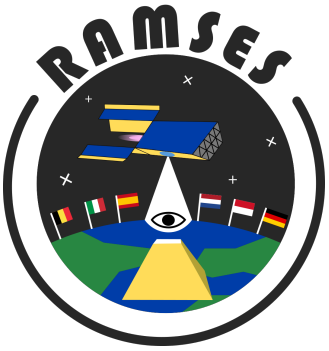

by

Florian Adam - 4560973
Mauro Villanueva Aguado - 4557825
Maximo Cravero - 4546067
Joey Dekker - 4538099
Andrea Iannone - 4567706
Martijn Jorissen - 4574869
Giulia Leto - 4577442
Yovanka Rucita - 4552903
Simon Venth - 4614577
Jeije van den Wijngaart - 4440463

on

July 2, 2019

version FR-1.1

Project duration:	April 23, 2019 – July 4, 2019	
DSE committee:	Dr. ir. A. H. van Zuijlen,	TU Delft, Tutor
	Dr. ir. F. F. J. Schrijer,	TU Delft, Tutor
	Ir. M. Rovira Navarro,	TU Delft, Coach
	Dr. M. Hamdi,	TU Delft, Coach
	Dr. A. G. Anisimov	TU Delft, Coach
	Dr. ir. L. M. G. F. M. Walpot	ESA ESTEC, External expert

TU Delft

Change Record

A brief overview of the changes per version are shown in Table 1.

Table 1: Change record, last update: 2 July 2019

Version	Date	Chapters affected	Description of change
FR-1.0	03 June 2019	all	New document
FR-1.1	28 June 2019	chapter 9	Corrected altitude and thus resolution, updated stability
	28 June 2019	chapter 14	Post-DSE Gantt chart updated
	30 June 2019	chapter 14	Improved mass contingency strategy, included exploded view and sub-assembly denotation
	30 June 2019	chapter 6	Corrected information on Kepler's constellation. Adjusted link budget, clarified communication block diagram. Lowered the value of compression ratio to 50, which is feasible for JPEG2000.
	30 June 2019	chapter 13	Adjusted diagrams, implemented feedback and clarified derivation of memory size.
	30 June 2019	chapter 7	Increased and horizontally mirrored figures, implemented feedback.
	30 June 2019	chapter 4	Clarification added to drag equation and C_D parameter.
	30 June 2019	chapter 5	Included Altitude Variation Graph in Figure 5.14. Changed orbit diagram in Figure 5.1. Changed symbols to be coherent with list of symbols.
	1 July 2019	chapter 10	Updated requirements & verification of requirements
	1 July 2019	chapter 12	Implemented feedback, clarified text, adjusted sensitivity analysis
	1 July 2019	chapter 8	Implemented feedback, added some comments to the sensitivity analysis, adjusted PCU block diagram and accompanying text
	1 July 2019	chapter 11	Added references for damping ratio. Added more context to the re-entry risk assessment. Some small clarifications based on the feedback.
	1 July 2019	chapter 15	Added clarification of meaning different categories and scale of the design wheel.
	2 July 2019	chapter 3	Updated method of market size.
	2 July 2019	all	Proof reading, small grammar/spelling corrections

Executive Overview

The present project embodies the completion piece of the aerospace engineering curriculum at TU Delft, namely the Design Synthesis Exercise (DSE). By applying and expanding the knowledge accumulated during the entire Bachelor program, students collaborate with tutors and external experts to experience the real-life design process and acquire the important skills of project management and systems engineering.

A. Iannone, F. Adam, G. Leto, J. van den Wijngaart, J. Dekker, M. Jorissen, M. Villanueva Aguado, M. Cravero, S. Venth and Y. Rucita are the students allocated to Group 08, whose designated project is the *Demonstrator for Air-Breathing Electrostatic Propulsion Earth Observation Satellite*. The stakeholders are two tutors from TU Delft, Dr. *ir.* A. H. van Zuijlen and Dr. *ir.* F. F. J. Schrijer, two coaches from TU Delft, MSc M. Rovira Navarro, Dr. *ir.* M. Hamdi and Dr. *ir.* A. G. Anisimov and one external expert from ESA ESTEC, Dr. *ir.* L. M. G. F. M. Walpot.

Mission Objectives

The mission objective is to demonstrate the feasibility of electrostatic air-breathing propulsion through in-depth analysis. Additionally, the benefits in terms of sustainability are highlighted, as well as the potential technological innovations that will arise due to the intended competitive nature of the spacecraft.

System Overview & Mission Profile

The mission profile has been divided into 3 stages. The initial orbital insertion manoeuvre of two RAM Satellites for Earth Sensing (RAMSES) is performed by LauncherOne. The satellite is inserted into a 'high' orbit where it will out-gas and slowly decay to its operational altitude over a period of 2 weeks. During nominal operations the satellite will constantly check its position and perform inclination or altitude change manoeuvre to ensure that it remains at the desired inclination, altitude and right ascension of the ascending node. During this time images are made and send via relay satellites to the earth. The end of life is driven by the safe disposal of the satellite, which must ensure safe disposal through re-entry in the atmosphere.

Previous Design Phases

Several milestones needed to be achieved before entering the final design phase. First, the most important one was the requirement discovery. From the acquired stakeholder requirements, more verifiable and specific requirements were derived. From the retrieved system requirements, more detailed subsystem requirements were formulated and discussed separately.

After deriving the requirements, the mission, and the alternate means to achieve it, could be seen more clearly. At this stage, multiple conceptual designs were conceived: they differed in terms of mission objective. The three concepts were studied more in depth and a trade-off method was established to eventually select only one conceptual design. The chosen concept aimed to fly at constant density such that its propulsion system could be designed for a constrained variation of conditions. The curious reader is referred to [1] for a more detailed explanation of all the concepts and the trade-off method.

Subsystems & Integration

The development of the selected concept was conducted in a detailed design phase, by examining each subsystem concurrently. Hereby, each subsystem is discussed independently. A description of the final integration follows.

Guidance, Navigation & Control

The guidance, navigation & control subsystem is responsible for the orbit design, orbit maintenance and orbit determination of the satellite. To achieve a constant density the altitude of the satellite has been determined to vary throughout its lifetime, starting at 240 km with a high solar activity to 214 km at a low solar activity.

Constant observed lighting conditions are beneficial for the imaging payload, to achieve this the satellite will have a sun synchronous orbit. To remain in a sun-synchronous orbit through the altitude range the inclination will vary from i=96.485° to i=96.379°. A right ascending node of Ω=30° was determined to provide the best compromise between payload performance and imaging quality.

An orbit determination system that relies on the existing attitude determination infrastructure was designed to determine the satellite's position. A combination of magnetometers and star sensor/gyroscope was found to provide the lowest positional error.

Communications

The communications subsystem has been designed in such a way to guarantee continuous communication with the ground with minimum power and mass requirements. To this end, the use of relay constellations has been considered: Kepler 140 nanosatellites at 575 km are sufficient to enable complete coverage for continuous up- and downlink. This type of communication allows for immediate delivery of customer's data, fast detection of commands from ground and the possibility of sending emergency signals at any moment in time. The subsystem's architecture is fully redundant to comply with the system requirement about reliability. Furthermore, the antenna chosen is an array bonded on the satellite's surface: this limits the amount of drag - already critical in VLEO - that RAMSES would experience. The signal beam is steered towards the relay antenna, thus the available power is used efficiently.

Propulsion System

The propulsion system is a critical part of the design of RAMSES. It was designed to overcome the drag encountered, as well as to change orbital altitude and inclination in order to take into account solar activity, repeat orbits, et cetera. The system design was based around an air-breathing, electrostatic thruster with an I_{sp} value of 3500 s and a thrust-to-power ratio of 13.8×10^{-6} N/W. It required an intake to supply particles and a power interface to provide the necessary power. The dimensions of the spacecraft were exploited to retrieve optimal drag and thrust values; these were then used to design the intake system and determine the power requirements.

Based on the frontal area dimension, a drag value of approximately 4.8 mN was acquired. To take into account a contingency margin, a thrust-to-drag ratio of 1.2 was implemented. Therefore, a necessary EOL-power of around 420 W was retrieved. Additionally, to ensure the required mass flow for the engine, an intake of 0.39 m^2 was sized with an estimated collection efficiency of 40%. To this end, an intake system was designed to capture and transport molecules to the thruster: it consisted of a 0.20 m long grid made out of 32 identical triangles. Once past the grid, only 9% of the particles bounced back out of the intake. Afterwards, the pressure is increased and equalised in the thermolizer, followed by a collimator. The latter's efficiency is required to be 8.4% or higher. This necessary efficiency is including the feed line to the thruster, which is less than 30% for the intake system of RAMSES.

Power

The power subsystem is responsible for generating and managing power such that it may be distributed to all of RAMSES' components under the right conditions. It is composed of solar arrays, batteries which provide power during eclipse time and peak conditions and two PCUs which regulate the input power accordingly.

The solar array was sized by accounting for inefficiencies such as degradation, array inclination and temperature variations, amongst others. A SpectroLab cell with a BOL efficiency of 32.2% is selected. The resulting area is 5.03 m^2 with a total mass of 4.23 kg.

The batteries were sized such that they can provide sufficient power during the eclipse period. The selected model was a 43Ah lithium ion battery with a capability of up to 40,000 cycles. The resulting configuration is two sets of five batteries, which includes one redundant battery per set. The total system mass is 12.7 kg.

The power control unit was split into two so that a dedicated Ion Propulsion PCU (IPPCU) could provide power to the engine reliably. The General PCU (GPCU) was designed to distribute a peak load of 144 W to all subsystem components except for the engine; the IPPCU delivers a power of 415 W to the engine.

Payload

The imaging payload achieved a ground resolution of 34 x 34 cm^2 to 38 x 38 cm^2, depending on the altitude (from 214 km to 240 km). This is slightly higher than the requirement of 30 x 30 cm^2 due to integration constraints. The payload achieved a focal length of 219 cm and an effective aperture of 42 cm, by using an annular folded optic [2]. The final integration of the payload is shown in Figure 1.

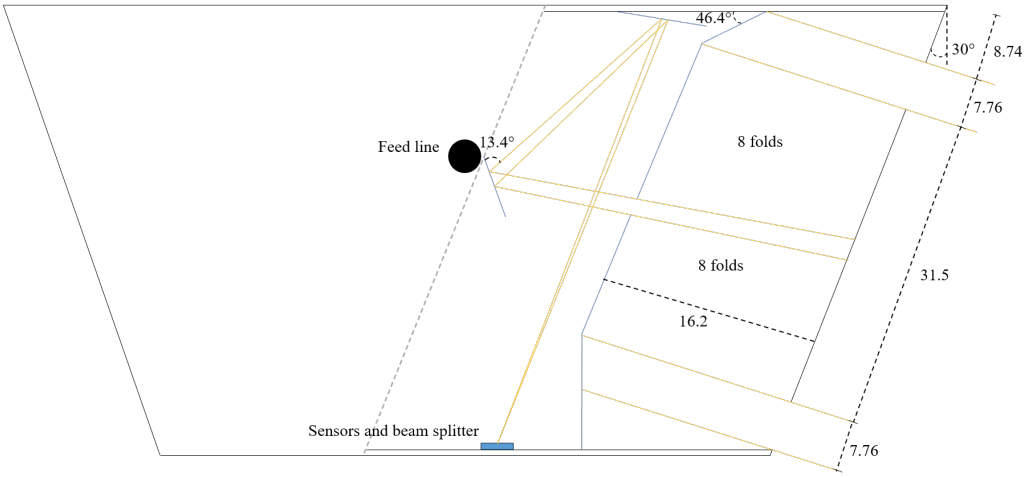

Figure 1: Schematic of the camera as integrated into the spacecraft (not to scale), the dimensions shown are in cm. The spacecraft moves into the paper

The main disturbances caused by the atmosphere and the geometry of the satellite/Earth-system can be corrected for by means of on-board processing [3].

The main risk for the payload was considered to be the degradation due to atomic oxygen. The carbon fibre reinforced silicon carbide had excellent properties for a space mirror [4], but atomic oxygen remains a problem [5]. The effect was mitigated as much as possible by means of a nanosphere/polyimide composite coating, which performed exceptionally well in tests [6], but still expected to degrade over the 10-year mission lifetime. Also, the payload was designed to tolerate very little changes in requirements or design before the concept becomes unfeasible or the performance is reduced.

The payload was estimated to weigh 30 kg and consume no more than 30 W of power, both including contingencies. The total payload cost for one satellite, including research and development, was estimated to be FY19 €23.7×10^6.

Attitude Determination & Control

The Attitude Determination and Control Subsystem (ADCS) of RAMSES deals with keeping the payload pointed towards the ground at all times, the solar arrays aligned within an angle of 30 degrees with the Sun, and the intake perpendicular to the flow direction. The stability of the spacecraft is also assured. The system was designed by estimating the disturbances which the spacecraft encounters at the operational altitude, and the pointing requirements of the camera and other subsystems. Attitude determination is achieved with a combination of Sun sensors, star sensors, Inertial Measurement Units (IMUs) and magnetometers. Magnetic torquers provide attitude control. The system was designed to be fully redundant, radiation resistant and with TRL level 9, guaranteed for 10 years of operations. The stability of the spacecraft is provided by deployable fins. The system was designed to be operational in a detumbling mode, for the phases immediately after launch, a nominal operations mode and a safe mode. Attitude control can be achieved up to a minimum altitude of 188 km, which allows for a certain degree of control of the velocity of the spacecraft in the first phases of the re-entry. The main risk associated with the subsystem was found to be the magnetic field interaction between magnetic torquers and propulsion system, which might in the worst case cause the shut-down of the engine. Integration considerations were done to prevent the issue. Extensive testing will be required.

Structures

The structure was designed to resist the launch loads of the LauncherOne launch vehicle. The vibration loading was found to be critical and was used for the sizing of the structural shell. This resulted in a load

carrying shell of 1.35 mm of carbon fibre reinforced polymer. The mass of this shell is equal to 13.16 kg. Additionally 5 kg was assigned for the adapter and 3.5 kg for the fasteners.

Apart from the launch loading, the structure was also designed to resist the erosive VLEO environment. This was accomplished by selecting two coatings, one for elements that require a transparent coating and one for elements that do not specifically have this requirement. A composite film of 7.5 µm with a transparency of over 92% was selected for the first elements. The other elements were coated using a perhydropolysilazane derived silica coating with an exceptional resistance to erosion and a thickness of 1.17 µm.

Finally the re-entry of the satellite was analysed using the SARA program. It was found that the fatality probability was 9.5×10^{-5}, which was deemed to be acceptable as the value is below values commonly used for space missions [7].

Thermal Control

The thermal control of RAMSES is to be done passively. This is beneficial as the system already has a tight mass and power constraint. Several surface finishes have been used on the various sides of the spacecraft, namely: Aluminium kapton of 5 mil and white paint. Heat generated in the engine is radiated off to space with a radiators placed on the outlet side of an area of 0.14 m^2. Heat pipes are sized to transfer heat from hotter sides to colder sides. This is mostly to also minimise the high temperature variations of the solar panels that leads to degradation. Two more radiators are placed on the zenith side and bottom side. Collectively, they have an area of 1.35 m^2. They are placed on sides that do not face the sun to increase the radiator efficiency. With all of this hardware, the temperature variation of RAMSES on all its sides accommodate the required operating temperature of all of its components. Finally, the total mass of the thermal control system is given to be 4.6 kg.

Command & Data Handling

Command & Data Handling represents the brain of the spacecraft: it is responsible for internal communications between the different subsystems and manages on-board operations. These tasks are undertaken mainly by the On-Board Computer(OBC). The significance of this subsystem with respect to all mission operations required per se a high level of reliability for its design; thence, the system has been conceived to be fully redundant. Two OBC are installed; nonetheless, to have an efficient design in terms of mass and power consumption, the unit has been customised. Proton2X box suite was selected amongst the most reliable OBC for small satellites: it has a TRL value of 9. Only the components deemed strictly required have been included. In particular, a large flash memory was chosen to store the large amount of data generated by the imaging payload. The storage was over-designed: the reason lies in the possibility to store larger files, such as a video, under specific customer's requests. To this end, also the processor and handling speeds are higher than the ones strictly needed.

Integration

One of the biggest challenges of system integration for RAMSES was the balance of the spacecraft. Due to the high drag forces, a misalignment between the centre of pressure and the centre of gravity will produce significant disturbance torques, which would need to be counteracted by a powerful ADCS. Thus, trimming the spacecraft accurately is crucial to the performance of the system. It was demonstrated that it is possible to move the centre of gravity to the right location by carefully positioning the various components. In addition to that, the mechanical, electrical, thermal, propellant and data interfaces of the spacecraft had to be considered and designed for. This introduced more constraints to the system layout, such as favourable and unfavourable component mounting positions.

Risk Assessment

For each subsystem the risks have been identified and mitigation measures have been taken where required. As a result the over risk of the project was minimised. To achieve this a risk map was presented in each section.

Cost Assessment and return of investment

RAMSES costs were estimated by the quasi-grassroot method and the cost for research, development and engineering aswell as the unit costs can be found in the following table. Besides these cost there is the

Table 2: Overview of the subsystem specific cost

Subsystem	R&D and engineering cost (10^6 2019 €)	Unit cost (10^6 2019 €)	Cost estimate accuracy	Technical Risk
Propulsion	40.6	1.8	Low	High
Power	0	1.1	Medium	Low
Thermal	0.6	0.1	Medium	Low
ADCS	0.2	0.2	High	
Payload	17	6.8	Low	High
Communication	0	0.2	High	Low
Structures	14.3	2.9	Medium	Low

launcher cost which is estimated to be 12 million dollar per launch and can take 2 satellites. Furthermore the general project costs of the rest of the project had to be estimated which is illustrated in the following figure. Using this cost estimation and the available market volume of 98 million dollar per year the following

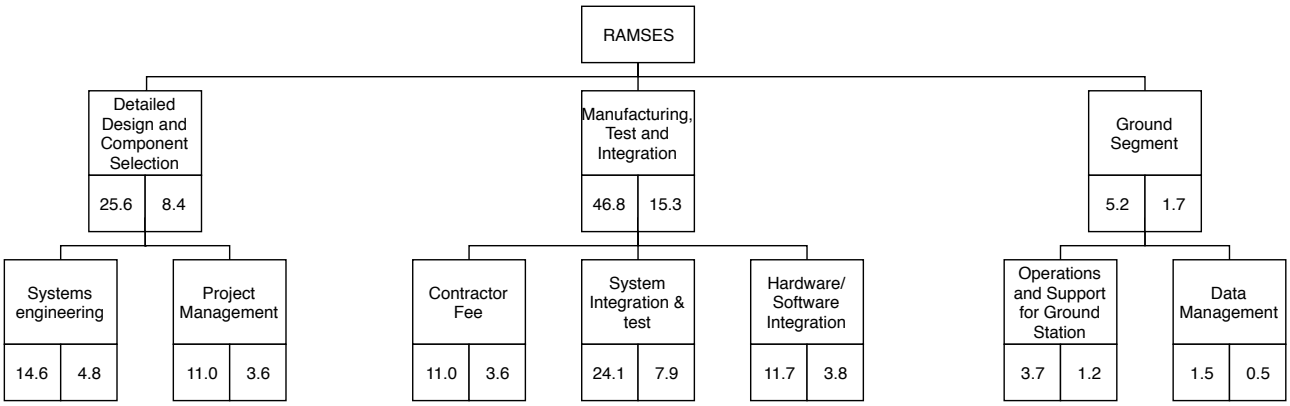

Figure 2: Cost breakdown structure of the post DSE phase. The number in the left box is the non-recurring cost and the number in the right box is the recurring cost. Both are given in 10^6 2019 €

parameters were derived in order show the return of investment. Together with a price course that would start at 10 dollars per km^2 and will decrease in steps of 2 years towards 2 dollars per km^2, this provides enough data to make the graph in Figure 3 where it can be seen that after 4 years the investment has paid off and profit can be made until 58% over 10 years.

Table 3: Cost overview of RAMSES

Parameter	Value	Comment
Non-recurring costs	150.6	million 2019 euro
Cost per spacecraft	39.8	million 2019 euro
Number of spacecraft	4	
Surface captured	37 000 km^2/d	
Yearly cost per spacecraft	0.15	million 2019 euro
Selling efficiency	26%	Assumption based on market share

Sustainability Approach

After the first design was completed its impact on the environment was assessed based on the materials and processes used. Based on this assessment some potential improvements were identified of which some were

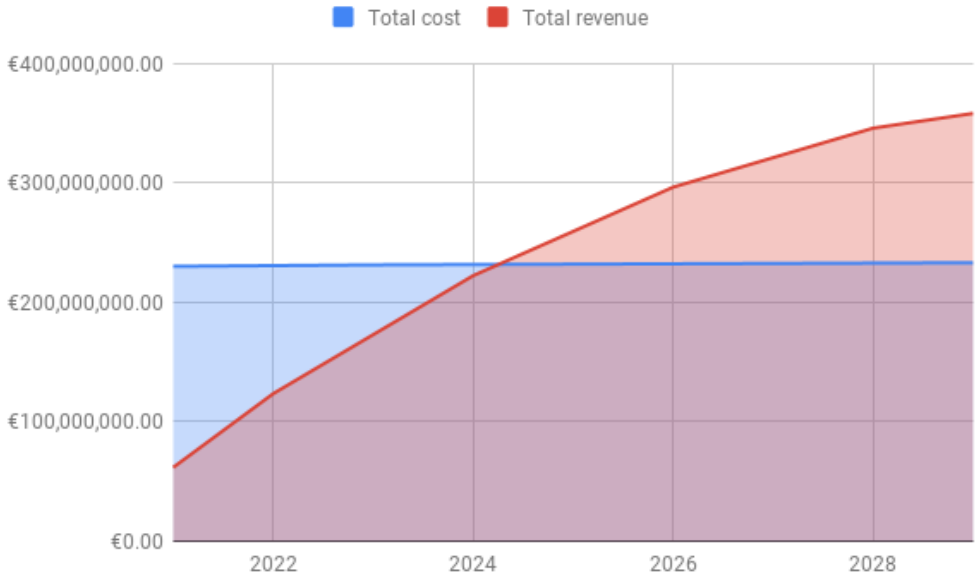

Figure 3: Graph that shows the total cost versus the total revenue.

incorporated in the design. The most important choices that were implemented in the design to improve the sustainability were the launcher and the recycling of composite waste. Another improvement that was identified was the use of aluminium as a material. This would great improve the sustainability of the design but was not feasible to implement within the mass budget.

Development & Production Plan

Having presented the complete design up to this stage, the future stages of development and production were briefly analysed. It was expected that a more detailed design would to be performed before the production could commence. With respect to production the design was split into six sub-assemblies to facilitate integration and testing. Production be followed by a testing phase in which the final design would be realised. Finally, after integration is complete the launch with the selected launcher is expected to occur.

Future Considerations

Lastly, some future considerations are outlined. Some considerations can be made to improve the current design by conducting more research into the collimator and the erosion due to atomic oxygen. Other improvements can come from improvements in imaging sensor technology [8], which can simplify the integration by shortening the required focal length. Some extra considerations can also be given to the communication system, where the VLEO altitude creates new problems in ground station availability.

The RAMSES mission can also be adapted to take a different type of payload. Interesting potential payloads are (1) a communication payload (possibly with a constellation of satellites) [9], (2) LIDAR measurements [10], (3) (synthetic aperture) radar [11], (4) gravity field measurements [10–12], (5) electromagnetic field measurements [10] and (6) direct sensing of the atmosphere (density, chemical composition, etc.) [10]. All these alternative payloads can benefit from the lower altitude and the long mission lifetime. Another benefit of air-breathing electrostatic propulsion is that it is not limited to Earth's atmosphere [13]. It can potentially be used on other planets with an atmosphere (such as Mars [13]) with similar payloads. Since Mars' atmosphere is significantly thinner than Earth's, the achievable altitudes are even lower, creating potentially more gains. To investigate such applications, the engine and intake systems will need to be tested with different densities and gas mixtures that mimic a non-Earth atmosphere.

Nomenclature

Abbreviations

ADCS	Attitude Determination System
AF-MPD	Applied-Field Magnetoplasmadynamic Thruster
BOL	Begin of Life
CBS	Cost Breakdown Structure
CCD	Charge Coupled Device
CMOS	Complementary Metal Oxide Semiconductor
COTS	Commercial-off-the-shelf
DOT	Design Option Tree
DRS	Data Relay Satellites
EO	Earth Observation
EOL	End of Life
EPS	Electrical Power System
ESA	European Space Agency
FBS	Functional Breakdown Structure
FEEP	Field-emission electric propulsion
FFD	Functional Flow Diagram
FOV	Field of view
GIT	Gridded ion thruster
GPCU	General Power Control Unit
GPS	Global Positioning System
GSD	Ground Sample Distance
HET	Hall-Effect Thruster
IMU	Inertial Measurement Unit
IPPCU	Ion Propulsion Power Control Unit
ISL/C	Inter Satellite Link/Communications
LEO	Low Earth Orbit
LIDAR	Light Detection and Ranging
MP	Megapixels
OBC	On-Board Computer
PF	Packing Factor
RAAN	Right Ascension of Ascending Node
RIT	Radio Frequency Ion Technology
ROM	Rough Order of Magnitude
S/C	Spacecraft
SAR	Synthetic apature radar
SDR	Software-Defined Radio
SF	Safety Factor
SSO	Sun-Synchronous Orbit
TRL	Technology Readiness Level
TT&C	Tracking, Telemetry and Control
VLEO	Very Low Earth Orbit

Constants

μ_E	Earth's Gravitational Constant	398 600.44 km^3/s^2
σ	Stefan-Boltzmann Constant	5.67×10^{-8} $W/(m^2 K^4)$
c	Speed of Light	3×10^8 m/s
F_s	Solar Constant	1358 W/m^2
g_0	Earth's Gravitational Acceleration	9.806 65 m/s^2
MM_E	Magnetic Moment of the Earth	7.96×10^{15} $T m^3$
R_E	Earth's Radius	6378×10^3 m
t_{ES}	Length of Sidereal Year	3.156×10^7 s

Subscripts

0	Initial
aero	Aerodynamic
avg	Average
BOL	Beginning-of-Life
c	Collection
comms	Communication subsystem
cond	Conduction
day	Daylight
div	Divergence
E	Earth
e	Eclipse
eff	Effective
env	Environment
EOL	End-of-Life
g	Gravity gradient
int	Internal
IR	IR radiation from Earth
l	Line
m	Magnetic
misc	Miscellaneous
N	Normal
nom	Nominal
orb	Orbit
p	Plasma
prop	Propulsion subsystem
r	Receiver
s	Space
sp	Solar radiation pressure
sp	Specific
T	Tangential
t	Transmitter
trans	Transceiver

Symbols

#	Number of Particles	–

α	Absorptivity	–
α	Latitude	°
β	Angle between Orbital Plane and Sun	rad, °
δ	Longitude	°
δ	Solar Declination Angle	°
ϵ	Emissivity	–
η	Efficiency	–
γ	True Anomaly	°
λ	Thermal conductivity	W/(m K)
λ	Wavelength	m
Ω	Right Ascension of Ascending Node	°
ω	Angular Velocity	rad/s
ω	Natural frequency	rad/ sec
ϕ	Roll angle	rad
ϕ	Roll angle measured from nadir	rad
ψ	Yaw angle	°
ρ	Angular radius of satellite with respect to earth	rad
ρ	Density	kg/m^3
σ	Stress	Pa
τ	Shear stress	Pa
τ	Transmission Probability	–
θ	Angle of incidence	°
θ	Misalignment of local vertical to Earth and z-axis	rad
θ	Pitch angle	°
J_2	J_2 Perturbation	–
A	Area	m^2
a	Acceleration	m/s^2
a	Albedo factor	–
a	Semi-Major Axis	km
A_s	Area exposed to solar radiation	m^2
B	Earth's magnetic field	T
C	Capacity	W/h
C_0	Orbit day fraction	–
C_a	Solar panel inclination efficiency	–
C_D	Drag coefficient	–
c_{ps}	Centre of solar pressure	m
cg	Centre of gravity	m
CR	Compression ratio	–
D	Day of Year	–
D	Dipole moment	Am^2
D	Drag force	N
d	Diameter	m
df	Yearly degradation factor	–
DoD	Depth-of-discharge	–
DR	Data rate	bit/s
E	Elastic modulus	Pa
E	Electric field	V/m
e	Eccentricity	–
E_b/N_0	Signal to noise ratio	–
F	Force	N
F	View factor	–
f	Focal Length	m
FoV	Field of View	°
FR	Frame rate	frames/s
G	Gain	dB
G	Shear modulus	Pa
GRC	Ground resolution cell	m
h	Altitude	km
h	Thermal conductance	W/K
H_0	Hour Angle	°
I	Area moment of inertia	m
I	Current	A
I	Mass moment of inertia	kgm^2
i	Inclination	°
I_{sp}	Specific impulse	s
IPS	Intructions Per Second	
J	Radiation intensity	W/m^2
K_a	Degree of collimated incoming solar energy	–
K_s	Shear coefficient	–
L	Angular Momentum	kgm^2/s
L	Length of Spacecraft Structure	m
L	Loss	dB
l	Length	m
M	Bending moment	Nm
M	Mass	kg
m_p	molecular mass	kg
MD	Magnetic dipole	Am^2
N	Number	–
n	Refractive index	–
o	Obscuration ratio	–
P	Power	W
p	Pixel size	m
Q	Heat	W
q	Charge	C
R	Radius	m
r	Reflectance factor	–
S	Shear force	N
S	Surface area	m^2
T	Tension	N
T	Thrust	N
T	Torque	Nm
t	Thickness	m
t	Time	s
T_s	System noise temperature	K
U	Electric potential	V
V	Velocity	m/s
V	Voltage	V
v	Orbital Velocity	m/s
w	Deflection	m
Y	Lifetime of the spacecraft	years

Contents

1. Introduction

The space industry has been continuously expanding over the course of the past few decades. It has become more prominent in our everyday lives than most people realise. With applications ranging from communications and network services to planetary sensing and asteroid mining, endless opportunities arise. There are even spacecraft that have managed to escape from our solar system and reach interstellar space. In spite of all the fascinating discoveries to be made in other planets and even beyond our solar system, there remains an environment which has, as of yet, remained relatively unexplored. Surprisingly enough, it happens to be in very close proximity to the earth itself - more specifically, it lies at an altitude of around 200 km. This environment possesses a number of interesting characteristics, both in a positive and a negative sense. Due to the low altitude, we find ourselves in a highly erosive, drag inducing environment. There is, however, value to be found in operating at this altitude, so long as the aforementioned obstacles can be overcome.

Electrostatic air-breathing propulsion is proposed as a solution to this problem. In order to investigate this further, it is necessary to understand the working principles behind this propulsion system and the environment in which it must operate. Additionally the implications the environment has for the remaining subsystems should be considered. Objectives are subsequently established in order to drive the design process and the performance of the satellite. Thus, the goal of the mission is to design an electrostatic air-breathing satellite which is able to reliably operate at an altitude between 100-250 km for a duration of 10 years, all the while producing images with a resolution of 30 cm. Alternative payloads are considered as well, but the focus remains on the imaging payload.

After conducting literature reviews for each subsystem, three designs were conceived, each with a different working principle. A trade-off was then performed to select the most promising design, which is further developed in this stage. Consequently, the purpose of this report is to analyse all subsystems on a more detailed level in order to understand how they interact, both with each other and their surroundings. This allows for a careful consideration of the required components and how they will be integrated in the spacecraft body, henceforth referred to as RAMSES (RAM Satellite for Earth Sensing). The resulting final configuration is then analysed in the contexts of risk, reliability, sustainability, sensitivity and technical performance. Lastly, the feasibility of the design is evaluated and further recommendations are provided to account for points of improvement.

The report is structured as follows. The mission and the system is outlined in chapter 2, which includes the requirements and the final design which arises as a result of a trade-off. Then, chapter 3 consists of the market analysis and a cost breakdown of the satellite. In chapter 4 an overview of the design space is provided and it concludes with a selected altitude. This is followed by chapter 5 through chapter 13 in which all the subsystems are analysed and sized in detail. Subsequently the integration procedure is described in chapter 14, after which the sustainability of the design is assessed in chapter 15. Finally, future considerations and conclusions are discussed in chapter 16.

2. Mission Overview

This chapter presents an overview of the mission the satellite RAMSES will pursue. First, in section 2.1, the objectives of the mission is addressed. These objectives are rooted from the requirements which are outlined in section 2.2. The preliminary concepts which were defined in the previous design phase are outlined in section 2.3. Following that, the final design is described in section 2.4. For clarity, the coordinate system used for the entire design is discussed in section 2.5. Further features of the final design are described in section 2.6, and the mission profile is described in section 2.7.

2.1. Mission Objectives

Given the challenging nature that the mission environment will impose on the spacecraft, one of the primary mission objectives is to demonstrate the feasibility of electrostatic air-breathing technology and its ability to satisfy the imposed requirements, particularly because this would not be possible using conventional methods. Accordingly, the project objective statement is to *inspire ESA to pursue air-breathing electrostatic propulsion as a sustainable future propulsion technology by designing a technology demonstrator.*

LEO missions are becoming increasingly attractive for the space market, not least due to the increased imaging capabilities, but also for applications related to weather forecasting or surveillance services for instance. Despite these orbits providing numerous advantages, there are also significant drawbacks which limit the operational feasibility of spacecraft, particularly in VLEO where the presence of the atmosphere introduces complications, such as high drag and high erosion due to atomic oxygen, which have consequences on all the subsystems. With the introduction of this technology, part of this hindrance can be turned around and actually be used to one's advantage.

By developing and deploying a satellite into VLEO for an extended period of time, a better understanding of the environment is obtained; this aids in future air-breathing spacecraft developments and in optimising the propulsion systems to operate under these conditions. As a consequence of this, numerous other applications can be explored; these include Earth sensing or even designing constellations which can be used to provide global internet services, amongst others. This constitutes one of the primary mission objectives, which is to introduce novel techniques to the market all the while remaining competitive.

The novelty of the technology imposes the need for research and development, meaning that additional costs will be required as compared to conventional satellites. The objective is that these development costs will be outweighed by cost reductions in the future, especially since no propellant will have to be carried on-board and launches will be cheaper due to the lower altitude. The other significant advantage posed by air-breathing technology is that it is more sustainable. The reason for this is twofold; on the one hand, it means that propellant does not have to be manufactured and accounted for in the mass budget, but it also means that longer mission lifetimes in VLEO would be feasible. This would reduce the required launch frequency, which also provides environmental and financial advantages.

As a result of all the potential applications that RAMSES could fulfil, it is also imperative that the design is highly reliable; if this is not the case, all the other mission objectives will become void because the space industry is inherently risk averse, particularly when conventional methods are readily available at lower prices, at least for the time being.

Summarising all the above, the primary mission objective is to demonstrate, through analysis and flight, the feasibility of electrostatic air-breathing propulsion and its applications in the real world. In doing so, it would present an alternative to the market, allowing stakeholders to impose mission requirements that were previously not possible, and it would stimulate innovation in satellite design.

2.2. System Requirements

The system requirements of RAMSES are derived from the user requirements. These are listed in Table 2.1

Before immediately translating to system and mission requirements, the killer and driving requirements have been identified. The killer requirements are negotiated and rectified such that the feasibility of the mission can be achieved. REQ-USER-SAFE-01 is declared to be a killer requirement as achieving such a reliability over a 10-year-period is unattainable. This has been negotiated and the accepted requirement

Table 2.1: Acquired user requirement

Identifier	Requirement	Derived Requirement(s)
REQ-USER-PERF-01	Lifetime of 10 years	REQ-SYS-003
REQ-USER-PERF-02	Max weight below 100 to 150 kg	REQ-SYS-005
REQ-USER-PERF-03	Operating in VLEO [100-250 km]	REQ-SYS-006
REQ-USER-PERF-04	Imaging should be performed in the visible spectral	Refer to chapter 9
REQ-USER-PERF-05	Image resolution below 30 x 30 cm^2	REQ-MIS-002,
REQ-USER-PERF-06	Field of view above 2 x 2 km^2	Refer to chapter 9
REQ-USER-SAFE-01	Reliability of the system should be 99.9%	REQ-SYS-001
REQ-USER-SUS-01	Should not contain toxic materials	REQ-SYS-022
REQ-USER-SUS-02	Safe disposal at end of life	REQ-SYS-019
REQ-USER-SUS-03	People on ground should not be harmed (end of life, satellite malfunction)	REQ-SYS-020
REQ-USER-SUS-04	The system should not interfere with other orbiting objects	REQ-SYS-021
REQ-USER-ENG-01	Choice for launcher to be based on existing/foreseeable launchers (but no launcher design required)	REQ-SYS-006
REQ-USER-ENG-02	Total system volume/size/mass should comply with launcher payload restrictions / interfaces	REQ-SYS-007,-008,-009
REQ-USER-ENG-03	Launching loads should be taken into account	Refer to chapter 11
REQ-USER-COST-01	A realistic cost estimation should be provided that covers: design, manufacturing, delivery and operation costs	REQ-SYS-003
REQ-USER-OTHER-01	The satellite should feature an air-breathing electrostatic propulsion system	REQ-MIS-001

is given in REQ-SYS-002. The driving requirements are identified to be: REQ-USER-PERF-01, REQ-USER-PERF-02, REQ-USER-ENG-02, REQ-USER-ENG-03 and REQ-USER-OTHER-01.

Table 2.2: Derived mission requirements

ID	**Requirement**	**Met [✓/✗]**	**Section**
REQ-MIS-001	RAMSES shall demonstrate the use of air-breathing electrostatic propulsion system	✓	chapter 7
REQ-MIS-002	RAMSES shall perform image acquisition of Earth with a resolution below 30 x 30 cm^2	✗(34 x 34 cm^2)	chapter 9

2.3. Previous Phases of the Project

Before a description of the detailed design is carried out, a summary of the three concepts and the trade-off from the previous design phase is given. These designs vary more significantly by their mission objectives, thus differing in a more general system level approach. The first concept is the ‘Constant Density’ concept that as its name suggests, flies at constant density. The propulsion can then be optimised for a narrow range of conditions and is lighter and more reliable.

Next, there is the ‘Low Altitude’ concept that sustains its flight at the lowest possible height. Higher levels of drag need to be compensated thus requiring more power for the propulsion system. Therefore, this concept needs to fly at dusk-dawn orbit which means that its light condition is sub-optimal for imaging. This concept is then idealised for taking measurements of Earth’s gravity field with the use of GPS.

The last concept, "Highly" Elliptic requires the spacecraft to fly in an elliptic orbit where the pericentre is at 160 km and the apocentre at 400 km. The limits in the altitude range are driven from thermal and

aerodynamic attributes for the lower end, and with debris and density restrictions on the upper end. A detailed description of each concept with a mass and power budget can be seen in Table 2.4. Curious readers are referred to [1] for a more extensive discussion regarding the different concepts.

With these concepts, a trade-off was conducted. An inclusive and effective trade method has been defined such that the most important aspects of the design that are needed to accomplish the mission are captured. The criteria in order of their weights are: reliability & durability (0.32), feasibility (0.26), sensitivity (0.16), complexity (0.14), and mission value (0.12). Each of these criteria is further dissected into sub-criteria to better understand their implications. Thus, a rubric is created for each criterion such that for each of its sub-criterion, a grading of one to five is outlined. This way, no confusion or bias should come to the people that carry out the trade-off and the final results are justified. A more detailed explanation of the full trade-off mechanism can also be found in [1].

The result of the trade-off is shown in Table 2.5. It can be seen that the 'Constant Density' concept wins the trade-off, followed by the '"Highly" Elliptic' and lastly the 'Low Altitude' concept. Its win can be explained by its general all-good grades for each criterion. It outperforms the others in reliability & durability and complexity. The 'low altitude concept loses more significantly in the reliability & durability criterion which is critical as all of the designs are already constrained in reliability with the use of the low TRL propulsion system. In the other hand, the '"Highly" Elliptic' concept lags in feasibility. This criterion focuses on the mass constraint which is a driving requirement thus it must be enforced strictly.

A sensitivity analysis on the trade-off weights have also been conducted such that it can be assured that the final winner is justified. With this established, the 'Constant Density' concept can be confidently chosen. This report then outlines how this design is further developed in more detail.

2.4. Final Design Description

The 'Constant Density' concept has been further developed in the final design phase. Each subsystem relevant for the spacecraft is defined with supporting calculations. The analysis of each subsystem is delivered in the latter chapters of this report. The final design is summarised in Table 2.6.

After a thorough analysis, the final iteration of the spacecraft RAMSES has some differences from the originally defined 'Constant Density' concept. RAMSES carries three image sensors on board with four mirrors that are needed to achieve the required focal length. It still flies with an electrostatic air-breathing propulsion system, a gridded intake and a collimator that funnels the air into the engine. RAMSES has a trapezoidal structure, where the long side of the trapezoid is referred to as the 'top' side and where a portion of the solar panels are placed. On one of the slanted side of the structure, the imaging payload will be integrated. This side is to face the ground directly at all times. At one end of the spacecraft, there is the gridded intake while two S-shaped fins are attached on both sides of the spacecraft. These fins are integrated in order to obtain static stability of the spacecraft, particularly in pitch and yaw. More details on the subsystem is further explained in the course of the report.

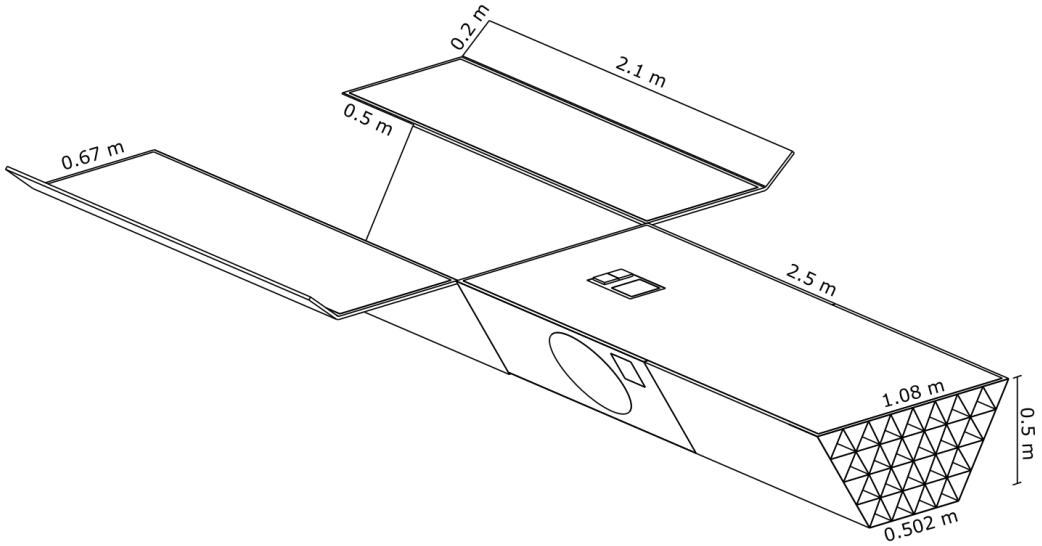

Figure 2.1: Final configuration and external dimensions of RAMSES

2.5. Coordinate System Description

The coordinate system used in this paper is the conventional spacecraft Cartesian coordinate system. The x-axis points in the velocity direction, the z-axis in the direction perpendicular to the bottom face, pointing outwards. The y-axis follows for a right handed coordinate system.

2.6. Functional Flow Diagram & Functional Breakdown Structure

The Functional Flow Diagram (FFD) can be found in Figure 2.2. In this, the various phases of the mission are identified, from design to end of mission, with particular care to the launch and operational phases, in order to use it as a tool to identify all aspects that have to be designed for. The blocks related to launcher operations are not further expanded, as this is outside the scope of the mission designers. Beginning and end of life of the mission are further discussed in section 11.3. The blocks of the FFD are expanded at least one level deeper in the Functional Breakdown Structure (FBS) in Figure 2.3. The lowest levels of the FBS correspond to the operation of the subsystems, which are discussed in dept throughout the report.

2.7. Mission Profile

The mission profile is described in this section and mentions the important mission aspects.

2.7.1. Beginning of life

A preferred launch date during a period of increasing solar activity is beneficial for the spacecraft. As the solar activity increases the uncertainty in the variations of the atmospheric conditions experienced by the satellite also increases. The larger power margin at the beginning of life results in the satellite being more resilient to these atmospheric variations. The launch date planned is ≈ 2033.

During launch the LauncherOne launch vehicle [14] is used to insert two units of the satellite into an orbit with an inclination of ≈96.485° and an altitude of 246 km to 252 km. The selected altitude depends on the exact solar and geomagnetic activity at the time of launch. The right ascending node will be selected based on the relative position of the Sun and the Earth such that it has an angle of 30°. Both satellites will not be able to operate their engines at these initial altitudes due to the low density. Over a period of two weeks the satellite will decay to their desired orbit and nominal operations can begin. This 2-week period before operations is to allow for the system to perform start-up checks and the out-gassing of the residual gasses present in the satellite.

As the two satellites are initially inserted into the same orbit, their orbits will have to be changed during operations. This is done by changing the right ascending node of one of the satellites using the on-board thruster. To maximise the Earth coverage of the 2 satellites, the orientation of the 2 orbits must be such that the ground track of one satellite cross in between the ground track of the other satellite.

2.7.2. Nominal operations

During nominal operations the satellite has to regularly check its orbital parameters. Firstly, it has to make sure the engine is operated at the density range that is designed for. This is done by finding and adjusting the orbital altitude by providing a small constant thrust. Secondly, the inclination has to be altered if the altitude is changed in order to maintain a Sun-synchronous orbit.

2.7.3. End of life

If no failure has occurred at the end of the lifetime, the power system will have degraded to a point where it is no longer able to supply the engine with the required power. At this point RAMSES will no longer be able to maintain its orbit and the EOL procedure will begin. At the low operating altitudes and thrust levels, no controlled re-entry is possible. As was analysed in section 11.3, the fatality probability for the re-entry is of an acceptable level for an uncontrolled re-entry. There are two strategies to initiate this re-entry procedure. The first is to simply reduce the thrust level to zero and allow the satellite to quickly decay and re-enter the atmosphere. The second strategy is to maintain the thrust level that can still be provided by the degraded system. Due to the reduced performance, this thrust level will not be sufficient to maintain the orbital altitude. As a result of this the satellite will slowly decay and eventually re-enter. During this extended decay time some data could be gathered on the behaviour of RAMSES during re-entry.

Table 2.3: Derived system requirements

ID	Requirement	Met [✓/✗]	Section
REQ-SYS-001	The system shall have a reliability of 90% over its lifespan.	✗(80%)	all subsystems
REQ-SYS-002	The system shall operate for at least ten years.	✓	
REQ-SYS-003	The cost affiliated for research, development, testing, and evaluation, and the unit costs of each component in the system shall be determined	✓	chapter 3, all subsystems
REQ-SYS-004	The system shall have a mass at launch between 100 and 150 kg	✓	chapter 14
REQ-SYS-005	The system shall orbit earth at an altitude between 100 and 250 km	✓	chapter 5
REQ-SYS-006	The system shall be launched with a reliable launcher.		chapter 11
REQ-SYS-007	The system shall have a centre of gravity location compliant with the chosen launcher.	✓	chapter 11
REQ-SYS-008	The system shall have outer dimensions compliant with the payload bay of the chosen launcher.	✓	chapter 11
REQ-SYS-009	The system shall interface with the payload bay of chosen launcher.	✓	chapter 11
REQ-SYS-010	The system shall have a thrust over drag of at least 1 when aligned with the flow.	✓	chapter 7
REQ-SYS-011	The system shall handle the power demands of each subsystem at any stage of the mission.	✓	chapter 8
REQ-SYS-012	The system shall be able to determine its orbital position and attitude	✓	chapter 5, chapter 10
REQ-SYS-013	The system shall be able to orient the spacecraft such that the optics on the payload-implemented side be able to directly faces the ground during nominal mode.	✓	chapter 10
REQ-SYS-014	The system shall be able to orient the spacecraft such that the solar panels point towards the Sun using minimum resources while maintaining power generation and a survivable thermal environment during safe mode.	✓	chapter 10
REQ-SYS-015	The system shall have passive static stability.	✓	chapter 10
REQ-SYS-016	The data handling system of the spacecraft shall manage the required data transfer and storage requirements of the relevant subsystems at any stage of the mission.	✓	chapter 13
REQ-SYS-017	The system shall be able to transfer the data acquired to the ground during its mission.	✓	chapter 6
REQ-SYS-018	The system shall be able to operate in the temperature ranges present in its environment throughout its lifetime	✓	chapter 12
REQ-SYS-019	The system shall perform a passive re-entry (no parachute, no active control).	✓	chapter 11
REQ-SYS-020	The system shall have a probability of less than 1e-4 of harming property, infrastructure or people during its lifespan.	✓	chapter 11
REQ-SYS-021	The system shall have a probability of less than 1e-4 of damaging other satellites during its lifespan.	✓	chapter 11
REQ-SYS-022	The system shall not use any material labelled as GHS08: Health hazard or GHS06: Toxic.	✓	chapter 11
REQ-SYS-023	The system shall use TRL 7 or higher technologies for mission critical systems except for the propulsion system	✗(TRL 3)	all subsystems

Table 2.4: Design characteristics for all three designs, including mass and power budgets

		Constant Density	Low Altitude	"Highly" Elliptic
Payload	Specifications	Spaceview 24 (2x) Resolution from 0.4 m/pixel to 0.48 m/pixel Engine sensors	Engine sensors GPS data for gravity field	Spaceview 24 Resolution from 0.29 m/pixel to 0.68 m/pixel Engine sensors GPS data for gravity field
	Mass & Power	20 kg, 20 W	0 kg, 0 W	10 kg, 20 W
Power	Power required	Day = 648 W Eclipse = 620 W	Day = 1140 W Eclipse = 1140 W	Day = 1170 W Eclipse = 607 W
	Solar Panels	Area = 5 m^2	Area = 6.8 m^2	Area = 7.2 m^2
	Batteries	Power density = 250 Wh/kg Depth of discharge = 0.25 Number of batteries = 2	Power density = 250 Wh/kg Depth of discharge = 0.25 Number of batteries = 2	Power density = 250 Wh/kg Depth of discharge = 0.25 Number of batteries = 1
	Mass & Power	46 kg, 0 W	64.9 kg, 0 W	46.3 kg, 0 W
ADCS	Disturbances	T_{aero} = 0.0024 N m $T_{sp} = 1.22 \times 10^{-5}$ N m $T_m = 5.59 \times 10^{-5}$ N m	T_{aero} = 0.0018 N m $T_{sp} = 1.52 \times 10^{-5}$ N m $T_m = 5.62 \times 10^{-5}$ N m	T_{aero} = 0.015 N m $T_{sp} = 1.84 \times 10^{-5}$ N m $T_m = 5.70 \times 10^{-5}$ N m
	Determination	Inertial measurement units: 2 Star sensors: 2 Sun sensors: 4	GPS-sensor: 2 Star sensors: 3 Sun sensors: 2	GPS-sensors: 2 Inertial measurement units: 2 Star sensors: 2
	Control	Magnetorquers: 6 (two sets of three) Passive aerodynamic fin	Magnetorquers: 3 Thrust vectoring	Magnetorquers: 6 (two sets of three) Reaction wheels: 4 (pyramid configuration)
	Mass & Power	7.6 kg, 36.6 W	6.8 kg, 25.6 W	7.6 kg, 36.6 W
Orbit	Type	Sun-synchronous	Sun-synchronous, dusk-dawn	Sun-synchronous
	Altitude	200 km to 240 km	190 km	160 km to 400 km
	Other	Circular orbit, small variations	Circular orbit	Eccentricity = 0.018
Communications	Specifications	Frequency = 19.7 GHz Antenna gain = 12 Antenna diameter = 20 cm Noise temperature = 400 K	Frequency = 19.7 GHz Antenna gain = 12 Antenna diameter = 20 cm Noise temperature = 400 K	Frequency = 19.7 GHz Antenna gain = 20 Antenna diameter = 40 cm Noise temperature = 600 K
	Mass & Power	8.2 kg, 13 W	6.5 kg, 10 W	11.1 kg, 17.7 W
Propulsion	Type	RAM-RIT-10 (1x)	RAM-RIT-10 (4x)	RAM-RIT-10 (2x)
	Characteristics per engine	$I_{sp} = 3.5 \times 10^3$ s Collection efficiency = 0.4 Max thrust = 5.8 mN	$I_{sp} = 3.5 \times 10^3$ s Collection efficiency = 0.35 Max thrust = 13.8 mN	$I_{sp} = 3.5 \times 10^3$ s Collection efficiency = 0.35 Max thrust = 7.05 mN
	Mass & Power	1.8 kg, 415 W	7.2 kg, 929 W	3.6 kg, 950 W
Aerodynamics		C_D = 2.5 Intake length = 3.22 m Intake area = 0.39 m^2 Frontal area = 0.47 m^2 C_DS = 1.18 m^2	C_D = 2.3 Intake length = 2.55 m Intake area = 0.24 m^2 Frontal area = 0.29 m^2 C_DS = 0.67 m^2	C_D = 2.6 Intake length = 4.55 m Intake area = 0.65 m^2 Frontal area = 0.78 m^2 C_DS=2.03 m^2
Miscellaneous		Intake = 25.8 kg, 0 W Structures = 32.1 kg, 0 W Other = 0 kg, 163.4 W	Intake = 9.6 kg, 0 W Structures = 27.9 kg, 0 W Other = 0 kg, 174.4 W	Intake = 31 kg, 0 W Structures = 34.2 kg, 0 W Other = 0 kg, 163.4 W
External Layout				
Internal Layout		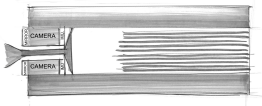	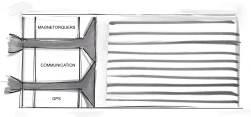	

Table 2.5: Trade Summary Table, legend: green is excellent, yellow is good, orange is sufficient and red is poort

Criteria / Concept	Reliability & Durability	Feasibility	Sensitivity	Complexity	Mission Value	Final Score
Constant Density	3.4	2.6	2.0	4.2	3.6	3.11
Low Altitude	2.7	3.3	3.3	2.9	2.1	2.89
"Highly" Elliptic	3.2	1.7	2.8	3.7	4.0	2.90

Table 2.6: RAMSES Design Overview

General	Total mass & power	129.82 kg, 487.11 W and 488.43 W average power during day and night
	Mission duration	10 years
	Launcher	LauncherOne
	Decommissioning	Passive re-entry
GNC	Orbit parameter	altitude range: 214 km - 240 km inclination change: 96.38° - 96.49° raan: 30°
	Orbit determination	magnetometer and star/sun sensors (budgeted in ADCS)
Communication	Specifications	Continuous contact with relay satellite 2× SWIFT KTX transceiver, 2× Ka-band antenna arrays, 2× power splitters for beam steering
	Mass & Power	2.55 kg, 34.2 W
Propulsion	Thruster	GIT RIT-10 I_{sp}: 3.5×10^3 s Min operating density: 0.65×10^{-10} kg/m^3 Max operating density: 1.5×10^{-19} kg/m^3-2.5×10^{-10} kg/m^3 Thrust: 2.3 mN - 5.8 mN
	Intake	Collection efficiency: 40%, Intake area: 0.396 m^2
	Mass & Power	16.8 kg, 415 W at maximum thrust
Power	Solar arrays	Mounted on main body and on fins Triple junction GaAs SpectroLab $Area_{main}$: 2.498 m^2 , $Area_{fin}$: 2.532 m^2 Power generated: 1171 W BOL, 957 W EOL
	Batteries	10 × 43Ah Lithium Ion Eaglepicher 3.6 V, 40,000 cycles at 40% DoD
	GPCU & IPPCU	Distribute 144 W and 415 W respectively
	Mass & Power	35.23 kg, 0 W (power included in internal efficiencies)
Payload	Specifications	Spatial resolution: 34 cm - 38 cm Chip: Gpixel GMAX3256 Spectral bands: red, green blue
	Optics	Focal length: 2.19 m Effective aperture: 42 cm 2× mirror out of C/SiC of 42 cm and 31.5 cm
	Mass & Power	30 kg, 30 W
ADCS	Determination	2× IMUs, 2× Magnetometers, 4× Sun sensors, 2× Star trackers
	Actuator	3× Magnetorquers
	Aerodynamic fins	S-shaped fins, Area: 5.5 m^2
	Mass & Power	12.1 kg, 29 W
Structures	Specifications	Material used: Carbon fiber reinforced polymer Coating: Polyimide Silica hybrid (transparent), perhydropolysilazane derived silica coating
	Mass & Power	32.8 kg, 0 W (no powered elements)
Thermal	Specifications	Passive system regulated with heat pipes Surface finish: aluminium kapton (5 mil), white paint Radiator area: 1.50 m^2 in total on zenith and bottom sides
	Mass & Power	4.6 kg, 0 W (passive)
C&DH	On-board computer	2× Proton2X-Box
	Mass & Power	2.2 kg, 21.3 W

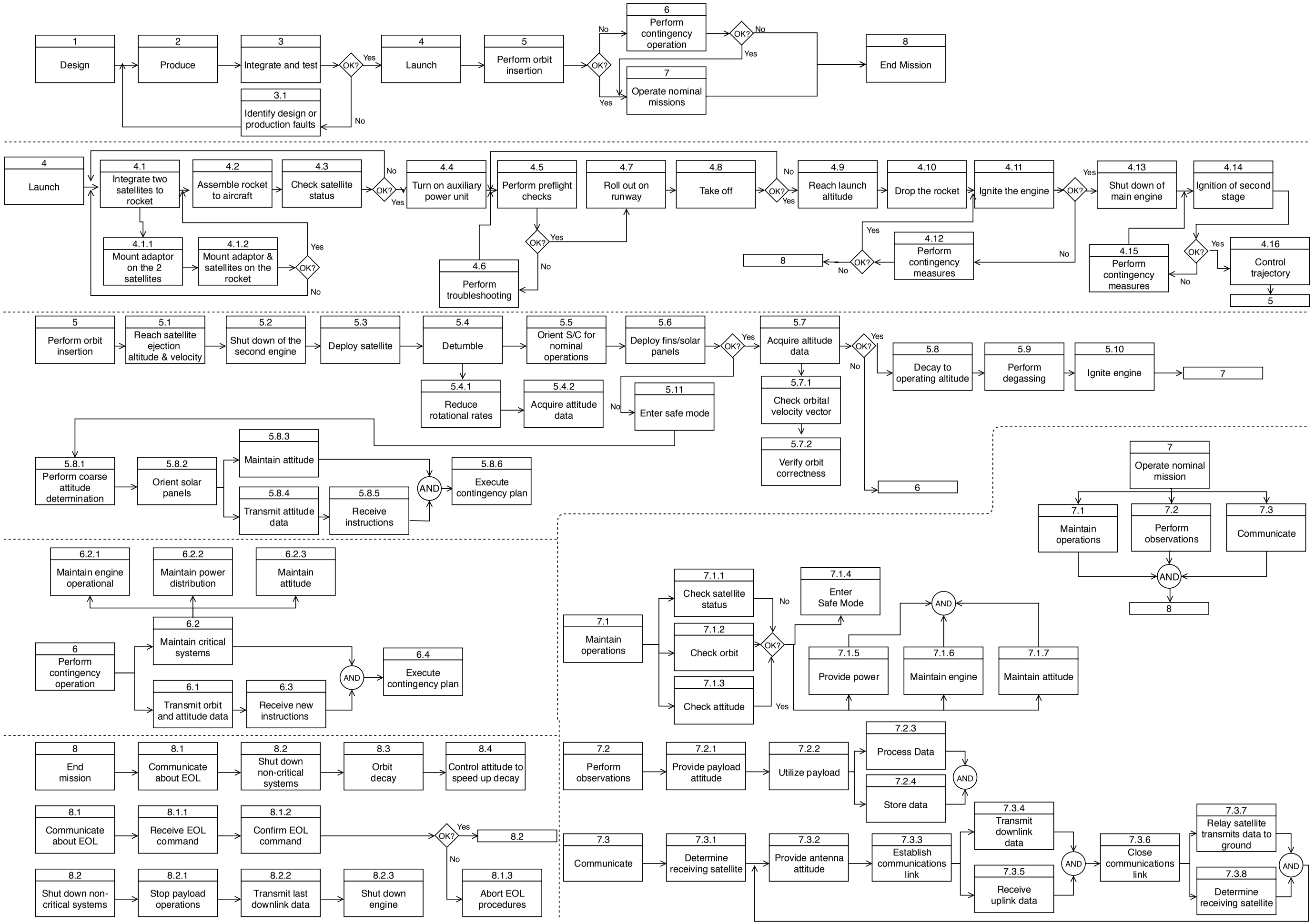

Figure 2.2: Functional flow diagram of the mission

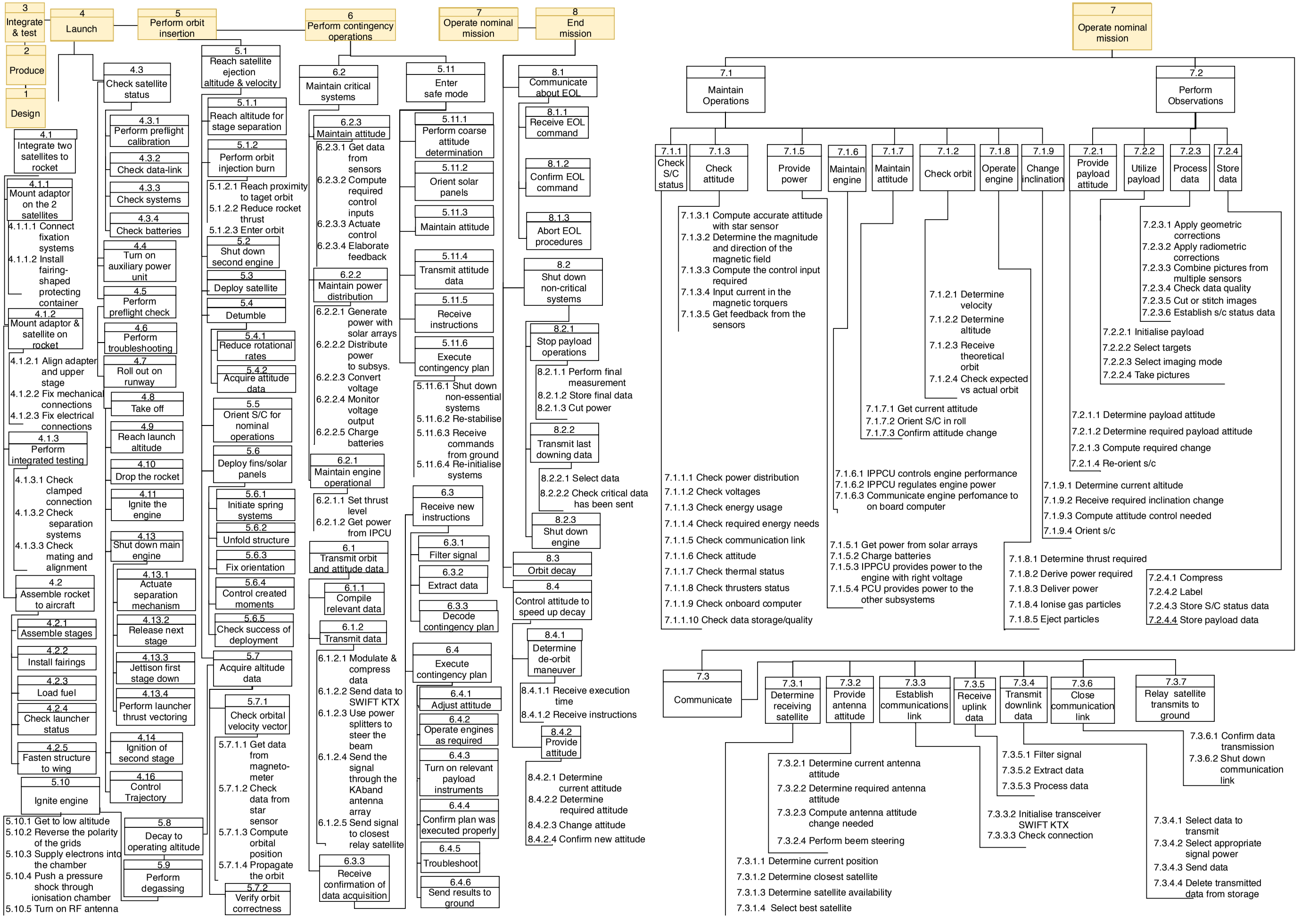

Figure 2.3: Functional breakdown structure of the mission

3. Market Analysis

This chapter describes the current Earth Observation (EO) market in section 3.1, followed by a consideration of the position of RAMSES in the EO market in section 3.2. To assess the competitiveness of RAMSES, a cost estimation is included in subsection 3.5.1, which is then compared to other EO missions in section 3.3. This section is concluded by discussing the use of air breathing propulsion for EO in section 3.4.

3.1. Current Market

The Earth observation (EO) market is worth 1.4 billion dollars in 2017 and is primarily dominated by the defence markets [15]. In 2027 it is expected that the EO market will reach a value of 2.4 billion dollars with the biggest growth in the non-defence market, although the defence market does remain the main driver [15]. The current price per square kilometre ranges from 0 to 500 dollars, with 1 m GSD optical images going for 5 dollars per square kilometre, as shown in Figure 3.1 [15]. Note that the trend currently pushes the high end sector to a higher price per square kilometre and a lower resolution and the high/medium resolution sector to a much lower price and lower resolution. This has to be taken into account when setting the price. Also note the announced competition from the constellations in pink and the aimed price for RAMSES in blue. This will be talked about in section 3.6. As a final note it is assumed that this data will be updated if a later launch data is selected.

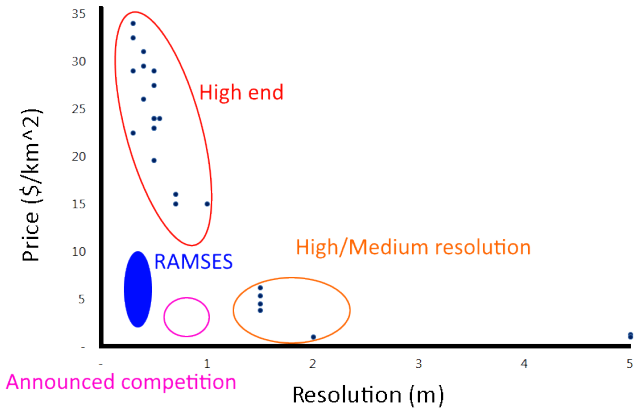

Figure 3.1: Prices of optical images per square kilometre in 2017 [15]

Currently earth observation missions that can provide a GSD below 0.5 m are taking the market share from satellites providing a GSD below 1 m; this trend of the smaller GSD market share increasing is likely to continue [15]. As can be seen in Figure 3.2, the market volume of ultra high resolution earth observation is steadily increasing. This will be advantageous for RAMSES as it operates well under the 0.5m resolution. It is therefore also expected that most of the potential customers are currently very high resolution consumers and will be drawn by the better resolution with a competitive price. In the near future some new competitors are announced to appear with resolutions between 0.5 and 1 m and prices under 5 dollar per square kilometre. This will have to be taken into account when considering the pricing over time. The interest in Synthetic Aperture Radar (SAR) is also worth mentioning as this can be used by algorithms and people almost as easily as optical systems but with smaller apertures.

3.2. Target Market

To identify the best markets for the RAMSES mission, the capabilities should first be identified. The imaging performance of RAMSES is shown in Table 3.1. How the payload achieves these performances is explained in chapter 9.

Currently the largest market for images from space is the defence market. The high resolution image capability of RAMSES as well as the capability to provide the images with very little delay via relay satellites to

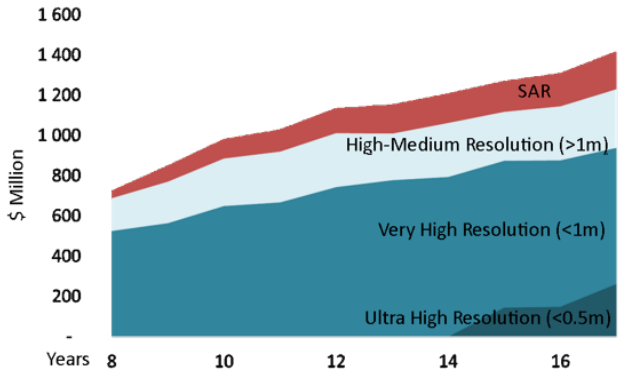

Figure 3.2: Market shares of different resolutions and their development over time [15]

Table 3.1: Capabilities of RAMSES

Parameter	Performance	Unit
GSD (maximum)	34	cm
FOV (average)	3.27 by 2.45	km
Spectral range	450-690	nm
Earth surface imaged a day	37000	km^2/d

virtually any place on Earth is very appealing for the defence market. Other interesting markets are the environment monitoring, infrastructure and natural resource markets. Currently these markets are relatively small, but they are expected to grow [15], making RAMSES future proof. Additionally, air-breathing propulsion satellites can be extended beyond taking images (see chapter 16). This opens up different markets where the use of air-breathing propulsion can also be more cost-effective [10].

3.3. Comparison to other Earth Observation Missions

An overview of some other Earth observation satellites is shown in Table 3.2. Comparing the values for the missions in the tables to the characteristics of RAMSES (Table 3.1), it can bee seen that RAMSES performs very well in terms of mass and resolution. The RAMSES mission performs less in terms of area imaged per day however. This is because of its small field of view and low altitude. The spectral range is also slightly lower than the other satellites, but that is because the RAMSES mission does not take images in the (near) infrared bands. It should also be noted that the satellite with the highest GSD in the table (WorldView-3) achieves this resolution only in the panchromatic band, not in colour as RAMSES does.

Table 3.2: Overview of Earth observation satellites [16]. The GSD listed is the lowest achievable

Mission	Imaged Area [10^3 km^2/d]	GSD [m]	Spectral Range [nm]	Weight [kg]
RAMSES	37	0.3	450-690	130
WorldView-3	630	0.3	450-800	2800
WorldView-2	785	0.5	450-800	2800
WorldView-1	750	0.5	450-900	2500
Quickbird-2	200	0.6	450-900	951
Ikonos	350	0.8	450-900	817
Asnaro	200	0.5	479-830	495
OrbView-3	210	1	450-900	360
SkySat-1/2	125	0.9	450-900	85
Pleiades	1000	0.5	479-830	970
GeoEye-1	500	0.5	450-800	1955

Overall, RAMSES can outperform some much heavier satellites in terms of resolution at the expense of some spectral bands and imaged areas. With a total mass of a little less than 150 kg, RAMSES is only second in mass, while producing the highest resolution colour images currently available.

3.4. Discussion on the Use of Air-Breathing Propulsion

The use of air-breathing propulsion on a spacecraft is a novel concept that has not yet been employed. Most customers are interested in the final picture and less in how the picture is obtained. They do however care about the cost and quality. The trend in earth observation satellites is to either go big in size or in quantity. Going bigger in size enables the satellites to have a much bigger aperture, a better accuracy and a longer lifetime, which translates to higher value pictures. The quantitative approach uses constellations that fly at lower altitudes with less mass and lower cost, but this is at the expense of reduced accuracy, lifetime and reliability. Moreover, in order for constellations to have a smaller GSD, lower altitudes are required with bigger apertures and often neither of these is possible while keeping cost low and lifetime long enough.

Drag compensation is done for most of these missions, as all satellites in low earth orbit experience considerable amounts of drag. Nowadays this is done with electric propulsion using some on-board propellant, but these systems become very heavy and therefore expensive very fast, especially when a mission of 5 years or longer is required. This is where air-breathing propulsion satellites like RAMSES come in. Air-breathing propulsion provides the capability to theoretically extend the mission life indefinitely and enables RAMSES to fly at very low altitudes of 200 km. This makes the GSD 3 times smaller than other earth observation satellites in low earth orbit at 600 km with the same aperture [11].

That being said, the current awareness of climate change is pushing the drive for more sustainable solutions. The space industry may be less affected by this push due to the difficulty of going to space, but more sustainable methods will increase the public acceptance. Air-breathing propulsion can provide a significant increase in this aspect. The use of air as a propellant also makes the propulsion system safer to work with due to the lack of dangerous chemicals. Additionally, it makes it much lighter thus requiring a much smaller launch vehicle.

3.5. Cost Breakdown

This section dissects the costs of the mission including development.

3.5.1. Cost Estimation

For the cost estimation, a quasi-grassroots approach (bottom-up) was chosen as any model that estimates the cost of a spacecraft assumes a conventional spacecraft without an air-breathing propulsion system. The costs are split up into research and development and unit costs, which will mainly be the production costs. This helps in finding the return on investment and can be used when exploring constellations. All the individual cost estimations can be found in the sections of the subsystems themselves, but an overview will be provided here in table Table 3.3.

The costs in Table 3.3 have both a cost estimation accuracy and technical risk attached to it. This serves to estimate the accuracy of the cost estimation. This shows that the cost estimation has a low average accuracy and a high technical risk, which is mainly attributed to inaccuracy and high technical risk of the most expensive components.

Not all costs can be attributed to subsystems as there are launch, operations, integration and testing costs. The launcher will be LauncherOne from virgin orbit and will cost 12 million dollar [1]. This will fit 2 RAMSES satellites and thus the cost per launch per satellite will be 6 million dollar or 5.3 million euros. The other additional costs will be broken down in subsection 3.5.2.

3.5.2. Post DSE Cost breakdown

To get an initial look into the potential cost for the post DSE phase an additional cost breakdown is made based on the post DSE Gantt chart (Figure 14.9). The cost is calculated using percentages (of the total spacecraft cost) reported in Reference [17]. The chosen percentages are shown in Table 3.4 and the cost breakdown structure itself in shown in Figure 3.3.

[1] `https://spacenews.com/virgin-orbit-plans-2018-first-launch/` [Cited on 25 June 2019]

Table 3.3: Overview of the subsystem specific cost

Subsystem	R&D and engineering cost (10^6 2019€)	Unit cost (10^6 2019€)	Cost estimate accuracy	Technical Risk	Notes
Propulsion	40.6	1.8	Low	High	See section 7.6
Power	0	1.1	Medium	Low	See section 8.7
Thermal	0.6	0.1	Medium	Low	See section 12.7
ADCS	0.2	0.2	High	Low	See section 10.7
Payload	17	6.8	Low	High	See section 9.7
Communication	0	0.2	High	Low	See section 13.7
Structures	14.3	2.9	Medium	Low	See section 11.7

Table 3.4: Percentages of total spacecraft cost per element

Element	Percentage	Comment
Systems engineering	20%	average
Project Management	15%	average
Contractor Fee	15%	high bound, higher risk due to demonstration aspect
System Integration & Test	33%	high bound, low TRL component that need testing before launch
Hardware/Software Integration	16%	average
Annual Operations and Support for Ground Station	5%	average
Data Management	2%	average

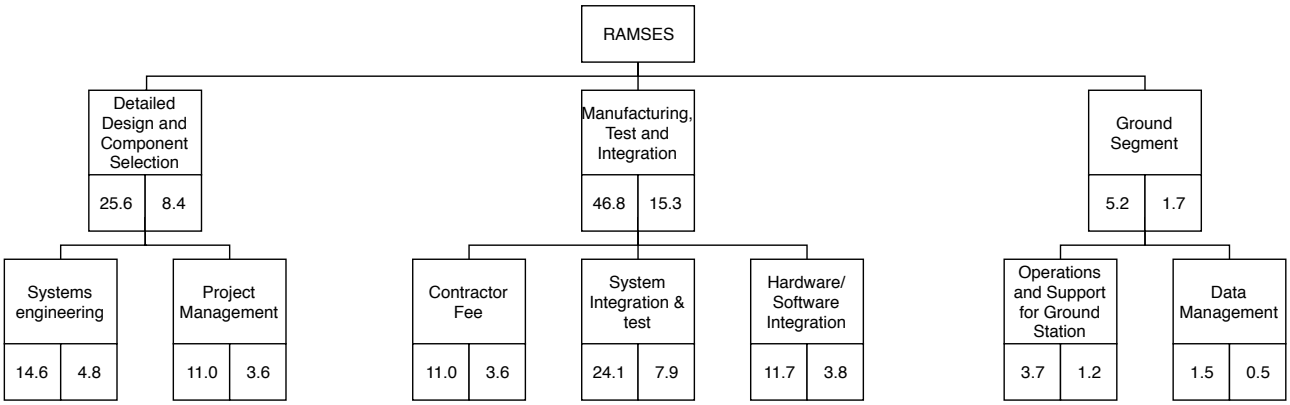

Figure 3.3: Cost breakdown structure of the post DSE phase. The number in the left box is the non-recurring cost and the number in the right box is the recurring cost. Both are given in 10^6 2019€

Adding all the costs the product will have a non reoccurring cost of 150,7 million 2019 euro and a unit cost per satellite of 39,8 million 2019 euro.

3.6. Return on Investment

In order to assess the economic viability the return on investment should be discussed. With the market price and volume as discussed in section 3.2, an achievable market share and price for the product can be set. Using the current market value in combination with the development, production and operational cost of the project determine the return on investment and the time this will take.

The market share was found in section 3.1 to be 1.4 in 2017 and growing toward 2.4 bilion in 2027 [15]. This suggests an average growth of 5.5% which is 77 million in the first year for the full earth observation

market and 125 million in the last year. Observing that the majority of the market has a resolution above 0.5 m and the interest in the lower resolution is rising. Therefore the market share that provide a lower than 0.5 m resolution will increase its share in the market as it grew by more than 50% in 2017. By taking on a very competitive pricing strategy and looking at the extreme grow of the ultra high resolution segment it is assumed that the available market share for RAMSES is 77-125 million dollars worth of pictures. Then looking at the pricing in this segment in Figure 3.1 prices range between 35 dollar per square kilometre and 20 dollar per square kilometre. In general satellites in this segment are however in more favourable orbit then RAMSES when looking at shadows, this should be taken into account when choosing a price. Therefore translating the market share of 77-125 million to square kilometres the market is interested in gives 10000 square kilometre. Then looking at the amount of pictures RAMSES captures (17.5% of the orbit). Because the available market volume is on average 100 million dollar per year and the average price 27.5 dollar per km^2, this gives 3.6 million km^2 when divided by 365 this gives 10000 km^2 which is 26% of the surface captured and therefore the selling efficiency is assumed to be 26%.

To figure the return on investment time out the cost should first be considered, see Table 3.5.

Table 3.5: Cost overview of RAMSES

Parameter	Value	Comment
Non-recurring costs	150.6	million 2019 euro
Cost per spacecraft	39.8	million 2019 euro
Number of spacecraft	2	
Surface captured	37 000 km^2/d	
Yearly cost per spacecraft	0.15	million 2019 euro
Selling efficiency	26%	Assumption based on market share

Using these costs in Table 3.5 the price course was set out in Table 3.6 to have a return on investment at 50% of the lifetime. This is the expected course of the price, however, it will be tried to keep the price higher if no significant market share loss is noticed to increase profits.

Table 3.6: Price overview of RAMSES over the years. Note that the years are only for indication and will have to be updated with more up to date data closer to the launch date.

Year	Price per km^2 ($)/(€)
2020	10/8.8
2021	10/8.8
2022	8/7.04
2023	8/7.04
2024	6/5.28
2025	6/5.28
2026	4/3.52
2027	4/3.52
2028	2/1.76
2029	2/1.76

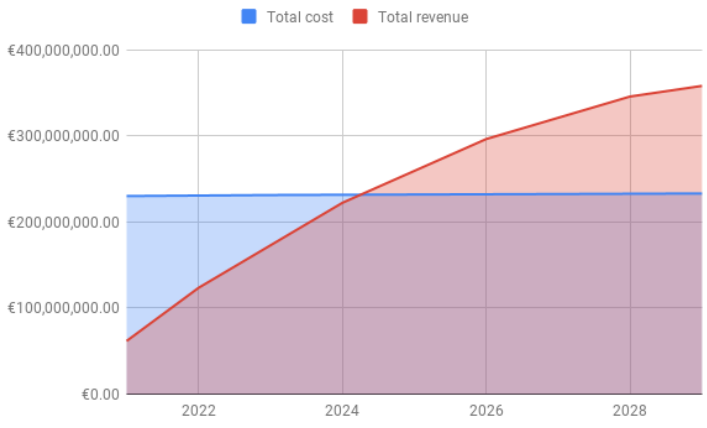

Figure 3.4: Total cost versus the total revenue.

Combining both Table 3.5 and Table 3.6 into the course of the total cost and total revenue gives the graph in Figure 3.4. It must be noted that increasing the amount of spacecraft would speed up the return on investment, this is however only possible if the available market share is big enough.

4. Initial Design Considerations

This chapter introduces the flow conditions encountered within the altitude range by looking more into the drag and thrust values for given altitudes and the accompanying densities. This will allow for an initial sizing of frontal area, intake and optimal range density. The exact altitude range will be further discussed in chapter 5.

4.1. Flow Conditions

The given altitude requirement of 100 to 250 km already determines the type of particles encountered quite well. The earth's atmosphere theoretically stops at 100 km, but that does not mean that there is suddenly no atmosphere at all. Within the earth's atmosphere, continuum flow exists. Far outside of the atmosphere, the aerodynamic conditions are called free molecular flow. This can no longer be considered as a flow, but more closely resembles individual particles coinciding with the spacecraft. To determine the border between the two flow conditions, the Knudsen number has to be calculated. This can be done by the use of Equation 4.1, where λ is the mean free path and L is the characteristic length [18].

$$Kn = \frac{\lambda}{L} \tag{4.1}$$

The mean free path of the particles, which represents the average distance between the collisions of particles, can straightforwardly be calculated when knowing the volume and the particle density, n_v. The characteristic length can be defined by any length that characterises the flow field. This value is mostly chosen based on reference values, so Knudsen numbers can be compared with other findings in literature.

When looking at this spacecraft's altitude range, the mean free path of the molecules is 0.16 m for 100km altitude. This means that free molecular flow is present at this altitude when the characteristic length is less than 0.16 m. Whether this is actually the case will be determined in section 4.2, where the dimensions of the frontal area will be determined, as well as the orbital altitude which determines the mean free path of the molecules. However, considering the density values at altitudes this low, free molecular flow conditions can be expected during further analyses.

The effects of free molecular flow on flow-surface interactions is based on the value of the accommodation coefficient which can be between zero and one. An accommodation coefficient of zero means that the molecule interaction is based on specular reflection, an accommodation coefficient of one forecasts diffuse reflection. For values in between, the amount of interactions of each type are determined to be proportional to the value. Specular reflection means that the molecules reflect under an angle, in the same fashion as optical reflection. Diffuse reflection is based on molecules colliding with the surface and reflecting in all directions randomly. This has large implications on force determination on the spacecraft as specular reflection creates forces normal to the surface of the object and diffuse reflections creates forces in the direction of impact.

4.2. Optimal Frontal Area Determination

An important part for the further design considerations is the determination of a starting intake area, extra frontal area and density range. This is done by finding an optimal equilibrium between the drag generated and the thrust produced by the engine. This gives an altitude range, directly coupled to a density range. This section will go through the parameters that influence the density range, as well as the methods used to acquire this range.

4.2.1. Parameters

One of the three main parameters is the drag value. Due to the free molecular flow conditions, the frontal area of the spacecraft is decisive for the total drag. Decreasing the frontal area thus has a large beneficial effect on the drag, but can have a detrimental effect on the other parameters.

One of these other parameters is the thrust that is produced. As opposed to the drag, increasing the frontal area to increase the intake area has a beneficial effect on the thrust. It will thus be a trade-off of

balancing drag and thrust and finding an optimal condition.

The third parameter that poses additional constraints on the previous two parameters, is the power required. Increasing the power to the system will increase drag, but there are limits as to what power can be generated within the limits of the mass requirements and space requirements.

4.2.2. Methodology

Calculating the drag is done using the standard drag formula for continuous flow given in Equation 4.2. This formula is seen as valid for atmospheric applications, as well as space applications. C_D is the drag coefficient, which is determined based on statistics, literature and the accommodation coefficient [18, 19]. The density can be retrieved from the atmospheric model, the velocity is determined by the orbit and the frontal area by the spacecraft lay-out.

$$D = C_D \cdot \frac{1}{2} \cdot \rho \cdot V^2 \cdot A_{frontal} \tag{4.2}$$

Thrust is largely affected by the engine parameters, including efficiencies, I_{sp}, Thrust-to-power ratio, et cetera. However, massflow does also have an influence on the thrust that can be produced as will be discussed in chapter 7. The available power is based on statistical estimations, as well as a first estimate of the amount of solar panel area that can be fitted. A reasonable number in terms of power generation for spacecraft of this size and weight was found to be around 500 W.

Combining these three different parameters is done by first choosing a thruster to size the design with. After considering a range of thrusters, the RIT-10 was chosen to be the one with the most potential. From this, the I_{sp} can be retrieved, as well as the efficiencies and the thrust-to-power ratio. Now the model can be started by inputting the power value that has been estimated to be 500 W. This power will give a thrust level, accompanied by an optimal mass flow requirement. This mass flow requirement is met by then re-sizing the intake, changing the frontal area and thus affecting drag. Finding the altitude where the thrust is 1.2 times higher than the drag can be done in this way by plotting the thrust and drag for each altitude.

To assess how sensitive these results are to changes in input parameters, a sensitivity analysis is conducted to asses C_D, efficiency, I_{sp}, power and thrust-to-power ratio.

4.2.3. Benefits of Constant Density on Design

This methodology outlined in subsection 4.2.2 calculates thrust and drag based on the altitude. The density at this altitude is retrieved using an atmospheric model discussed in chapter 5, so when calculating using constant inputs, the program is actually based on density more than on altitude. That is why the constant density design is very beneficial in terms of thrust and drag performance. The spacecraft can be designed based on one density and so, optimised in terms of intake and frontal area sizing.

4.2.4. Results

In an attempt to find a balance of drag and thrust, based on the power budget, it is found that the optimal altitude is somewhere around 200 km for minimum solar intensity and around 250 km for maximum solar intensity. This altitude range corresponds with a density of above 1.3×10^{-10} kg/m^3, which can be used to determine the intake size. At these altitudes, the mean free path is between approximately 10 and 15 kilometres, which results in a Knudsen number that is higher than 4000 when taking the length of the spacecraft as characteristic length. Since this is far higher than one, the assumption of free molecular flow is considered to be valid.

To supply the particle density required for optimal engine operations, the intake will have to be made large enough, taking into consideration its efficiencies. To take into account the 40% intake efficiency, the intake size is determined to be 0.39 m^2.

To create sufficient margin for other subsystems and take into account contingency, an additional frontal area of 20% of the intake area is assumed to account for systems that will create extra frontal area. This brings the estimated frontal area to 0.47 m^2, which will generate a total drag of around 4.8 mN, ensuring a thrust-to-drag ratio of just upwards of 1.2. This will allow for sufficient margin to comply with density changes, as well as orbital changes. It is thus determined that the system is expected to work at this density value, with these thruster parameters and intake area. Taking into account these values, the rest of the spacecraft can be designed on subsystem level in the following chapters.

5. Guidance, Navigation & Control

The functions and requirements of the GNC subsystem have been outlined in section 5.1. The relevant Keplarian elements of the satellite's orbit are briefly mentioned in subsection 5.2.1. In subsection 5.2.2 the required inclination to have a sun-synchronous orbit (SSO) and inclination change manoeuvre are described. In subsection 5.2.3 the influence of the right ascension of the ascending node (RAAN) on the eclipse time and observed lighting conditions are discussed and the optimal RAAN is chosen. The satellite's ground track is determined in subsection 5.2.4. In subsection 5.2.5 the atmospheric conditions experienced by the satellite and the altitude required to remain at a constant density are determined. In section 5.3 the verification and validation is performed, followed by a sensitivity analysis in section 5.4.

5.1. Functions & Requirements

The Guidance, Navigation & Control (GNC) subsystem has 3 main functions. Guidance refers to the determination of satellite's desired trajectory. Navigation refers to the determination of the satellite's state vector that describes the satellite's current orbit and position. Control refers to the necessary manipulation of the orientation and thrust of the satellite required to perform guidance commands while maintaining vehicle stability.

The requirements of the GNC subsystem have been outlined in Table 5.1. Requirement **GNC-001** is derived from the systems requirement **REQ-SYS-005** from section 2.2. The compliance of the requirements is checked in the outlined sections.

Table 5.1: Subsystem requirements for GNC

ID	Requirement	Notes	Met [✓/✗]	Section
GNC-001	The system shall orbit earth at an altitude between 100and 250 km.	REQ-SYS-005	✓	subsection 5.2.5
GNC-002	The satellite shall have a sun-synchronous orbit.	-	✓	subsection 5.2.2
GNC-003	The satellite shall determine its position with a maximum accuracy greater than 1 km.	-	✓	subsection 5.2.6
GNC-004	The satellite shall experience an average density of $1.3 \cdot 10^{-10}$ kg/m^3 at BOL and $1.05 \cdot 10^{-10}$ kg/m^3 at EOL.	-	✓	subsection 5.2.5

5.2. Methodology

This section includes the methodology and results regarding the determination of the desired inclination in subsection 5.2.2, RAAN in subsection 5.2.3 and altitude in subsection 5.2.5. The orbit determination system architecture and performance is outlined in subsection 5.2.6.

5.2.1. Orbital Parameters

Satellite orbits can be elliptic or circular, to reduce the density variation the satellite will have a circular orbit. The satellite's circular orbit and position can be described by using 4 Keplarian elements (a, Ω, γ & i) as visualised in Figure 5.1.

The ascending node is the location where the satellite crosses upwards through the plane of reference, for Earth orbiting satellite's it is the celestial equator. The descending node corresponds to the downward crossing of the celestial equator. The anti-nodes are located between the ascending and descending node.

For circular orbits, the semi-major axis (a) is the distance between the centres of the 2 orbiting bodies. The semi-major axis is given by $a = R_E + h$ where h is the altitude of the satellite above the Earth's surface.

To remain at a constant density the orbital altitude will vary from $h \approx 240$ km at high solar activity to $h \approx 214$ km at low solar activity. The required altitude to remain at a constant density is investigated in detail in subsection 5.2.5. The inclination (i) describes the vertical tilt of the orbit with respect to the celestial equator at the ascending node. The required inclination of a SSO is determined by the orbit's altitude. As the altitude of the satellite's orbit will vary, so will the inclination, from $i = 96.485°$ at $h = 240$ km to $i = 96.379°$ at $h = 214$ km. The inclination and inclination change manoeuvre are outlined in subsection 5.2.2.

The RAAN (Ω) horizontally orients the ascending node of the orbit. The RAAN influences solar panel integration, eclipse time and lighting conditions observed. A RAAN of $\Omega = 30°$ with respect to the sun resulted in the best compromise. The determination of the RAAN is discussed in further detail in subsection 5.2.3.

The true anomaly (γ) determined the position of the satellite within the orbit.

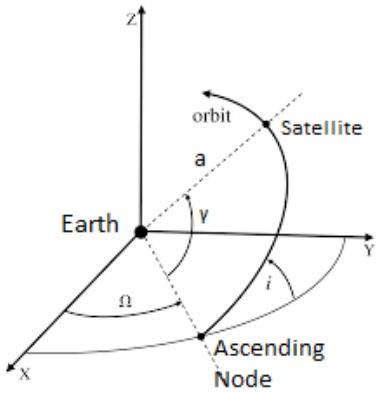

Figure 5.1: Visualisation of satellite orbit using Keplarian elements. Adapted from [1]

5.2.2. Sun-Synchronous Orbit

Irregularities of the Earth's shape and density result in a variation of the Earth's gravity field experienced by Earth orbiting satellites. The largest of these variations is known as the J_2 perturbation which models the flattening of the Earth at the equator. When a satellite crosses the equator the increased mass at the equator causes the satellite to be slightly pulled sideways with a changed RAAN but unchanged h and i.

The linearised perturbation of the J_2 effect on the rate of change of the RAAN is given by Equation 5.1. The magnitude of the J_2 perturbation on rate of change of the RAAN can be altered by changing the inclination of the satellite's orbit. If the rate of change of the RAAN is such that it matches the rotation of the Earth around the Sun, $\dot{\Omega} = \frac{2\pi}{t_{ES}}$, the orientation of the orbital plane with respect to the Sun will remain unchanged. This is known as a Sun-Synchronous Orbit (SSO). The RAAN of a perfect SSO will remain constant as the RAAN is defined with respect to the direction of the Sun.

$$\frac{d\Omega}{dt} = -3\pi J_2 \left(\frac{R_E}{a}\right)^2 \cos(i) \frac{1}{2\pi} \sqrt{\frac{\mu_E}{a^3}} \tag{5.1}$$

A SSO is useful for imaging satellites as the illumination angle of the surface below the satellite will be nearly the same. The inclination of the orbital plane required for a SSO is given in Figure 5.2 with $J_2 = 1.08263 \cdot 10^{-3}$ from [2]. The variation of the RAAN at $h = 214$ km and $i = 96.379°$ from Equation 5.1 has been simulated by propagating the satellite's orbit using Cowell's method for one days in Figure 5.3 using the python module poliastro. In Figure 5.3 the RAAN changes by approximately the angle the Earth has rotated around the sun in one day is $\Delta\Omega = 2\pi / t_{ES} \cdot t_{day} \approx 0.986°$. As the RAAN varies the orientation of the orbital plane with respect to the Sun will remain unchanged.

The orbital altitude of the satellite will vary from $h = 214$ km to $h = 240$ km throughout its lifetime to remain in a constant density. For the satellite to remain in a SSO, which is desirable in terms of payload performance, it will need to perform a low-thrust inclination raising/lowering manoeuvre. For an altitude variation of $h = 214$ km to $h = 245$ km the inclination of the orbital plane will change a maximum total angle of $\Delta i < 2(96.485° - 96.379°) = 0.212°$.

[1] `http://totaleclipse.eu/Astronomy/VSOP87.html` [Cited on 29 June 2019]

[2] `https://ai-solutions.com/_freeflyeruniversityguide/j2_perturbation.htm` [Cited on June 29 2019]

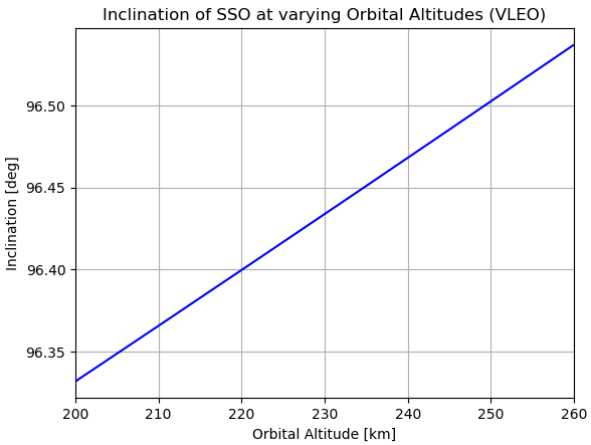

Figure 5.2: Orbit inclination angle at VLEO for SSO

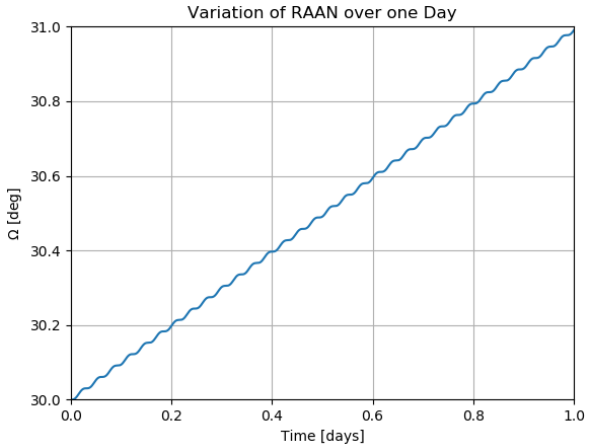

Figure 5.3: Variation of the RAAN using Cowell's method over 2 days with $h = 214$ km, $i = 96.379$ & $\Omega = 30°$

Methodology

Low-thrust manoeuvres for the efficient correction of the orbital inclination angle have been analysed. The Gauss form of the Lagrange Planetary Equations in Equation 5.2 [20] provides the time rate of change of the inclination angle for a normal acceleration a_n. The normal acceleration a_n is given by $a_n = T_{nom} sin(\psi)/M$ with $T_{nom} = 5.8$ mN, the nominal thrust of the engine.

$$\frac{di}{dt} = \frac{a_N \cos(\gamma)}{V} \tag{5.2}$$

The yaw angle (ψ) to achieve the maximum instantaneous change of inclination is given by Equation 5.3 [21], it has a magnitude of $\psi = 90°$ switching direction at the anti-nodes of the orbit corresponding to $\gamma = 90°, 270°$.

$$\psi = \text{sgn}(\cos(\gamma)) \cdot \frac{\pi}{2} \tag{5.3}$$

While $\psi = 90°$ results in the greatest change in inclination, the satellite is not capable of generating thrust at a yaw angle of $\psi = 90°$ as the inlet would no longer be aligned with the direction of the flow. The maximum yaw angle achievable by the spacecraft while generating sufficient thrust to compensate for drag in the axial direction was calculated in subsection 10.3.3 to be $\psi = 4.3°$.

Results

The variation of the inclination angle for a continuous normal acceleration over one orbit is shown in Figure 5.4 with $m = 150$ kg and $h = 214$ km at various yaw angles $\psi \in [0°, 3.5°]$. The highest rate of change of inclination is achieved at the nodes of the orbit where $\gamma = 0°$, 180°, while the smallest rate of change of inclination is achieved at the anti-nodes of the orbit where $\gamma = 90°$, 270° which corresponds to the flattening at t=1400 s, 4100 s in Figure 5.4. The effect of multiple inclination change manoeuvres on the orbital plane of the satellite is shown in Figure 5.5.

A high yaw angle will increase the inclination change after one orbit, however, the propulsion and ADCS subsystems must maintain this yaw angle throughout the orbit. A yaw angle of $\gamma = 1.0°$ was found to be optimal between these 2 conflicting interests. At this yaw angle the change in the inclination angle after one orbit is $\Delta i = 1.685 \cdot 10^{-5}$ °.

A first order estimation can be performed to estimate the amount of orbits in which the orbital inclination change must be performed to achieve the required inclination change of Δ i < 0.212° throughout the satellite's lifetime. A total of $0.212/1.685 \cdot 10^{-5} = 12{,}581$ orbits in which the inclination change manoeuvre is performed are required throughout the satellite's lifetime, this corresponds to 21.2% of the total amount of orbits.

The efficiency of the orbital inclination change manoeuvre could be further increased by only having an out of plane acceleration close to the nodes of the orbital plane, where the rate of change of the inclination angle is highest. This would reduce the amount of time the spacecraft is not aligned with the flow. Furthermore, the inclination change manoeuvre could only be performed over sea when the payload is not being

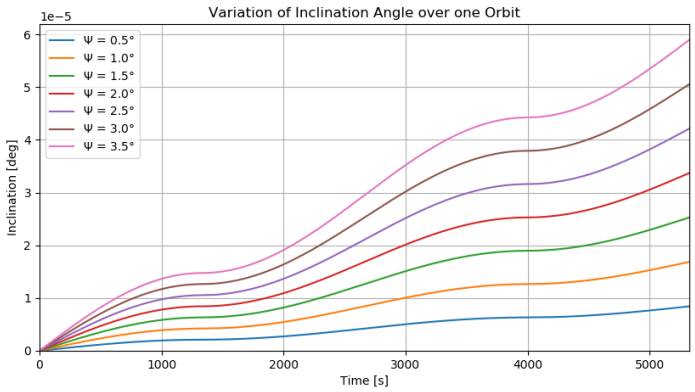

Figure 5.4: Variation of inclination angle for a continuous normal acceleration over one orbit using yaw angles $\psi \in [0°, 3.5°]$, $m = 150$ kg & $h = 214$ km

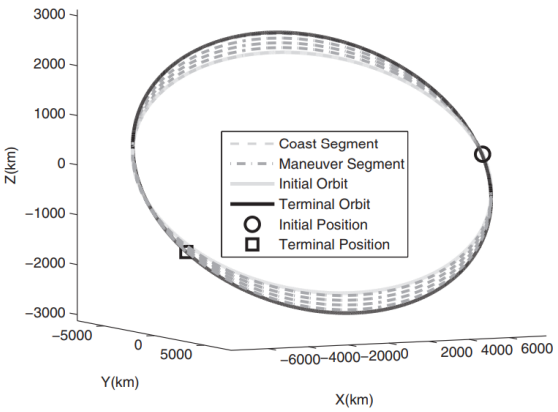

Figure 5.5: Trajectory of continuous inclination change manoeuvre [22]

used such to not affect the orientation of the pictures taken by the payload.

Effects of other gravity field irregularities such as the J_3 & $C_{2,2}$ perturbations will to a lesser extent also influence the orbit of the satellite. These perturbations should be investigated in further design phases.

5.2.3. Eclipse Time

The eclipse time is the amount of time throughout one orbit where the satellite is in shadow. The satellite will be in eclipse when it enters the shadow cylinder of the Earth as pictured in Figure 5.6. This occurs when the earth is located between the satellite and the Sun. The satellite eclipse time is dependant on the altitude, inclination and RAAN of the satellite's orbit.

The eclipse time is a driving parameter for the power, thermal & payload subsystems, thus the eclipse time must be accurately determined.

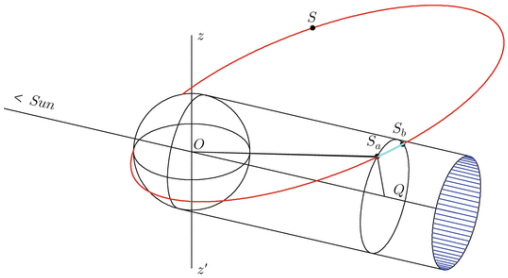

Figure 5.6: Satellite eclipse time visualisation [23]

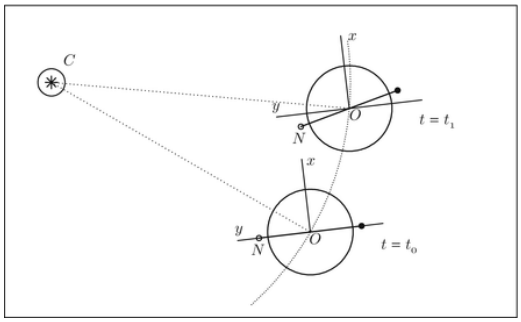

Figure 5.7: Position of geocentric frame (0) with RAAN (N) at two times t_0 and t_1 where C is the centre of the Sun [23]

The assumptions made in the calculation of the satellite eclipse time are outlined below:

- When the satellite enters the shadow cylinder of the earth it will experience a short period of penumbra in which part of the sun is covered by the earth. In [24] the penumbra time for a LEO high inclination satellite was determined to be less than 4% of the eclipse time, thus it can be considered to be negligible.
- Solar eclipses caused by the moon over the Earth have been neglected due to their sparse occurrence and complexity to model. The maximum duration of solar eclipses for VLEO orbiting satellite's is in the range of a few seconds and will only last 2 orbits [3], thus their effect can be considered negligible when compared to Earth eclipses.

Methodology

To determine the eclipse time of the satellite first the angle between the direction of the Sun and the orbital plane of the satellite β must be computed. For SSO the β angle is determined by solving Equation 5.4 [23]

[3] http://agi.com/news/blog/may-2012/impact-of-may-20-solar-eclipse-on-satellite-power?feed=AGIBlogsFeed [Cited on June 29 2019]

with H_0 from Equation 5.5 [23] and δ from Equation 5.6 [23].

$$\beta = \arcsin\{\sin i \cos\delta \sin H_0 + \cos i \sin\delta\} \tag{5.4}$$

The dihedral angle between the meridian plane of the Earth containing the ascending node (O) of the satellite and the plane containing the Sun (C) shown in Figure 5.7 is denoted by the hour angle. For SSO the hour angle does not vary, as the orientation of the orbit with respect to the sun remains unchanged due to the J_2 perturbation. The hour angle is determined by the RAAN of the satellite using Equation 5.5.

$$H_0 = 90° - \Omega \tag{5.5}$$

The axis about which the Earth rotates has an inclination of 23.45° to the plane of the Earth's meridian and the Sun's equator. The Earth's axis results in a variation of the angle between the Earth-Sun line and the Earth's meridian. This angle is the solar declination (δ) and may be estimated for any day of the year (D, $D = 1$ to $D = 365$) using Equation 5.6 to within 0.2°.

$$\delta(D) = asin\left\{0.39795 \sin\left[\frac{360}{365}(D-81) + 1.92 \sin\left(\frac{360}{365}\right)(D-3)\right]\right\} \tag{5.6}$$

The eclipse time of the satellite t_e is then computed by solving Equation 5.7 with $\eta = \frac{h}{R_e+h}$.

$$\mathfrak{U} = \frac{\sqrt{1-1/\eta^2}}{\cos\beta} \Rightarrow \begin{cases} t_e = \frac{T}{\pi} \arccos\mathfrak{U}, \text{ if } \mathfrak{U} < 1 \\ t_e = 0, \text{ if } \mathfrak{U} \geq 1 \end{cases} \tag{5.7}$$

Results

The orbital altitude and inclination of the satellite are fixed to achieve a constant density and a SSO, thus only the RAAN can vary. The eclipse time throughout one year with $h = 214$ km and $i = 96.379°$ and $\Omega \in [0°,60°]$ is shown in Figure 5.8.

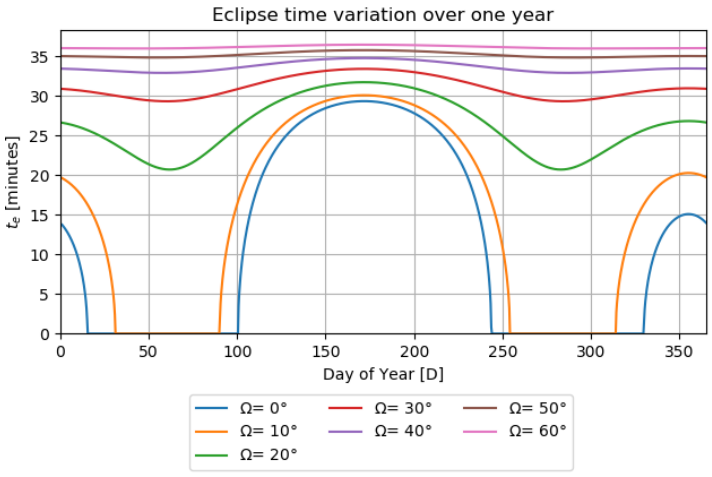

Figure 5.8: Satellite eclipse time variation throughout one year with $h = 214$ km and $i = 96.47°$ and $\Omega \in [0°, 60°]$

Orbits that have a high RAAN will experience a low variation in eclipse time throughout the year and will obtain better lighting conditions for the regions observed, however the satellite will also experience long eclipse times. For orbits with a lower RAAN, the satellite will experience large variations in eclipse times and poorer lighting conditions, however the eclipse time will decrease. An orbit with a RAAN of $\Omega = 0°$ corresponds to a Sun-dusk orbit, in this orbit the satellite will experience long periods with no eclipse time, however the satellite will constantly observe dusk conditions resulting in poor quality images.

A compromise between the eclipse time and lighting conditions was performed to determine the RAAN. A RAAN of $\Omega = 30°$ was found to be best suited for our satellite, as the variation of eclipse time is relatively small (14%) and the payload has good solar lighting conditions corresponding to 16:00 o'clock in the day.

The longest eclipse time experienced by the satellite is 33.3 minutes ($t_e/t_{orb} = 0.376$) it will occur at $h = 214$ km, $i = 96.379°$ and $\Omega = 30°$ with D = 170. The shortest eclipse time is 28.3 minutes ($t_e/t_{orb} = 0.319$) it will occur at $h = 240$ km, $i = 96.485°$ and $\Omega = 30°$ with D = 60, 270.

5.2.4. Ground Track

The satellite ground track is the path of the satellite over the Earth's surface as the spacecraft travels through its orbit. Due to the Earth's rotation the spacecraft will create a spiral pattern as it moves over the Earth's surface, with successive displacements at equatorial crossings proportional to the satellite's orbital period.

The calculation of the satellite ground track is necessary to determine the atmospheric conditions the satellite experiences throughout its orbit in subsection 5.2.5. Additionally, the satellite ground track and camera swath angle influence the satellite coverage & imaging capabilities of the satellite.

The assumptions made in the calculation of the satellite's ground track have been outlined below:

- The Earth is assumed to be perfectly spherical. Topological irregularities on the surface of the Earth lead to slight discrepancies between the calculated and true satellite ground track values.
- The change of the longitude of the RAAN due to the flattening of the earth (J2 perturbation) will rotate the orbital plane, leading to a difference of 6.73 km in the satellite ground track after one orbit. However, compared to the effect of the rotation of the Earth on the ground track, it accounts for less than a 0.3% difference thus it has be considered negligible.
- The satellite is assumed to have a southern velocity component, i.e. the satellite is rotating clockwise along its orbital plane when viewed from the sun.

Methodology

The ground track of a satellite orbiting in a circular orbit can be calculated by solving the dual axis problem visualised in Figure 5.9. Point $P(\alpha,\delta)$ represents the location of the satellite on the Earth's surface with latitude (α) and longitude (δ). Point P is at a constant angular distance $\rho_1 = i$ and constant angular velocity $w_1 = 2\pi / t_{ES}$ from point $S(\alpha_2,\delta_2)$. Point $S(\alpha_2,\delta_2)$ also rotates at a constant angular distance $\rho_2 = 90°$ from C and at a constant angular velocity $w_2 = 2\pi / t_{orb}$ around C.

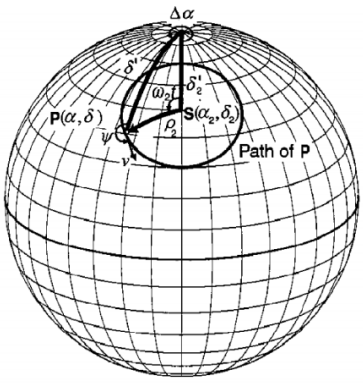

Figure 5.9: Dual axis problem diagram [25]

When evaluating inverse cosine trigonometric functions over the full range of 0° to 360° it is convenient to define an acos2 function in Equation 5.9. The acos2 function must be dependant on 2 variables because the function has 2 solutions over this range. For this purpose we also define the hemisphere function in Equation 5.8.

$$\begin{aligned} H(\varphi) &= 1 \quad if(0 \leq mod_{360}(\varphi) \leq 180°) \\ H(\varphi) &= -1 \quad if(180 \leq mod_{360}(\varphi) \leq 360°) \end{aligned} \tag{5.8}$$

$$acos2(cos(\varphi), H(\varphi)) = mod_{360}(H(\varphi)acos(\varphi)) \tag{5.9}$$

The equations governing the motion of the satellite using the dual axis problem from [25] are outlined in Equation 5.10, Equation 5.11, Equation 5.12 & Equation 5.13. The latitude and longitude of the satellite orbit represented on the earth's surface are determined by solving for α and δ.

$$\begin{aligned} \varphi_{20} &= -acos\left(\frac{sin\delta_0}{sin\rho_1}\right) \\ \varphi_{10} &= \alpha_0 + acos2\left(\frac{-sin\delta_0 cos\rho_1}{cos\delta sin\rho_1}, H(\varphi_{20})\right) \end{aligned} \tag{5.10}$$

$$\begin{aligned} \varphi_1 &= \varphi_{10} + \omega_1 t \\ \varphi_2 &= \varphi_{20} + \omega_2 t \end{aligned} \tag{5.11}$$

$$\delta'_P = a\cos\left(\cos\rho_1\cos\rho_2 + \sin\rho_1\sin\rho_2\cos\varphi_2\right) \qquad (5.12)$$
$$\delta = 90 - \delta'_p \quad (-90 \leq \delta \leq 90)$$

$$\Delta\alpha_{SP} = a\cos 2\left(\frac{\cos\rho_2 - \sin\delta_2\sin\delta}{\cos\delta_2\cos\delta}, -H\left(\varphi_2\right)\right) \qquad (5.13)$$
$$\alpha = \alpha_S + \Delta\alpha_{SP} \quad (-180 \leq \alpha \leq 180)$$

Results

The satellite's initial position at $t = 0$ must be known to determine its ground track. An initial latitude of $\alpha_0 = 0$ and longitude of $\delta_0 = 30°$ which correspond to the satellite crossing the RAAN at $t = 0$ where used. The satellite ground track after one orbit and one day at $i = 96.4°$ and $h = 214$ km is shown in Figure 5.10 and Figure 5.11. The percentage of the ground track over land is a driving parameter of the data rate, as the satellite will typically take pictures only over land. The percentage of ground track over land after 1000 orbits is 33.7%, however a conservative value of 35% is used for the communication system sizing.

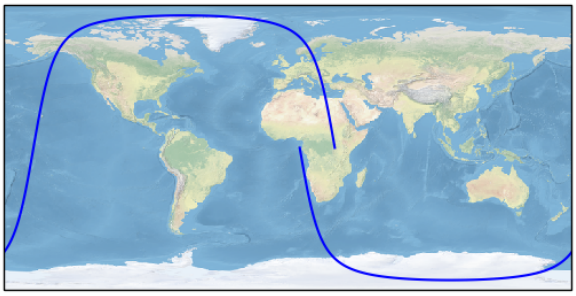

Figure 5.10: Satellite ground track over one orbit with $i = 96.379°$, $h = 214$ km, $\delta_0 = 30°$ & $\alpha_0 = 0$

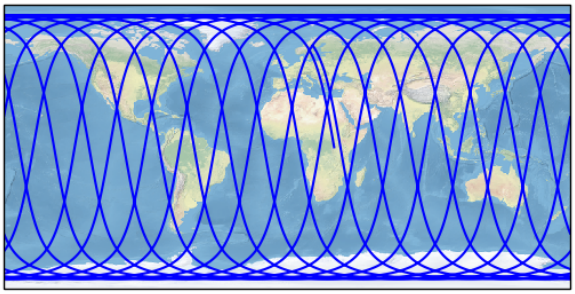

Figure 5.11: Satellite ground track over one day with $i = 96.485°$, $h = 214$ km, $\delta_0 = 30°$ & $\alpha_0 = 0$

The effect of the rotation of the earth is evident in Figure 5.10. The longitude of the ground track crossing the equatorial plane will shift by $-22.17°$ which corresponds to $\Delta\alpha = \omega_E t_{orb}$ after one orbit, as the Earth has rotated rightwards with respect to the satellite.

The satellite's ground track velocity affects the imaging frequency and data rate of the payload. The satellite's ground track velocity has been determined by calculating the distance ρ_E in and angular velocity ω_e of the satellite with respect to point $E(\alpha_E, \delta_E)$, the instantaneous centre of rotation. The highest satellite ground track velocity occurs at the lowest orbital altitude of $h = 214$ km with an average ground track velocity of 7840 m/s.

5.2.5. Atmospheric Conditions

The very low orbital altitude of the spacecraft allows for an unparalleled imaging quality at the cost of higher atmospheric drag. To compensate for this high drag the satellite uses a novel air-breathing electrostatic propulsion technology that accelerates the atmospheric particles to produce sufficient thrust. The operating density range of the engine, at which the engine is capable to function, is $\rho = [0.6{\cdot}10^{-10}\ \mathrm{kg/m^3}, 2.50{\cdot}10^{-10}\ \mathrm{kg/m^3}]$ at BOL and $\rho = [0.6 \cdot 10^{-10}\ \mathrm{kg/m^3}, 1.55 \cdot 10^{-10}\ \mathrm{kg/m^3}]$ at EOL. To determine the required orbital altitude to remain in this density range and analyse the density variations experienced by the satellite a detailed analysis of the atmospheric conditions experienced by the satellite is required.

Methodology

To determine the atmospheric conditions at any position over the Earth's surface an atmospheric model is required. The NRLMSISE-00 atmospheric model was chosen due to its wide adoption in the satellite industry and large amount of historical data. The NRLMSISE-00 is an empirical model developed by the US Naval Research Laboratory, it is based on earlier MSIS-86 & MSISE-90 models but updated with satellite drag data. The inputs of the NRLMSISE-00 model are the position (latitude, longitude & h), time (year, month, day, sec), geomagnetic AP indices and the solar flux F10.7 & F10.7A indices.

The geomagnetic AP indices, measured every 3 hours, represent the geomagnetic activity relative to a quiet-day scenario. The solar flux F10.7 index is an indicator of solar activity measured every day. The F10.7

index corresponds to the solar radio flux at 10.7 cm (2800 MHz). The F10.7A index is the 81-day averaged F10.7 index. The daily solar flux F10.7 index since 1955 is taken from the National Oceanic and Atmospheric Administration (NOAA)[4]. The geomagnetic *AP* indices are also taken from NOAA[5]. The processing and indexing of the solar flux and AP indices for a given time is managed by the Index Return program.

The location of the satellite over the Earth's surface is taken from the Satellite Ground Track program outlined in subsection 5.2.4.

The assumptions made in the atmospheric conditions determination are outlined below:

- The NRLMSISE-00 atmospheric model is not a perfect model of the Earth's atmosphere. Due to the complexity of the Earth's atmosphere and the lack of data at the altitude range analysed, this will lead to significant deviations of the modelled and true atmospheric conditions. In [26] the modelled derived to accelerometer derived atmospheric densities was determined to be 1.28 during high solar activity and 1.64 during low solar activity for the satellite Grace-A at h = 500 km. The atmospheric composition determined offers a first order approximation of the atmospheric conditions encountered by the satellite, further analysis of the atmospheric conditions at and variations at VLEO is required.
- The effect of the J_2 perturbation on the RAAN of the satellite is not considered in the determination of the satellite's location. The effect of the variation of the RAAN on the atmospheric conditions was found to be quite insensitive.
- The orbital altitude of the spacecraft to achieve the desired constant density is assumed to be only dependant on the F10.7 solar flux index. In reality, the density experienced by the satellite is also dependant on the time and geomagnetic AP index.

Results

The degradation of the power supplied by the satellites leads to a reduction in the density range at which the engine can operate, this leads to a reduction in the desired constant density throughout the lifetime of the satellite from $\rho = 1.3 \cdot 10^{-10}$ kg/m^3 at BOL to $\rho = 1.05 \cdot 10^{-10}$ kg/m^3 at EOL. The density experienced by the satellite throughout it's orbit, i.e. the density profile, will also vary. To ensure that the density variations are within the density range the engine can operate at, the average of the density experienced throughout it's orbit should correspond to the desired constant density of the engine.

The solar cycle follows a sinusoidal shape with a 11 year period, the satellite which has a lifetime of 10 years will nearly experience one full solar cycle. A time-varying seasonal analysis was performed on the $F10.7$ index data to determine the maximum and minimum seasonal $F10.7$ index. The maximum and minimum seasonal $F10.7$ index was determined to be $F10.7 = 190$ and $F10.7 = 43$ respectively.

According to the mission profile outlined in section 2.7, the satellite will be launched during a period of high solar activity. To achieve the desired constant density of $\rho = 1.3 \cdot 10^{-10}$ kg/m^3 during maximum solar activity the satellite requires an orbital altitude of $h = 240$ km. The density profile experienced by the satellite during high solar activity at h=240 km is shown in Figure 5.13. The minimum density of $\rho = 1.13 \cdot 10^{-10}$ kg/m^3 is experienced during eclipse conditions while the maximum density of $\rho = 1.48 \cdot 10^{-10}$ kg/m^3 is experienced when orbiting over sun lit areas. As the satellite approaches it's end of life, it will experience a low solar activity however the desired constant density will have decreased to $\rho = 1.05 \cdot 10^{-10}$ kg/m^3. To achieve this constant density the satellite requires an orbital altitude of $h = 214$ km. The density profile experienced by the satellite during a low solar activity at $h = 214$ km is shown in Figure 5.12.

The atmospheric composition (i.e the amount of particles per m^3) and atmospheric density (ρ) for high solar activity at h= 240 km and low solar activity at h = 214 km is included in Table 5.2.

Table 5.2: Average atmospheric conditions over one orbit

Altitude (km)	**O** (#/m^3)	**O^2** (#/m^3)	**N^2** (#/m^3)	**Ar** (#/m^3)	**H** (#/m^3)	**He** (#/m^3)	$\boldsymbol{\rho}$ (kg/m^3)
214	$1.56 \cdot 10^{15}$	$1.17 \cdot 10^{14}$	$1.22 \cdot 10^{15}$	$1.05 \cdot 10^{12}$	$8.20 \cdot 10^{11}$	$9.06 \cdot 10^{12}$	$1.05 \cdot 10^{-10}$
240	$2.24 \cdot 10^{15}$	$4.37 \cdot 10^{13}$	$1.46 \cdot 10^{15}$	$1.21 \cdot 10^{12}$	$6.02 \cdot 10^{10}$	$6.80 \cdot 10^{12}$	$1.30 \cdot 10^{-10}$

[4] `https://www.ngdc.noaa.gov/stp/space-weather/solar-data/solar-features/solar-radio/noontime-flux/penticton/penticton_observed/listings/listing_drao_noontime-flux-observed_daily.txt` [Cited on 24 June 2019]

[5] `ftp://ftp.ngdc.noaa.gov/STP/GEOMAGNETIC_DATA/INDICES/KP_AP'` [Cited on 24 June 2019]

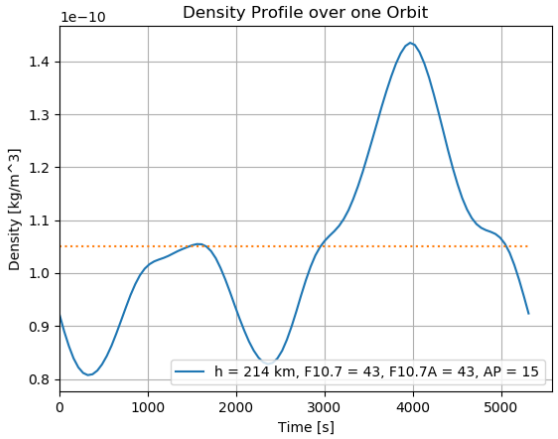

Figure 5.12: Density profile experienced by satellite over one orbit with h = 214 km, i=96.379° at Low Solar Intensity F10.7=F10.7A=43 & AP = 15

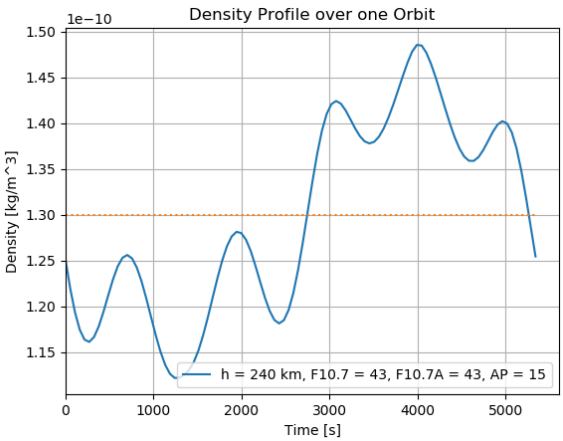

Figure 5.13: Density profile experienced by satellite over one orbit with h = 240 km, i=96.485° at High Solar Intensity F10.7=F10.7A=190 & AP = 15

A first order approximation of the altitude variation over the mission lifetime is shown in Figure 5.14. The altitude of the spacecraft is assumed to be dependant on the seasonal solar flux F10.7 index, thus the altitude profile follows the sinusoidal shape of the solar cycle over the mission lifetime. The degradation of the desired constant density of the engine is assumed to decrease exponentially from $\rho = 1.3 \cdot 10^{-10}$ kg/m^3 at BOL to $\rho = 1.05 \cdot 10^{-10}$ kg/m^3 at EOL.

The spacecraft will be launched during a period of increasing solar activity corresponding to an altitude of $h \approx 225$ km. It will reach a peak altitude of $h = 240$ km at high solar activity and then will slowly decay to an altitude of $h = 214$ km at low solar activity to remain at the desired constant density.

The change in semi-major axis a for a tangential acceleration a_T is given by Equation 5.14 [20] with $a_T = T_{nom}/M$ with $T_{nom} = 5.8$ mN.

$$\frac{da}{dt} = \frac{2a}{V} \cdot a_T \tag{5.14}$$

The required thrust to increase the altitude of the spacecraft to remain at the desired altitude for constant density was determined to be not larger than 0.2 mN. With a nominal thrust of $T_{nom} = 5.8mN$ and drag of $D_{nom} = 4.8mN$ the engine is more than capable of delivering this thrust.

Earth repeat orbits occur when the satellite ground track repeats itself after a certain amount of orbits. These orbits are beneficial for imaging specific areas with a high temporal resolution. Various repeat orbits have been implemented in the altitude profile in Figure 5.14 with a temporal resolutions of 6 - 14 days. Earth repeat orbits are of interest during decreasing solar activity, the satellite would attempt to remain at the designated altitude as long as the engine can operate and then "drop" to it's nominal operational altitude.

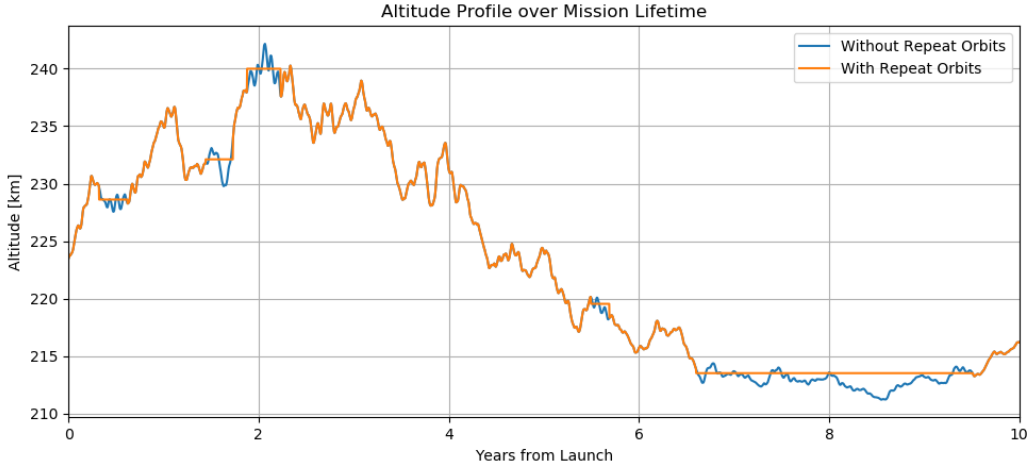

Figure 5.14: Altitude Profile over Mission Lifetime

5.2.6. Orbit Determination System

Perturbation of the gravitational field, atmospheric drag and other disturbances on the satellite lead to unforeseen variations of the satellite's orbit which increase with time. An accurate orbit determination system that computes the current orbit of the satellite and its corresponding Keplarian elements is required to known the current position of the satellite accurately throughout its lifetime. Orbit determination can be classified as the along-track, across-track and radial positions of the satellite, the orbit estimation accuracy refers to the total error of the combination of these three differences.

Orbit determination can be achieved with a range of sensors, typically the position of the satellite is computed through the use of a GPS receiver, 3-axis magnetometer, IMU, doppler tracking or through a combination of these sensors. The design philosophy of the orbit determination system was to rely on the existing attitude determination infrastructure outlined in section 10.3. Relying on the existing attitude determination system prevents the need to further increase the mass and power of the satellite and the creation of a new failure mode.

A combination of magnetometer and gyroscope/sun sensor measurements was found to estimate the orbital position to an accuracy that complies with the GNC-003 requirement and relies on existing attitude determination sensors. The measurement of the three-axis magnetometer is used to calculate the change rate of the geomagnetic field intensity vector. After being processed through a Kalman filter the rate of change of the geomagnetic field intensity vector is then compared against a geomagnetic field model. This provides an estimate of the position and velocity of the satellite from which the orbital elements can be derived. However, the position and velocity estimation derived from magnetometer measurements was found to be no better than a few tens of kilometres for positional errors in [27]. To reduce the position errors in the orbit determination system the measurements of the magnetometers are combined with those from the star sensor.

The orbit estimation accuracy can be reduced by combining the magnetometer and star sensor measurements. For a satellite at $i = 88.1°$ and $h = 550km$ the maximum error in along-track direction is 379 m, cross-track is 206 m and radial is 90 m according to [28]. The corresponding position estimation accuracy of the satellite is 675 m.

5.3. Verification & Validation

The verification and validation performed on the code used in subsection 5.2.2, subsection 5.2.3, subsection 5.2.4 and subsection 5.2.5 is outlined in this section.

The effect of the inclination on the RAAN of the satellite's orbit has been simulated over a period of one sidereal year (365.255 days) using Cowell's propagation method. The RAAN of the satellite is expected to rotate 360° over this period for the orbit to be sun-synchronous. However the RAAN was found to rotate 363.44° instead, this deviation is caused by the assumption of the linearization of the J_2 perturbation and having a discrete orbital inclination to 3 decimal places.

An analytical solution for the satellite eclipse time is provided in [29], this solution was used to validate the eclipse times determined in subsection 5.2.3. The analytical solution using $h = 214$ km, $i = 96.379°$ and $\Omega = 30°$ gave an eclipse fraction t_e/t_{orb} of 0.356 which lies within the upper and lower bound of the eclipse time calculated in subsection 5.2.3 of $t_e/t_{orb} = 0.330, 0.376$ for the same orbit.

The validation of the satellite ground track code was performed by using the test provided[6]. The inputs of the two test are provided in Table 5.3, the results obtained are compared to the reference values in Table 5.4. The values calculated by the ground track program match the reference values provided for the tests.

The atmospheric conditions obtained from the atmospheric model were compared against those obtained from the online NRLMSISE-00 atmospheric model[7] using the same inputs. The results were found to vary a maximum of ≈ 3%, expected from rounding errors.

5.4. Sensitivity Analysis

The sensitivity of the variation of the orbital elements (h, i & Ω) on the eclipse time, rate of change of the RAAN and density have been analysed in the sensitivity analysis.

[6] R. Noomen, "Space Mission Design: Full-sky spherical geometry V4-10," Delft, 2015. [Cited on 23 June 2019]

[7] `https://ccmc.gsfc.nasa.gov/modelweb/models/nrlmsise00.php` [Cited on 25 June 2019]

Table 5.3: Satellite ground track validation results

Parameter	Units	Test 1		Test 2	
		Ref.	Comp.	Ref.	Comp.
δ	°	46.04	46.04	56.08	56.08
α	°	335.48	335.48	37.05	37.05
v	rad/s	1.440	1.439	1.132	1.132

Table 5.4: Satellite ground track test scenarios

Parameter	Units	Test 1	Test 2
ρ	°	40	40
ρ_2	°	20	20
φ_1	°	5	5
φ_2	°	90	300
ω_1	rad/s	1	1
ω_2	rad/s	3	3

The sensitivity of the eclipse time to a change in the RAAN node of the satellite is included in Table 5.5. The maximum eclipse time of the satellite has a low sensitivity to a change in the RAAN of the satellite, varying by only 1.52 minutes for a change in RAAN of 10°. However, the minimum eclipse time shows a high sensitivity to a change in the RAAN of the satellite, varying by 5.72 minutes for a change in RAAN of 10°.

The change of the RAAN of the satellite's orbit shows a high sensitivity to a variation of the inclination of the satellite. A change of 0.1° on the inclination of the satellite's orbit will lead to a deviation of the RAAN of the satellite of at least 4° for the conditions analysed. The inclination change manoeuvres outlined in subsection 5.2.2 combined with an accurate orbit determination system outlined in subsection 5.2.6 is required to ensure that the satellite remains at the desired inclination to achieve a SSO.

Table 5.5: GNC Sensitivity Analysis

	Orbital Altitude h	Ω_{low} = 25°	Ω = 30°	Ω_{high} = 35°
$(t_e/t_{orb})_{max}$	h = 214 km	$-\Delta$ = 0.81 mts	33.34 mts	$+\Delta$ = 0.72 mts
$(t_e/t_{orb})_{min}$	h = 240 km	$-\Delta$ = -3.45 mts	28.47 mts	$+\Delta$ = 2.27 mts
		i_{low} = 96.279°	i = 96.379°	i_{high} = 96.479°
$\Delta\Omega$	h = 214 km	Δ = 5.360°	$\approx$ 360°	$-\Delta$ = 5.88 °
		i_{low} = 96.385°	i = 96.485°	i_{high} = 96.585°
$\Delta\Omega$	h = 240 km	Δ = 4.338°	$\approx$ 360°	$-\Delta$ = 6.753°

The sensitivity of the orbital altitude on the density range experienced by the satellite was also investigated. A variation of ± 5 km on the orbital altitude was investigated at BOL and EOL conditions. At BOL conditions corresponding to a high solar activity at h = 240 km, the average density experienced at h = 235 km and h = 245 km was computed to be $\rho = 1.428 \cdot 10^{-10}$ kg/m^3 and $\rho = 1.127 \cdot 10^{-10}$ kg/m^3 respectively. At these orbital altitudes the engine is able to operate within it's desired density range. At EOL conditions corresponding to a low solar activity at h = 214 km, the average density experienced at an orbital altitude of h = 209 km and h = 219 km was found to be $\rho = 1.28 \cdot 10^{-10}$ kg/m^3 and $\rho = 8.601 \cdot 10^{-11}$ kg/m^3 respectively. At an orbital altitude of h = 209 km experiences an atmospheric drag higher than the engine operational density range, to remain in orbit the engine requires more power that could be obtained from the redundant batteries.

6. Communications

Although the communications subsystem is not one of the mission's primary objectives, it is crucial to ensure the spacecraft's Telemetry, Tracking and Control (TT&C), to support nominal operations and to transmit data from the imaging and scientific payloads [17]. In this chapter, the requirements that drive the communications system design are firstly introduced in section 6.1; the approach to the design itself follows in section 6.2. The subsystem architecture and performance are described subsequently in section 6.3. Verification and validation of each of the previous section is performed in section 6.4. Moreover, section 6.6 is dedicated to the illustration of the system's risks and their mitigation, as well as a Reliability, Availability and Safety (RAS) analysis. The chapter is concluded with a sensitivity and cost analysis, in section 6.5 and section 6.7, respectively.

6.1. Functions and Requirements

The communications subsystem functions comprise command reception and detection, telemetry modulation and transmission, carrier tracking and the like. Its performance is strongly linked to the Command & Data Handling Subsystem. The main requirements for the communications of RAMSES are listed in Table 6.1.

6.2. Methodology

In this section, the strategy followed to design the communications subsystem is outlined. After having defined and verified the system's requirements and its expected functionalities, the standard procedure to size the communications subsystem is to adjudicate the type of link. The trade-off is illustrated in subsection 6.2.1. Thence, in conformity with the International Telecommunication Unit (ITU) regulation a frequency range is allocated in subsection 6.2.2.

6.2.1. Communication Link Type

In order to comply with **REQ-MIS-003**, from section 2.2, the design choices must be driven towards verified and used equipment (COTS and high TRL products); as a consequence, Radio Frequency (RF) is preferred to optical links and other frequencies (green block in in Figure 6.1). In the previous phases of the design process, directional links have been selected over omni-directional ones due to the constraints in the power budget. This choice is, hereby, confirmed; nonetheless, the direct contact with a ground station is now discarded. The nature of the orbit (near-polar, Sun-synchronous) implies that the satellite could commu-

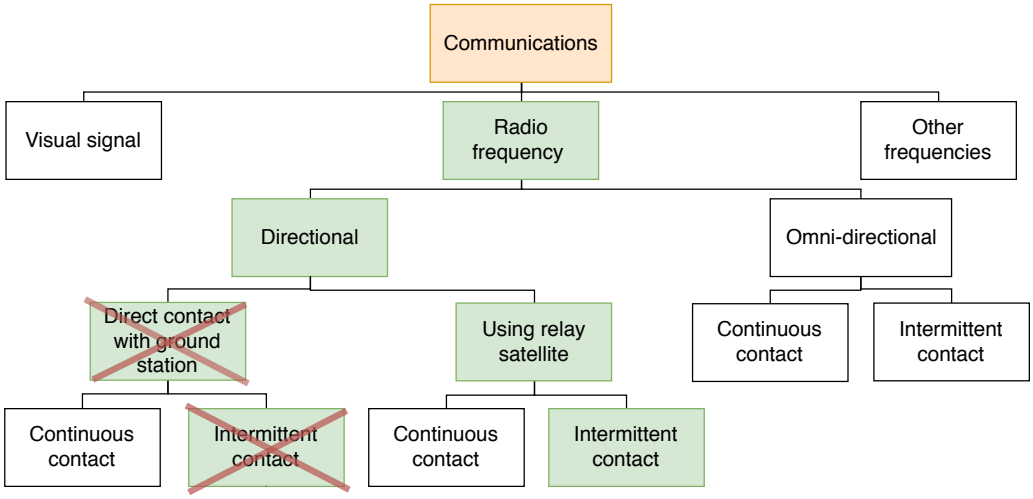

Figure 6.1: Design option tree for Communications

nicate with only two ground stations, and not in every orbit; moreover, the low altitude and, thus, the high orbital velocity would limit the contact time and, therefore, yield to enormous data rates (tens of Gbps)

Table 6.1: Subsystem requirements on the communications system.

ID	Requirement	Notes	Met [✓/✗]	Section
COMMS-001	The communications subsystem shall comply with RECOMMENDATION ITU-R SA.1414-2	[30]	✓	subsection 6.2.3
COMMS-002	The communications subsystem shall be able to receive signals from and transmit to constellations of relay satellites.	Use Kepler Constellation	✓	subsection 6.4.2
COMMS-003	The communications subsystem shall use Ka-band for uplink and downlink.		✓	subsection 6.2.3, 6.4.2
COMMS-004	The maximum Bit Error Rate during data downlink and uplink shall be better than 10^{-6} and 10^{-9}, respectively.	[30]	✓	subsection 6.4.2
COMMS-005	The communications link budget shall have a link margin of at least e dB.	[31]	✓	subsection 6.2.3,6.5
COMMS-006	The communications subsystem shall be able to downlink all data produced on-board.	see also on-board storage capacity in C&DH, section 13.2	✓	subsection 6.4.2
COMMS-007	The communications subsystem shall transmit a data rate lower than 100 Mbps.	Constraint from ITU Regulations	✓	subsection 6.4.2
COMMS-008	The communications subsystem shall be able to send down through a relay satellite a first sanity check at the moment of orbit insertion (204 or 214 km).	Refer to section 2.7	✓	section 6.4
COMMS-009	The link budget shall close with a transmitter power not exceeding 20 W.		✓	subsection 6.2.3
COMMS-010	The communications system shall be fully redundant.		✓	section 6.3

and to a substantial capacity of on board storage. In light of these considerations, the use of relay satellites is preferred. Miniaturised spacecraft flying in coordinated formations, constellations, are becoming more and more popular to enable inter-satellite links and other advanced functions, such as clock synchronisation and data exchange [32]. Existing LEO relay constellations are made by CubeSats at an altitude range of 495-850 km of altitude [33]. The QB-50 project [34] designed a 50 CubeSats constellation placed in one polar orbital plane at 300 km [33]. This link is deemed ideal for continuous communications of RAMSES; nonetheless these CubeSat do not operate in Ka-band, yet. As a consequence, Kepler 140 nanosatellites spinning around the Earth at 575 km altitude have been selected. These space birds orbit from pole-to-pole

providing continuous and complete coverage for the communications link in Ka-band[1]. The nanosatellites of this constellations are now being sent to space and they will be fully operative by 2022, before any expected RAMSES launch time.

An example of inter-satellite communications architecture is schematically represented in Figure 6.2.

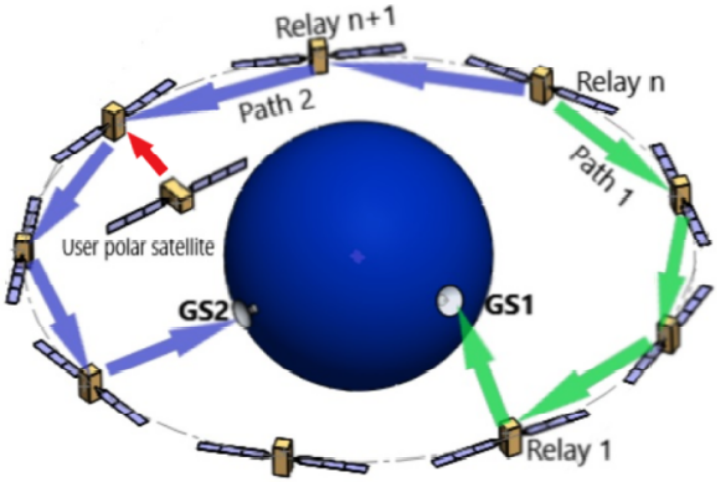

Figure 6.2: Scheme of communications to relay constellations [33]

6.2.2. Frequency Allocation

The appropriate frequency range can be selected in the pool of the possible bands given by the spectrum regulations of the (ITU) [32]. The bandwidth is related to the maximum data rate to transmit/receive via the Shannon-Hartley theorem [31]. Therefore, the data rates, both for downlink and uplink, must be retrieved first. These are, hereby, described and derived.

Downlink-Payload data

Over one orbit, the imaging payload is operational for about 17.5% of the orbital period. Only during one half of the orbit the ground track is illuminated and pictures can be taken. During about 65% of this period the camera would point to the oceans: the continuous variation in ground track implies that oceans' levels, ships and the like cannot be monitored constantly, making the use of the camera over these areas unnecessary. The derivation of the payload downlink data and its rate is shown step by step in Table 6.2.

Downlink-Housekeeping data

For the housekeeping data a safe estimate is 10 kbps [17]. The amount of downlink housekeeping data is double the value estimated for similar missions: this stems from the fact that RAMSES is a technology demonstrator, therefore on-board sensors must be used to monitor the engine performance. The entire housekeeping data comprises the S/C location, attitude, health and status conditions and, if need be, emergency messages.

Uplink data

RAMSES must be able to receive ranging tones and commands from ground via DRS:

- Orders about when to begin, modify and end operations. Entering safe mode might be needed, as well.
- Checks on the compliance of payload performance with the requirements.
- Possible extra requests from customers, for example to take video.
- Indications on attitude and motions changes needed.
- Emergency information and commands.
- Miscellaneous directives.

[1] `https://www.keplercommunications.com/network` [Cited on 20 June 2019]

[2] `https://business.esa.int/newcomers-earth-observation-guide/#eo_annex` [Cited on 18 June 2019]

Table 6.2: Imaging payload downlink data rate

Parameter	Symbol	Unit	Value	Source	Comments
Orbital Period	T_{orbit}	[s]	5306 to 5354.5	GNC section	to design for worst case, the minimum value is taken
Period in light	T_{light}	[s]	2653	$\frac{T_{orbit}}{2}$	GNC
Period for pictures	T_{pic}	[s]	928.55	$T_{light} \cdot 0.35$	GNC
# sensors GMAX3265	n	[-]	3	section 9.2	Red, Green, Blue
Pixels/image/sensor	pix	[Mpix]	65	section 9.2	9344 (H) x 7000 (V)
Frame rate	r_{frame}	[fps]	max 31	section 9.2	For images 6 fps at 11 bits are used
Frame rate efficiency	η_{fr}	[-]	0.95	[35]	Educated estimate
bits per pixel	bpp	[-/pix]	11	Comparison with similar missions[2]	
Compression ratio	CR	[-]	50	Comparison with literature data[36]	Max for JPEG 2000 Lossless compression
Rate code	ρ	[-]	1/2	[31]	for BpSK
Payload data rate	DR_{PL}	[Gbps]	12.2	$fps \cdot pix \cdot bpp \cdot n \cdot \eta_{fr}$	When payload is operative
Payload data/orbit	D	[Gb]	75.7	$DR_{pl} \cdot \frac{T_{pic}}{n \cdot CR}$	Processed & compressed
Payload downlink rate	DR	[Mbps]	28.5	$D/(\rho \cdot T_{orbit})$	Includes forward error correction

- Memory reload.

An educated estimate about a realistic value of the uplink data rate can be performed by looking at near-Earth missions values [17]: satellite normal and emergency modes would require a maximum of 2 kbps and 1 kbps, respectively. The memory reload delineates the highest contribution to the uplink: 1 Mbps. Thus, the maximum value of data rate that the satellite can expect to receive is 1.03 Mbps.

Downlink and Uplink Frequency

With respect to the uplink data rate, the downlink part is crucial and limiting to determine the necessary frequency range. The total downlink rate is the sum of processed data rate from the imaging payload and the housekeeping data: maximum 28.5 Gbps. For this high data rate a wide bandwidth is required; Ka-band is recommended [32]. The use of a single antenna type for both links, namely similar frequencies, might yield to interferences between uplink and downlink signals. To avoid these disturbances, a specific Software-Defined Radio (SDR) and transponder, SWIFT KTX , discussed in section 6.3, is implemented on board. Moreover, the use of Ka-band single antenna is recommended because, given a fixed antenna size, higher frequency than would be actually needed for uplink are favourable for higher signal gain [37].

6.2.3. Link Budget

In order to design the communications subsystem, evaluating the link budget for both downlink and uplink is useful to fix the values of transmitter power and the antenna gains for the various links involved [31]- once the link closes. In Table 6.3, the values used for the downlink link budget are listed and commented;

respective sources are provided to justify the figures and make the link repeatable.

Table 6.3: Downlink link budget

Parameter	Symbol	Unit	Value	Comments
Downlink Frequency	f_{down}	[GHz]	18	[17] Mid range of Ka-band
Transmitter Power	P_{tr}	[dBW]	17.2	Adjusted value to close the link budget
Transmitter Line Loss	L_l	[dB]	-0.96	[31] Educated estimation
Transmit Antenna Beamwidth	θ_t	[deg]	12	[38] Ka-Band Antenna
Peak Transmit Antenna Gain	G_{pt}	[dB]	12	[38] Gain for 8 element linear array
Transmit Antenna Pointing accuracy	e_t	[deg]	0.5	[39] Estimate from Ka-band CubeSat arrays
Transmit Antenna Pointing Loss	L_{pt}	[dB]	-0.02	$-12\left(e_t/\theta_t\right)^2$, derived from [31]
Transmit Antenna Polarisation loss	L_{pol}	[dB]	0.2	[39] Estimate from Ka-band CubeSat arrays in LEO
Transmit Antenna Gain	G_t	[dB]	11.8	G_{pt}-L_{pt}-L_{pol}, derived from [39]
Equiv. Isotropic Radiated Power	EIRP	[dBW]	23.17	$10\cdot\log(P_{tr})$+ L_l +G_t, derived from [31]
Propagation Path Length	S	[km]	361	h_{const}- $h_{s/c\text{-}min}$ Minimum s/c altitude to size for the worst case scenario
Space Loss	L_s	[dB]	-168.61	$L_s = \left(\frac{c}{4\pi S f_{down}}\right)^2$, c = 299792458 m/s [31]
Receive Antenna Gain	G_r	[dB]	49	[30] ITU Regulations for Europe (LEO)-comprises losses
System Noise Temperature	T_s	[K]	800	[30] ITU Regulations for Europe (LEO)
Data Rate	DR	[Mbps]	25.8	subsection 6.2.2, Both payload and housekeeping data
Bir Error Rate	BER	[-]	10^{-6}	[40] [31] Acceptable value from literature
Ratio of Received Energy per Bit to Noise Density	E_b/N_o	[dB]	10.20	EIRP+L_s+G_r- $10\cdot\log T_s$+228.6 - $10\cdot\log DR$ [31]
Required E_b/N_o	$Req E_b/N_o$	[dB-Hz]	5	[31], From chart of BEP vs E_b/N_o for selected modulation type
Implementation Loss	loss	[dB]	-1.5	[17] Educated Estimation
Margin	M	[dB]	3.70	E_b/N_o-$Req E_b/N_o$+loss, Relation from [31]

In Table 6.3, the margin results to be 3.70 dB, which is deemed enough[31].It is custom to design the system for a larger margin: the reason for this is to accommodate atmospheric and rain losses, and link availability. Notwithstanding, the aforementioned losses can be neglected insofar as the ISL have been selected. Additionally, the European section of Radiocommunication sector of ITU [30] defines the reliability of forward DRS-to-spacecraft link and return spacecraft-to-DRS link to be 99.6% (Rec. ITU-R SA.1414-2). In light of these considerations, 3.70 dB of margin is considered sufficient; therefore, the transmitter antenna power is fixed to 17.2 W. Finally, it is worth noticing that all the receiver data are taken from the ITU specifications of European LEO DRS.

As far as the uplink is concerned, the frequency is defined to be 28 GHz, in the mid range of the Ka-band for uplink. The European ITU-R S.672 regulation for uplink to a LEO DRS specifies the requirements of the receiving spacecraft. Therefore, instead of computing the entire link budget, the compliance of RAMSES characteristics with the required features is hereby verified. For a link reliability of 99.6%, $req\mathrm{E_b/N_o}$ and BER are necessitated to be 2.8 dB at and 10^{-9}, respectively. For this incredibly low value of BER, the $\mathrm{E_b/N_o}$ is estimated to be 7.5 dB [31]. After having fixed the antenna power to 17.2 as before and using the relay satellite's characteristics from [30], the link budget safely closes.

6.3. Architecture & Performance

The data rate and the link budgets investigated in section 6.2 have been indispensable to size the entire communications subsystem architecture, whose schematic representation is shown in Figure 6.3.

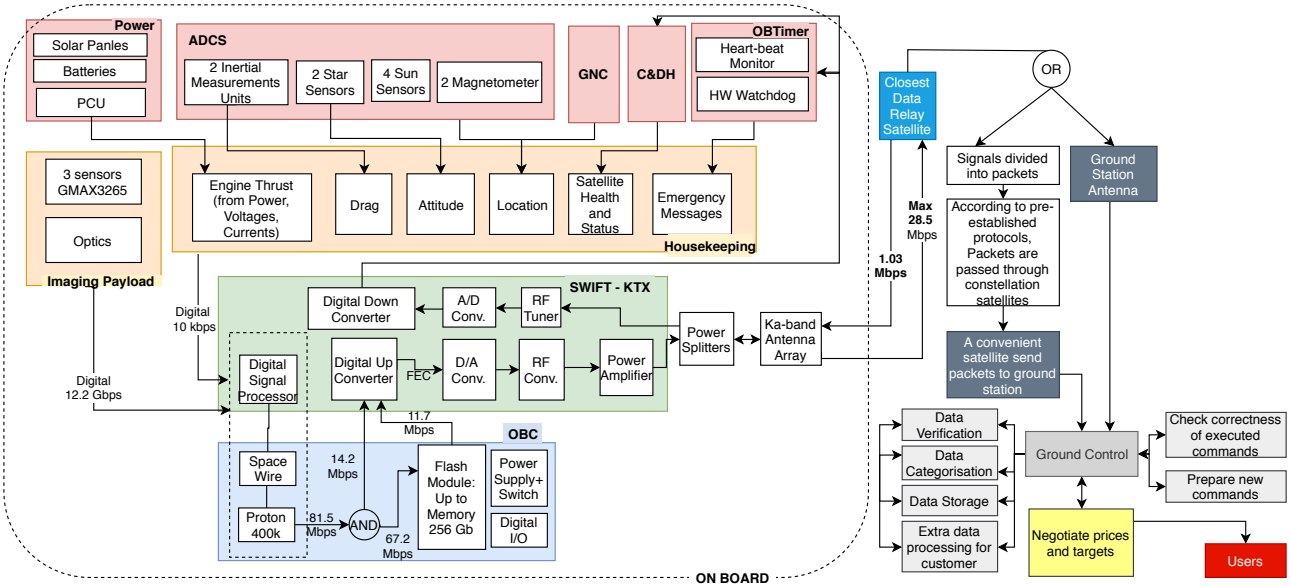

Figure 6.3: Communications subsystem block diagram and scheme of data flow

In Figure 6.3, the red blocks represent the satellite subsystems interacting with the communications architecture. In details, the latter comprises two SWIFT KTX, Software-Defined Radio (SDR) and transceiver, two eight-entries power splitters and three Ka-band antenna arrays (two on the top surface and one on the side)- all components have redundancy.

The power subsystem feeds all the components and its PCU furnishes data on the power, voltages and currents used by the engine; with these, it is possible to compute the thrust level, which is retrieved to study the propulsion system's performance. The rest of the housekeeping data includes the satellite's drag, derived by the on-board accelerometers, the attitude, delivered by the ADCS sensors, the spacecraft location, computed by ADCS and GNC. C&DH provides information upon the satellite's health and status, whilst the on-board timer might send emergency messages, if need be. The housekeeping data sums up to 10 kbps, as discussed in section 6.2. The major components of the downlink data is received from the imaging payload: its raw rate amounts to 12.2 Gbps. The unprocessed data rate enters the SWIFT-KTX: its Digital Signal Processing (DSP) is connected through the SpaceWire interface to the processor: the data is processed and compressed. Parts of it is stored temporarily to reduce the downlink data rate. The rest passes through Digital Up Converter DUC and the Digital-Analog Converter. The analog signal is modulated at the correct radio frequency and Forward Error Correction (FEC) is applied. The SWIFT-KTX is connected to power splitters that are responsible for the antenna beam steering. The 25.8 Mbps beam is steered from the antenna array (see image in Table 6.2) towards the nearest DRS.

From Figure 6.3, the uplink can be easily traced, as well: it is similar yet less complex than the downlink process and its data is transmitted to the OBC, C&DH and the OBTimer.

It is worth noticing that the communications system has to operate even outside of the nominal operations windows: right after the orbit insertion, the satellite has to send down status check signals and might need to receive some commands from the ground. Therefore, communications must be possible also at the

altitude of the orbit insertion, nominally 204 km. Note that this value might vary according to the launch date (for more details see chapter 5).

After having considered the subsystem performance, the architecture specifications are illustrated.

Ka-band Antenna Array

The Antenna Array has been chosen in the OrbanMicrowave catalogue [38], visible in Figure 6.4. The use of COTS is to enhance the system's reliability: this element is high radiation resistant.

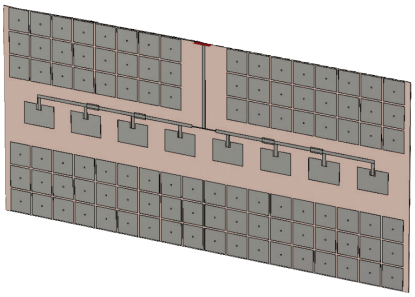

Figure 6.4: Ka-band Antenna from OrbanMicrowave [38]

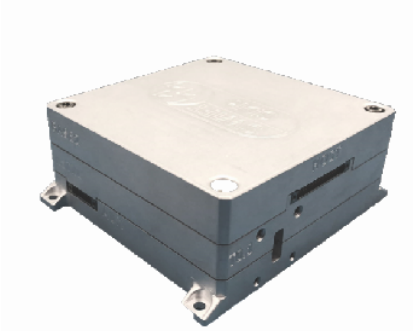

Figure 6.5: SDR and Transceiver: SWIFT-KTX [41]

Figure 6.6: Power splitters from Instockwireless [42]

It represents a linear array with integrated feeding network. Through the use of power splitters, the signal beam can be steered towards the receiving antenna. It covers the Ka-band and has a gain of 12 dB. The 8 by 8 by 1 cm and 25 gr antenna is bonded on the surface of the spacecraft: the use of an array does not augment the drag experienced by the spacecraft. This array design has been tested to be high radiation resistant in LEO. Two antennas are brought on board for redundancy. More details on its installation on RAMSES can be found in chapter 14.

SWIFT-KTX

This component is a high-performance SDR and transceiver for small satellites that communicate in Ka-band. Two are taken on board for redundancy, with a total mass of less than 1 kg. Its volume is 86 by 86 by 40 mm and it consumes about 16 W of power. The manufacturers and company, Tethers Unlimited, guarantees a TRL of 7.

Signal/Power Splitters

As the two selected antennas are 1 by 8 elements linear arrays,two signal splitters with eight ports are installed to allow for beam steering. The components have 750 grams of mass each and a size of 202.7 by 75.7 by 22.2 mm. They were chosen also for their limited power losses (about 1 dB).

6.4. Verification & Validation

In this section, all the previous design choices and approaches are verified and validated.

6.4.1. Requirements

As visible from the "✓" in section 6.1, the communications subsystem design complies with the initial requirements. Some of the requirements have driven the design itself, such as the use of RECOMMENDATION ITU-R SA.1414-2. The others have been taken into account in section 6.3 and are hereby formally verified.

6.4.2. Methodology

In subsection 6.2.1, Kepler constellation of 140 nanosatellites has been chosen as DRSs for RAMSES. From Figure 6.1, it is evident that the satellite would continuously downlink data to the closest satellite. This implies that 140 S/C at 575 km are sufficient to guarantee continuous communications with RAMSES. To verify this, a straightforward approach has been sported [43].

The coverage surface for communication of RAMSES with a Kepler nanosatellite is pictured in Figure 6.7 (R_e indicates the radius of the Earth, R_s the altitude of the user satellite, RAMSES, and R_r the altitude of the

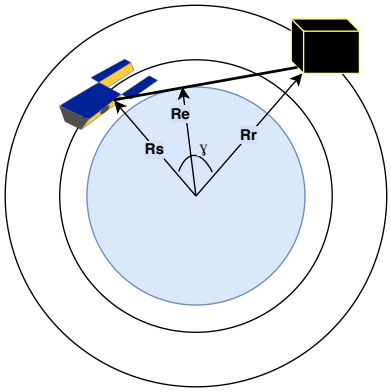

Figure 6.7: Scheme of Kepler relay satellite coverage.

relay S/C). From [43], the required total number of relay satellites (T) required to ensure a full coverage of the in-polar-orbit user sphere is derived to be:

$$T = \frac{360}{3 \cdot \gamma} \frac{360}{\sqrt{3 \cdot \gamma}} \tag{6.1}$$

where, from simple trigonometry, $\gamma = \arccos \frac{R_e}{R_s} + \arccos \frac{R_e}{R_r}$ and is used in degrees. The first fraction in Equation 6.1, refers to the total number of orbital planes required to cover the equator, whilst the second fraction indicates the number of satellited necessitated to cover an entire single orbital plane [43]. By fixing R_r to $(R_e + 575\ km)$ and taking into account a R_{smin} of $(R_e + 214\ km)$ and a R_{smax} of $(R_e + 240\ km)$, T is computed to be 106 and 103, respectively. As mentioned in subsection 6.2.2, Kepler nanosatellites in orbits are 140, therefore the type of communication has been verified.

The derivation of the imaging payload downlink data rate must be verified, as well, whilst the housekeeping data rate and the uplink data rate necessitate validation. Table 6.2 includes all the parameters, and their value, useful to retrieve the downlink rate of payload data. In the fifth and sixth column of Table 6.2, the choices made and the formulas involved are listed. All the given values have been double checked with the specification sheets of the sensors. The period during which the payload is operative is given by the GNC department, responsible for this time allocation's verification. Additionally, the CR has been extrapolated from an empirical relationship, that accounted for number of pixels per image and lossless compression ratio of 17 files converted to JPEG 2000 [36]. JPEG 2000 is per se a verified losslessly-compressed format; moreover, the 3-order polynomial interpolation has been verified analytically and through sanity checks with unit tests: when filling the polynomial equation with the number of pixels from one of the input parameters (to which a correspondent CR is given and used for the regression), the obtained CR matches the respective CR input value. Finally, the equation used to compute the payload data/orbit and payload downlink rate have been verified by checking the unit of each parameter and ensuring that the relation between them gives the expected output unit. It is worth noticing also that the different metric prefixes used are uniformed when utilised together. Furthermore, the estimation of the housekeeping data and the uplink data have been validated by comparing the values to literature [17, 31].

As far as the link budget is concerned, its verification consists in unit tests and integration tests of the Python code implemented thereof. The input values have been checked by confronting them again with the respective source. The equations used are verified, as well. In Table 6.3, each relation used has a correspondent source. It would be sufficient to say that references such [31] include already-verified equations. Yet, for redundancy's sake, the equations are equal in different sources, when confronting for example [31] to [44]. While doing so, it has been assured that the references had same assumptions and/or simplifications. The dowlink link budget for RAMSES has been developed in Python. The program has been verified as follows: firstly, the consistency of the units and metric prefixes has been established (especially in the case of conversion to decibels). Additionally, the code has been divided into single blocks: in each of those input for which there were clear expected output have been inserted in the code to perform the unit test. For example, by setting the transmitter power to 1 W, the EIRP, printed in dB, matched just the sum of the antenna gain and the losses (the power in decibel resulted indeed 0). Trends have been tested, too. By doubling the signal propagation path length, the space loss reduced to one quarter of the initial value (dimensionless-not in dB), which was expected due to its inverse dependency from the distance squared. With respect to the in-

tegration test, the link budget presented in [39] has been used to assess the correctness of the program. The input values from that paper have been used in the code and the output matched. Moreover, the validation of E_b/N_o, EIRP and the like has been performed by confronting the obtained values with the link budgets of similar and comparable missions (sanity checks), for example [31, 39].

6.4.3. Architecture-Performance

All the components of the communications subsystem are COTS items. All of them have been used already and have fairly high TRL. Therefore, verification and validation of those components is not demanded. To verify that the satellite would be able to send the first status check message once injected in its orbit, the link budget has been analysed for an altitude of 204 km, as discussed in section 6.3. The link margin results to be 4.18 dB. In light of the foregoing considerations about the link margin, this value means that communicating at 204 km is feasible.

With respect to the uplink, the same approach used for the downlink was not needed. The required parameters to close the link budget were specified by [30]. A meticulous check of these values correspondence is deemed enough for this link verification.

6.5. Sensitivity Analysis

For the communications subsystem,in light of the approaches sported for its design, the aspect that requires sensitivity analysis is the downlink link budget. To close the budget, the link margin should be at least 3 dB[31]. If this value becomes too low, the design might not be able to fulfil its nominal operations anymore. Thence, the dependency of the link margin on the downlink input parameters is studied. Amongst all of the input variables, the ones that are not constrained by the COTS item selected, such as antenna gain, are taken into account: namely, BER, altitude, transmitting frequency within the ka-band and transmitter power. The impact of these parameters' variation on the link margin value is shown in Figure 6.8. The for plots are derived using equations from Table 6.2.

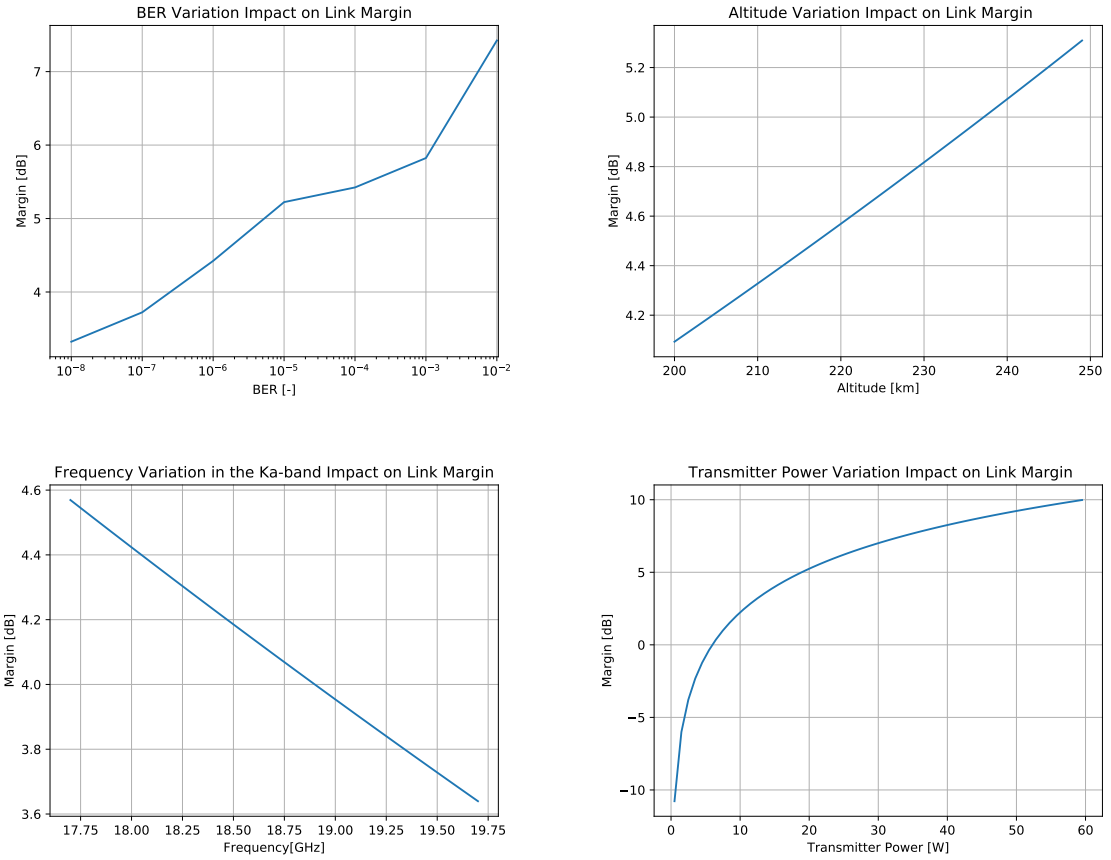

Figure 6.8: Graphs for (down)link margin sensitivity study.

The four graphs in Figure 6.8 can be used to understand the acceptable limits before a full redesign must be performed.

- **BER**. The chosen value for downlink is 10^{-6}. In order to deliver high resolution images it is not recommended to increase the BER at all. Hence, the opposite case must be considered: if a lower BER is required, the communications system would not need major changes: from the top left plot in Figure 6.8 it is possible to notice that the graph gets less and less steep going towards the origin. On top of this, even lower altitudes ensure acceptable link margin values.
- **Transmitting Frequency in Ka-band**. If only the frequency is changed in the link budget, the design would still be fully functional. The upper limit of the ka-band guarantees a margin above the critical one.
- **Transmitter Power**. If the transmitter power value increases, there are obvious advantages in the link budget. Vice versa, a power lower than ~ 12 W would not suffice for the link budget to close. The communications would not happen, unless other variables are modified (increase in altitude, decrease in frequency and the like). Due to the redundancy of the power subsystem, it is unlikely to have a power shortage that would halt communications.

6.6. Risk & RAMS Analysis

The communications subsystem is designed for fully redundancy (requirement COMMS-010). Thence, components with high TRL have been selected and redundant units have been taken into account. As a consequence, the analysis of this subsystem risks does not shown any catastrophic and very likely risk. In fact, the risk are categorised using the following scale: **Catastrophic** is associated to a significant degradation in technical performance and total mission failure; **Critical** involves the success of mission being compromised; **Marginal** limits the failure only to secondary missions; **Negligible** is when performance is not affected, rather inconveniences are introduced.

RSK-COM-01 **Event**: The satellite is not in the contact window of any relay satellite.
Risk: Continuous communication is no more available. Data to downlink might be lost and/or delayed. Commands might not be received in time. Especially in this case, this risk might be critical, yet from the verification performed in section 6.4, is deemed rare.
Mitigation: Place a redundant antenna on another side of the s/c to increase its level of visibility with respect the relay constellation. Have a redundant storage on board. After mitigation, this risk is considered rare and marginal.

RSK-COM-02 **Event**: Detachment of antenna array from satellite's surface.
Risk: Debris that might damage the rest of the spacecraft. Failure of communications system. This risk is deemed possible and critical.
Mitigation: Use adequate bonding and have a redundant antenna (there are three!). With this strategies, the risk turns then to be rare and negligible.

RSK-COM-03 **Event**: The power splitters fail.
Risk: The antenna beam cannot be steered and communications are interrupted. The power splitters used have a TRL of 9 therefore the risk is defined rare and marginal.
Mitigation: Have a redundant unit on board. Therefore, the risk becomes rare and negligible.

RSK-COM-04 **Event**: Interference between downlink and uplink messages.
Risk: signals can be corrupted and ultimately lost. Especially if commands are involved, the risk can be critical and, since the same band is used for up- and downlink, likely.
Mitigation: Install a transceiver with different ports for uplink and downlink (SWIFT KTX) and use different frequencies within the ka-band. The risk reduces to marginal and possible.

RSK-COM-05 **Event**: Power shortage.
Risk: If the antenna does not receive enough power it would not transmit/receive the link data. Or even the SWIFT KTX might shut down. This is a critical and possible risk.
Mitigation: Have an electronic connection to redundant batteries on board. Therefore, the risk becomes rare, yet still critical.

RSK-COM-06 **Event**: Failure of the entire SWIFT KTX.
Risk: Communications are interrupted, as well as some kinds of data processing (e.g. filtering). The risk is rare since the component has a TRL of 7, nonetheless critical.

Mitigation: Install a redundant unit. Share functions with the OBC, via common bus interfaces. The risk hereby turns marginal.

The risks are visually categorised in Table 6.4. The arrows indicate where the risk was before the mitigation. In the risk matrix, the colour legend for the risk is: **HIGH** in red, **MODERATE** in orange and **LOW** in yellow.

Table 6.4: Risk map showing the severity and likelihood of the risks before and after mitigation

Severity \ Likelihood	Almost Certain	Likely	Possible	Rare
Catastrophic				
Critical		RSK-COMMS-04	RSK-COMMS-02/05 →	RSK-COMMS-01/06
Marginal				RSK-COMMS-03
Negligible				

The only catastrophic risk that might happen is the failure of all components of the communications subsystem. This has been neglected because it is deemed highly unlikely.

From the foregoing discussion, it is evident that the communications system is highly reliable, especially if compared with the other subsystem on board. As a consequence, it is not necessitated to perform an extensive reliability analysis. Also the availability of the communications links is safely guaranteed due to the TRL (antenna and power splitters 9, SWIFT KTX 7) and number of redundant units for each component: two more antennas, one more power splitter and an additional SDR-transceiver. It is indeed necessary to perform adequate tests of the integrated subsystem, to make sure that the interfaces and circuits in between the different components would not fail.

Finally, as far as safety is concerned, three major fields must be analysed.

- Humans' safety. as the mission is unmanned, humans might be endangered only during the pre-launch phases, in particular production, integration and testing. The communication architecture's components are made up of non-toxic materials that do not require special measurements from the personnel responsible of development phases. Moreover, the fact that each component is available in the market and that has been used already, implies that safety instructions exist, are available from the manufacturer and have been tested.
- Satellite system's safety. As mentioned in RSK-COM-02, the detachment of the antenna from the surface might create indentations on the structure in case of collision. This risk has already been mitigated. On top of this, being the SWIFT KTX a closed box, its internal failure would most likely not affect the rest of the satellite. A higher danger might be represented by a short circuit in the proximity of the power splitters. Nonetheless, this is related to the electrical system.
- Environment's safety. As mentioned before, the antenna, if detached, might represent a space debris and, therefore, a potential danger to the environment. Notwithstanding, there are no other satellites at RAMSES specific altitude that might experience a collision. On the other hand, it is very likely that the antenna would burn up rather quickly decaying in the atmosphere.

6.7. Cost Analysis

The cost analysis for each component of the communications architecture is presented in Table 6.5.

The TRL and the price of the power splitters can be found in the company's website[3]. The specifications of the SWIFT KTX have been received by the company's customer support. The antenna TRL and price [45] have been derived for analogy[4].

[3] `https://www.instockwireless.com/gps-antenna-signal-splitter-gps820.htm` [cited on 20 June 2019]
[4] `https://ntrs.nasa.gov/archive/nasa/casi.ntrs.nasa.gov/20110000775.pdf` [cited on 20 June 2019]

Table 6.5: Cost and TRL levels of the communications subsystem

Component	N	Estimate Hours of Labour	Total Cost in 2019 Euros	TRL	Estimate Methodology	Estimate Accuracy	Technical Risk
Ka-band Antenna Array	2	Continuous labour during entire mission	2 × 450	9	Analogy	Medium	Low
Power Splitter	2	Continuous labour during entire mission	233.72 (for 9 pieces)	9	Specs sheet	High	Low
SWIFT KTX	2	Continuous labour during entire mission	2 ×171110	7	Specs sheet	High	Medium/ Low

7. Propulsion

The propulsion system consists of an intake, which collects the atmospheric gases, and a thruster that accelerates the captured gases. The following chapter provides the reader with an overview of the design of such system for the RAMSES satellite.

7.1. Functions and Requirements

The propulsion system main objective is to keep the average thrust equal to the drag, to maintain a constant orbit. This is done by utilising air-breathing electrostatic propulsion, which consists of an intake and a thruster, as specified in **SYS-001**. The intake collects and traps atmospheric gasses and transports 40% of the encountered gasses to the thruster ($\eta_{coll} = 0.4$). Once the gasses arrive in the thruster they are ionised and accelerated. The exhaust velocity and mass efficiency provide a specific impulse (I_{sp}).

The propulsion system requirements in Table 7.1 are derived from the system requirements in section 2.2. The requirements on the propulsion system are derived in Table 7.1. In the table, the last section provides the reference to the sections in which the requirements are shown to be complied with. Requirement **PROP-001** is derived from **SYS-038** in the system requirements and the drag estimate in chapter 4 and results to 5.8 mN of thrust required.

Table 7.1: Subsystem requirements on the propulsion system

ID	Requirement	Notes	Met [✓/✗]	Section
PROP-001	The propulsion system shall provide a thrust of minimum 5.8 mN.		✓	Figure 7.10
PROP-002	The intake shall have a collection efficiency of 40%.	Assumed collection efficiency for sizing, and thus collection efficiency required to run the engine and achieve a thrust to drag ratio above 1, with an specific impulse of 3500 s	✓	subsection 7.3.3
PROP-003	The intake shall weight less than 16 kg.	Allocated mass budget of the intake	✓	
PROP-004	The thruster will weight less than 1.8 kg.	Allocated mass budget	✓	
PROP-005	The thruster will use less than 415 W of power.	Allocated power budget	✓	Figure 7.10

The required thrust for the thruster can be determined from the drag calculated in chapter 4. The thruster is thus driving the design of the entire subsystem, based on its required mass flow, pressure, power, et cetera. It has to be able to produce a thrust of 5.8 mN over the entire mission to compensate the drag derived in chapter 4, to ensure orbit maintenance. This propulsive power includes some margin to perform orbital manoeuvres, also when the thruster is not perfectly aligned. At Beginning Of Life (BOL) conditions, the power produced by the solar panels is much higher than the power required. This knowledge can be used to increase the thrust until 9.19 mN at 640 W, to compensate for changes in the density and enable the S/C to operate in Earth repeat orbits.

7.2. Methodology

The methods and models used are outlined for each of the different elements within the propulsion system. For clear structuring, the system is divided in parts, which are discussed, from thruster to intake. The thruster, being the driver of the system, is the first one examined, and is selected in subsection 7.2.1. The intake is be build on top of the thruster in steps: feedline, collimator, thermolizer and grid are discussed as part of the intake in subsection 7.2.2.

7.2.1. Thruster

To provide the required propulsive power, a multitude of different thrusters are available. They can be distinguished into three categories, namely electromagnetic, electrothermal and electrostatic. Since erosion is an important consideration within this mission, the electromagnetic thruster type is chosen for of its electrode-less design. If electrodes would be used, the risk of eroding away with the exposure to the atmospheric gasses present at the missions orbital altitude is high, leading to reduced reliability and lifetime [46]. Nevertheless, electromagnetic thrusters have a lower TRL and have not been tested as extensively as the electrostatic type [47].

The trade-off comes down to the two available electromagnetic thruster types, the Gridded Ion Thruster (GIT) and the Hall Effect Thruster (HET), each having their benefits and drawbacks. The GIT has the advantage of a simple design, with no need for active compression. It can achieve a higher I_{sp} compared to the HET, as seen in Figure 7.1. The drawback is that it requires a high voltage difference that imposes important requirements on the power system. On the other hand, HET is more efficient over its lower range of Isp and has a higher thrust per power ratios, as can be identified from Figure 7.2. Furthermore, it requires lower voltages to operate. It does however need active compression, which is a major drawback for a spacecraft of this weight class [48].

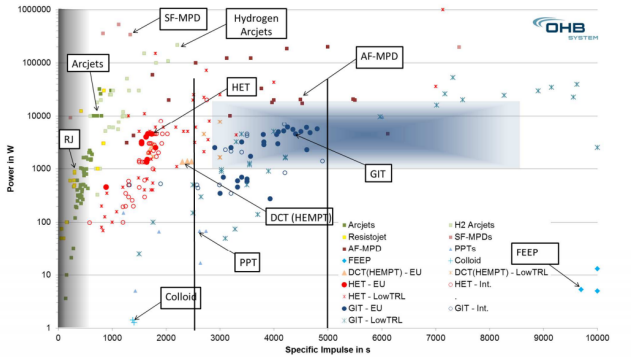

Figure 7.1: Comparison of different thrusters based on their I_{sp} values

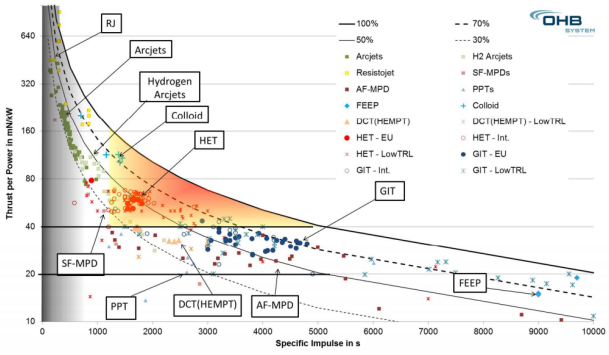

Figure 7.2: Comparison of different thrusters based on their thrust-to-power ratios

In terms of reliability, solely based on thruster type, HET is considered more developed than GIT. However, since HET's are only tested extensively for thrust levels much times higher than necessary for RAMSES, both HET and GIT are considered to be on TRL 9[1]. Considering the use of atmospheric propellant, the TRL becomes 4 [46, 49, 50]. This is true for both thrusters, however during initial tests GIT showed better performance with an atmospheric propellant supply. The arguments raised above thus point more towards GIT, when compared to HET. This is due to its simplicity, and therefore better predictability, higher I_{sp} levels, as well as better compliance with the propellant.

The choice of which GIT to use is treated in section 7.3 by looking at the I_{sp}, efficiency and thrust-to-power needed to achieve drag compensation. Once the thruster is chosen, the required particle density and exact required have to be defined. The exact power will be derived using the thrust-to-power ratio of the thruster and the exact thrust needed. The ionisation mechanism will be set from the choice of thruster. In the rest of the of this section a Radio Frequency (RF) Ion thruster will be used to analyse the system, as the existing alternatives, namely a hollow cathode and DC discharge, have potential life and power supply issues [51]. The use of a microwave ion thruster would be even more beneficial when considering life issues, but

[1] `http://epic-src.eu/wp-content/uploads/LS.1.5.-George-Herdrich-MPD-Thrusters-Part-2.pdf` [Cited on 20 June 2019]

it relies on matching the particle density and the frequency of the waves exactly, and as the particle density is fluctuating through the operation of RAMSES, RF ion thruster was still considered to be better suited for the mission.

For a RF ion thruster the ionisation mechanism uses a solenoid around an insulated chamber to excite and ionise the neutral particles through induction [51]. Typical frequencies for this RF solenoid is 1 MHz, during half a period (0.5 microseconds) the electric field exists in one direction and the electrons travel a larger distance than the length of the ionisation chamber. If they collide prior to leaving the chamber, they retain this velocity and are heated [51]. To ensure the electrons are heated there should be enough collisions in the electric field interaction region, which is the case when this region is in the same order of magnitude as the mean free path of the electrons and thus the collision probability is about 10% [51]. Using Equation 7.1 the minimum pressure required for these conditions can be found. This is translated in an ionisation rate in Figure 7.3 [51]. From this, it is found that the initial pressure needed for ignition is 50 mPa. The pressure needed after ignition drops significantly and values in the range of 0.1-1 mPa are reported [52]. This values allow passively achieve a pressure of 4 mPa, as estimated using Bernoulli (see Equation 7.2).

$$P = 1 - \exp^{-\frac{p_{min}\lambda}{kT}} \tag{7.1}$$

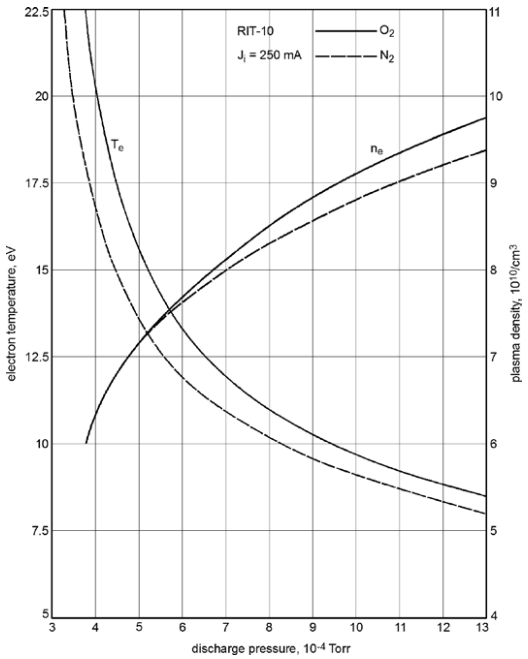

Figure 7.3: Ionisation rate at different discharge pressures

In order to acquire the required massflow and pressure, an intake is designed. This calculation is described in subsection 7.2.2, while the numerical sizing is performed in section 7.3.

7.2.2. Intake

In front of the engine there is the intake system shown in Figure 7.4 that consists of a feed line (2), a collimator (3), a thermolizer (4) and a grid (5). This system is in place to ensure correct engine operation at the orbital altitude determined in chapter 4.

The propellant supply required into the engine is realised by the use of a feed line (2) running through the middle of the spacecraft bus. This feed line sizing is an important step in assuring the total intake efficiency is sufficient for the engine to operate. The feed line has its own transmission efficiency, which indicates the ratio of the amount of particles going in, to those coming out on the other side. This is determined based on the L/R-ratio, which has to take into account spacecraft integration, but has to be straight since otherwise the efficiency reduces. Having the feed line running straight through the bus however, limits the payload integration massively, as effectively less than half of the volume of the S/C can be used. Although this is necessary as the thruster has to be aligned with the centre of gravity to have no thrust misalignment.

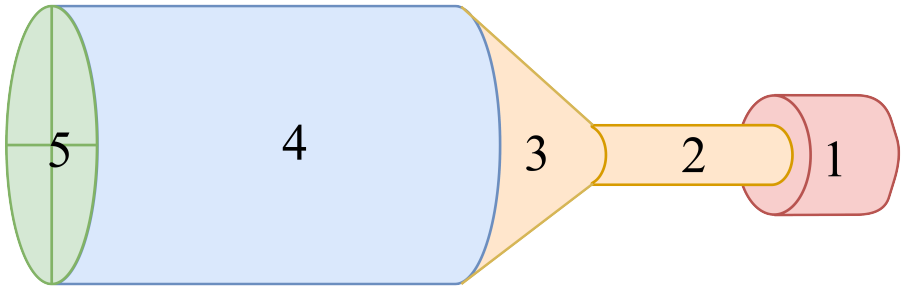

Figure 7.4: Overview of the propulsion system, where the following parts are numbered: 1. thruster, 2. feed line, 3. collimator, 4. thermolizer, 5. grid

The length of the feed line determines the spacecraft length and volume that can be used, as such the length is sized keeping in mind the necessity to fit the payload and spacecraft bus.

The particles are fed into this feed line by the use of a type of collimator (3). This device has as function feeding the particles from the intake with a large cross-section, to the feed line with a small cross-section. RAMSES investigates the use of a funnel as collimator, which tries to capture as much particles as possible. Although, because of the free molecular flow dynamics, this will be highly inefficient since most of the particles will bounce out of the funnel again. In order to increase the efficiency of this part of the system, other systems will have to be developed to ensure functioning in free molecular conditions.

In front of the collimator, there is an empty volume called the thermolizer. The function of this section is to equalise the pressure of the incoming particles. It needs to have a certain length to assure this is the case. Otherwise, large differences in pressures occur along the collimator, creating an unsteady thrusters system. This is not beneficial in terms of the constant thrust level, neither for the reliability of the thruster. Exactly how long this section has to be in order for the pressure to be evenly distributed is determined using Direct Simulation Monte Carlo methods (DSMC) for different lengths. These simulations can be visualised in Figure 7.5 [10]. The total pressure at the end of this thermolizer can be calculated using Equation 7.2 [10].

$$P_{\text{stag}} = P_{\text{atm}} + \frac{1}{2} \cdot \rho \cdot V^2 \tag{7.2}$$

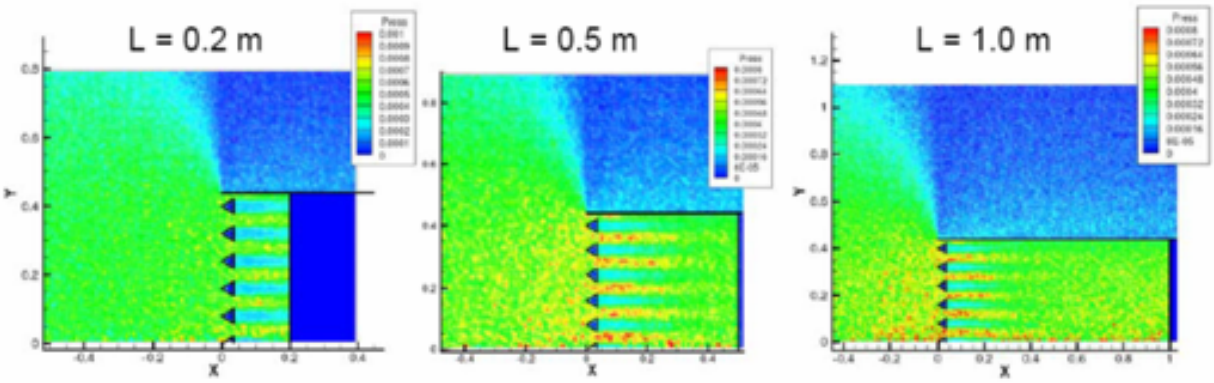

Figure 7.5: The effect of the length of the thermalizer illustrated by monte carlo simulation [10]

To keep the particles from bouncing directly out of the intake, a grid has to be designed to allow particles to enter the intake and trap them inside of the thermolizer. To find the correct sizing of this grid, the perfect L/R-ratio of the straws within this grid has to be determined. The perfect ratio ensures the highest difference between the inflow transmission efficiency, determined from Figure 7.6, and the backflow transmission efficiency, identified using the line for scattered particles in Figure 7.6. Within the graph, the X represents a non-dimensional driving value calculated using Equation 7.3 [13]. Both equations are based on assumptions. The line for fast particles assumes incoming particles are travelling fast and parallel to the spacecraft axes. The line for scattered particles assumes outgoing particles to travel in different directions, having low velocities. The differences between the two are visualised in Figure 7.6 [13], where the dependence of the

transmission efficiency on the particle type and L/R-ratio becomes clear by seeing the effect of changing X.

$$X = \frac{\sqrt{\frac{k_B T_{in}}{m_p}}}{v_{in}} \frac{L}{R} \tag{7.3}$$

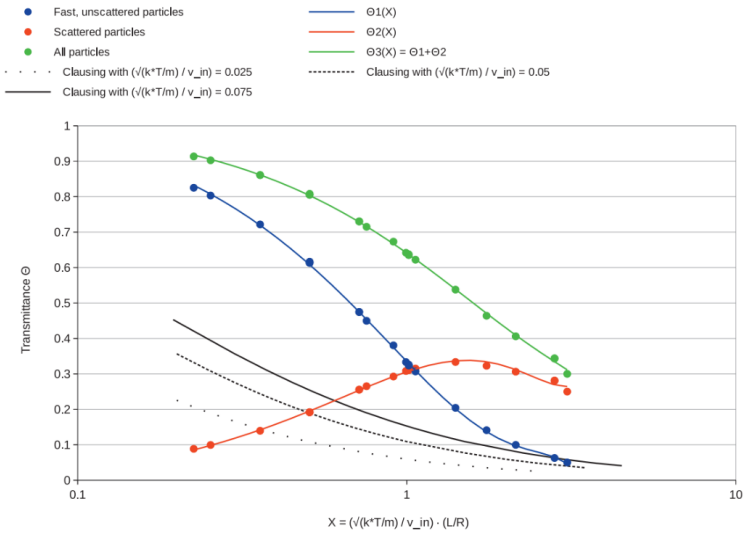

Figure 11: Generalized Cylinder Transmittances

Figure 7.6: Transmission efficiencies of particles with different energies for different L/R-ratios

All of the intake sections thus each have their own function and location. Their combined goal is to take in as much particles as possible, and keep as much of them in so they transfer to the thruster to be used as propellant. When looking at literature, the overall collection efficiency of the intake has to be between 25% and 40% in order to make the design feasible [53]. The exact efficiencies of the intake of RAMSES will be discussed in section 7.3.

7.3. Performance

The methodology for the entire propulsion system has been outlined in section 7.2. In subsection 7.3.1 and subsection 7.3.2, all the results acquired based on that methodology are presented and discussed. Figure 7.7 represents a schematic overview of the propulsion system parts and interfaces, which will be used as a guideline to go through the entire system from back to front in the same fashion as section 7.2 and subsection 7.3.3. After that, the black box approach for parts under development is explained and applied.

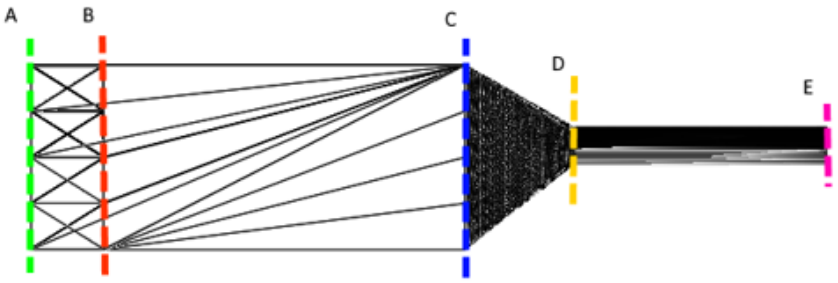

Figure 7.7: Propulsion system overview of parts and interfaces

7.3.1. Thruster

The first step in quantifying the propulsion system is to determine a usable thruster. The intake area and velocity of the spacecraft, as well as the density at the orbital altitude, are already determined in chapter 4.

With this information, together with the assumption that a total collection efficiency of 40% will be needed to make the system feasible, the mass flow through the engine can be acquired using the following equation: $\dot{m} = \eta_{collection} \cdot \rho \cdot V \cdot A_{intake}$. This results in a mass flow of approximately 1.6×10^{-7} kg/m^3. The minimum operational mass flow however, equals 0.65×10^{-4} kg/m^3. So sufficient margin is taken into account to ensure the thruster remains operative under the expected atmospheric conditions. Having retrieved the mass flow, and the required thrust level of 5.8 mN from chapter 4, and using the standard gravitational constant (g_0), the required thruster I_{sp} can be calculated from the thrust equation given as $T = g_0 \cdot I_{sp} \cdot \dot{m}$.

Based on the I_{sp} range, as well as the ability of the thruster to cope with atmospheric propellant, the RIT-10 thruster is chosen out of the list of GIT. To now determine the power necessary, the graph shown in Figure 7.10 is used. This graph shows the different thrust settings of the thruster and couples them to a colour scale which represents the amount of power the setting requires. The graph is made from the graphs in Figure 7.8 and Figure 7.9. In order to acquire a thrust setting high enough to counteract the drag at a certain density, the dot has to be above the blue line, representing the minimum needed thrust. Looking at the nominal thrust level calculated in chapter 4, the nominal required power is determined to be around 415 W. If there is a moment when the input power into the propulsion system increases or decreases, the thrust will thus vary significantly. This means the thruster is throttle-able to adapt to varying conditions and also has excess power and thrust at BOL, since the nominal thrust and power is chosen based on EOL power.

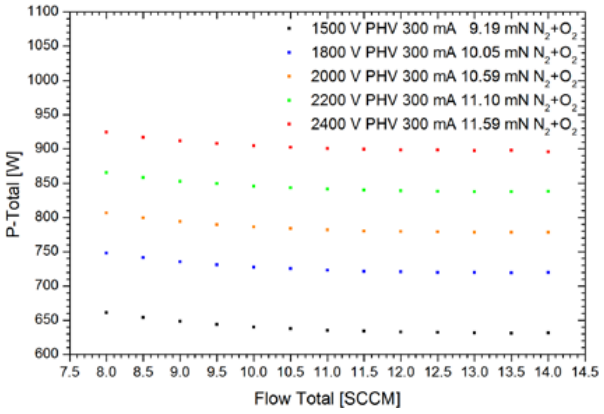

Figure 7.8: Thrust settings at higher power settings [52]

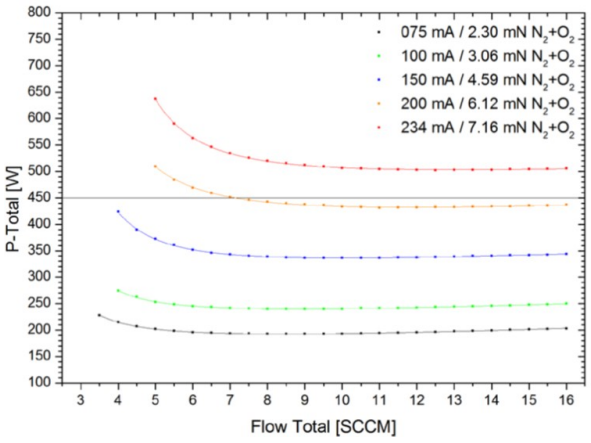

Figure 7.9: Thrust settings at lower power settings [52]

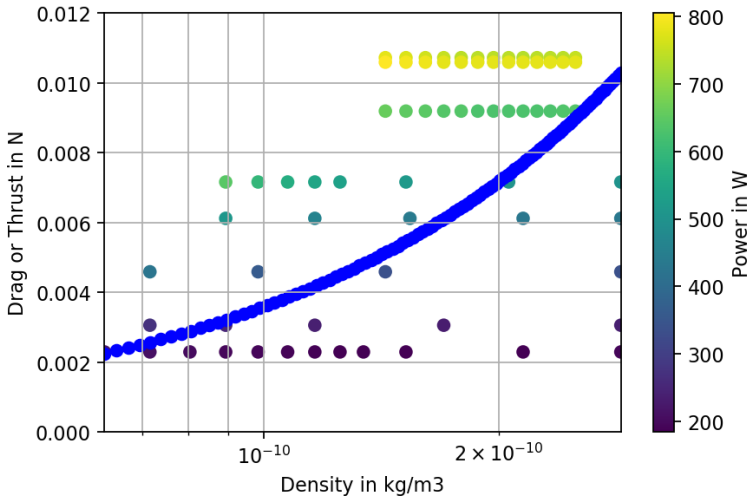

Figure 7.10: Engine settings with their thrust and density needed to for their required massflow with a collection efficiency of 0.4, an orbital velocity of 7.9 km/s, intake area of 0.39 m^2, plotted next to the drag force at a density with a C_D of 2.4, frontal area of 0.48 m^2 and same orbital velocity.

Having determined the required power, there is another unknown regarding the power supply. Namely

the voltage difference that has to be ensured for the thruster to function as expected. The limits of how high this voltage can be lies mainly with the PCU, discussed in chapter 8. With the current configuration, the thruster functions at a maximum voltage of 1800 V at BOL. This nominal voltage however will be lower as the power supply is not able to cope with the power demand for such high voltages. Just as in Figure 7.10, Figure 7.2 also indicates different thrust levels. So varying the voltage will result in thrust changes, but also in different power requirements.

The ignition of a RF gridded ion engine can be achieved in different ways. The engine chosen uses the grid itself to insert electrons in the chamber by reversing polarity, then it will use a pressure shock to increase the pressure and achieve ignition [52]. The pressure needed for ignition is in the range of 4-8·10^{-4} Torr, this can be seen in Figure 7.3 [52]. After ignition the polarity is set back to normal and the ionisation can be sustained with the free electrons in the chamber.

During the operation of the engine, heat is produced which should be dissipated, the dissipation is described in chapter 12. The heat that is produces by the engine is equal to the total power input minus the energy actually used in the acceleration of the particles, called the beam power [51]. The beam power is equal to the beam current times the effective potential difference. For the nominal thrust setting the total power is 415 W, the effective beam potential 1500 V and current 200 mA, which gives 115 W of heat to be dissipated.

$$P_{heat} = P_{total} - P_{beam} = P_{total} - I_{beam} V_{beam} \tag{7.4}$$

7.3.2. Intake

Sizing the intake is also done from back to front, thus starting with the feed line. The transmission efficiency of this feed line is determined using the scattered transmission probability shown in Figure 7.6, presented in section 7.2. Hereby the assumption is made that the particles entering the feed line are scattered and travel in every direction with a velocity of more than 6.5e+3 m/s. This results in a transmission efficiency of less than 30% with an X value of less than 1. The transmittance of particles is thus not large for this assumption. This can be improved by adapting the L/R-ratio, as well as the incoming particle velocity, but technological improvements will most probably be needed to increase this transmittance and make the propulsion system more feasible. The efficiency of the feed line is highly dependent on the collimator, which transfer particle to the feed line. To improve the transmission efficiency of the feed line, it would be beneficial if the collimator is able to focus the flow of particles before sending them down the feed line.

Within RAMSES, the collimator is a passive system based on the principles of a funnel. The efficiency of a funnel is mainly based on the area ratio of the in- and outlet. Increasing the inlet area will quickly decrease the transmission efficiency since the particles need to be focused more to fit through the outlet. Considering free molecular flow, this ratio is even more important since the efficiency for each case is already a lot lower than for normal flow. In the case of RAMSES, the area ratio of the intake area of 0.39 m^2 over the feed line area of 0.0078 m^2 approximates 50. This ratio leads to a very low transmission probability to the feed line and thruster and a magnifying effect on the particles that flow back out of the grid.

The thermolizer performance consists of its ability to increase the pressure of the flow but also by what consistency it does this with. The size of the thermolizer is therefore mainly based on research that showed that after a length of 1 m the pressure is somewhat consistent radially and creates a compression ratio of 100 [10]. This pressure distribution can be seen in Figure 7.5. The theoretical maximum pressure that the flow can be raised at follow Equation 7.5:

$$P_{\text{stag}} = 10e-5\frac{1}{2}\cdot 1.3e-10\cdot(7.9e+3)^2 \approx 4 \text{ mPa} \tag{7.5}$$

After a L/R-ratio is taken as described in subsection 7.2.2 at 3.2 this is translated to a L/$\sqrt{A}$-ratio of 1.8. Then a shape is chosen to optimise the packing density in the trapezoidal shape of the spacecraft determined in subsection 11.2.1, and triangles are chosen, as an equal area for the triangles can be obtained by dividing the trapezoidal shape by an integer. Ideally, the system would require an infinite amount of triangles. However, the walls of these triangles are non-zero and therefore the triangles were enlarged until a size that is easily manufacturable. As discussed in chapter 15, these sheets of carbon (material choice is explained in chapter 11) need to be handmade and coated. Thus a length of 20 cm is chosen, which equates to 32 triangle tubes that divide the 0.4 m^2 intake area. With a thickness of less than 1 mm this would equate to an intake area loss of about 0.01 m^2.

7.3.3. Black Box

The overall collection efficiency needed is set to be 0.4, however, this is proven to be impossible to achieve with a passive intake due to the big difference of cross-section between thruster and intake, together with the pressure increase needed to make ionisation happen. In addition the feed line has a certain transparency, which is low for scattered particles and will decrease the overall collection efficiency even further. Equation 7.6 shows the collection efficiency in terms of transmission probability of fast particles through the grid (τ_b), scattered particles through the grid (τ_c) and scattered particles through the collimator and feed line in the engine (τ_t^*) [53]. This is is assuming that all particles get thermolized perfectly by the thermolizer and that they can only leave the thermolizer by the grid or the thruster [53].

$$\eta_c = \tau_t^* \frac{\tau_b}{\tau_t + \tau_c} \tag{7.6}$$

Using this it is easy to show that a collection efficiency of 40% is impossible as:

$$\tau_t^* = \tau_t \cdot \frac{A_t}{A_c} \tag{7.7}$$

already gives 2% for a $\frac{A_t}{A_c}$ of 50 with a τ_t of 1 and using Equation 7.6 with τ_b 83% and τ_c 9% a minimum of 8.4% is found as minimum τ_t^*. Therefore for this design to work an active collimator is needed, for example a turbomolecular pump or a particle lens of some sort to focus the particles in the feed line with enough speed to minimise the transparency loss by particles hitting the walls and arriving at a τ_t^* of 8.4% or higher. The overview of the efficiencies needed can be seen in Figure 7.11.

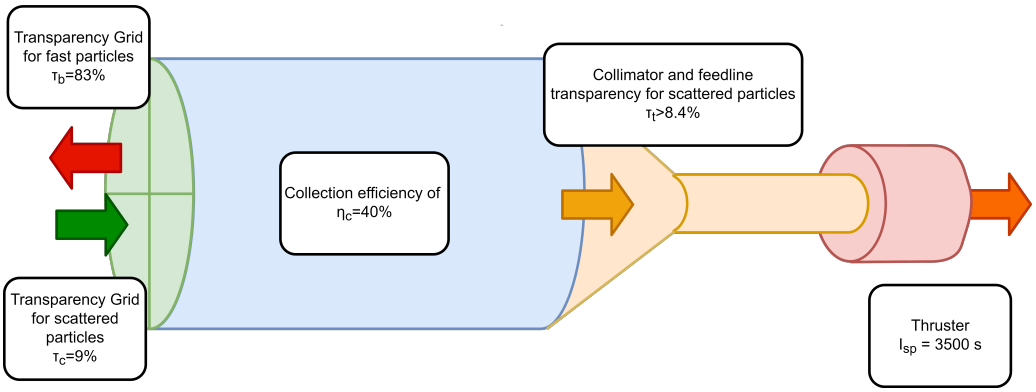

Figure 7.11: Efficiencies needed in the engine for a collection efficiency of 40%

7.4. Verification & Validation

This section explains the verification and validation procedures applied on the entire propulsion system. This includes both intake system and thruster.

7.4.1. Verification

Verification of the intake model is an important step in determining its feasibility, since calculations are based on estimations. The largest aspect to check is the efficiency of the system. The analysis on the intake that is done in subsection 7.3.2 was verified using Molflow, a Monte Carlo simulator for vacuum systems, which confirms the infeasibility of the passive funnel as collimator. The verification simulation is done using Figure 7.7 as reference, at point B particles are created with an axial velocity towards the feed line and a radial random velocity, and plane B also absorbs all the particles that hit it. Then two cases are made, in case 1 the plane C absorbs all particles and in case 2 plane C is transparent and plane D absorbs all particles hitting it. This simulation is then run until almost all particles departed the volume and the follow was observed:

$$Case1 \rightarrow \frac{n_{outA}}{n_{inB}} = 34.4\% \frac{n_{outC}}{n_{inB}} \approx 65\% \tag{7.8}$$

$$Case2 \rightarrow \frac{n_{outA}}{n_{inB}} \approx 97.6\% \frac{n_{outD}}{n_{inB}} \approx 1.5\% \tag{7.9}$$

This simulation suggest a τ_t^* of 1.5% for the passive intake design, which would suggest a τ_t of 75% with

$\frac{A_t}{A_c}$ of 50. This verifies the conclusion that the passive intake would not work. Case 1 shows that even the thermolizer has a transmission probability, however, in the analytical model this would be captured by the τ_t.

7.4.2. Validation

The thruster data and thrust settings are validated by testing the thruster in a vacuum chamber for several hours [52]. It is mainly found that too low massflow would lower the thrusters lifetime significantly, as more atomic oxygen would be created during ionisation [52].

The entire assembly would still need validation as the interfacing between the intake and thruster has a lot of uncertainties. The thruster should also be tested with different fluctuations of densities of atmospheric gasses, as these vary over the orbit as seen in subsection 5.2.5.

7.4.3. Sensitivity Analysis

This subsection will go deeper into the sensitivity of different parameters and discuss their impact on obtainable orbital altitude. subsection 7.4.3 will go over the parameters, Figure 7.4.3 will go over the feasible ranges for each of the parameters, Equation 7.4.3 will discuss the sensitivity of the parameters and Figure 7.4.3 contains a discussion on this sensitivity.

Parameters

Reference [53] notes the relationship between collection efficiency, I_{sp} and the C_D, in addition to their collective importance on the design space. Furthermore, it is noted that the orbital velocity does not vary enough to be of importance in our altitude range. Subsequently, these parameters are selected to conduct further analysis. The collection efficiency is defined as the ratio of incident atmospheric particles to the particles used for propulsion. Power supply is another parameter that has to be taken into account and determines the thrust generated.

$$\eta_c g_0 I_{sp} = \frac{1}{2} V C_D \tag{7.10}$$

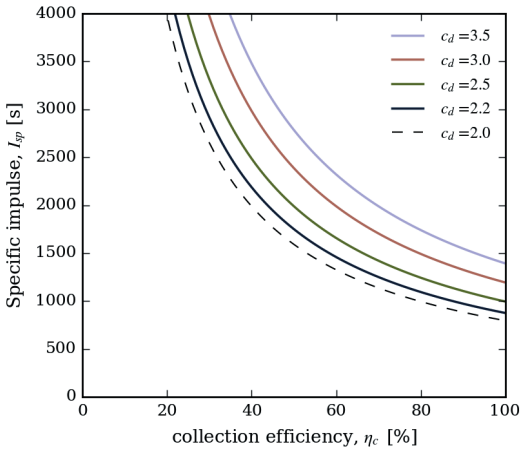

Figure 7.12: Plot that shows the limit of feasible designs space [53]

Expected Variation

To have a reasonable sensitivity analysis, a realistic range for the variation of the parameters should be considered. Starting off with the collection efficiency, it is seen by [53] that a collection efficiency between 25 and 40% is needed. Some preliminary simulations by [54] showed that a collection efficiency between 25% and 35% is more realistic with current technology; however, a range of 25 to 40% is used to account for future technological advancements. For the varying values of I_{sp} [53] in Figure 7.12, it can be seen that for a reasonable η_c (25-35%), a I_{sp} of 2500 s or higher is needed. This limits the choice of engine severely, as engines with an I_{sp} of 2500 s or higher are Gridded Ion Thrusters (GIT), Applied-Field MagnetoPlasmaDynamic thruster (AF-MPD) and Field-Emission Electric Propulsion (FEEP). The FEEP uses metals as a propellant[2] and can-

[2] `https://www.cubesatshop.com/product/ifm-nano-thruster/` [Cited on 14 May 2019]

not use air, whereas the AF-MPD is a magnetic thruster which can use nitrogen as propellant but not with an I_{sp} above 2500 s[3]. GIT's have been tested with a nitrogen and oxygen mixture by [52]. Therefore, the variation of GIT's is used for the I_{sp} range, which starts at 2500 s and goes until 5000 s, as shown in Figure 7.1 from [55]. Note that the higher I_{sp} is generally achieved with a much higher power and therefore in reality this would be too heavy to meet the weight requirement. These GIT's all use xenon as propellant, switching requires modification [52]. The modification in [52] does not change the I_{sp} significantly as the positive effect of air having a much lighter m_{ion} than xenon is counteracted by the mass efficiency (η_m) being much lower due to the gas conductivity of the grid, as depicted in Equation 7.11 [52]. In Equation 7.11, $\eta_m \sim \sqrt{m_0}$, $\frac{I_{sp}}{\eta_m} \sim \sqrt{\frac{1}{m_{ion}}}$, U_+ is high positive potential, U_p is plasma-potential, η_{div} is the divergence efficiency factor q_{ion} is the charge of the ion [52].

$$I_{sp} = \frac{1}{g} \cdot \eta_{div} \cdot \eta_m \cdot \sqrt{2 \cdot \frac{q_{ion}}{m_{ion}} \cdot (U_+ + U_p)} \tag{7.11}$$

Using the same set of GIT's from Figure 7.2 for the thrust per power ratio variation, a range of 20 mN/kW to 40 mN/kW is obtained. This range, however, is based on xenon as propellant. The modification needed for these engines will actually change the power consumption per thrust force [52]. The power consumption of GIT's consists of power for induction of the propellant, acceleration of the ions and power losses. Because most of the power consumed relies heavily on the physical properties of the propellant, the increase in total power consumption of the modified engine in [52] can be assumed as the general factor of power consumption increase. The thrust to power ratio of xenon is 0.030 86 mN/W and for a N_2 and O_2 mixture it is 0.014 15 mN/W, both from [52], coming to a ratio of 0.458 (-). Using this ratio, the range becomes 9.17 mN/kW to 18.3 mN/kW. The power is selected such that it can be achieved with a reasonable solar panel area that fits on comparable spacecraft like GOCE [56].

Sensitivity of Parameters

To asses the sensitivity of the parameters that affect the thrust and drag, each parameter is varied individually, ceteris paribus. The constant values used for these parameters are typical values obtained by averaging the expected variation discussed in Figure 7.4.3, except for the I_{sp}, where 3500 s is used instead of the average of 3750 s. To stay within realistic ranges for the varied values, the upper and lower limits of the expected variations are taken as the other values for the parameters. This thus results in three different values for each parameter.

To aid in understanding the influence of changes in these parameters, drag versus density altitude curves are plotted for each of the variations of a parameter. Because the calculations all use the same constants to calculate the intake area and drag, the middle curve will always be the same in each of the plots. Although all plots use the same mutual base, there are some differences in between them. First, looking at Figure 7.13, four curves and a straight line can be seen. The black straight line shows the maximum obtainable thrust for a 1500 W power input. Because the thrust over drag ratio has to be at least one, this line also represents the maximum drag possible to sustain in orbit. The three dashed curves represent the minimum, maximum and average value of the expected variation discussed in Figure 7.4.3. It can be seen that one of the curves does not cross the straight line at all, which will make it hard to compare the values numerically in Figure 7.4.3. That is why another curve is added in the form of a solid red line, which shows the lowest collection efficiency that still crosses the black line before 300 km. Figure 7.14 also shows the minimum I_{sp} of 3140 s, which is required for that altitude with typical values.

Figure 7.15 and Figure 7.16 show the sensitivity for power and thrust-to-power-ratio respectively. The power graph looks noticeably different. This is because changing the input power changes the thrust that can be produced instead of the drag created. Thus, on Figure 7.15, only one drag curve can be distinguished and the other three straight lines represent the different power inputs. At first sight, it looks like the input power is very sensitive at higher altitudes, but quickly gets less sensitive at lower altitudes. This is however implying that the frontal area and total mass does not increase when increasing power. This is thus entirely based on solar panel properties changing. In real life, it is more realistic to assume changes in these budgets as well, but to show the pure influence of power on the system all the rest is set to be constant. Figure 7.16 shows the impact of the thrust-to-power-ratio, which with a constant power supply has a direct influence

[3] `https://alfven.princeton.edu/tools/afmpdt-database` [Cited on 14 May 2019]

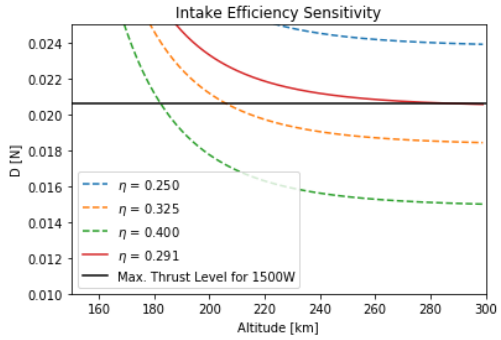

Figure 7.13: The effect of collection efficiency on the operational altitude of the spacecraft

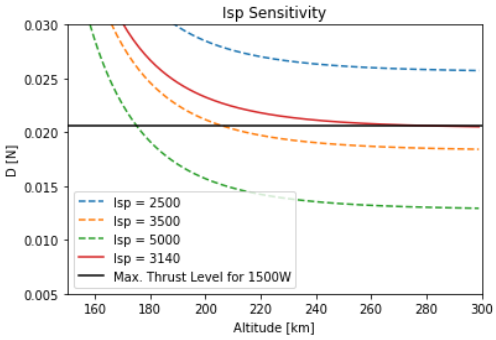

Figure 7.14: The effect of the I_{sp} of the engine on the operational altitude of the spacecraft

on the thrust. Changing this parameter changes thrust linearly, which makes for a small impact at lower altitudes, but a larger impact at higher altitudes. If compared with changing power, the thrust-to-power ratio varies in the same way and is thus also classed as medium sensitivity.

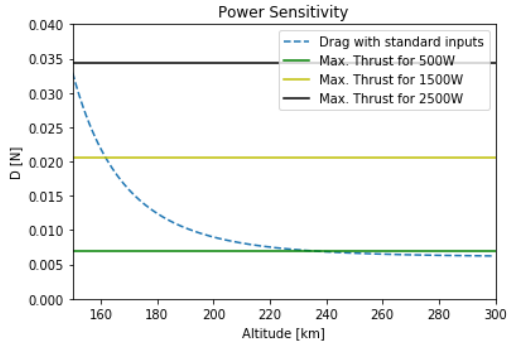

Figure 7.15: The effect of the power used by the propulsion system on the operational altitude of the spacecraft

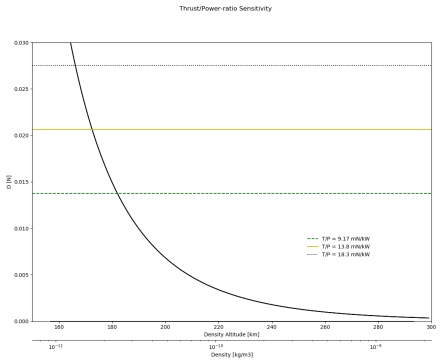

Figure 7.16: The effect of the thrust to power (T/P) ratio on the operational altitude of the spacecraft

Discussion

While Equation 7.4.3 used graphs to explain the results, this section will use Table 7.2 in combination with the graphs to explain the sensitivity of each parameter. Table 7.2 gives two values. The second column gives the lower bound of the altitude range, the third column gives the upper bound of the altitude range for the input parameter. The typical value that determines the separation between the two columns is shown next to the parameter name in the first column. The last column gives an indication of the sensitivity of the parameters.

Table 7.2: Numerical sensitivity analysis of thrust & drag parameters

	Typical	Lower Bound [km]	Upper Bound [km]	Sensitivity
Isp	3500 s	175 @ 5000 s	> 300 @ < 3140s	Very High
nc	0.325	181 @ 0.4	> 300 @ < 0.291	High
Pprop	1500 W	149 @ 2500 W	238 @ 500 W	Medium
T/P	13.8 mN/kW	167 @ 18.3 mN/kW	183 @ 9.17 mN/kW	Medium

Starting with the engine parameters of I_{sp} and collection efficiency, the table indicates a very high and high sensitivity respectively. However, this is not necessarily true for the whole range and depends a lot on altitude. For I_{sp}, going lower than the typical value leads to a large increase in altitude of the upper bound, up to where the altitude is far above 300 km. Which makes the lower part of the I_{sp} range very sensitive. Going higher than the typical value only leads to a decrease in altitude, but not as extreme as the upper bound, which shows that the parameter becomes less and less sensitive when the value increases. For collection efficiency, a similar effect can be noticed, although sensitivity remains high to very high along the whole range.

The last two parameters in Table 7.2 are power required for propulsion and the thrust over power ratio in mN/kW. The propulsion power is only medium sensitive. Increasing the power above 1500 W will have very little influence on the total altitude range. Lowering the power will increase the lowest altitude more, but still not enough to be considered high sensitivity. Considering the thrust over power ratio, it can be seen that changing this parameter has a similar effect. This is because it affects the thrust linearly and is also more sensitive at higher altitudes than at lower altitudes.

7.5. Risk & RAMS Analysis

The importance of considering any potential risks which the propulsion subsystem may be subjected to can not be underestimated. For this reason, the most critical ones will be identified and mitigation strategies will be devised. The risks include the following:

RSK-PROP-01 **Event:** Mechanical failure of the thruster during launch.
Risk: A mechanical failure of the thruster would lead to the inability of the spacecraft to counteract the drag encountered at the altitude range. This will lead to a fast decay rate and shortening of the mission life to a matter of days. This likelihood is deemed possible and the consequences are considered catastrophic.
Mitigation: Creating a more simple and robust thruster will make for less components that can fail, as well as a reduced likelihood of failure for each component. The RIT-10 thruster, with its passive compression, is a good example of how this mitigation is applied.

RSK-PROP-02 **Event:** Reduced lifetime due to dissociation of N_2 and O_2.
Risk: Dissociation of N_2 and O_2 has an effect on the amount of wear the atmosphere causes on the thruster. Increased wear will cause a reduction of lifetime and will pose an issue in terms of completing the lifetime set beforehand. The likelihood of this event occurring is deemed likely, with critical consequences.
Mitigation: Run thruster tests to check for dissociation levels and if needed, apply extra protective surfaces and counter measures to prevent erosion by these particles.

RSK-PROP-03 **Event:** Space debris hits the intake or thruster.
Risk: Collisions with space debris could potentially damage the spacecraft structure, causing local weaknesses or complete structural failure. The space debris, or collision debris could enter the intake system and damage the collimator, while potentially also damaging the internals of the thruster system. This likelihood is deemed rare and the consequences are considered catastrophic.
Mitigation: Reduction of grid size and reinforcing structure leads to more impact resistance and lower likelihood of debris entering the intake system.

RSK-PROP-04 **Event:** Lower or non-existent power supply to the thruster.
Risk: This event would lead to the inability of the spacecraft to ionise and accelerate the particles supplied by the intake. The effect of this is that no thrust will be produced anymore, leading to fast decay and re-entry. The likelihood of this event occurring is deemed likely, with catastrophic consequences.
Mitigation: Ensure proper contingency for power system. Take into account degradation of the power supply system.

RSK-PROP-05 **Event:** Higher levels of erosion than expected, caused by the atmospheric conditions.
Risk: Higher levels of atomic oxygen, as well as other erosive molecules in the atmosphere increase the risk of degradation and the possibility of earlier than expected system failure. This likelihood is deemed likely and the consequences are considered critical.
Mitigation: To ensure increased erosion will not lead to failure of the system, contingency will need to be added to the coatings and materials used for the intake and thruster system. Propulsion system tests, exposing it to an erosive environment, will increase knowledge on erosion resistance.

RSK-PROP-06 **Event:** The collection efficiency of the intake is different than designed for.
Risk: A decrease in collection efficiency would in the worst case lead to a too low particle density for the thruster to operate in. This would lead to a large decay rate and re-entry within a few days. Increased collection efficiency can create a too high particle density in the thruster inducing extra drag generation because the thruster has a delay in processing particles. This possibly causes thruster shutdown. The likelihood is deemed likely and the consequences are considered critical.
Mitigation: Increasing the density operating range of the engine reduces the likelihood of thruster

shutdown. Performing more detailed intake tests and calculations will also increase the level of certainty related to the intake collection efficiency.

RSK-PROP-07 **Event:** The required collimator efficiency is not reached during the development stage.
Risk: The required mass flow into the thruster is not reached, resulting in the thruster not being able to provide sufficient thrust to stay in orbit. This likelihood is deemed Likely and the consequences are considered catastrophic.
Mitigation: By designing for a contingency in mass flow, as well as allowing a certain flexibility in altitude and power range will reduce the constraints posed on the collimator.

Table 7.3: Risk map showing the severity and likelihood of the risks before and after mitigation

Severity \ Likelihood	Almost Certain	Likely	Possible	Rare
Catastrophic		RSK-PROP-04, RSK-PROP-07 →	RSK-PROP-01 →	RSK-PROP-03 ↓
Critical		RSK-PROP-02, → RSK-PROP-05, → RSK-PROP-06 →		
Marginal				
Negligible				

Determining the reliability of the propulsion subsystem is mainly based on the technology readiness level of its components. The two important parts that determine its reliability are the thruster and the collimator. The TRL of the thruster is determined to be 4, which already reduces reliability. The collimator TRL is only 1, which means a lot of research will have to be done still to increase certainty and reliability. In terms of availability the thruster system is doing better than the intake system. Once fully developed, the thruster system is simple to produce and does not use very expensive or rare materials. The intake system, namely the collimator, is however not fully developed yet. There is still little known about the feasibility of the system and a lot of research will be required to make this system readily available for spacecraft applications. With the exception of possible coating on the system, the propulsion subsystem is considered to be safe as well. No toxic materials are used within the system and neither of the parts of the subsystem are posing a hazard to the people interacting with it or their environments.

7.6. Cost Analysis

The cost will be split up in two parts: development and unit costs. The propulsion system currently has a TRL of 3 as there has been a proof of concept of the intake, but no full validation has been done as of yet. The thruster has a TRL level of 4 as it was fully tested with atmospheric gasses [52]. Therefore the TRL of the propulsion system is 3. Filling this in this equation which represents the cost of the development of an electric propulsion system[57]. The equation is based on data from both NASA and Mankins which was then intigrated into a equation by J. Reinchbar[57].

$$Cost_{development} = 33.4 \cdot 10^6 - 23700 e^{0.907(TRL)} \tag{7.12}$$

Gives 33 million 2002 dollar which is 40.5 million 2019 euro. For the theoretical first unit cost (TFU) [31]:

$$Cost_{TFU} = 247000(m_{total} - m_{prop})^{0.73} - 483000 \tag{7.13}$$

For a total propulsion system mass of 16.8 kg (including intake) minus zero propellant mass gives 1.4 million 2002 dollar. The theoretical first unit cost therefore is 1.8 million dollar in 2019 euros.

8. Power

The role of the Electrical Power Subsystem (EPS) is to generate, manage and store the power required by RAMSES throughout the duration of the entire mission. The general system and its driving requirements are outlined in section 8.1, followed by the general approach taken to design and size the solar arrays in section 8.2. The system architecture and performance specifications are provided in section 8.3. The selected methods and results are verified and validated in section 8.4, followed by a sensitivity analysis in section 8.5. Finally, the risks associated with this subsystem are identified and a RAMS analysis is conducted in section 8.6.

8.1. Functions & Requirements

The EPS is responsible for generating sufficient power to continuously maintain nominal operating conditions on-board the spacecraft. The system comprises three primary constituents, namely the power generation unit, the power storage unit and the power control unit. These must all operate in unison to provide the required power and protect the system from failing, which would have catastrophic consequences on the mission. The EPS configuration and sizing is driven by the total power required, in addition to a number of more specific details regarding the mission profile. Table 8.1 outlines the relevant components and how frequently they require power, which is the basis for the subsequent calculations conducted in section 8.2.

Table 8.1: Power consumption under different operational modes

		Day		Eclipse	
Component	**Power [W]**	**Duty Cycle [%]**	**Average Power [W]**	**Duty Cycle [%]**	**Average Power [W]**
Payload	30	26.5	7.95	0	0
Engine	415	100	415	100	415
IMU	8	100	8	100	8
Sun Sensor	0.8	0	0	0	0
Star Sensor	3.25	100	3.25	100	3.25
Magnetorquer	3.18	100	3.18	100	3.18
Magnetometer	1	100	1	100	1
Transponder	35	73.5	25.73	100	35
Computer	23	100	23	100	23
Total	519.23	-	487.11	-	488.43

In addition to this, it is important to take other factors such as mission lifetime and environmental conditions into consideration. Given the long lifetime and high power requirement (for a satellite of this class), solar arrays are a fitting choice for power generation, particularly due to their ability to do so reliably for extended periods of time in an Earth orbit. The alternatives include primary batteries, fuel cells and radioisotope generators; however, these would not be able to provide sufficient power throughout 10 years, especially with the given mass constraints [58]. The downside of the solar arrays is that they cannot generate power during eclipse periods. Due to this limitation it is necessary to make use of a secondary source of energy. For this, secondary batteries will be used; they will be charged during the day and employed during eclipse times. Additionally, as can be seen in Table 8.1, the batteries will be used to provide power during peak conditions as not all components will be operating continuously. Lastly, it is necessary to manage all the power being generated such that it may be distributed to all the relevant subsystems under the required conditions. This includes charging and discharging the batteries at the required rates such that their cycle life may be enhanced [59]. The demands imposed on the EPS are summarised in more detail in the following list of requirements, whose compliance is discussed in the section mentioned Table 8.2:

Table 8.2: Power subsystem requirements

ID	Requirement	Notes	Met [✓/✗]	Section
PWR-SC-01	The solar arrays shall provide sufficient power to accommodate the 497.71 W daytime consumption and the 488.43 W eclipse consumption	-	✓	subsection 8.3.1
PWR-SC-02	The solar arrays shall have a lifetime of at least 10 years	-	✓	subsection 8.3.1
PWR-BAT-03	The batteries shall have a sufficiently large capacity and an extensive cycle life to accommodate eclipse power requirements throughout 10 years	-	✓	subsection 8.3.2
PWR-BAT-04	The batteries shall be able to supply power to the spacecraft in safe mode for 5 hours	-	✓	subsection 8.3.2
PWR-PCU-01	The GPCU shall reliably regulate and distribute power to the other subsystems	-	✓	subsection 8.3.3
PWR-PCU-02	The IPPCU shall reliably regulate and distribute power to the propulsion system	-	✓	subsection 8.3.3

8.2. Methodology

In this section the methodology used to design the power subsystem is described.

8.2.1. Solar Arrays

In order to size the solar arrays, multiple factors which degrade the output power have to be taken into consideration. These include variations in the inclination with respect to the sun vector, temperature variations, degradation due to electron fluence and reductions in the surface transparency due to coatings [60]. Furthermore, one must consider the transmission efficiency from the solar array to the relevant components, the charging efficiencies of the battery and the packing factor of the solar cells.

The selected approach involves computing the energy generated per solar cell over the course of one orbit. The duration of the orbit is split into time intervals of one second, wherein all the aforementioned factors are incorporated to determine a realistic value for the energy. The variation in inclination is accounted for by applying a method which makes use of three inputs: $'\beta'$, the angle between the sun vector and the normal to the orbital plane, $'a'$, the orbital altitude and $'\theta'$, the roll angle of the spacecraft [29]. It is derived for fixed array configurations and assumes that the orientation of the satellite is tangent to the orbital path throughout, meaning that the array orientation with respect to the sun is continuously varying. The outputs are two parameters, C_0 and C_a. C_0 represents the efficiency of a panel that is continuously oriented towards the sun vector perpendicularly; in essence, it provides the portion of the orbit spent in daylight. If $C_0 = 1$, this means that there is no eclipse in that particular orbit. C_a on the other hand represents the efficiency of a fixed panel in that same orbit, accounting for both the eclipse period and the angular misalignment. Plugging in the relevant parameters leads to $C_0 = 0.629$ and $C_a = 0.41$. However, the eclipse times vary throughout the year; the maximum eclipse time experienced by the satellite was found to be 37.6% of the orbit in chapter 5, which is used to size the arrays. In addition, the code is implemented in such a way that the power and energy values are set to 0 during the timesteps pertaining to the eclipse period. Consequently, this leads to the use of C_a/C_0 such that eclipse times are not accounted for doubly. This factor is multiplied by the power output of the solar cells during each timestep.

The next important parameter to take into consideration is the degradation due to electron fluence. In order to account for this, electrical data pertaining to an equivalent fluence level of $1 \cdot 10^{15}$ e/cm^2 at an energy level of 1 MeV is implemented. This corresponds to a degradation of approximately 2% per year, leading to a total of $0.98^{10} = 0.82$ [60], which is used to size the arrays for EOL conditions. This factor also

accounts for the inherent degradation experienced over the course of the solar array's life.

Lastly, the power generation at each timestep has to be multiplied by the transparency due to the coating. The temperature variations are accounted for by making use of the following equation:

$$P_{cell} = \left(V_{base} - \| \frac{dV}{dT}(T_{base} - T_i) \| \right) \cdot \left(I_{base} - \| \frac{dI}{dT}(T_{base} - T_i) \| \right) \tag{8.1}$$

The symbols for the absolute value arise due to the fact that any deviations from the base temperature (28°C) result in a decrease in power output. The subsequent plots showcase the temperature variations in the body and fin arrays respectively, as obtained in chapter 12, in addition to the power generated throughout an orbit.

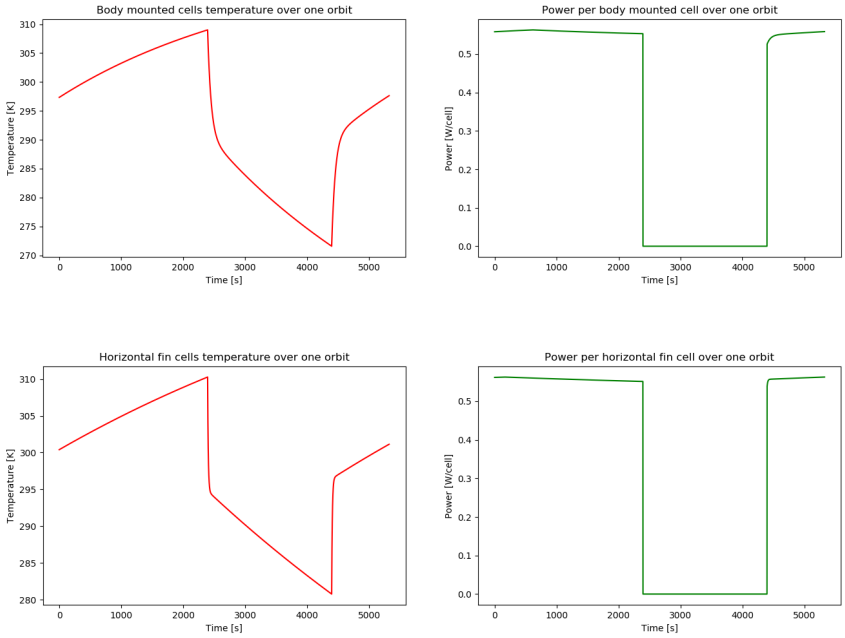

Figure 8.1: Temperature and power variations in the solar cells

The total energy required over the orbit is subsequently used to determine the required area. Additionally, the temperature variation efficiency is calculated by dividing the output power of the solar cell at the orbiting temperatures by the power produced by a cell at its base temperature.

8.3. Architecture & Performance

In this section, the configuration of all of the main components will be discussed. The methodology discussed in section 8.2 will be used to size the solar arrays with a selected solar cell model in subsection 8.3.1. Furthermore, the power requirements and eclipse conditions will be used to pick suitable batteries in subsection 8.3.2, after which a suitable power control unit is described in subsection 8.3.3.

8.3.1. Solar Cells

Solar cells function by converting solar energy into electrical energy. This is done by absorbing photons radiated by the sun in order to excite electrons in the semiconductor material, generating a potential difference. The success of the photon absorption is dependent on the band gap of the semiconductor, which is the energy level required to raise an electron from the valence band to the conduction band [59]. The photon energy is a direct consequence of the photon's wavelength, meaning that only a small portion of the solar radiation is absorbed by any given material. As a consequence, solar cells have been developed with multiple junctions such that a larger amount of the solar energy may be converted to electrical energy. Other variants such as thin film solar cells exist, but multiple junction cells are generally preferred for space applications due to their superior efficiencies [61]. It is useful to compile a table with performance data in order to select a suitable solar cell model, as shown in Table 8.3.

Table 8.3: Solar cell models

	Max Power per Unit Area [mW/cm^2]	BOL Efficiency [%]	Mass per Unit Area [mg/cm^2]	Temperature Coefficient [mW/ΔK]
Azurspace 3G30C[1]	40.30	29.5	86	-0.00161
SolAero Z4J Cell[2]	40.71	30	84	-0.00148
SpectroLab XTE-SF[3]	45.29	32.2	86	-0.000941
CESI CTJ30-80[4]	39.83	29.5	81	-0.00233

One can see that they all have similar performances across the board; however, the SpectroLab cell has the best BOL efficiency and temperature coefficient. Additionally, this cell is Gallium Arsenide based which means that it has a high degradation performance and efficiency, as well as absorbing photons with wavelengths between 350-850 nm [59], which is in accordance with the applied protective coating discussed in section 11.2. It is thus selected as the solar cell of choice and is used to perform the computations with the previously described simulation. This results in an area of 5.03 m^2 and a mass of 4.23 kg. The solar cells will be arranged such that the output voltage of each string is close to the main bus voltage; this will reduce power losses due to voltage conversions [62]. It is also worth noting that the resultant area accounts for a packing factor of 90% and a safety margin of 10%. This result is verified in section 8.4.

8.3.2. Batteries

One of the main priorities in selecting an appropriate battery is the cycle life. The satellite will go through approximately 59300 cycles over the course of this mission; it is crucial to find a good compromise between batteries with high energy densities or high cycle lives. If they are lacking in either of these criteria, the resulting mass of the batteries will increase significantly. Consequently, a 43 Ah Lithium Ion battery produced by Eaglepicher is selected; this is both due to its long term performance and its durability to a wide variety of operational temperature ranges [63]. In order to determine the required configuration it is necessary to determine the total required capacity such that an efficient configuration may be devised. The following equation is used:

$$C = \frac{P_{eclipse} \cdot t_{eclipse}}{V_{nominal} \cdot DoD \cdot n_e} \tag{8.2}$$

Given an eclipse power of 488.43 W, an eclipse time of 33 minutes, a nominal voltage of 3.6 V, a recommended depth of discharge (DoD) of 40%, and a charge-discharge efficiency of 90%, a capacity of 207.3 Ah is obtained. With this one can search for combinations of batteries that will provide the necessary capacity at a low mass. Given the capacity of the selected battery, the resulting number of required batteries is 5 when rounded up. However, given that the total number of required cycles during the 10 year mission lifetime is 59300 and the fact that each of these batteries can endure around 40,000 cycles at the recommended DoD, a second identical set will be required. This would exceed the required battery power during 10 years, but this can be rectified by increasing the depth of discharge of the batteries at the expense of its cycle life. Assuming that a 25% increase in the DoD would lead to an equivalent decrease by 25% of the cycle life [63], which would still provide a sufficient number of cycles, the calculations would look as follows:

$$C = \frac{488.43 \cdot 33/60}{3.6 \cdot 0.5 \cdot 0.9} = 165.83 \text{ Ah} \tag{8.3}$$

This implies that in this case, 4 batteries would be sufficient to provide power during the eclipse. In order to ensure the system is redundant, two additional batteries will be provided to the system (one for each set). Furthermore, the discharge rate will be $C/1.1$ such that a DoD of 50% is reached by the end of the eclipse duration. The batteries will provide power during safe mode as well in the case that the spacecraft encounters any problems. Assuming that the 5 batteries in one set are charged at a capacity of 70%, the

[1] http://www.azurspace.com/images/0003429-01-01_DB_3G30C-Advanced.pdf [Cited on June 15]
[2] https://solaerotech.com/wp-content/uploads/2019/04/Z4J-Datasheet-April-2019-10.pdf [Cited on June 15]
[3] https://www.spectrolab.com/photovoltaics/XTE_32_Percent.pdf [Cited on June 15]
[4] https://www.cesi.it/services/solar_cells/Documents/CTJ30-2015.pdf [Cited on June 15]

batteries could provide the required 86.95 W to the spacecraft for approximately 6.23 hours, although this is probably an optimistic estimate due to the fact that batteries provide lower amounts of power as they approach full discharge. Regardless they provide a useful time frame in which control of the spacecraft may be regained.

8.3.3. Power Control Unit

The purpose of the power control unit is to ensure that power is distributed to all the subsystems at the required voltage levels. Additionally, it is meant to protect all electronics from inadequate voltage and current levels. In the context of this mission, two separate PCUs will be implemented; an Ion Propulsion Power Control Unit (IPPCU) and a General Power Control Unit (GPCU). The decision to split these two components arose due to the fact that the power requirements for the engine and the remaining subsystems vastly differ. Furthermore, it is of utmost importance to ensure that the propulsion system is maintained at optimal operating conditions in order to extend its lifetime, hence why extensive research is being conducted on this specialised component [64].

A more general overview of the entire electrical block diagram incorporating both of the PCUs is shown in the following figure. It illustrates the links between the power generation, storage and distribution, as well as how all of these work in unison.

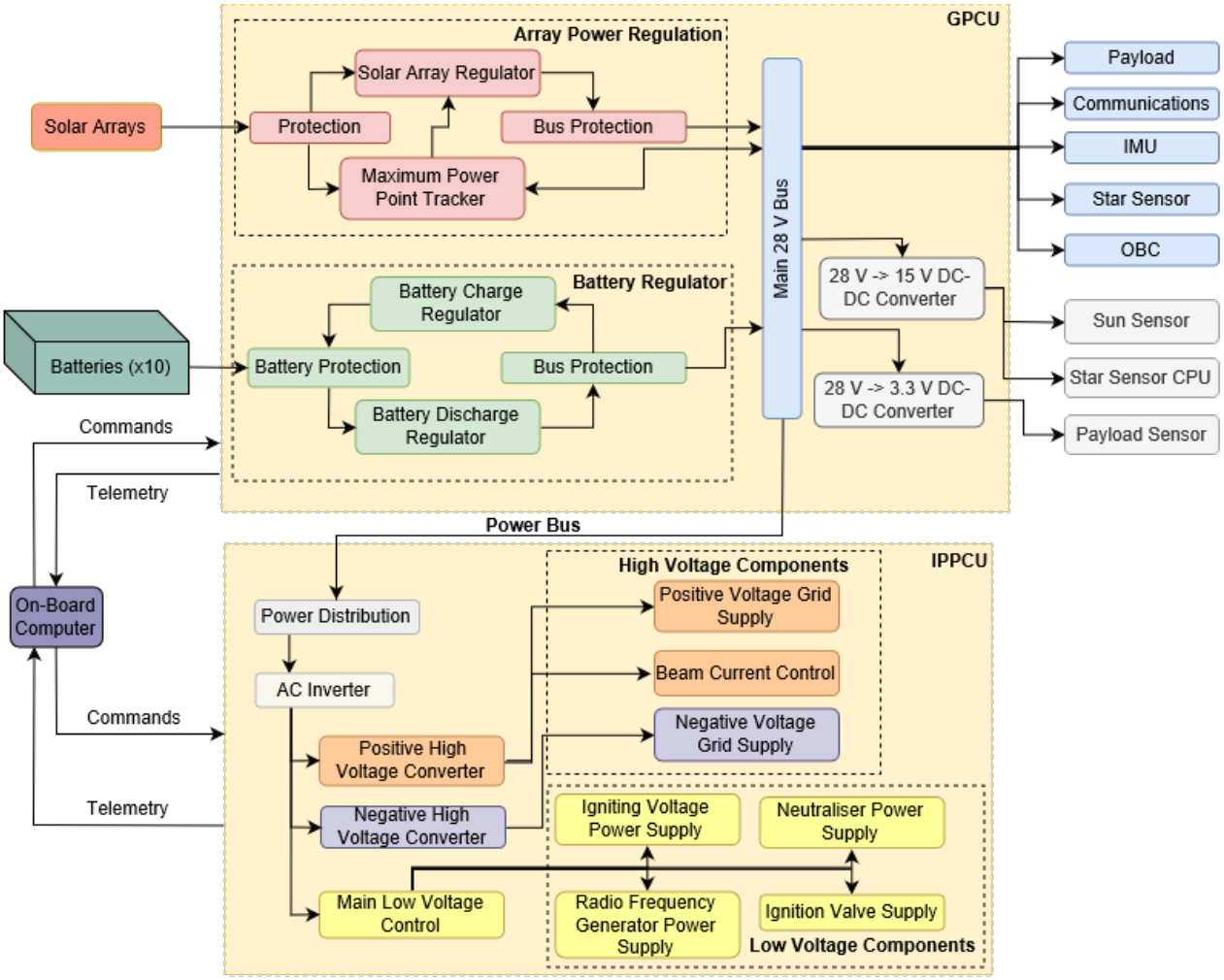

Figure 8.2: Overview of the electrical power subsystem

The GPCU must regulate the power provision to the majority of the subsystems, excluding the engine. In this case however it is also responsible for charging and discharging the batteries optimally. Moreover, it has to prevent any over-currents from being generated, as well as isolating any failed components so that they do not cause any further damage. For this, a number of latch up current limiters are implemented

at the main bus node [59]. A number of different design choices are available for the design of the GPCU; for instance, one must select whether the system will be centralised or decentralised, whether a high or low voltage bus will be used, or whether it will be regulated or unregulated, amongst others. These choices influence the overall performance of the system and must be carefully considered in the context of the specific mission profile.

In the case of selecting the distribution of the system, a more centralised topology is chosen due to only three distinct voltages being present within the subsystems, namely 3.3 V, 5 V, and 28 V. For this buck-boost boosters will be required [59] in order to step the voltage up or down accordingly. The GPCU employs a standard 28 V regulated bus due to the importance of providing the correct voltages to all the components, as well as the fact that the majority of the components operate at this voltage level. Furthermore, the GPCU is based on a highly modular architecture[5] which can allow for more voltage outputs if need be. Maximum power point trackers are used to optimise the solar array performance and maintain the desired bus voltage. This is selected over the use of Direct Energy Transfer due to the fact that the arrays are directly connected to the loads, which requires that the solar arrays, batteries and main bus all have common voltages. This is not ideal for a mission of this duration due to potential voltage variations as a result of the environmental conditions. Additionally, the Power Point Tracking architecture introduces a regulation device between the solar arrays and the loads, regulating the current in order to maintain the solar arrays at their peak power levels. This allows for mismatches between the solar array and load voltages, facilitating the design of the solar arrays. It is however still recommendable to match them to a certain extent as this minimises conversion losses. In addition to this, the GPCU contains a battery regulator; this protects and regulates the batteries during charge and discharge, as well as ensuring that all batteries are charged equally as cell balancing is crucial to ensuring their longevity. All the voltage outputs are maintained constant with respect to one another by having a common ground. The resulting mass of the overall system is 8.3 kg with a volume of 267 x 238 x 158 mm^3.

The IPPCU will serve a number of roles, ranging from power provision and regulation for all the relevant engine components to monitoring engine performance and transmitting this data back to the on-board computer. It provides an interface between the propulsion system and both the satellite main bus and the on-board computer. Power will be provided for the radio-frequency generator, the neutraliser, the accelerator grid and the ion beam converter, as outlined in chapter 7. An overview of the IPPCU and how it is incorporated into the power distribution system, based on an existing architecture [65], can be seen in Figure 8.2.

The IPPCU is connected directly to the main 28 V bus located in the GPCU. The power is initially distributed by a latching high power relay, which regulates the power passed through and can even cut it off entirely if need be. Subsequently, it is passed through an AC inverter which is used to more efficiently step the voltage up or down, particularly due to the fact that voltages of -600 V and 1200 V are required for the grid supply [66]. Three distinct voltage controller modules are responsible for supplying steady voltages and regulating them if need be. The neutraliser supply provides both power for igniting the neutraliser as well as maintaining a constant discharge level. The on-board computer receives data from the IPPCU regarding the thrust output and power consumption, as well as transmitting any necessary commands. The resulting overall mass of the IPPCU is 5 kg with dimensions of 180 x 350 x 250 mm^3 [65].

8.4. Verification & Validation

In order to make sure that the code that was implemented throughout the sizing process functions as one would expect it to, it is necessary to conduct some test cases and verify that the resulting values correspond to what one would expect. First starting off with the code used for the inclination, a number of tests can be performed. It is of interest to consider how a satellite with fixed panels whose normal is aligned with that of the orbit varies with the orientation of the orbital plane with respect to the Sun vector. This is shown in Figure 8.3 where the orbital plane is revolved once entirely and plotted against C_0 and C_a which were described in section 8.2.

The plot for C_0 displays minima at the first and third quarters of the revolution of the plane. This makes sense as the normal to the plane is perpendicular to the sun vector at these points, meaning that this is where the shortest daytime periods are experienced. The full daytime periods are experienced when the

[5] `https://www.terma.com/media/177710/power_conditioning_unit.pdf` [Cited on June 15]

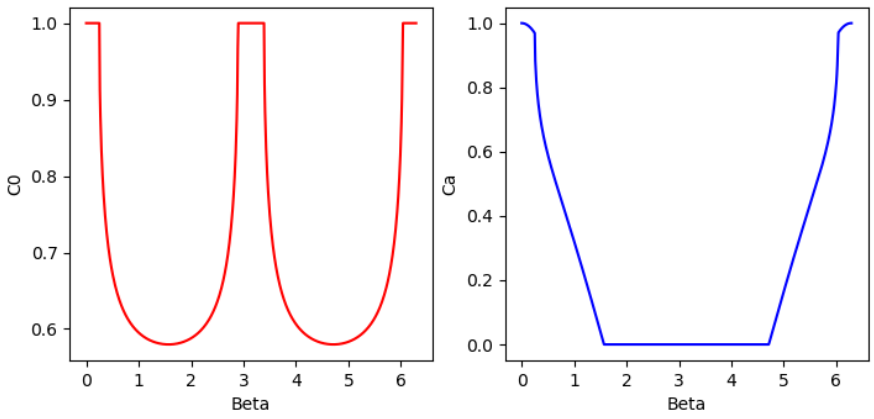

Figure 8.3: Effect of varying beta on Ca and C_0

orbital plane is normal to the sun vector. The reason that the C_a plot differs is that it assumes a fixed panel orientation; once the orbital plane is revolved 90 degrees, the solar arrays receive no more solar energy. This persists until the plane has revolved 270 degrees after which point the solar arrays begin to generate power again. Testing limit cases such as setting $a = 0$ leads to $C_0 = C_a = 0$ throughout, hence the program is deemed to work smoothly.

The solar array area from section 8.2 can be verified by carrying out the calculations analytically. First it is necessary to determine the power that must be generated accounting for internal efficiencies and the eclipse time, i.e. the power that the subsystems require the solar arrays to output at the end of life. The following equation is used:

$$P_{EOL} = \frac{P_{day} \cdot t_{day} + \frac{P_{eclipse} \cdot t_{eclipse}}{\eta_{charge-discharge}}}{t_{day} \cdot \eta_{trans}} = \frac{487.11 \cdot 3322 + \frac{488.43 \cdot 2002}{0.9 \cdot 0.9}}{3322 \cdot 0.9} = 904.6\,\text{W} \tag{8.4}$$

Subsequently, the required area can be computed by accounting for the remaining external factors:

$$A_{array} = \frac{P_{EOL} \cdot SF}{J_s \cdot \eta_{coating} \cdot \frac{C_a}{C_0} \cdot \eta_{temp} \cdot \eta_{BOL} \cdot df^T \cdot PF} = \frac{904.6 \cdot 1.1}{1400 \cdot 0.92 \cdot 0.65 \cdot 0.97 \cdot 0.322 \cdot 0.98^{10} \cdot 0.9} = 5.17\,\text{m}^2 \tag{8.5}$$

Whilst the array area produced by the simulation differs from this by 2.9%, this can most likely be attributed to the differing temperatures in the body mounted and fin mounted solar cells. As demonstrated by this equation, the code did not produce any irregular results. Tests such as increasing the overall temperature by large amounts also leads to diverging array areas.

With regards to validation, one can compare the current satellite mission profile with that of others to see if the environmental conditions are properly accounted for. A relevant measure with which this can be done is the power per unit area of comparable missions. Due to the special operating conditions, it is difficult to find multiple relevant cases; however, GOCE, designed by ESA, generates approximately 1 kW at EOL with a body fixed array of 5 m^2. This is directly comparable to the power per unit area of RAMSES, suggesting that the solar arrays have been sized reasonably.

In terms of validating the PCUs, breadboards would first have to be created for preliminary testing, followed by actual testing of a more finalised design.

8.5. Sensitivity Analysis

It is important to check the sensitivity of the designed components in order to understand how any unexpected variations in the operating conditions during the mission may affect the overall performance of the satellite. Given that the array was sized using the worst case eclipse conditions, as outlined in chapter 5, it is useful to consider how the lowest case eclipse will affect the resulting solar array area. Intuitively it will lower the area, but it is also important to consider that this will lead to increased temperatures due to prolonged exposure to the sun. With the current eclipse time that has been used for sizing the solar arrays, an area of 5.03 m^2 and a temperature variation efficiency of 97% are obtained. Using the temperature variations

obtained in chapter 12 and the new minimum eclipse time of 28 minutes, this leads to a solar array area of 5.01 m^2 and a temperature variation efficiency of 96%. Evidently this change is rather insignificant; a 15% change in the eclipse time leads to a 0.4% change in the required array area.

Two other factors which are important to consider are the duration of the mission and increases in temperature with respect to the current conditions.

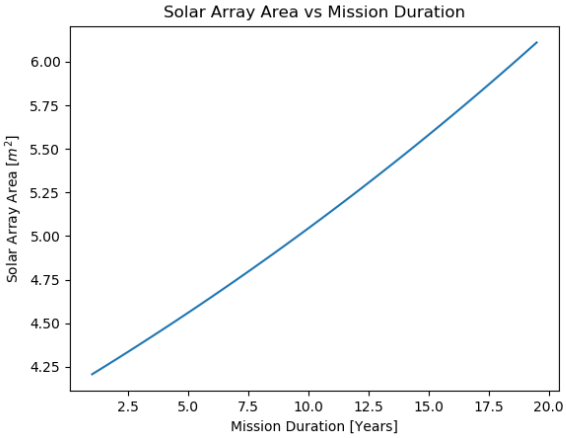

Figure 8.4: Effect of mission duration on required solar array area

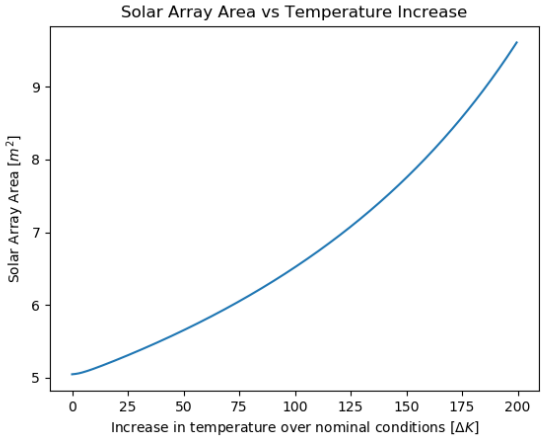

Figure 8.5: Effect of temperature increases on required solar array area

The relation between the required area and the mission duration is an exponential function of the yearly degradation. Due to the degradation value being so close to one, the relationship appears to be linear. It must be noted that the required array area increases by more than what is depicted in the figure because solar arrays begin to degrade more rapidly towards the end of a long life mission. This is in part due to the fact that they experience increased amounts of thermal fatigue as well as being subject to increased amounts of both atomic and electron fluence [67]. If the yearly degradation of the array increases then the exponentiality of the curve becomes more pronounced, which would be the case for other types of solar cells, for instance Silicon based cells, which provide a far worse degradation performance than Gallium Arsenide.

Looking at the plot of the temperature increase over nominal conditions, it is apparent that it has a significant impact on the required array area. The sensitivity to the temperature becomes larger as it approaches higher values due to its quadratic nature. This arises because the effect of the temperature is accounted for in both the current and voltage output. It is important to note that the solar cells would not actually be able to sustain a temperature higher than 150 °C as this exceeds their operational range. In addition, the higher the temperature, the more rapid the degradation, meaning that the required areas provided in the plot are likely understated for the upper region.

If other parameters such as the BOL efficiency are altered, it would merely shift the entire curve in Figure 8.4 upwards, but the variations in lifetime would increase or decrease the array area by the same amount, as this is dictated by the yearly degradation. The same can be said about varying the transparency of the coating. Both of these were tested in order to ensure that the program works as one would expect it to.

8.6. Risk & RAMS Analysis

In this section, the risk analysis for the power subsystem is described. The presented risks are addressed by considering mitigation strategies, after which the risk level is re-evaluated. Furthermore, a RAMS analysis is conducted in order to assess this subsystem in further detail and consider non-operational aspects as well.

8.6.1. Risk Analysis

It is of utmost importance to consider any potential risks which the power subsystem may be subjected to. For this reason, the most critical ones will be identified and mitigation strategies will be devised. The risks include the following:

RSK-PWR-01 **Event:** A string of solar cells is damaged irreversibly.

Risk: This may lead to two different consequences: first, it may damage other strings in the solar array, and secondly, it leads to a slight reduction in power output. This is only deemed as possible due to the heritage and reliability of the selected solar cells. It would however have catastrophic consequences.
Mitigation: Ensure that the strings of cells are properly isolated from each other, or account for some margins in order to ensure that slight reductions in power do not compromise the mission.

RSK-PWR-02 **Event:** The batteries are not charged and discharged according to their optimal conditions.
Risk: This may lead to strings of batteries which are connected in series and have different capacities; this can reduce the cycle life of the batteries, as well as their overall performance. This is deemed as a rare occurrence however, given that the charging conditions have been specified by the manufacturer and they have been extensively tested. It would have catastrophic consequences on the mission if it were to occur however.
Mitigation: Ensure that the PCU is properly designed to manage the power inflows and outflows and include redundant batteries.

RSK-PWR-03 **Event:** Batteries explode due to improper power management.
Risk: Not only removes the ability to generate power during eclipse, but may very well also damage other components in their vicinity. This would be a rare occurrence with catastrophic consequences.
Mitigation: Firstly ensure that the PCU is capable of managing the battery conditions and limiting current if it is in excess. Secondly, ensure that the batteries have proper casings to prevent other subsystems from being damaged.

RSK-PWR-04 **Event:** Failure of either of the power control units.
Risk: This would be catastrophic as it would lead to a complete end of the mission as most of the other subsystems would not be able to perform their respective tasks. The likelihood is deemed to be possible due to the high demands imposed on power distribution for an extended period of time, particularly in the case of the IPPCU.
Mitigation: Include redundant components in the PCU such that they become more reliable and robust.

RSK-PWR-05 **Event:** The power subsystem malfunctions for a limited period of time or provides power in a non-constant manner.
Risk: This could lead to undesired orbital variations or even destabilisation due to disturbance torques and the inability to provide thrust or maintain the desired attitude. It could also affect all the other subsystems although this would not have the same consequences. The likelihood is deemed likely and the consequences are considered critical.
Mitigation: This can be mitigated by ensuring the spacecraft can enter safe mode with power being provided by the batteries. Power fluctuations can also be compensated for by the batteries.

RSK-PWR-06 **Event:** Vibrations due to launch or disturbance torques lead to disconnections in the wiring.
Risk: This would either lead to the failure of a component or the inability to distribute power. The likelihood is deemed as possible with catastrophic consequences.
Mitigation: Ensure that they have a number of attachment points, both at the connection points and between components.

Table 8.4: Risk map showing the severity and likelihood of the risks before and after mitigation

Severity \ Likelihood	Almost Certain	Likely	Possible	Rare
Catastrophic			RSK-PWR-04, → RSK-PWR-02, RSK-PWR-06 → RSK-PWR-03	
Critical		RSK-PWR-05	RSK-PWR-01	
Marginal				
Negligible				

Following the risk mitigation, the two most critical remaining risks are those associated with the PCU failure and the wires being disconnected. It is thus crucial that these risks are prioritised above the rest.

8.6.2. RAMS Analysis

It is important to consider the reliability, availability and safety of the power subsystem in order to account for factors that were not included in the analyses conducted previously. The maintainability aspect of this analysis is not considered due to the nature of space missions.

The reliability of the solar cells is considered first. Given that the arrays were sized accounting for all the inefficiencies, in addition to a safety margin of 10%, and the fact that they can sustain higher levels of electron fluence than that which is anticipated, they will be able to provide sufficient power throughout the entire mission barring any damage caused by debris. Furthermore, atomic oxygen erosion is accounted for, as described in chapter 11. Concerning the batteries, they have been specifically designed for LEO environments and the configuration includes redundant units. The battery charge-discharge modules also ensure that capacity does not degrade excessively. The reliability figure quoted by the manufacturer of the PCU upon which the GPCU is based is 98.2% for a period of 10 years. Whilst the configuration is altered, it still makes use of the some of the similar components and includes redundancies. Finally, for the IPPCU, it is difficult to establish a reliability; further testing would have to be conducted in this specific configuration to obtain an estimate, especially given the fact that it has not been validated to function during a period of 10 years.

With regards to the availability of the components, the batteries and the solar cells are COTS components, so they are readily available. The solar cell manufacturers were contacted and a delivery time of 14 weeks is to be expected. The GPCU and IPPCU however are custom builds, so a considerable amount of time would have to be spent developing and testing them.

A number of safety considerations have to be taken into account concerning the safety of the solar cells. These contain harmful substances (i.e. arsenic and phosphorous), which requires the use of appropriate tools for handling. Furthermore, they must be stored in dry conditions in order to avoid oxidation and corrosion of the germanium substrate [68]. For the batteries it is important to avoid any conducting material from touching the terminals as this can electrocute the user. Direct contact with the batteries should also be avoided due to the risk of being harmed by corrosive battery acids. For the PCUs, the main safety consideration is that qualified facilities with the necessary precautionary measures are used during the testing procedures.

8.7. Cost Analysis

In order to estimate the cost of the subsystem, two approaches were taken. With regards to the solar cells, the suppliers were contacted and asked for a quote. For the selected model, a ROM price of €240 per cell is given; this translates to a total price of FY2019 €456,000 for the solar arrays. In order to estimate the PCU costs, a statistical average of the cost per unit mass of experimental missions is used [69]. A cost density of $39,800\$/kg$ leads to a total cost of $39,800 \cdot (8.3+5)$ = FY2008$530,000, or FY2019 €560,000. Lastly, the batteries are estimated to cost approximately FY2019 €70,000.

9. Payload

In this chapter, the payload will be described. Firstly, the requirements will be presented in section 9.1, then the methodology and architecture & performance will be described in section 9.2 and section 9.3, respectively. After that, a sensitivity analysis will be presented in section 9.5 followed by the verification and validation of the used models in section 9.4. Then a risk and RAS analysis will be performed in section 9.6. Lastly, the cost of the payload subsystem will be estimated in section 9.7.

9.1. Functions & Requirements

In section 2.2, the system requirements were presented. Three of these requirements can be directly transferred to payload requirements. The total list of requirements for the payload is shown in Table 9.1 along with the section where their compliance is discussed.

Table 9.1: Payload requirements overview

ID	Requirement	Notes	Met [✓/✗]	Section
PL-001	The payload shall take images in the visible spectrum	From REQ-USER-PERF-04 (section 2.2)	✓	section 9.2
PL-002	The payload shall take images with a resolution of 30 cm × 30 cm or better	From REQ-USER-PERF-05 (section 2.2)	✗(34 cm × 34 cm)	section 9.2
PL-003	The payload shall have a field of view of 2 km × 2 km or better	From REQ-USER-PERF-06 (section 2.2)	✓	section 9.2
PL-004	The payload shall weigh less than 30 kg.	Allocated mass budget	✓	section 9.3
PL-005	The payload shall use less than 30 W of power.	Allocated power budget	✓	section 9.3

As will be explained more extensively in section 9.2, the ground resolution of 30 cm × 30 cm cannot be met due to integration constraints and the required aperture and focal length. The resolution is instead 34 cm to 38 cm, depending on the exact altitude. This was deemed an acceptable increase, based on the physical limitations and the market position (see chapter 3).

9.2. Methodology

There are two main limiting factors for an imaging payload: an optical limit and an electronic limit. The optical limit comes from diffraction limited optics that can optically resolve an element with an accuracy $\Delta\theta$ (in radians) of $\Delta\theta = \frac{1.22 \cdot \lambda}{d}$ [31, 70], where λ is the wavelength and d is the aperture diameter (in the same dimensions). Multiplying this formula by the orbital altitude h will give the optically resolvable ground resolution: $\Delta\theta h = \frac{1.22 \cdot \lambda \cdot h}{d}$ [31]. The electronic limit comes from the relation between the pixel size p, orbital altitude h, focal length f and the ground resolution of a pixel GRC, all in the same units: $GRC = \frac{p \cdot h}{f}$ [71].

Requirement PL-001 states that the payload shall make pictures in the visible spectrum, which is interpreted as making colour images. To make a colour picture, two approaches can be taken: (1) use one chip to create a colour picture by using the information of multiple pixels (Bayer filter), or (2) use three chips (one for blue, one for green and one for red) and combine the value of the corresponding pixels to create the final colour image. Option one is simpler for design, but will result in a final image resolution that is 3-4 times lower than the chip can achieve, due to the combining of pixels [72]. Option two requires more design

effort, but will be able to produce a picture of the native resolution of the chips. Therefore, considering the very high required resolution, the latter option is chosen for this design.

Optical Limit

For the optical characteristics, the wavelength of the light is important. The camera will image in the visible spectrum and will thus image a wavelength range, the wavelength in the middle of the green band is chosen. This wavelength is 545 nm. The resolutions given in this subsection correspond to this wavelength.

To achieve the required spatial resolution of 30 cm x 30 cm at an altitude of 240 km an aperture diameter of 53 cm is required, see Figure 9.1. Due to the limited space available (see section 2.4), the maximum (effective) aperture that can be integrated into the spacecraft is approximately 42 cm. This is below the required aperture for the initial requirement of 30 cm x 30 cm. Therefore, this resolution cannot be met. With an effective aperture of 42 cm and at an altitude from 214 km to 240 km, the achievable spatial resolution (diffraction limited) is 34 cm to 38 cm, respectively, see Figure 9.1.

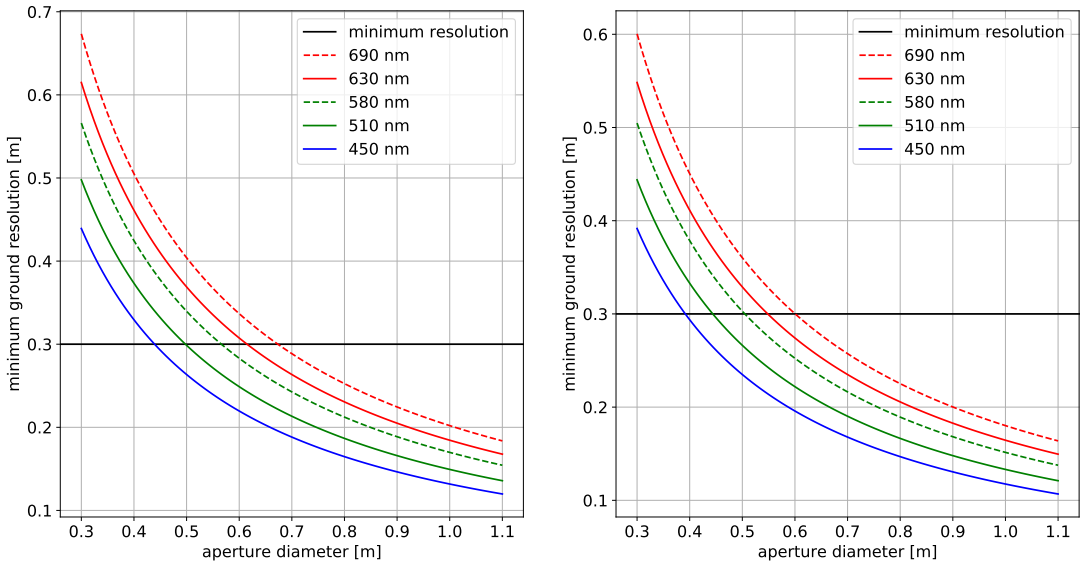

Figure 9.1: Required aperture diameter at various wavelengths, for an altitude of 240 km (left) and 214 km (right)

Chip Selection

Additionally to the optical limit, there is an electronic limit where the two main influencing factors are the chip pixel size and the focal length. A smaller pixel size gives a smaller focal length, resulting in an easier integration. The goal is therefore to select a chip with a small pixel size. Other important factors to consider for the chip are the type, number of pixels, shutter type and frame rate.

There are two main chip types that can be used; CCD and CMOS. Historically, charge coupled devices (CCDs) were preferred over complementary metal oxide semiconductors (CMOS) due to their better performance and the amount of research already conducted with these sensors. However, as technology progressed, CMOS-sensors have increased their performance. So much so, that CMOS-sensors can now outperform CCD-sensors [73, 74]. The main advantages of CMOS-sensors over CCD-sensors for the RAMSES mission are: significantly lower power usage, no smear, little blooming, better resistance to radiation and high achievable frame-rates [74]. The last advantage can relax the requirements on the ADCS (see chapter 10) as well as provide the option to take videos [75]. Taking videos is not a hard requirement, but it can make the spacecraft more competitive in the market (chapter 3). Considering the significant advantages of current CMOS-sensors, CMOS-sensors are the best choice for this mission.

The number of pixels of sensor determines the mode in which the pictures can be taken. The most common modes are whisk-broom scanning, push-broom scanning and staring modes [35]. In the whisk-broom case, the camera is moved in the across-track direction while the spacecraft motion moves it forwards. In the push-broom case, only the forward spacecraft motion is needed and the camera can remain still. In the staring mode, the sensor can image the entire FOV in one go. For a FOV of 2 km x 2 km with a resolution of

30 cm x 30 cm, the required number of pixels in both the horizontal and vertical directions is 6667 resulting in 44.4MP in total.

No matter the type of the imaging chip, rolling and global shutters are available. "Global shutter means that every pixel of the entire pixel array acquires the image during the same time period, while the rolling shutter shifts exposure time for each row in the image" [76]. Global shutters are therefore better for applications that involve fast moving objects [76], such as this mission.

For the frame rate, the sensor must be able to take sufficient images per second, as the spacecraft moves with a large velocity over the target. In order to be able to stitch all images together to create a long strip of image, an overlap of about 50 % should be used [71]. Since the maximum ground track velocity is 7.848 km/s, the required number of pictures per second is 6. Significantly higher frame rates (about 30 frames per second) will allow the camera to also take videos of a target.

Keeping all the above considerations into account, the Gpixel GMAX3256[1] was chosen. This chip is a CMOS chip with 3.2 µm pixels, 9344(H) x 7000(V) pixels (65MP), a maximum frame rate of 31 frames per second (fps) at 12-bits per pixel and a global shutter[1]. The number of pixels in this chip allow the sensor to be used in staring mode, requiring no movables to capture the required FOV. This increases reliability and reduces complexity and is therefore a large advantage of this chip. Additionally, due to its high achievable frame rate, the sensor can also take videos.

Pointing Accuracy & Stability

To take image without blur and of the correct place, the imaging payload requires a certain pointing accuracy and stability. These two parameters affect the design of the ADCS (chapter 10).

The payload needs to achieve a FOV of 2 km x 2 km. To do this in the nadir direction, where the highest resolution is achieved, the spacecraft will need to be able to point the payload with a certain accuracy. In the across-track direction the imaging sensor has 9344 pixels. With a ground resolution of 34 cm at 214 km altitude, the FOV is 3177 m. This means that the allowable deviation of nadir pointing in the roll direction is $\arctan(\frac{(3177-2000)/2}{214000}) = 0.16°$ to keep the target area in view. For the upper altitude bound of 240 km with a ground resolution of 38 cm the allowable deviation is 0.19°. This means that the required pointing accuracy for the camera in roll is 0.16°. For the pitch angle, in the along track direction, the same logic as for the roll angle can be used. In the along-track direction the imaging sensor has 7000 pixels. With a ground resolution of 34 cm at 214 km altitude, the FOV is 2380 m. This means that the allowable deviation of nadir pointing in the pitch direction is 0.05° to keep the target area in view. For the upper altitude bound of 240 km with a ground resolution of 38 cm the allowable deviation is 0.08°. This means that the required pointing accuracy for the camera in pitch would be 0.05°, which is very strict. However, in the along track direction, the pictures are stitched together and already have a 50% overlap. Taking this into account, the accuracy can be relaxed to 0.20°. For the yaw direction, the spacecraft only rotates the field of view, without changing its size. This means that independent of the yaw angle, a FOV of 2 km x 2 km can be achieved in the nadir direction. Therefore, there is no requirement from the payload on the yaw accuracy.

Pointing stability is related to the pointing accuracy as well as the sensor shutter speed. However, for stability, the deviation may not be more than one half of the pixel size in the shutter time [75]. As the ground resolution is square, the pointing stability is independent on the direction. The exact shutter time of the chosen chip is not available, but looking at a comparable chip, the CMV50000[2], the shutter time can be assumed to also be 100 µs[2] (the minimum of the sensor, if desired, the sensors can be run at slower rates). This means that the minimum required stability in roll is $\frac{0.34/2/214000}{100*10^{-}6} = 0.45\,°/s$ at the lower bound of the altitude range. For a relaxed shutter time of 10 ms, which is a normal shutter time of the comparable chip[2], the required pointing stability is increased to 0.0045 °/s, also for the lower altitude bound. For the upper altitude bound, the stabilities become $\frac{0.38/2/240000}{100*10^{-}6} = 0.51\,°/s$ for the fast shutter time and 0.0051 °/s. These stabilities are very strict, but due to the fins, the ADCS is still more than capable enough to handle this (see chapter 10).

Disturbances

Regardless of the performance and design of the optical system, distortions will always be present and need to be addressed. There are two main categories of distortions; radiometric distortions and geometric dis-

[1] `http://en.gpixelinc.com/productMechanies/36.html` [Cited on 18 June 2019]

[2] `https://ams.com/cmv50000` [Cited on 19 June 2019]

tortions [3]. Radiometric distortions are errors in the brightness values of the pixels while geometric distortions are errors in the representation of the geometry. Both distortion categories can be treated by post-processing [3], but some factors will have a larger influence than others, depending on the mission. The different influential factors and their importance for this mission are discussed in this section.

Radiometric distortions are caused by the presence of the atmosphere and/or by instrumentation effects. The instrumentation effects are generally ignored by comparison to the atmospheric effects [3]. The main detector error that could have an effect are the errors within a band [3]. The in-band errors are caused by detector noise (called dark current noise [3, 70]). This can be corrected for by using an independent reference value for the brightness and by means of a simple linear correction [3]. This correction is especially important when using multiple sensors in the same band [3]. Since this mission only has one sensor per band, this is of lesser importance to this mission. In addition, the dark current noise increases with increasing temperature [3, 70]. The imaging payload will be operated in a temperature range that is on the low side (see section 12.3), reducing the initial error further. The atmospheric influence can be characterised by three effects; transmittance, sky irradiance and path radiance [3]. The part of the sunlight that reaches the sensor is the transmittance [3]. Since the atmosphere blocks part of this light, the light intensity will be reduced. Sky irradiance and path radiance are caused by scattering [3]. This will result in light reaching a pixel that did not originate from the target. Atmospheric effects are more important when the camera is detector limited and has a wide field of view [3]. The camera aboard RAMSES is diffraction limited and has a narrow field of view, reducing the importance of this error source. The most important parts of the atmospheric effects are the Rayleigh and Mie scattering phenomenons, which are wavelength dependant [3, 70], causing changes in brightness in the pixels. The atmospheric influences can be mitigated in two main ways; using a detailed correction or using a bulk correction [3]. The detailed correction is usually not necessary and requires information about the atmosphere that is not always available [3]. The bulk correction varies with the wavelength λ as $\lambda^{-\alpha}$, with alpha between 0 and 4 depending on the extend of Mie scattering [3]. By determining the exact shift (with respect to a scattering free case) in brightness of each pixel in the same band, the shift due to scattering can be determined [3]. This shift can then be subtracted from the brightness value of each pixel in the band [3], compensating for the atmospheric effects. This method is also known as haze removal [3].

Geometric distortions can have many different sources but all are caused by the geometry of the overall system (satellite, camera and object on the ground). For these errors it is important to consider the mode in which images are taken. The RAMSES satellite uses a staring mode that does not move the camera at all. The main geometric error source are: "the rotation of the earth, a finite scan rate of the sensors, the wide FOV of some sensors, the curvature of the earth, sensor non-idealities, variations in platform altitude, attitude and velocity and panoramic effects related to the imaging geometry" [3, p.37]. The finite scan rate as well as the wide field of view of some sensors are not applicable to the RAMSES payload and are thus not further discussed. Consequently, the panoramic distortions from scanning are also not an issue. In addition, due to the low altitude and narrow FOV, the curvature of the earth also has a negligible effect [3]. The first error source, the rotation of the earth, is important when using line scanner, as the object on the ground will move while taking the picture [3]. In the staring setup of the RAMSES satellite, the pictures are taken almost instantaneously and no stitching of the lines is required. The only situation in which the rotation of the earth can have an effect on this mission is while stitching numerous pictures together. Sensor imperfections are most important for scan sensors. The error sources of the sensors have already been discussed previously. The variations in platform altitude, attitude and velocity are important for this mission. The altitude variation experienced by the spacecraft is negligibly small compared to the image time, as the altitude is varied in accordance to the 11-year solar cycle (see also chapter 5). As a result, a similarly small variations occurs in the velocity. The changes in attitude, however, are significant and lead to image rotations [3].

There are two main ways to compensate for geometric distortions, modelling the nature and magnitude of the error source or to create a mathematical model between image pixels and the target by means of a map [3]. The latter is more general and requires less knowledge of the problem, but is computationally more expensive. Since the two main error sources for this mission are the rotation of the earth and the attitude change of the spacecraft, the error sources can be modelled. The rotation of the earth is known and is ideal for compensation is this manner [3]. The attitude of the spacecraft is continuously monitored and managed by the ADCS (see chapter 10) and transmitted as housekeeping data (see chapter 6). Since these

errors source are already known on the spacecraft, these corrections can be made on-board.

To increase the market value (see chapter 3), the spacecraft can be temporarily rotated to point the camera at a point of interest to a customer. Due to this rotation, the camera will no longer be nadir pointing. Depending on the extend of the rotation, the distortions caused by the curvature of the earth and the panoramic distortion can become important. As the attitude with respect to the earth as well as Earth's radius is known, similar techniques to process these images can be used [3]. More important, at least for the customer, is the change in spatial resolution. The size of a pixel on the ground (GRC) in nadir direction is 34 cm to 38 cm, but will increase according to $GRC_{\text{new}} = GRC_{\text{nadir}} / \cos\phi$, where ϕ is the roll angle measured from nadir. The resolution can not be increased by means of post-processing, only the disturbances can be removed. The maximum allowable roll angle depends on the required time the spacecraft has to be at the new angle, as the power generation (see chapter 8) will be affected. To give an idea of the effects, the resolution will become 5% worse (from 34 cm to 35.7 cm) at a roll angle of 17.75°, which corresponds to a horizontal distance of 68.5 km off nadir.

9.3. Architecture & Performance

With the discussions of the previous sections in mind, the integration of the camera can start. The chosen image sensor with 3.2 µm pixels requires a focal length of 2.02 m. Currently, smaller pixel sizes on chips with a global shutter are not available. In the near future, sensors with pixel sizes of 1.1 µm with global shutter will be available [8], but these are not available yet and therefore not selected. Reducing the pixel size to 1.1 µm would reduce the required focal length to 0.69 m, simplifying the integration. The post-processing of the images is done on-board, but these tasks are delegated to the on-board computer (see chapter 13).

One valuable aspect of imaging satellites is their ability to image the same spot regularly. This is captured in the temporal resolution. If RAMSES would fly its orbit with the least variations in density, no Earth repeat orbit and therefore a very low temporal resolution would be achieved. To improve this aspect, RAMSES can fly periods of Earth repeat orbit, as explained in chapter 5, creating periods where the temporal resolution is between 4 and 14 days, depending on the altitude.

Payload Integration

To integrate the required focal length of 2.02 m, multiple options are available. Since the available height is only 36 cm, numerous folds are required. For small satellites in general, current research focuses on extendable telescopes [77–79]. However, for this design, extending the telescope outside of the spacecraft would result in a significant unsymmetrical increase in drag which cannot be tolerated, as this would increase the mass and power of the propulsion system and ADCS significantly. Recently, MIT researchers published a form of optics that folds the optical length in time [80]. While promising, this reduces the light intensity, which is already low in space and radiation might cause severe noise. One promising option is to use annular folding [2], in particular the (air) gap version. An example of an annular folded optic is shown in Figure 9.2. The gap version can also be squeeze focused by moving one of the mirrors closer to the other [2].

Figure 9.2: Example of an 8-times folded annular optic [2]

A large portion of the focal length can be achieved by using annular folding. For an annular optic with N folds, a thickness of t and a refractive index n_s (1.0 for vacuum/air), the effective focal length f_{eff} is given by $f_{eff} = \frac{tN}{n_s}$ [2]. For an 8-times folded optics with a thickness of 16.2 cm, the achievable focal length is 129.5 cm. This thickness is found by maximising the space used by the annular optic to benefit from its efficient focal length integration (space wise). The annular optic also has an effect on the aperture. As discussed in section 9.2, the required (effective) aperture must be 42 cm. For an annular optic, because the one mirror blocks part of the aperture, the effective aperture diameter d_{eff} is given by $d_{eff} = d_{outer}\sqrt{1-o^2}$, with d_{outer} the outer diameter of the optic and o the obscuration ratio [2]. In order for the 16.2 cm thick optic to fit inside the spacecraft, the maximum outer diameter can be 47 cm, resulting in an obscuration ratio of

0.45. This results in a diameter of 31.5 cm for the mirror that blocks part of the aperture, which will have its back pointed towards Earth.

The other part of the required focal length is achieved by bouncing the light two more times via mirrors before it reaches the beam splitter that is connected to the three chips. This increases the total focal length to 219 cm, leading to a diffraction limited camera system. A schematic of the camera as integrated into the spacecraft cross-section can be seen in Figure 9.3. The dimensions shown are in cm.

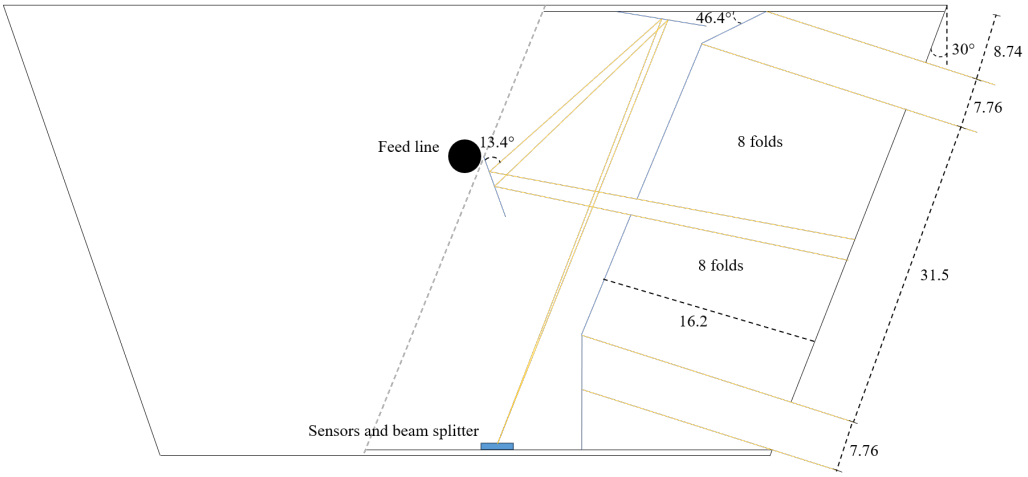

Figure 9.3: Schematic of the camera as integrated into the spacecraft (not to scale), the dimensions shown are in cm. The spacecraft moves into the paper

Materials & Mass

With the layout of the system known, the material can be selected. The material for the payload needs to be lightweight, keep its shape over different temperatures and be erosion resistant. Different materials have been used over time for mirrors in space [81]. A very promising material is carbon fibre reinforced silicon carbide (C/SiC) [4, 81]. This material is very strong, lightweight, compatible with a large temperature range and has good optical properties [4]. As an additional useful property, it is also impact tolerant due to the fibre reinforcements [82]. Even though C/SiC is erosion resistant, atomic oxygen still poses a problem [5]. C/SiC can be coated with different coatings that can protect the material [81]. The selected material for coating the optics is a hollow silica nanosphere/polyimide composite. This type of coating has not shown any degradation of optical properties during testing [6]. However, as other coatings do degrade over time and the mission lifetime is longer than what was tested for, some degradation is expected. A more elaborate discussion of the coatings can be found in section 11.2. Also, a thin protective layer (coating) on the reflective surfaces of the annular optic does not introduce significant aberrations [2].

Depending on the thickness of the mirrors, the mass can be estimated. From previously made C/SiC mirrors [83, 84], the average areal density can be interpolated. This results in an areal density of 18 kg/m^2.

The annular optic consist of two mirrors, one with a diameter of 47 cm and the other with a diameter of 31.5 cm. Using 18 kg/m^2 as areal density, the mass of these mirrors will be 3.1 kg and 1.4 kg, respectively. The two smaller mirrors have a diameter of about 6 cm, resulting in a mass of 0.05 kg each. The total mass of all the mirrors is therefore 4.6 kg. For the support structure, which will be made of the same material, because this is compatible with the mirrors and has high thermal conductivity, avoiding local temperature changes that could interfere with the shape of the mirror. Also, C/SiC has not shown any deformation over a wide temperature range [85]. The density of C/SiC is 2.7 g/cm^3 [4]. The support structure has an inner diameter of 55 cm, a height of 33 cm and a thickness of 1 cm, resulting in a total mass of 4.9 kg. This results in a structural weight (including mirrors) of 9.5 kg. Adding a mass for the sensors (and their metal protection case), beam splitter, DC/DC converters for the chips, potential actuators for squeeze focusing the annular optic, attachments as well as extra contingency because of the various uncertainties in the payload design results in a final mass of 30 kg, which is in line with other camera's with a similar effective aperture[3] and with design tools that estimate payload mass from total spacecraft mass [86].

[3] `https://www.harris.com/sites/default/files/downloads/solutions/55475-spaceview-24-35-42-datasheet-final-web.pdf` [Cited on 23 June 2019]

The power required by the payload is used by the chips (6.3 W), electrical converters (3 W), potential actuators for squeeze focusing the annular optic (15 W) and for contingency (5.7 W). The total budgeted power (30 W) is therefore deemed sufficient. Compared to the other cameras[3], the power is still on the low side, but this can be attributed to the use of CMOS sensor, which are very power efficient [74].

The volume for the payload envelope is straightforwardly given by the volume encapsulated by the support structure and equals 0.45 m^3.

9.4. Verification & Validation

The verification & validation of the models used for the payload subsystem can be relatively brief, as few models were used. The two main equations used $\Delta\theta h = \frac{1.22 \cdot \lambda \cdot h}{d}$ [31] and $GRC = \frac{p \cdot h}{f}$ [71], are already proven and applicable to the design of this imaging system. The implementations were checked by running the examples given in the related references and the result were identical. For the first formula, the $\Delta\theta h$ terms is a small angle approximation for the ground resolution (GRC), which is applicable as the angle $\Delta\theta$ is approximately 1.58×10^{-6} rad (from $\Delta\theta = \frac{1.22 \cdot \lambda}{d}$ [31, 70]).

The more critical part to check is the integration. The integration used for this system is not a conventional system. As mentioned before, due to time constraints, ray-tracing software could not be used. To verify that the integration was done correctly, a scale drawing was made and the geometric considerations were reviewed. It was found that the initial configuration had two different definitions of the thickness of the annular optic, causing the integration to be wrong. After redoing the integration, the current layout was found. The drawings made for this layout were deemed consistent and accurate after careful inspection. The equations used to size the annular optic are taken from Reference [2] in which they were validated by making prototypes of small lenses, as well as by mathematical models. In the design of the annular optic, it was assumed that the work done in Reference [2] could be scaled to the required size without alterations and that the loss of light intensity will not have a severe effect. This will have to be validated with future models (such as ray tracing) and tests.

Another important part of the payload is the calculation of the pointing accuracy and stability requirements. The numbers have been verified by comparing them to design rules [31] and by other models [87]. They were found to be of the correct order of magnitude. After expert feedback related to the previous version of this report, the values were corrected, especially the pointing accuracies, making them stricter. The previous values were too high, but due to values reported in literature as high as 700 rad/s [75], this was not found initially. The updated stability requirements pose no problems for the ADCS. The new roll accuracies are very strict, but the ADCS is just able to cope with this, see chapter 10. Improved calculations of the requirements is left for a future design phase, when the optical path through the payload can be taken into account.

Other than the above described parts, the payload design is based on numbers from manufacturers and/or on the explanations or number from the cited papers. These are considered verified and no further verification and validation is done for them.

As discussed throughout this chapter so far, the payload will meet all requirements except for requirement PL-002, as has been explained in section 9.2.

9.5. Sensitivity Analysis

The design of the payload is sensitive to changes of required altitude, resolution and spectral range. The space available for the integration of the payload is limited and cannot be enlarged. Therefore, if the required focal length increases, only very small changes can be made to the payload before it becomes unfeasible or the performance is reduced.

Changes in the altitude are normal for this mission. Therefore, as long as the altitude stays within the range as described, the payload performance is as reported. In the case that the altitude decreases below 214 km, the payload performance in terms of resolution can increase slightly. The opposite will happen when the altitude is increased above 240 km. If the spacecraft stays below an altitude of 214 km for a significant amount of time, the degradation due to the atmospheric effects will be accelerated.

The resolution cannot be made better with this design. It is already slightly above the initial requirement (section 9.1) so increasing the resolution required will require a full redesign of the payload and since the payload is limited by the integration constraints, a redesign of the entire spacecraft would be required. This

is therefore not possible.

The spectral range can be varied sensors wise, as CMOS sensors can use the same optics to image in different spectra, though the sensitivity of the sensors will be different. However, as there is a beam splitter in front of the sensors, which will cause only the red, green and blue spectra to reach the chips with full intensity. Small changes can be made to the beam splitter to facilitate different configurations, but this will affect the ability to take images in the visible spectrum.

Overall, the payload design can tolerate very little variations before major design changes are required.

9.6. Risk & RAMS Analysis

Now that the payload design has been presented, potential risks can be identified and a RAMS analysis can be performed. These are outlined in this section.

9.6.1. Risk Analysis

Various parts of the payload are at risk during all stages of the project. These risk are listed below. For each risk, a mitigation strategy is also presented. A likelihood and severity is given to each risk before and after mitigation. The payload is the revenue generating element of the mission. However, as this is also a demonstration mission for air-breathing propulsion, failure of the payload does not have to end the mission. The payload severity's are therefore not classified as catastrophic.

RSK-PL-01 **Event:** Mirror surface quality is insufficient.
Risk: The surface quality of a mirror is one of the most important aspects of a mirror. If the surface finish is not as expected, the performance of the overall system will be decreased and the severity is thus critical. As bare C/SiC has been shown to change its optical properties due to atomic oxygen [6], the current likelihood is almost certain.
Mitigation: During manufacturing, each mirror must be thoroughly checked for surface finish to avoid launching mirrors of low quality. During mission operations the environment, especially atomic oxygen, can have an effect. To mitigate this as much as possible a suitable coating has to be selected. As it is uncertain if and how this coating will behave for a 10-year mission, but the coating has shown no degradation under the tested conditions [6], the mitigated likelihood is possible.

RSK-PL-02 **Event:** Mirror alignment is inaccurate.
Risk: As with mirror surface quality, the alignment of the mirrors is very important. Misalignment of the mirrors reduces the performance of the overall system and is thus deemed critical.
Mitigation: After assembly, proper alignment must be confirmed before launch. In addition, the setup must be tested to ensure that launch loads do not significantly change the alignment. Once these tests and inspections have been performed, the risk can be classified as rare.

RSK-PL-03 **Event:** Debris shatters a mirror.
Risk: Debris can potentially break a mirror, which would be critical as well. However, C/SiC is already more resistant than other ceramics due to its fibre reinforcements [82] and the amount of debris in VLEO is low. The likelihood is therefore rare.
Mitigation: No mitigation required.

RSK-PL-04 **Event:** Payload pointing is wrong.
Risk: If the payload is pointed in the wrong direction, the output is useless and the quality is reduced, which is critical. However, the ADCS system would have to fail permanently, which is unlikely (see section 10.6) and is therefore deemed rare.
Mitigation: No mitigation required.

RSK-PL-05 **Event:** Sensor failure.
Risk: A failure of one of the sensors would cause one colour band to disappear, leading to pictures without proper colours, leading to a critical severity. A sensor can fail due to a failure of the GPCU or due to radiation. Failure due to radiation is possible, but a failure of the GPCU is rare (see section 8.6). The overall risk is therefore deemed possible.
Mitigation: To provide extra shielding for the sensors, they can be surrounded by a small metal casing (but not in front of the sensor). This will reduce the likelihood to rare.

The above listed risks are shown in the risk matrices in Table 9.2.

Table 9.2: Risk map for the payload. The arrows indicate where RSK-PL-01 and RSK-PL-05 will be after mitigation

Severity \ Likelihood	Almost Certain	Likely	Possible	Rare
Catastrophic				
Critical	RSK-PL-01 →		RSK-PL-05 →	RSK-PL-02, RSK-PL-03, RSK-PL-04
Marginal				
Negligible				

9.6.2. RAMS Analysis

Now that the payload has been discussed and several risks have been identified, a reliability, availability and safety analysis (RAS) can be made. Usually, maintainability is also part of such an analysis, but as this is a spacecraft that will not be serviced, this aspect is left out.

The first part of the analysis is critical, because one of the requirements (see section 2.2) is for the spacecraft to have a reliability of 90% over 10 years. The payload integration is not conventional nor has the annular optic been used for space applications before. Materials very similar to C/SiC are already operational for space telescopes [88] and the exact material has been used to make mirrors [83, 84]. Therefore, when it comes to the manufacturing and integration, the payload should not experience any problems. The annular optic and integration should first be verified by more detailed analysis and tests before the reliability can be confirmed. During operation, the main risk for reliability is atomic oxygen. The applied coating looks promising, but as already mentioned before, further testing is needed to confirm its performance for a 10-year mission. Overall, the payload reliability will need to be checked by tests.

In terms of availability, the parts for the payload can be easily obtained. The sensors and beam splitter can be ordered and the support structure can be made using conventional machining techniques [4]. The more difficult part are the mirrors. The mirrors need to be polished, which is the most time consuming part of making mirrors from C/SiC [4, 81, 82, 88]. Therefore, the payload has to be planned in advanced and replacement mirrors need to be ordered on time. Otherwise, the payload has no problems with availability.

The last aspect of RAS is safety. For the payload, there are some safety aspects to consider during manufacturing and end-of-life reentry. The material is reinforced with short carbon fibres, which, when inhaled, can cause respiratory problems. This can be avoided when a proper face mask is used. Also, the disposition of the reflective layer happens at elevated temperatures, so care must be taken. The end-of-life aspect is discussed in detail in section 11.3. The mirrors and support structure are all made from C/SiC, but this material has the potential to survive reentry. By the analysis done in section 11.3, it was found that the parts that survive do not have sufficient energy to be of danger. Therefore, the payload is considered safe.

9.7. Cost Analysis

The last section of the payload chapter concerns the cost of the payload subsystem. The cost of the payload is difficult to estimate, as most parts need to be custom made and even the sensors do not have a listed price. To come up with a cost estimate, a parametric cost estimate is used. The cost model used for the payload is the Demonstration Satellite Cost Model (DSCM), which "is a parametric model designed to estimate the cost and schedule of advanced technology demonstration satellites of all sizes." [89, p.6]. This model generally overestimates the costs of the subsystems [89], so the value found using this model can be taken as an upper bound. For an optical payload the forumla is [Cost (FY06$K)] = $760[\text{Payload Weight (lb)}]^{0.69} \cdot (\log[\text{Spectral Range (A)}])^{0.37} \cdot 0.28^{[\text{Cryostat}]}$ [89].

For the RAMSES mission, the payload is budgeted at 30 kg or 66.14 lb, the spectral range range from 450 nm to 690 nm or 4500 Å to 6900 Å and it does not have to operate under cryogenic temperatures. This results in a total cost of FY06$21.5 \times 10^6$. To convert to FY19 euros a factor of 1.096 is used. The final cost of the payload then becomes FY19€23.7×10^6. This includes research and development cost. Using Reference [31], which gives a ratio of unit over development cost for optical payloads, the development cost is estimated to be FY19€16.9×10^6 and the unit cost is FY19€6.8×10^6. These costs were also shown in chapter 3.

10. Attitude Determination & Control

This chapter describes the design of the Attitude Determination and Control Subsystem (ADCS). In particular, a general overview of the system and the requirements are specified in section 10.1, while the steps taken in the design are discussed in section 10.2. The architecture of the system is defined in section 10.3, together with the expected performance and the compliance with the requirements. The verification of the methods used to design the system is treated in section 10.4, together with the validation of the results. After this, the sensitivity analysis is shown in section 10.5. Finally the risks associated with the system and in particular with the design for RAMSES are identified in section 10.6, and an estimation of the costs is given in section 10.7.

10.1. Functions & Requirements

The Attitude Determination and Control Subsystem (ADCS) takes care of providing the required pointing accuracy and stability to the subsystems of the spacecraft. These accuracies are formulated as requirements, and can be identified by examining the operations of the spacecraft in a systematic manner. Pointing the spacecraft along one axis is obtained by controlling the angular positions about two axes perpendicular to the pointing direction. As such, only two pointing requirements can be satisfied at the same time [31]. For the demonstrator that is being designed in this report, the most important requirements on the ADCS come from the propulsion subsystem, the solar panels and the payload. The pointing of the antenna used for communications is discussed in section 6.3, since the antenna is designed to be self steering.

To meet all the requirements at the same time, multiple options are possible: using gimbals, designing movable solar panels, relaxing the pointing accuracy requirement for the solar panels. After further considerations regarding the high weight and complexity of gimbals, these systems are discarded. Additionally, the reliability of the spacecraft would be compromised by using such mechanically moving systems. As for movable solar panels, the same considerations hold. Furthermore, only part of the required solar array area will be on external panels, as solar cells will also be mounted on the body of the spacecraft in order to minimise drag. Movable panels would still not fully meet the requirement. Also, the external solar panel would be mounted on the same structure of the aerodynamic fins, so, moving them would compromise the stability of the spacecraft. It is instead decided to relax the requirement on the solar arrays, by sizing them for a worst case incidence angle of 30 degrees.

The requirements can be found in Table 10.1. To be noted, there is no requirement on the slew rate, since the S/C does not need to be re-oriented in nominal operations for pointing of its subsystems.

The critical requirement for angular deviations about the y and z axes is the requirement on the alignment of the S/C with respect to the flow, ADCS-003. In pitch and yaw, the ADCS has to guarantee 0.05 degrees accuracy. For angular deviations about the x axis, the critical requirement is the pointing accuracy required for the payload, from ADCS-001: 0.16 degrees.

10.2. Methodology

The first step for designing the ADC system is to calculate the disturbance torques which can be encountered by the spacecraft at the operating conditions. Then, a trade-off is done in order to come up with a suitable configuration for the sensors and actuators included in the system, considering all phases of operation, from detumbling after launch, to nominal and safe mode operations. The parameters required for the actuators to compensate for the disturbances are then approximated, and sensors and actuators are chosen off-the-shelf. Furthermore, the attitude of the spacecraft is described using a state space system, and the motion of the satellite is simulated. The following subsections describe the entire process in detail.

10.2.1. Disturbances

These torques can be differentiated in external and internal torques. The most significant external torques are aerodynamic, gravity gradient, magnetic and solar radiation disturbances. Internal disturbances can also have notable effects on the attitude of the spacecraft, and are usually more difficult to quantify at this stage of the design, as integration is a crucial factor in their influence.

Table 10.1: Subsystem requirements on the ADCS.

ID	Requirement	Notes	Met [✓/✗]	Section
ADC-001	The system shall autonomously maintain the payload pointed in the Earth's direction with an accuracy of 0.16 deg in roll and 0.05 deg in yaw and pitch.	Requirement derived in section 9.2.	✓	subsection 10.4.2
ADC-002	The system shall autonomously maintain the solar array oriented towards the Sun with an accuracy of 30 degrees.		✓	subsection 10.4.2
ADCS-003	The system shall autonomously maintain the S/C oriented in the flow direction with an accuracy of 0.8 degrees.	Requirement derived in subsection 10.3.3.	✓	subsection 10.4.2
ADC-004	The system shall have a maximum angular rate of 0.0045 deg/sec in roll, yaw and pitch.	Requirement derived in section 9.2.	✓	subsection 10.4.2
ADC-005	The spacecraft shall be three axis stabilised.		✓	subsection 10.4.2
ADC-006	The system shall be able to sense the attitude with an accuracy of 0.001 degrees within 0.1 seconds.	One order of magnitude more accurate than the control requirements [31].	✓	subsection 10.4.2
ADC-007	The system shall autonomously maintain the antenna pointed to the receiver direction with an accuracy of 0.3 degrees.	Typical requirement from [31]. This requirement is met by use of a steered beam as discussed in section 6.3.	✓	subsection 10.4.2

External Disturbances

The worst case aerodynamic torques T_{aero} are estimated for the altitude range, by computing the value of drag as explained in section 4.2, for maximum solar intensity [31]. It is calculated with, $T_{aero} = D \cdot (c_{pa} - cg)$

$$T_{aero} = D \cdot (c_{pa} - cg) \tag{10.1}$$

The moment arm $c_{pa} - cg$ is the distance between the centre of aerodynamic pressure and the centre of gravity of the spacecraft. The torque generated by this disturbance is minimised by designing the spacecraft to have the two parameters coincide. Nevertheless, it is decided to quantify and design for the disturbance assuming a misalignment of 15 cm, to account for minor design changes and production errors.

The gravity gradient torque T_g is estimated from the mass distribution of the satellite, accounted for by using the mass moments of inertia I_X, I_Y and I_Z, as well as orbital radius a and the Earth's gravity constant μ. The angle θ defines the misalignment of the local vertical to the Earth with the z axis of the spacecraft [31]. This is computed with, $T_g = \frac{3\mu}{2a^3}|I_Z - I_X|sin(2\theta)$, obtained by iteration with the CAD model. The worst case gravity gradient disturbance is found by plugging in the equation the lowest between I_X and I_Y. For the case of RAMSES, the lowest is I_X. The values of the moments of inertia are the following: I_X= 21.46 kgm^2,

I_Y= 86.57 kgm^2 and I_Z= 102.81 kgm^2.

The torque generated by the solar radiation pressure depends on the distance between centre of solar pressure c_{ps} and centre of gravity cg. This distance is assumed from statistical values to be 0.2 m [31]. This torque is calculated with, $T_{sp} = \frac{J_s}{c} A_s(1+r)cos(i)(c_{ps} - cg)$. This equation takes into account the solar intensity flux J_s, taken to be 1358 W/m^2, the speed of light c, the reflectance factor r and surface area A_s exposed to the solar ray. Finally, the incidence angle i is also taken into account. The value of the reflectance factor for solar panels is approximated by a unity minus the transmissivity of the coating that covers the solar array: 1-92.3% = 0.04 [90]. The worst case incidence angle is for RAMSES is 0 degrees, with the solar rays perpendicular to the surface of the spacecraft. The largest surface area which is the largest area that can be exposed at once to solar radiation is estimated as the top view projected area of the satellite, and is equal to A_s = 7.08 m^2.

The magnetic disturbance torque is estimated by considering the highest magnitude of the magnetic field which can be encountered at the lowest altitude, as $B = 2 \cdot MM_E/a^3$, where MM_E is the magnetic moment of the Earth and a again the orbital radius. The disturbance torque is then computed by examining the interaction of the magnetic field B with the magnetic moment of the spacecraft, MD [31]:

$$T_m = MD \cdot B. \tag{10.2}$$

As a preliminary estimation, the magnetic moment of the spacecraft MD is taken to be 1 Am^2 [31]. This estimation will be refined with testing of the S/C and extra magnetic moment will be compensated locally using magnets.

Finally, meteoroid impact were considered. They are deemed not significant both because of the operating altitude of RAMSES and for the torques which an impact can generate: based on a statistical approach on the amount of debris present at higher altitudes, it is estimated that dynamic disturbances caused from meteoroids are in the order of 10^{-10} Nm [91].

Internal Disturbances

Internal disturbance might arise from operations of mechanical and electrical systems, as well as from temperature fluctuations, which will cause transient deformations on the structure of the spacecraft. The presence of cabling is also to be considered: a non uniform distribution of the cables will cause the spacecraft to have a dipole moment that will cause disturbance torques [92]. In most cases, the mechanical disturbances are the most relevant out of the ones mentioned before, amounting to up to 5% of the torque generated by the motors [92].

For the design of RAMSES, there are no mechanical actuators. The main internal disturbance is deemed to be the magnetic field that the ionised particles in the engine generate. Other disturbances are neglected in this phase, and can be addressed for example, while testing the spacecraft configuration in order to evaluate the residual magnetic dipole, to calibrate the magnetic field sensors [93]. The internally generated magnetic moment can be in part nullified by using compensation magnets [94].

The magnetic disturbance generated in the engine is calculated from the value of the electric field in the exhaust, measured by Lotz in [52]: E = 5 V/cm. By relating the electric and magnetic field with the speed of light c, the value of the induced magnetic field is found to be $B = E/c = 1.7 \cdot 10^{-6}$ T. The value of the torque generated by this field is estimated using Equation 10.2, and is found to be $T = 1.7 \cdot 10^{-6}$ Nm, by assuming again a spacecraft dipole moment of 1 Am^2. Testing and simulations should be performed to precisely know the direction of the applied torque, and a control software developed in order to account for the variation of the magnetic field.

Magnitude of the Disturbance Torques

The worst case disturbance torques are calculated as explained in the previous sections. Their value for the case of RAMSES are reported in Table 10.2.

Table 10.2: Magnitude of the disturbance torques

Disturbance	Gravity Gradient	Aerodynamic	Solar Pressure	Magnetic	Internal
Magnitude	$8.5 \cdot 10^{-5}$ Nm	$7.8 \cdot 10^{-4}$ Nm	$9.9 \cdot 10^{-6}$ Nm	$5.6 \cdot 10^{-5}$ Nm	$1.7 \cdot 10^{-6}$ Nm

From this table, it can be noted that the disturbance with causes the highest torque is the aerodynamic disturbance. The control system is designed for the combination of these torques, for a maximum of $T = 9.4 \cdot 10^{-4}$ N m. This is the disturbance the actuators will be designed for in case the spacecraft is aligned with the flow. When the spacecraft becomes misaligned with the flow, the drag force caused by the increased frontal area will be higher, and will be compensated for by designing a passively stable spacecraft.

10.2.2. Design Option Tree

The Design Option Trees relative to the attitude determination and control architectures are shown respectively in Figure 10.1 and Figure 10.2. The attitude determination is carried out with conventional sensors. The only option excluded which is further discarded since the trade-off of the midterm phase is the use of GPS. This is mainly due to the weight constrain of mission: attitude determination using GPS can only be carried out with at least three GPS antennas on board [95]. Using conventional sensors provides the same information, but with better accuracy and less weight, so the GPS option was discarded.

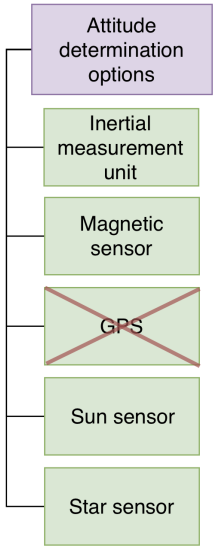

Figure 10.1: DOT for the attitude determination system

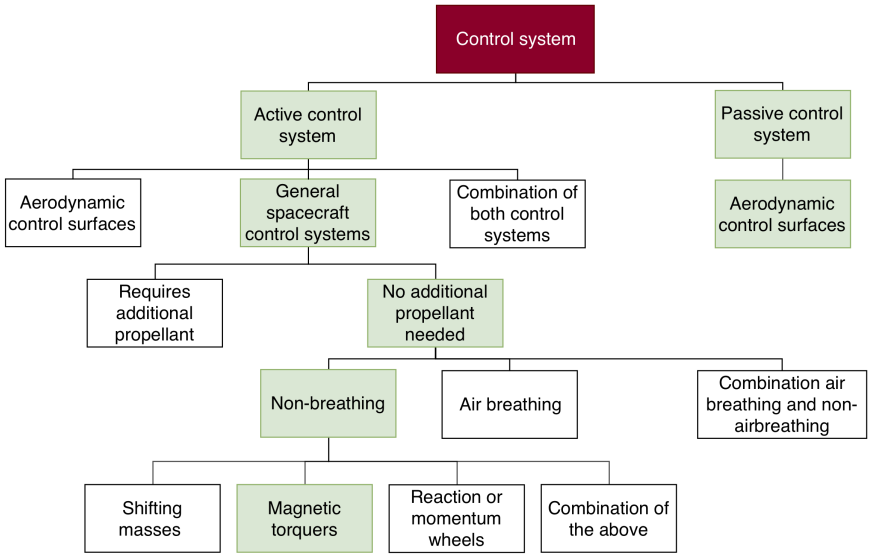

Figure 10.2: DOT for the attitude control system

For the attitude control subsystem, magnetorquers are required to carry out detumbling operations after launch. These systems are therefore selected as the main control actuators, accompanied with fixed aerodynamic fins, for fast responses to destabilising torques in pitch and yaw.

Sizing of magnetorquers

The magnetorquers are sized in order to counteract the worst case torque, discussed in subsection 10.2.1. The required dipole moment, in order to counteract the maximum disturbance torque T_{max} that can be encountered is given by,

$$D = \frac{T_{max}}{B}, \tag{10.3}$$

with B the value of the magnetic field.

Sizing of Stabilising Fin

The spacecraft, with its large hollow intake in the front is highly unstable on its own. The centre of pressure is in front of the centre of gravity, which indicates it is unstable. In order to meet the stability requirements set out in section 10.1, fins will thus have to be designed in order to provide a degree of passive stability. This will help shift the centre of pressure back, on, or behind the centre of gravity by creating counteracting torques when disturbed. An important consideration during this sizing process is the extra drag generated, which is not allowed to surpass 83% of the thrust level to ensure a proper margin.

Free molecular flow conditions do not allow for straightforward calculations of the centre of pressure location. So determining stability is done in a similar, but not identical way, compared to the standard centre of pressure determination techniques. Because the forces on the spacecraft sections can be determined, the

torque around the centre of gravity is calculated instead. If this torque acts in the opposite direction of the disturbance, it will counteract the disturbance and prevent the spacecraft from diverging too much from perfect alignment. Based on this torque, the location of the centre of pressure can be derived by dividing the total torque by the sum of all the forces on the spacecraft.

Determining these forces can be done in two different ways, depending on the accommodation coefficient. If the accommodation coefficient is one, forces transmitted to the spacecraft only act in drag direction. If the coefficient is zero, forces are transmitted normal to the surface they act on. Accommodation coefficients are however hard to determine exactly, since it depends on both the flow conditions and the material used. Since the coefficient is most likely to be close to one, calculating stability based on drag forces is prioritised. This method of calculation works by first calculating the force on each component by using Equation 10.4. Where C_D is assumed to be 2.4 on average, based on analytical calculations and literature [18, 19]. $A_{frontal}$ is the frontal area of the particular component. By then calculating the distance from the centre of gravity perpendicular to this force and multiplying it with the force, the torque around the centre of gravity is acquired.

$$F = C_D \cdot 0.5 \cdot \rho \cdot V^2 \cdot A_{frontal} \tag{10.4}$$

The larger this generated torque, the faster the system will react to the disturbance. Because they provide little damping, they will only prevent the spacecraft from diverging too much from the nominal alignment axis. Then it will slowly oscillate with slightly decreasing amplitude, which can be corrected with the use of magnetorquers.

10.3. Architecture & Performance

This section describes the architecture chosen for the attitude determination and control systems, highlighting the performance of the sensors and actuators and the operational profile of the system. Their compliance with requirements is also discussed.

10.3.1. Attitude Determination

The design of the attitude determination subsystem is carried out by examining separately the various phases of operations of the satellite, in particular detumbling after launch, nominal operations and safe mode, and defining for each of them the optimal configuration.

Detumbling Mode

Immediately after launch, the spacecraft will start tumbling in space. According to the specifications of the launcher, whose selection is treated in section 11.3, the spacecraft will have a rate deployment margin from the target value of ±1 degree/s[1]. The sensors will have to perform a first acquisition of the attitude, in order for the actuators to damp the remaining angular momentum and for the spacecraft to begin nominal operations. Coarse attitude measurements are sufficient for this phase, and in particular Sun sensors can be used especially for their large field of view. Furthermore, these sensors are highly reliable, and are able to operate at high rotational rates [95].

Nominal Mode

The requirement for nominal operations for pointing accuracy is given as 0.16 degrees in ADCS-001 for roll, and as 0.07 degrees in ADCS-003 for pitch and yaw. The attitude sensing capability of the spacecraft has to be at least one order of magnitude lower than the control accuracy. For this, star sensors are used. These sensors identify star patterns in 3-axis stabilised satellites [96], with an accuracy of 0.0001 degrees[2]: the identification of two stars is sufficient in nominal operations, four stars are needed for initial acquisition [95]. The star sensor requires a clearance of at least 30 degrees angle from the Sun, and 25 degrees from the Earth's pointing direction to function. Radiation either from the Sun or reflected from the Earth blind the sensor, and over time, degrade its performance [95]. An Inertial Measurement Unit (IMU) is used to accompany the accurate attitude values produced by the star sensors. This kind of sensor uses fiber optic gyros and accelerometers to track the angular rates, position and velocity of the spacecraft, without requiring the input from an external reference. It accurately keeps track of the attitude of the spacecraft, smoothing out

[1] `https://www.rocketlabusa.com/assets/Uploads/Rocket-Lab-Payload-Users-Guide-6.4.pdf` [Cited on 20 June 2019]

the data from the star sensors, which only provide measurements with frequencies up to 10 Hz[2]. This sensor is always used in conjunction with other sensors, because its measurements drift with time, so the IMU has to be calibrated periodically using the data from Sun and star sensors [31]. These sensors fully determine the attitude, but for the design it is chosen to include also a three-axis magnetometer. This sensor is required in order to provide a feedback control loop for the magnetorquers, which will be used as the main control actuation, in order to increase their accuracy. Moreover, the magnetometers will be used for altitude determination, as explained in subsection 5.2.6.

Safe Mode

Sun sensors only provide two-axis information, but are very useful in safe mode operations. Their large field of view angle allows to determine the position with respect to the Sun, and for the solar panels to be effectively pointed with an accuracy high enough to provide the power required for safe mode operations. In addition to this, they have a high acquisition rate, which allows them to function even when the spacecraft is tumbling. For an almost complete spherical coverage, four sensors are required, to be mounted on different sides of the body.

Attitude Determination Architecture

The sensors mentioned above for the various operational phases are collected in Table 10.3.

Table 10.3: Architecture of the attitude determination system

Sensor	N	Accuracy	Weight	Power	Dimensions	Notes
Sun Sensor[3]	4	0.15 deg	0.65 kg	200 mW	160 x 145 x 56 mm	FOV 128°
Star Sensor[2] + Electronics Box	2 2	0.0001-0.0025 deg	1 kg	3.25 W	155 ⌀ x 281 mm 100 x 100 x 40 mm	FOV 20°
IMU[4]	2	0.05 °/h	0.7 kg	5-8 W	88.9 ⌀ x 73.7 mm	
Magnetometer[5]	2	75 µT	0.3 kg	1 W	100 x 82 x 34 mm	
Total			6.6 kg	25.3 W		

10.3.2. Centre of Pressure

The centre of pressure has to be behind the centre of gravity, in order to have a stable spacecraft. As already mentioned, calculating the centre of pressure for free molecular flow is not as straight forward as in continuous flow. In these conditions, the centre of pressure can be located using the torques generated around the centre of gravity, as explained in subsection 10.2.2. The torque for the input angles can be calculated based on the drag, by multiplying this drag force with the perpendicular distance from the centre of gravity. Dividing this torque by the total sum of forces gives the location of the centre of pressure.

For these conditions, the centre of pressure moves with the angle of misalignment. Because no torque is generated around the centre of gravity at perfect alignment, the centre of pressure perfectly coincides with the centre of gravity. As soon as the misalignment angle increases, the centre of pressure moves back and stability increases. This centre of pressure shift is shown in Figure 10.3, where it can be seen that its location shifts back faster for yaw angles than for pitch angles, which is expected as it is coupled to the torque values which show the same trend. Also here, the same conclusion can be taken, which is that the spacecraft is stable. Although, due to the centre of gravity being close to the centre of pressure, some support of the magnetorquers will improve its dynamic stability, in particular, the magnetorquers will take care of constant torques, in order to trim the flight condition to a specified angle.

[2] https://www.terma.com/media/437079/t1_t2_star_tracker_rev2.pdf [Cited on 11 June 2019]
[3] https://www.jena-optronik.de/en/aocs/fss.html [Cited on 11 June 2019]
[4] https://www.kvh.com/Military-and-Government/Gyros-and-Inertial-Systems-and-Compasses/Gyros-and-IMUs-and-INS/IMUs/1750-IMU.aspx [Cited on 5 June 2019]
[5] https://www.zarm-technik.de/products/magnetometer/ [Cited on 6 June 2019]

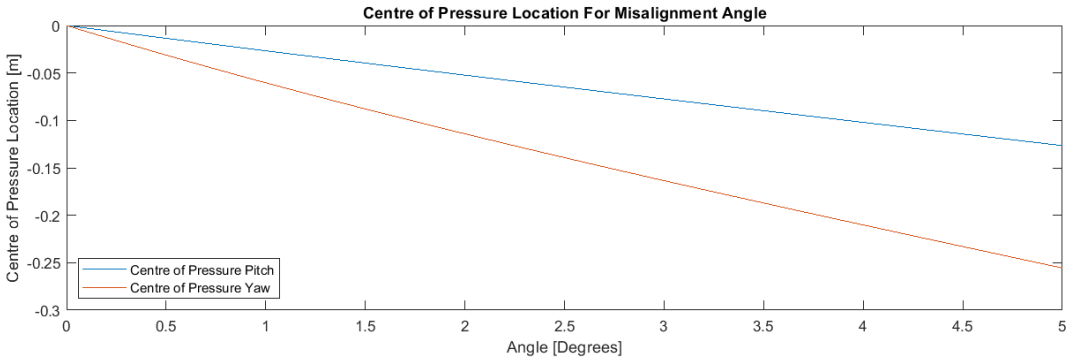

Figure 10.3: Centre of pressure location for misalignment angles

10.3.3. Attitude Control

The attitude control subsystem is designed for the determination system for the three main operational phases: detumbling, nominal and safe mode. An overview of the modes is drawn, and the architecture discussed.

Detumbling Mode

Detumbling with magnetorquers has been broadly investigated for LEO satellites. The magnetorquers are used for detumbling until the angular rate of the spacecraft reaches values as high as 1 deg/s. Already for 3 deg/s the probability of Sun acquisition by the Sun sensors is above 99% from statistical values [97].

Nominal Mode

After the spacecraft has been detumbled, the stabilising fins will be deployed to provide stability in pitch and yaw. For nominal operations, the attitude will be controlled by the combination of magnetorquers and passive stability for fast responses to high disturbances such as the aerodynamic torques. Advantages of magnetorquers are the low weight and low complexity of the systems, as well as their high reliability and long lifetime [98]. However, in a time invariant magnetic field, they can only provide two axis control torques, as the torque they can produce varies from a maximum achieved when the local magnetic field is perpendicular to the magnetic moment of the torquer, to a null when the two vector components are parallel to each other [99]. Three axis control is achievable thanks to the variation of the geomagnetic field of the Earth with respect to the orbital plane, as shown by multiple study cases [100, 101], especially in VLEO polar orbits, where the magnetic field is stronger than at conventional higher orbits, and the spacecraft experiences high magnetic flux. Moreover, this configuration has been used in the reference mission GOCE, which flew at 270 km of altitude in a situation similar to the one studied for this concept [102]. An adequate control algorithm, such as one using B-dot control laws, together with the readings of a three axis magnetometer has to be used to achieve the required accuracy values.

Safe Mode

Safe mode has to roughly point the solar arrays and the antenna, and maintain a certain degree of stability [95]. The magnetorquers can be used to maintain the solar arrays oriented towards the Sun: they can operate at low power, have a high reliability and can be used in case of high rotational rates. The antenna is self steered, and will be discussed in section 6.2.

Attitude Control Architecture

The relevant characteristics of the control actuators are listed in Table 10.4.

Three-axis control of the spacecraft is obtained with a set of three orthogonal rods [95]. The required magnetic dipole of the magnetorquers is calculated as in Equation 10.3, using a safety factor of 3, to account for the variation in magnetic field strength along one orbit, as well as the rotation of the Earth [31, 103]. The required dipole moment is found to be 50 Am^2.

[6] `http://www.zarm-technik.org/prefinal/downloadfiles/ZARMTechnikAG_MagneticTorquers_web2010.pdf` [Cited on 4 June 2019]

Table 10.4: Architecture of the attitude control system

Actuator	N	Accuracy	Weight	Power	Dimensions	Notes
Magnetorquers[6]	3	0.1 deg	1.78 kg	5.3 W	60 x 500 x 398 mm	
Stabilising Fins	3 panels on each side	Stabilising torque up to 0.05 degrees	11.16 kg	0 W	575 x 1600 x 15 mm 670 x 2100 x 15 mm 200 x 2100 x 15 mm	

Fin Configuration

Based on the method described in subsection 10.2.2, the dimensions of the fins can be determined, along with the effect they have on the attitude and dynamics of the spacecraft. The program used takes the angle of misalignment with the velocity vector and based on that, calculates the torque around the centre of gravity based on generated drag. To simplify the process, the torque in pitch and yaw is split up and calculated separately. The centre of gravity location is set based on spacecrafts limitations in size and based on fin size limitations, the centre of gravity should not be more than 1.6 m behind the front of the spacecraft. This ensures a proper margin, taking into account the effects on the volume, weight and cost budgets.

Sizing fins for stability, the first improvement is achieved by extending the sides of the trapezoids backwards by 1.6 m. This foldable fin panel perfectly aligns with the side of the trapezoid, so it is effectively in the shadow of the spacecraft, not increasing the frontal area when perfectly aligned. Since this fin is under an angle of 30 deg with the vertical axis, it will improve stability in both pitch and yaw. The fin is only extended 1.6 m to provide enough clearance for the thruster exhaust. The half-angle clearance from the engine, which is 10 deg, means that in this configuration the exhaust particles are able to pass the fins without causing any damage.

Stability in pitch still lacks. So, to improve pitch stability and increase the solar panel area, horizontal fins are added that are attached to the previously discussed fins. To provide sufficient control torque, the dimensions of each of these horizontal fins is 2.1 m x 0.67 m x 0.015 m. The panel is set to be 2.1 m long based on that same thruster clearance angle discussed for the sizing of the angled fins. This time, because the fins are further away from the exhaust, the fins can be longer and are extended to 2.1 m. Combining the solar panel requirements together with the pitch stability, the horizontal fins are calculated to be 0.67 m. Structure-wise, the 0.015 m thickness is based on the structural limits of the sandwich panels discussed in subsection 11.2.4.

The fins present at this moment provide sufficient stability in pitch, but still lacks in yaw. To solve this lack of stability, a winglet type of fin is added to the horizontal panel. This is a fin of 2.1 m x 0.2 m x 0.015 m that is rigidly fixed to the most outer part of the horizontal fin at an angle of 50 deg with the horizontal axis of the spacecraft. The reason for this angle is to avoid creating shadows on the horizontal fins, which would reduce the solar panel efficiency of the fin mounted solar panels. They are mounted along the entire 2.1 m length of the horizontal fin and are 0.2 m wide to ensure yaw stability and still fit within the launcher fairing.

Inputting these fin sizes, together with the overall spacecraft weights and dimensions, the method returns a torque for an input angle. Next to this, it produces a drag estimation for the input angle and combining these results in a conclusion if the counteracting torques are high enough to sustain the disturbance torques while still generating enough thrust to overcome drag. In Figure 10.4, this exact amount of torque generation at the angles is visualised in a graph. Here, it can be seen that yaw is more stable than pitch, but when looking at Figure 10.5, it can be seen that the stability margin is large enough in terms of misalignment angle to keep the drag generation lower than the thrust value.

These torques do however not provide fast dynamic stabilisation, so to reduce oscillations a combination of the fins and the magnetorquers is used to improve overall spacecraft performance.

Adding these stabilising fins does create an increased drag value. To asses the amount of drag generated, the angle of misalignment with the velocity vector at which drag becomes higher than thrust is determined for both pitch and yaw. With the current configuration, drag is higher than thrust for misalignment angles of 2.1 deg in pitch and 4.3 deg in yaw. When rotating past this value of misalignment angle, the fins are designed to bring the spacecraft back to within this range to limit the decay when having a thrust-to-drag ratio of lower than one.

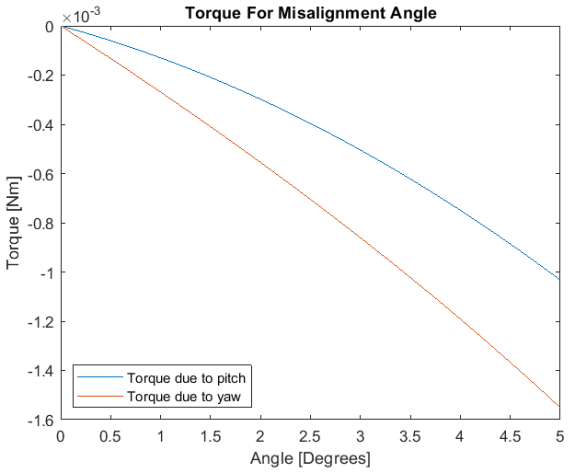

Figure 10.4: Torque values for misalignment angles

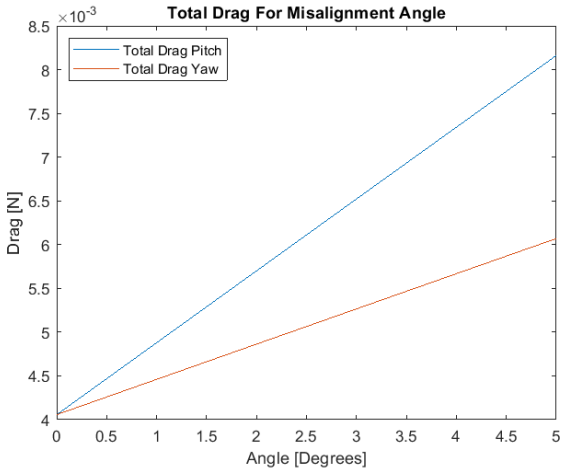

Figure 10.5: Total drag values for misalignment angles

10.4. Verification & Validation

In this chapter, verification is performed for the models described in section 10.2 and used to estimate the disturbance torques and the fin sizing. Validation of the trends of the torques variation with altitude is treated, followed by the validation of the design against the requirements.

10.4.1. Verification

The calculation of the disturbance torques explained in section 10.2 is straightforward. Verification of the units of the program are done by changing input values and examining the output of the functions. For the aerodynamic torque in Equation 10.1, the results are compared changing the density input values. For null density, no aerodynamic torque is experienced. Changing the value of the drag to a negative number also provides a negative torque, as expected. Increasing the distance between centre of gravity and centre of pressure, generates a larger torque, while decreasing it has the opposite effect. The verification procedures are conducted in a similar intuitive way for all the other disturbance torques, as well as for the dipole moment calculation.

10.4.2. Validation

The disturbance torques obtained from the model in section 10.2 are validated by comparing the behaviour of the disturbance with varying altitude. In Figure 10.6 from [91], the trend of the aerodynamic, gravity gradient, magnetic and solar pressure disturbance torques are plotted against altitude for a typical spacecraft. Figure 10.7 shows the same plot, obtained with the parameters of RAMSES, again for a range of altitude values.

Although the magnitude of the torques are highly dependent on the spacecraft considered, as shown in section 10.2, the trend of the disturbances is the same, and thus, the calculations are validated.

Compliance with Requirements

Compliance with requirement ADC-001, regarding the accuracy required in roll, is validated by referring to Tewari [104]: the control system developed in the paper for magnetorquers simulated in the paper is able to achieve an accuracy of 0.1 degrees in roll.

The compliance of the requirement ADC-004 for the angular rate in roll is derived by Figure 10.8 from Psiaki [105], for a spacecraft orbiting at around 600 km, with lower moments of inertia than RAMSES and therefore inherently higher rotational velocities about each axis. The system oscillates between -0.5 degrees and 0.5 degrees in about 1/14 of 10 hours, as can be seen in the graph. The stability is calculated as $\frac{1\text{degree}}{1/14*10*3600\text{s}} = 3.89 \cdot 10^{-4}$ degrees/s.

The compliance with requirements ADC-001 for the accuracy in pitch and yaw is demonstrated by examining Figure 10.4: for a deviation of 0.05 deg from the y and z axes, the fins cause a stabilising torque respectively of -5.5×10^{-6} N m and -1.3×10^{-5} N m. These values have been calculated based on the model explained in section 10.1, where only forces in drag direction are taken into account. To validate these

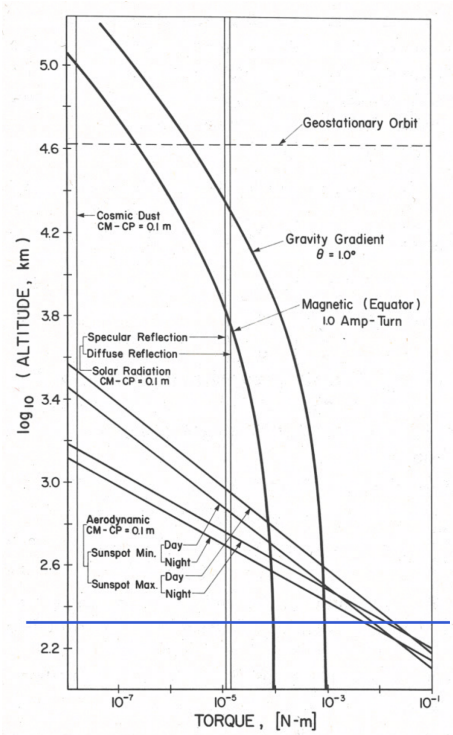

Figure 10.6: Disturbance torque trend according to Hughes [91]

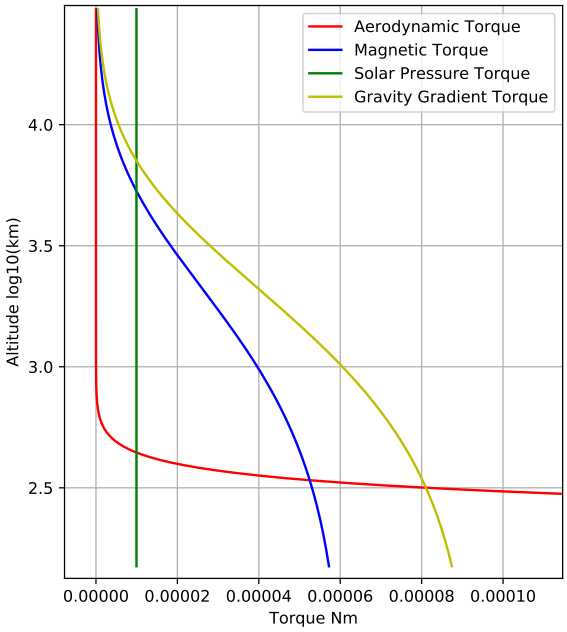

Figure 10.7: Disturbance torque trend calculated from model

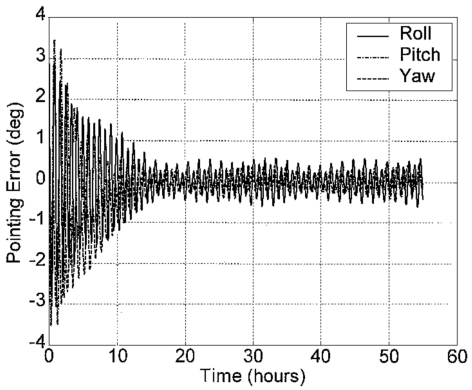

Figure 10.8: Pointing accuracy of the closed loop system proposed by Psiaki [105]

results, the same analysis has been performed by using a model which assumes an accommodation coefficient of one. This assumption implicates that the forces that act on the spacecraft are taken normal to the surfaces. This is a large change in terms of force applications, but in the end did not change the stability considerably. It even improved stability in pitch, but did decrease the stability margin in yaw to a point where the torques at 0.05 deg for pitch and yaw become -2.5×10^{-5} N m and -3.1×10^{-6} N m respectively. As it is considered that the accommodation coefficient will be somewhere between zero and one, but closer to one. And the spacecraft is stable for both accommodation coefficients, the current fin configuration is validated to be enough for passive stabilisation.

In order to validate the compliance with the angular rate requirement ADC-004 in pitch and yaw, an attitude simulation is used, from which a misalignment angle can be determined as well. The simulation input is determined to be 1×10^{-4} N m, based on the maximum constant disturbance torque. The angle of misalignment is given in Figure 10.9, where pitch and yaw response is given. It can be seen that the spacecraft starts oscillating, but average out at around 0.8 deg of pitch and around 0.35 deg of yaw. Concerning the angular velocities, Figure 10.10 indicates the angular velocities for the same disturbance input. After analysis of this graph, it can be determined that with the given disturbance torque, a maximum angular velocity of 5.2×10^{-3} deg/s in pitch and 3×10^{-3} deg/s in yaw is achieved. This is well within the angular

velocity requirement posed in requirement ADC-004.

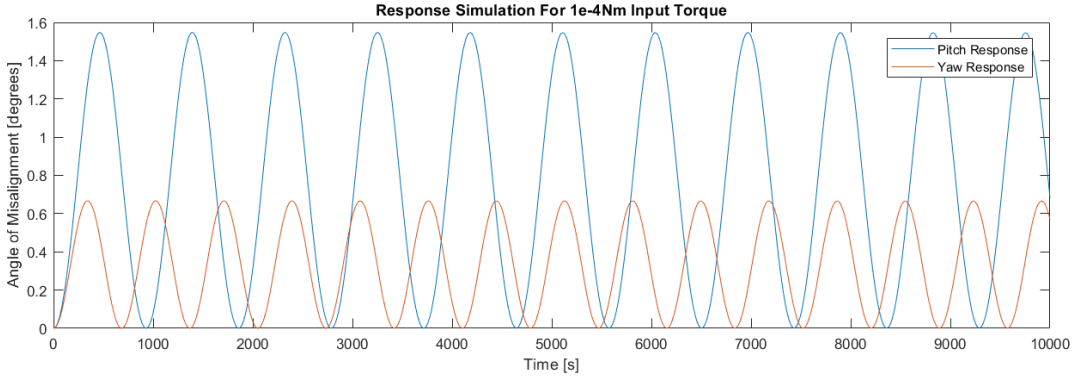

Figure 10.9: Simulation of the reaction of the spacecraft in terms of misalignment angle for a constant disturbance torque of 1×10^{-4} N m in pitch and yaw.

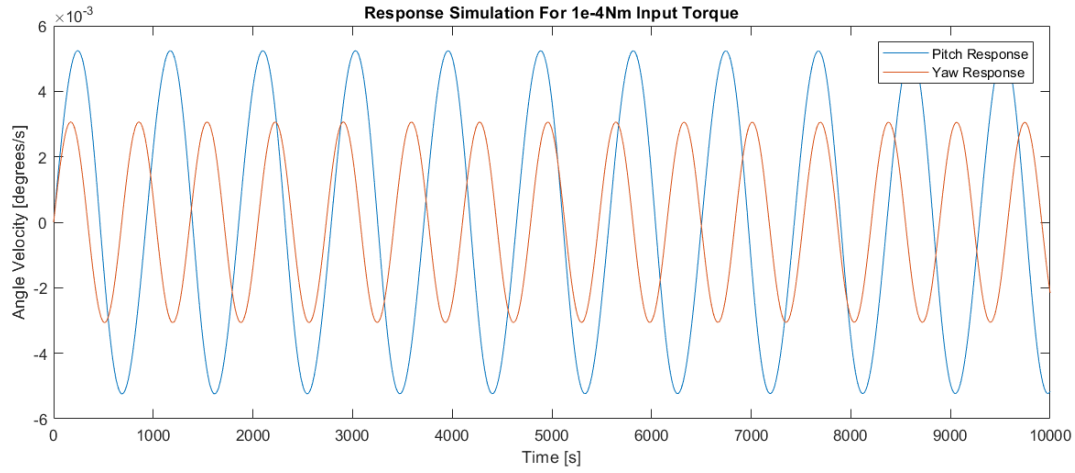

Figure 10.10: Simulation of the reaction of the spacecraft in terms of angular velocity for a constant disturbance torque of 1×10^{-4} N m in pitch and yaw.

The other requirements are less strict than the ones mentioned above. Compliance with all requirements is therefore demonstrated.

10.5. Sensitivity Analysis

The analysis of the robustness of the estimation of the disturbance torques made in section 10.2 is described in this section. In particular, the parameter examined is the aerodynamic disturbance torque, which is the worst case torque experience by the spacecraft, as well as the design driver.

In particular, this parameter depends on the air density and distance between centre of gravity and centre of pressure, as described in Equation 10.1. Of these parameters, the latter is a design safety factor. For a value of 2% higher, the required dipole moment will increase linearly of 2%. As for the density, the value which is used as the worst case is the highest value of density that the spacecraft experiences. The safety factor taken on the dipole moment of the magnetorquers, discussed in section 10.2, allows the spacecraft to be somewhat controllable up to an altitude of 188 km, where the density encountered averages to the maximum operating density times the safety factor considered for RAMSES. This is particularly beneficial for the design, as in order to speed up re-entry and cause less damage once it reaches the ground, the spacecraft might be required to be oriented in a particular orientation.

It is determined before in subsection 10.3.3 that drag compensation can be achieved up to 2.1 deg in pitch and 4.3 deg in yaw. Which means that the drag increases beyond 5.8 mN rotating past these angles. When with the help of the magnetorquers the spacecraft is rotated even further from the normal axis, and considering nominal drag is only 4.1 mN, drag will rise considerably by performing these manoeuvres

and thus will help with speeding up the re-entry process, also reducing the impact of possible damage on ground.

10.6. Risk & RAMS Analysis

This section provides the analysis of the performance of the system, in terms of risks and reliability. Some quick considerations are made on the safety risks to living being as well as to the environment.

10.6.1. Risk Identification and Mitigation

Risks are identified for the ADC system and categorised, following the risk severity scheme explained in section 6.6, their foreseeable consequences discussed. Finally, under mitigation, ways to address the risks and to reduce their impact on the mission are identified, giving to the mitigated risks a new categorisation. The risk are visually presented in a risk map in Table 10.5.

RSK-ADC-1 **Event**: The spring loaded deployment of the fins fails.
Risk: This will cause the satellite to have slow responses to disturbances in pitch and yaw, and in particular to misalign the propulsion system. If the torques are high enough, it might cause the satellite to decay. The risk is deemed catastrophic and possible.
Mitigation: A redundant mechanism is included, reducing the probability of it failing. While still being catastrophic, the risk probability is reduced to rare.

RSK-ADC-2 **Event**: The fins are deployed but not correctly aligned, or a structural failure occurs.
Risk: This will cause unwanted constant torques on one or more axis. This risk is deemed catastrophic and possible. Both payload operations and satellite survival might be compromised.
Mitigation: The magnetorquers can counteract constant disturbance torques generated by the fins, and correct the attitude, up to a constant torque of about 10^{-3} Nm. The risk is therefore reduced to rare and marginal.

RSK-ADC-3 **Event**: The sensors give incorrect readings of the attitude.
Risk: The attitude of the spacecraft is not correctly actuated. The payload takes pictures of the wrong targets. The engine and solar panels performances are reduced. The risk is likely and critical.
Mitigation: The problem can be noticed by sending to the ground housekeeping data about the power generated by the solar panels, and reduced by having multiple sensors. The risk is reduced to likely but negligible.

RSK-ADC-4 **Event**: The star sensors are blinded by the Sun.
Risk: The CCD camera is damaged and attitude cannot be measured with the required accuracy. This risk is categorised possible and critical.
Mitigation: The problem is reduced by using a baffle with blocks the light incoming from the sides of the sensors. With the baffles, the risk is categorised as critical and rare.

RSK-ADC-5 **Event**: The reading of the magnetometers are compromised by the magnetic field of particles in the exhaust or by the magnetic field of the electrical components.
Risk: The magnetorquers experience a different magnetic field than the one that the magnetometers experience, and the attitude actuation is not accurate. This risk is critical and possible.
Mitigation: To minimise the impact of the magnetic fields generated on board the spacecraft, these have to be identified as early as possible, and their influence on the instruments modelled. Magnetic field compensation methods are used to reduce these interference. The risk is further reduced by placing the magnetometers as far as possible from the engine and the exhaust, and by shielding the PCU and the other electrical components so that no interactions occur. After mitigation, the risk is marginal and rare.

RSK-ADC-6 **Event**: The engine performance is compromised by the strong magnetic field generated by the magnetorquers.
Risk: The engine shuts down and the spacecraft decays. The risk is seen as catastrophic and likely.
Mitigation: The magnetorquers are placed far away from the engine and from each other in order to minimise the risk. Furthermore, the configuration will be tested before launch. After mitigation, the risk is considered critical but rare.

RSK-ADC-7 **Event**: The sensor performance is compromised by the corrosive environment, and the high radiations.

Risk: The sensors are not able to perform measurements with the required accuracies. This risk is categorised possible and marginal.
Mitigation: The risk is mitigated by using sensors that have been tested and are guaranteed for the radiation profile of the orbital altitude, and by using coatings on the parts which are exposed to atomic oxygen. After mitigation, this risk is considered marginal but rare.

RSK-ADC-8 **Event**: The spacecraft starts tumbling because of higher disturbances than designed for.
Risk: This event could cause the generation of higher thrust than designed for, causing a degradation of payload performance and eventually orbit decay. The risk is seen as catastrophic and possible.
Mitigation: This risk is minimised by designing the spacecraft for worst case disturbance torques, which can be encountered at the operating conditions. A safety margin is applied to the design to further minimise the risk. After the mitigation, the risk reduces to critical and rare.

RSK-ADC-9 **Event**: Electrical disturbances compromise the functioning of the computers on board.
Risk: The elaboration of the star patterns is compromised and the attitude cannot be measured with the required accuracy. The risk is categorised as possible and marginal.
Mitigation: The risk can be mitigated by designing the spacecraft following the 'cleanliness' specifications. In particular, this includes avoiding the use of ferromagnetic materials on the spacecraft and diminishing the amount of current loops present in the cabling [93]. Furthermore, the engine is shielded by a Faraday cage in order to avoid electrical errors in the readings. Now the risk reduces to marginal and rare.

10.6.2. Risk Map

The risk map helps visualise the severity and probability of all the risks defined in the previous section. In Table 10.5 the risks are given before and after mitigation. The categories used in these maps are explained in section 6.6.

Table 10.5: Risk matrix showing the severity and likelihood of the risks before and after mitigation.

Severity \ Likelihood	Almost Certain	Likely	Possible	Rare
Catastrophic		RSK-ADC-6	RSK-ADC-1, RSK-ADC-2, RSK-ADC-7	
Critical		RSK-ADC-3	RSK-ADC-4, RSK-ADC-5	
Marginal			RSK-ADC-7, RSK-ADC-9	
Negligible				

10.6.3. RAS Analysis

The analysis of reliability, availability, and safety of the subsystem is discussed in this section. All the sensors chosen for the system are designed to operate for 12 years or more in a LEO environment, at the cost of weight when compared to state of the art technologies. Moreover, all sensors and actuators have TRL levels of 9, and are included in a redundant architecture. In particular the chosen Sun sensor is internally redundant. Two co-aligned star trackers can be used for cold redundancy as common practice in satellite engineering [106]. In this case the electronics box and the optics of these sensors are physically separated[2], and their integration can be decoupled. The IMU and the magnetometer are also doubled. As for the chosen actuators, the magnetorquers are internally redundant. The fins will have a redundant deployment mechanism, as discussed in subsection 14.6.1.

The sensors included in the design are not harmful to living being, their integration to the spacecraft is to be performed by specialised personnel, with care to the light sensitivity of the instruments and in clean rooms. It is however unlikely that they will cause any harm to people or instruments in the process of manufacturing the spacecraft. On the contrary the magnetorquers might be harmful if caution is not used, because of the high current going through the coils and the high magnetic field that they can generate. Testing should be performed in a controlled environment. As for the fins, manufacturing of the sandwich panel will involve materials with are harmful for both environment and living beings. Furthermore, at reentry, part of the fins is likely to reach the ground. The safety risks concerning this aspect are examined in

subsection 11.2.7.

10.7. Cost Analysis

The cost overview is provided in this section for the ADCS system. The sensors and actuators are off-the-shelf components, and their cost is estimated either by analogy with similar components or by parametric extrapolation. Table 10.6 gives an overview of the estimation of the costs and the work hours dedicated to the integration of each component, as well as the accuracy of the estimation and the technical risks related to the use of the component specified. The TRL levels of the components are also stated. The costs provided in the table is the total cost, already accounting for the number of components which are included in the design. The parameters for the attitude determination & control subsystem are shown in Table 10.6.

Table 10.6: Cost and TRL levels of the attitude determination & control system

Sensor	N	Estimate Hours of Labour	Total Cost in 2019 Euros	TRL	Estimate Method-ology	Estimate Accuracy	Technical Risk	Notes
Sun Sensors	4	200	44000	9	Analogy	High	Low	[2]
Star Sensors	2	200	53200	9	Analogy	Medium	Low	[7]
IMUs	2	200	22600	9	Parametric	Medium	Low	[8]
Magnetometer	2	500	26600	9	Analogy	High	Low	[9]
Magnetorquers	3	1000	44400	9	Parametric	High	Medium	[10]

For the Sun sensors and magnetometers, the cost estimation is deemed accurate, as the prices given refer to instruments which have similar operational profile to RAMSES. The estimation for the star sensors and the IMUs are less accurate, because they come from components operating at different radiation profiles. It is assumed that the price of the actual component will be slightly higher than the presented value.

The working hours which will be dedicated to the components are estimated accounting for the physical integration of the sensor, as well as the control software integration and testing. The magnetometers will require more labour hours, because they will be part of the feedback loop for the control software of the magnetorquers, which will need fine tuning.

The technical risks associated with the attitude determination subsystem is considered quite low, since all components are already fully tested and flight proven, with TRL 9.

The cost estimation of the magnetorquers is done by linear interpolation of the cost of torquers with higher and lower dipole moment. The estimation is deemed accurate, since the actuators considered have the same operational profile of the selected torquers. The technical risk is estimated to be medium, since the mission is relying on the development of an appropriate control software in order to meet the roll accuracy requirement. However, the torquers are flight proven technology, and as such, score 9 in the TRL scale. The labour hours which have to be dedicated to the integration of the magnetorquers are quite high, since the control software development is included in the estimation.

[7] https://www.cubesatshop.com/product/kul-star-tracker/ [Cited on 13 June 2019]
[8] http://instk.org/blog/index.html%3Fp=165.html [Cited on 13 June 2019]
[9] https://www.cubesatshop.com/product/nss-magnetometer/ [Cited on 13 June 2019]
[10] http://spaceflight.com/wp-content/uploads/2015/05/201501-Torque-Rods-Datasheet.pdf [Cited on 13 June 2019]

11. Structures

In order to connect and protect all the subsystems a structure has to be designed. In this section the exact functions and requirements of the structure are outlined in section 11.1. Following this, the method applied in designing the structure to fulfil these requirements is presented in section 11.2. The results of this are shown in section 11.3 These methods are verified and validated in section 11.4. After, the sensitivity of the performance of the structure to certain parameters is examined in section 11.5. The risks and RAS analysis of the structure are presented in section 11.6. Finally the cost of the structure is computed in section 11.7.

11.1. Functions & Requirements

The structure will have several functions during the operation of the mission. Firstly it has to resist the loads experienced during launch. Moreover, it has to protect the other subsystems from the environment during the mission operation. Finally the structure has to be designed such that the risk of fatalities is minimised during re-entry. To fulfil these functions, several requirements have to be met by the structure. These requirements are presented in Table 11.1, with the compliance indicated alongside.

Table 11.1: Subsystem requirements on the structure

ID	Requirement	Met [✓/✗]	Section
STR-001	The structure shall resist an axial acceleration of 8g as well as accelerations of 5g and 8g in the two transverse directions	✓	section 11.3
STR-002	The structure shall allow for secure connections for all other subsystems, such that these are secure during launch	✓	chapter 14
STR-003	The structure shall ensure that the exposure of all contained subsystems to atomic oxygen is minimised	✓	subsection 14.2.1
STR-004	The structure shall resist the erosive environment for at least 10 years	✓	section 11.3
STR-005	The structure shall resist the launcher's vibration loads [14]	✓	section 11.3

11.2. Methodology

For the structural analysis of the satellite there are three main subject areas to be considered. The first is the launch loads that need to be resisted, consisting of vibration loads and quasi-static loads. The second is designing for the erosive environment experienced by the satellite. Finally the re-entry of the system and the risks associated with this have to be considered.

11.2.1. Cross-Sectional Properties

As the design for all loads is highly dependent on the properties of the cross-section, these will be defined first. The loads carrying structure will be modelled as a thin-walled shell. The dimensions of this shell are mostly driven by the integration of the subsystems, the size of the intake and the available space in the fairing of the launcher. Therefore the thickness is used as an input to change to cross-sectional properties to the required values. The cross-sectional profile can be seen in Figure 11.1. The moment of inertia was then calculated using the thin-walled assumption [107].

11.2.2. Natural Frequency

During launch the structure experiences vibrations in two directions: axial and transverse. In order to be qualified as safe, the natural frequency of the system needs to be known. This is required to estimate the loading experienced due to this frequency. For transverse vibrations, the deformation definition, the axial load and the internal loading definitions are defined in Figure 11.2.

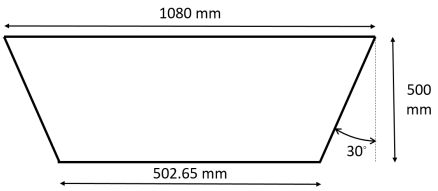

Figure 11.1: Cross-sectional dimensions of the structural shell

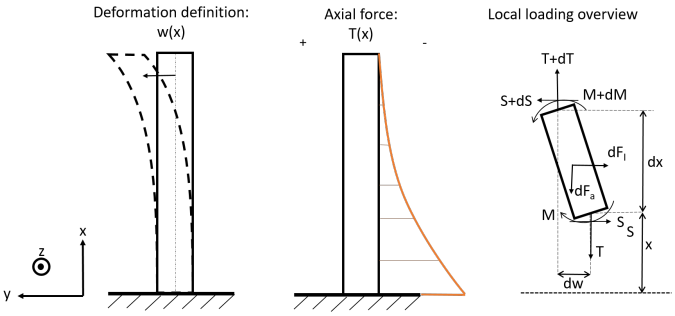

Figure 11.2: Definitions used for the frequency analysis of the system

From Figure 11.2 the governing equation can be derived by imposing an equilibrium of forces and moments. The resulting equilibrium equations are shown in Equation 11.1.

$$\begin{aligned} \sum F_x &= T + dT - T - dF_a = 0 \\ \sum F_y &= S + dS - S - dF_I = 0 \\ \sum M_z &= M + dM - M + (T + dT) \cdot \frac{dw}{2} + T \cdot \frac{dw}{2} + (S + dS) \cdot \frac{dx}{2} + S \cdot \frac{dx}{2} = 0 \end{aligned} \tag{11.1}$$

To arrive at a usable form of the governing equation some substitutions are made. These are shown in Equation 11.2. In this equation a_x is the nominal axial acceleration experienced during launch.

$$\begin{aligned} T(x) &= -M_{total} \cdot a_x + \int_0^x m(x) dx \cdot a_x \\ dF_a &= m(x) \cdot dx \cdot a_x \qquad dF_I = m(x) \cdot dx \cdot \ddot{w} \end{aligned} \tag{11.2}$$

The governing equation can now be derived from Equation 11.1 by substituting in the definitions from Equation 11.2. Any terms containing a multiplication of increments are eliminated. An example of this would be $dT \cdot dw$, which is assumed to be negligible. The resulting equation is $dM = T \cdot dw - S \cdot dx$.

The governing equation is now derived by rewriting and differentiating the previous equation. The result is shown in Equation 11.3. However this form of the equation has to be rewritten before it can be used to solve for the natural frequency. This is done using the definitions found in Equation 11.2 and the other equilibrium equations. Moreover, the moment is rewritten using Euler-Bernoulli beam theory [107]. The final equation that will be solved for is Equation 11.4.

$$\frac{d^2 M}{dx^2} + \frac{dS}{dx} - \frac{d}{dx}(T \cdot \frac{dw}{dx}) = 0 \tag{11.3}$$

$$\frac{d^2}{dx^2}(E \cdot I(x) \cdot \frac{d^2 w}{dx^2}) + m(x) \cdot \ddot{w} - m(x) \cdot a_x \cdot \frac{dw}{dx} - (\int_0^x m(x) dx \cdot a_x - M_{\text{total}} \cdot a_x) \cdot \frac{d^2 w}{dx^2} = 0 \tag{11.4}$$

Now the governing equation has been defined, a method of solving this differential equation has to be chosen. To arrive at a solution the solution was assumed to be a combination of N modes that satisfy the boundary conditions. Therefore the total solution can be described as in Equation 11.5. In this equation a_i is an unknown modal contribution factor, j is the imaginary unit and ω is the natural frequency.

$$w(x,t) = \sum_{i=1}^{i=N} a_i \cdot w_i(x) \cdot e^{-j\omega t} \tag{11.5}$$

To solve for the natural frequency a collocation method will be used [108]. In this method, the solution created by the combination of different modes is evaluated at a number of locations along the structure. The number of locations is equal to the number of modes. At each of these locations it is imposed that the solution found by combining the modes is such that the governing equation, Equation 11.4, is satisfied. The result of this process is a system of N equations, Equation 11.6. In this equation K and M are NxN matrices that are defined as in the equations below. In these definitions j is the mode number and i is the location along the structure at which the solution is evaluated. Both j and i range from 1 to N. The other elements in Equation 11.6, λ and **a**, are the square of the natural frequency and a vector of all modes contribution

factors, respectively.

$$K\mathbf{a} = \lambda M\mathbf{a} \qquad K = [k_{ji}], \quad M = [m_{ji}] \tag{11.6}$$

$$k_{ji} = E \cdot I''''(x_i) \cdot w_j(x_i) + E \cdot I'''(x_i) \cdot \frac{dw_j}{dx}(x_i) + E \cdot I''(x_i) \cdot \frac{d^2 w_j}{dx^2} - m(x_i) \cdot a_x \cdot \frac{dw_j}{dx}(x_i) - (\int_0^{x_i} m(x)dx \cdot a_x - M_{\text{total}} \cdot a_x) \cdot \frac{d^2 w_j}{dx^2} \tag{11.7}$$

$$m_{ji} = m(x_i) \cdot w_j(x_i) \tag{11.8}$$

The application of this collocation method results in an eigenvalue problem as defined in Equation 11.6. Since the mass and stiffness distribution are assumed to be an input, matrix K and M are fully defined. Therefore, the natural frequencies can be solved for using the eigenvalue problem solver which is present in the Numpy package for Python.

Finally, as the solution is a combination of modes, the selection of said modes is critical for the success of the method. The modes that were used are shown in Table 11.2. The coefficients a to e are chosen such that the boundary conditions were satisfied and the deflection at the end of the structure was equal to one. In equations containing Euler's number the coefficient e has been replaced by f, in this equation e simply stands for Euler's number. The assumed boundary conditions for the structure were those for a cantilever beam, no deflection or slope at the root and no loading at the end of the structure.

Table 11.2: Mode shapes used in analysis

Mode	Used in frequency analysis	Used in quasi-static loading analysis
1	$a \cdot cos(\frac{\pi x}{2L}) + b \cdot sin(\frac{\pi x}{2L}) + c \cdot cos(\frac{\pi x}{L}) + d \cdot sin(\frac{\pi x}{L}) + e$	$a \cdot cos(\frac{\pi x}{2L}) + b \cdot sin(\frac{\pi x}{2L}) + c \cdot cos(\frac{\pi x}{L}) + d \cdot sin(\frac{\pi x}{L}) + e$
2	$a \cdot cos(\frac{\pi x}{L}) + b \cdot sin(\frac{\pi x}{L}) + c \cdot cos(\frac{3\pi x}{2L}) + d \cdot sin(\frac{3\pi x}{2L}) + e$	$a \cdot cos(\frac{\pi x}{L}) + b \cdot sin(\frac{\pi x}{L}) + c \cdot cos(\frac{3\pi x}{2L}) + d \cdot sin(\frac{3\pi x}{2L}) + e$
3	$a \cdot cos(\frac{\pi x}{L}) + b \cdot sin(\frac{\pi x}{L}) + c \cdot cos(\frac{2\pi x}{L}) + d \cdot sin(\frac{2\pi x}{L}) + e$	$a \cdot cos(\frac{\pi x}{L}) + b \cdot sin(\frac{\pi x}{L}) + c \cdot cos(\frac{2\pi x}{L}) + d \cdot sin(\frac{2\pi x}{L}) + e$
4	$a \cdot cos(\frac{3\pi x}{2L}) + b \cdot sin(\frac{3\pi x}{2L}) + c \cdot cos(\frac{2\pi x}{L}) + d \cdot sin(\frac{2\pi x}{L}) + e$	$a \cdot cos(\frac{3\pi x}{2L}) + b \cdot sin(\frac{3\pi x}{2L}) + c \cdot cos(\frac{2\pi x}{L}) + d \cdot sin(\frac{2\pi x}{L}) + e$
5	$a \cdot e^{\frac{-x}{L}} + b \cdot e^{\frac{-2x}{L}} + c \cdot e^{\frac{-3x}{L}} + d \cdot e^{\frac{-4x}{L}} + f$	$a \cdot e^{\frac{-x}{L}} + b \cdot e^{\frac{-2x}{L}} + c \cdot e^{\frac{-3x}{L}} + d \cdot e^{\frac{-4x}{L}} + f$
6	$a \cdot x^4 + b \cdot x^3 + c \cdot x^2 + d \cdot x + e$	$a \cdot cos(\frac{\pi x}{2L}) + b \cdot sin(\frac{\pi x}{2L}) + c \cdot cos(\frac{2\pi x}{L}) + d \cdot sin(\frac{2\pi x}{L}) + e$
7	-	$a \cdot e^{\frac{-x}{4L}} + b \cdot e^{\frac{-2x}{4L}} + c \cdot e^{\frac{-3x}{4L}} + d \cdot e^{\frac{-x}{L}} + f$

All of the previously presented frequency analysis can be used to find the transverse natural frequencies. For the longitudinal natural frequency a similar method could have been applied. However, the cross-sectional area in the current design is constant over the length of the spacecraft. Therefore the only varying parameter along the length is the mass distribution. Therefore the analytical solution for longitudinal natural frequency of beams with a constant mass distribution was used, Equation 11.9. If this frequency is sufficient for the worst case mass distribution, it can be said that the structure is able to resist the axial vibrations. The worst case mass distribution is the minimum mass per unit length occurring in the design.

$$f_{\text{natural}}[rad/s] = \frac{\pi}{2L} \cdot \sqrt{\frac{AE}{m}} \tag{11.9}$$

11.2.3. Vibration Loading

Using the natural frequency, found using the method described in the previous section, the vibrational loading experienced during launch can be computed. To do this the power spectral density function for vibrations of the selected launcher needs to be examined. This function will describe the maximum predicted random vibration environment for different frequencies. To relate this function to the accelerations

experienced Equation 11.10 is used [109]. In this formula Q is the amplification factor which is defined as $\frac{1}{2\zeta}$, where ζ is the damping ratio. As the damping ratio is not known a typical value of 0.01 is assumed [110, 111]. Moreover, in Equation 11.10, f_n is the natural frequency and PSD(f_n) is the power spectral density function evaluated at the natural frequency.

$$a_{rms} = \sqrt{\frac{\pi \cdot f_n \cdot Q \cdot PSD(f_n)}{2}} \tag{11.10}$$

The result of Equation 11.10 is the root mean squared value of the accelerations [109]. The value of acceleration that will be sized for is the 3σ value, which is equal to three times this acceleration [109].

11.2.4. Fin Sizing

Some fins will be used to move the centre of pressure sufficiently back for stability. The size of the fins is determined in chapter 10. To size for the vibrations during launch the accelerations are determined using Equation 11.10. For the natural frequency the fins will be treated as beams that are pinned on both sides. To achieve this some mechanisms are required, which are described in chapter 14. With this assumption the equations used for natural frequency and maximum stress are shown in Equation 11.11. The maximum stress is required to be 1.5 times smaller than the yield stress of the material. To compute the moment of inertia only the contribution of the skin was considered.

$$f_n = \frac{\pi}{2}\sqrt{\frac{EI}{mL^4}} \qquad \sigma_{\max} = \frac{M_{\text{total}} a L t_{core}}{8I} \tag{11.11}$$

11.2.5. Quasi-Static Loading

The structure will have to resist the accelerations created by the vibrational loading as well as the quasi-static accelerations. In this section a method will be presented to predict the resistance of the structure to these loads. The accelerations will be in both the longitudinal and transverse directions. It is assumed that these loads are introduced to the structure at the adapter, x = 0. This means that the local compressive force and shear force are known. The method used will be similar to the one applied for finding the natural frequencies. The governing equation will be slightly different as this is a quasi-static analysis and therefore the time derivative of the deformation is zero. The shear force will now also be a function of x similar to the normal force. The governing equation for the quasi-static problem is shown in Equation 11.12.

$$\frac{d^2}{dx^2}(E \cdot I(x) \cdot \frac{d^2 w}{dx^2}) - m(x) \cdot a_y - m(x) \cdot a_x \cdot \frac{dw}{dx} - (\int_0^x m(x)dx \cdot a_x - M_{\text{total}} \cdot a_x) \cdot \frac{d^2 w}{dx^2} = 0 \tag{11.12}$$

As the solution is not a function of time the modal decomposition applied in the frequency analysis is also no longer valid. Therefore a new decomposition is introduced for the quasi-static problem which is shown in Equation 11.13. The mode shapes that were used to solve this problem are pretested in Table 11.2.

$$w(x) = \sum_{i=1}^{i=N} a_i \cdot w_i(x) \tag{11.13}$$

Using the same collocation method that was used in the frequency analysis a linear system of N equations is obtained. From this system the N unknown modal contribution coefficients can be found. The deformed shape is then derived from the combination of the modes. From this shape, using the Euler-Bernoulli beam theory, the second derivative of the deformation can be related to the internal moment. This second derivative is obtained from the deformed shape using a numerical scheme [112]. The used scheme for most locations on the beam is shown in Equation 11.14. This scheme can not be used at the ends of the structure. As the loads at the root can be critical the moments here should be evaluated. The derivatives here are evaluated using Equation 11.15. This scheme was chosen as the order of accuracy was the same as for the scheme presented in Equation 11.14.

$$\frac{d^2 w}{dx^2} = \frac{x_{i-1} - 2x_i + x_{i+1}}{dx^2} \tag{11.14}$$

$$\frac{d^2 w}{dx^2} = \frac{2x_i - 5x_{i+1} + 4x_{i+2} - x_{i+3}}{dx^2} \tag{11.15}$$

After fully defining the internal loading, the local stresses have to be defined. For the shear and compressive loads these are estimated by dividing the load by the available load carrying area. The stresses caused by the moments are found using $\sigma = \frac{M \cdot d}{I}$ [107], where d is the distance from the centroid to the location at which the stress is computed. The location of the centroid is known as the cross-sectional properties are considered an input for the models.

Finally all the stresses are combined using $\sigma_{\text{combined}} = \sqrt{\sigma^2_{\text{normal}} + \tau^2}$ and compared to the yield stress [107]. It should be noted that other transverse accelerations are given in two directions, the y and the z direction. In this case, the loading will be considered as a combination of two two-dimensional problems. Each of these will be solved with the method presented above. Finally, after combining the two problems, the shear and normal stresses are also combined. If the combined stress, multiplied by a safety factor of 1.5, does not exceed the yield stress, the quasi-static loads are considered to be supported appropriately.

11.2.6. Erosion Resistance

Apart from being able to resist the loading the spacecraft experiences, the structure also has to protect the other subsystems from the erosive environment. The main mechanism for erosion that is encountered is erosion due to atomic oxygen exposure. In the chapter 5 a particle density of atomic oxygen was presented in Table 5.2, of 1.9×10^{15} atoms/m^3. This results in a total fluence of 4.7×10^{23} atoms/cm^2 over the lifetime of the mission. Due to the long lifetime of the currently presented mission this exposure is significantly higher than other missions [113]. Even when compared to missions operating at a similar altitude [114].

Obviously not all surfaces will be directly exposed to atomic oxygen. Moreover, the incidence angle of the surface with respect to the RAM direction will influence the fluence experienced by the material [115]. Materials exposed to indirect attack erode at approximately 25 to 50% of the rate of direct attack [116].

In order to maintain operations after being exposed to these extreme levels of atomic oxygen the structure and other exposed elements might have to be protected with a coating. In selecting these coatings there are several properties that need to be considered. In this section these properties and their origins are outlined. At a later stage in the design, specific coatings will be selected.

The first consideration for erosion resistance is the loss of material after atomic oxygen exposure. This loss is characterised by the erosion yield, which is a measure for the volume lost after each collision with an atomic oxygen particle. Generally metals have erosion yields in the order of magnitude of 10×10^{-26} m^3/atoms [113, 117]. Moreover most metals form a layers of metal oxides on their surface after exposure. This layer does not react with atomic oxygen and thus protects the metal underneath [116]. Therefore metal structures do not require any coatings. However, polymers and composites display erosion yields that are one or multiple orders of magnitude higher [113, 117]. Moreover, these material are not capable of the same self-protection mechanism as metals. Coatings will thus be required for these materials.

To size the coatings used, the material loss in a coating is an important characteristic. Clearly, a lower erosion yield is beneficial for a coating, as then a thinner coating is required. This erosion yield can be improved by having metals contained in the coating which form a protective layer as described earlier [118]. Moreover, some coatings exhibit self-healing properties which allow for a more uniform erosion [118].

The second consideration to maintain operations after exposure to atomic oxygen is the change in optical and thermal properties of materials exposed. Many materials commonly used in the optical system change their optical properties significantly due to atomic oxygen erosion [113, 119]. The same goes from the thermal properties of any paints used. Organic paints especially are significantly affected [113]. Therefore, exposed areas that are critical for optical and thermal components have to be protected by a coating.

For these elements that require exposure to light, a critical characteristic is the transmittance. This is measure of the amount of radiation that is allowed to pass the coating and is dependent on the wavelength of the incoming radiation. Especially the solar panels and optics require a coating that allows for a high transparency to the certain wavelengths, as described in section 8.3 and section 9.2. Moreover, this transmittance has to be maintained even after exposure to the erosive environment. This behaviour is dependent on the erosion mechanism present, which depends on the type of coating. Atomic oxygen tends to create "pits" in the surface of organic materials [118, 120, 121]. This will change the optical properties of the material towards a dull surface, with decreased specular transmittance [119, 122]. Non-organic coatings or hybrid coatings on the other hand tend to have a more uniform surface after exposure to atomic oxygen [6, 118], which allows these coatings to have more consistent optical properties.

Finally, the coating also experiences other erosion effect than exposure to atomic oxygen. Two important effects are the vacuum and the ultraviolet radiation exposure. The vacuum will remove any volatile products remaining in the coating and could therefore cause particles to surround the spacecraft [121]. This phenomena is called outgassing. The UV (ultraviolet) radiation mostly effects organic materials by affecting the links between the different molecules present in the polymer [120]. Moreover, the UV radiation can also affect the thermal properties of the materials exposed [120].

11.2.7. Re-Entry

During the End-of-Life (EOL) procedure the risk of creating a hazardous situation on Earth should be minimised. This responsibility is also part of the structures department.

In order to analyse the risk at EOL the SARA model is used. SARA Is part of the Debris Risk Assessment and Mitigation Analysis (DRAMA) software developed by ESA [123]. It allows the user to define a geometry, the material properties and some other characteristic properties such as the drag coefficient [124]. Based on these inputs the software simulates the re-entry behaviour of the defined spacecraft. Then, based on a population growth model and the estimated impact area, the risk of casualties is provided [123].

The risk of casualties upon re-entry is analysed once the geometry of the spacecraft is defined. This risk is required to be lower than 10^{-4} to be acceptable [7], which is a common practise for spacecraft. If the computed risk is higher, the spacecraft is to be redesigned such that the EOL procedure is sufficiently safe.

11.3. Architecture & Performance

In this section the methods that have been presented in section 11.2 are applied to design the structure of RAMSES. This is done by first determining and sizing for the loads experienced. After this the coatings are selected and the re-entry risk of the spacecraft is computed.

11.3.1. Launch Characterisation

To characterise the loads experienced during launch a launch vehicle needs to be selected. For the current mission several options are considered. The first option is the Electron launcher [125]. This launch vehicle has the payload mass of 225 kg [125], which is the closest to our mass requirement out of all the options. However the dimensions of the fairing are not sufficiently large to fit in the entire satellite. Despite this, as is stated in the user guide [125], a custom fairing could be constructed for the RAMSES mission that exceeds the standard envelope. This custom fairing would mainly have to be elongated as the diameter of the standard fairing is only a couple centrimeters to small. Therefore it is seen as a reasonable option to design a custom fairing for the Electron launcher.

The second option considered is the Vector-H, which is currently being developed. Therefore not all information on the loading is currently available. However, as the size is similar to the Electron the loading is expected to be similar [126]. As the development of the Vector-H is in an advanced stage, the system will probably be operational before the RAMSES satellite is fully developed. The main advantage of the Vector-H is that the fairing dimensions are more suitable for the outer dimensions of the spacecraft [126].

The final option is the LauncherOne developed by Virgin Orbit [14]. This launch system uses an aircraft for the first part of the launch and smaller rocket to bring the payload to orbit. The capacity of this launcher exceeds the mass of the RAMSES satellite significantly, being able to launch over 300 kg into Sun-synchronous orbit [14]. However the dimensions of the fairing would allow for two satellites to be launched [14]. To achieve this the satellites would be installed facing each other with the long sides of the trapezoid.

Out of the potential launch vehicles, two have specified launch loading. The quasi-static loads are specified in Table 11.3. For the vibration analysis the power spectral density (PSD) functions are used to find corresponding accelerations, shown in Figure 11.3.

Table 11.3: Quasi-static loads of the launchers

Launch vehicle	Axial acceleration [g]	Acceleration in y direction [g]	Acceleration in z direction [g]
Electron [125]	+8/-1	+/-2	+/-2
LauncherOne [14]	+8/-4	+/-5	+/-8

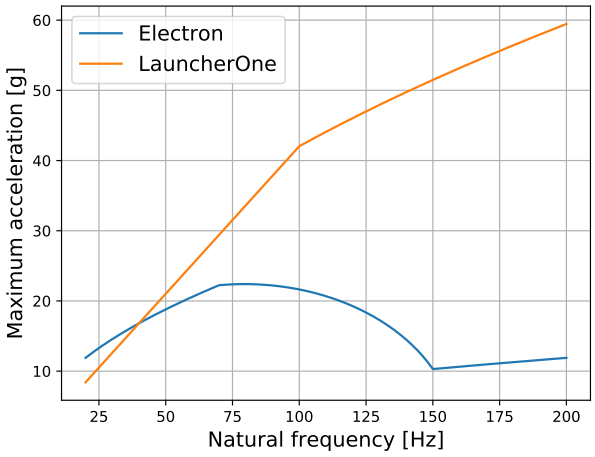

Figure 11.3: Maximum accelerations for the two different launch vehicles

11.3.2. Sizing for the Vibrations

As the goal of the design is to be able to launch in both the Electron launcher, using an adapted fairing, or in the LauncherOne launch vehicle, the structure is designed to resist the loads of both launchers. The outer dimensions are fixed by the required intake size and integration requirements, therefore the thickness of the load carrying shell is the parameter that is to be designed for. This is done by selecting a thickness and computing the natural frequency for this thickness. Then, the corresponding accelerations are computed using the PSD functions of the different launchers, which are plotted in Figure 11.3. Knowing the accelerations experienced by the structures, the corresponding loads are computed using the previously presented method for quasi-static loads. If the stresses can not be supported by the structure, the thickness is increased and the same procedure is followed again. This iteration is repeated until the accelerations can be supported.

The mass distribution has a significant influence on the value of the natural frequency as is demonstrated in section 11.4. Therefore, having a relatively accurate estimation for this is essential for a proper analysis. Using a CATIA model, in which the preliminary masses of the subsystems were modelled, the distributed mass was computed at several locations. Finally, a third order polynomial was fitted through these locations to estimate the mass distribution. The resulting mass distribution is shown in Figure 11.4. The increase in mass at the end represents the grid, which is placed at this location. However, the estimated mass distribution increases to a value larger than the mass of the grid. As this is an overestimation, it will cause an increase in the natural frequency and thus the loads experienced, which is considered an acceptable estimate. However, it should be noted that due to this inaccuracy in the mass distribution, the obtained natural frequency was multiplied by a safety factor of 1.5 for the sizing procedure.

Using this mass distribution, the structure was sized for the vibration loads using the method described in the beginning of this section. Sizing was performed using two materials, aluminium and carbon-fibre composite. The results of this are presented in Table 11.4. It should be noted that the non-isotropic behaviour of the composite has not been explicitly taken into account. However as the shear stresses are a factor 16 smaller than the axial stresses this effect is assumed to be insignificant. To compensate for this effect a slightly higher safety factor of 1.6 was taken for the composite structure.

Table 11.4: Vibration sizing using two materials

Material used	Yield strength [MPa]	E-modulus [GPa]	Density [kg/m^3]	Thickness [mm]	Total mass [kg]
Aluminium[1]	505	68.3	2700	1.75	32.5
Carbon-fibre composite EP5/5 [127]	647	71.58	1416	1.35	13.16

[1] `https://www.azom.com/article.aspx?ArticleID=2863` [Cited on 13 June 2019]

With the thickness presented in Table 11.4 the natural frequency and resulting maximum stress are 79 Hz and 387 MPa. The stresses distributions over the length of the structure are presented in Figure 11.5. For the aluminium structure the natural frequency and maximum stress are 83.3 Hz and 316 MPa. The axial vibration was also analysed, which has a natural frequency of 227 Hz and thus a resulting acceleration in the x direction of 60g. However, the resulting stress is insignificant with an absolute value of 16 MPa.

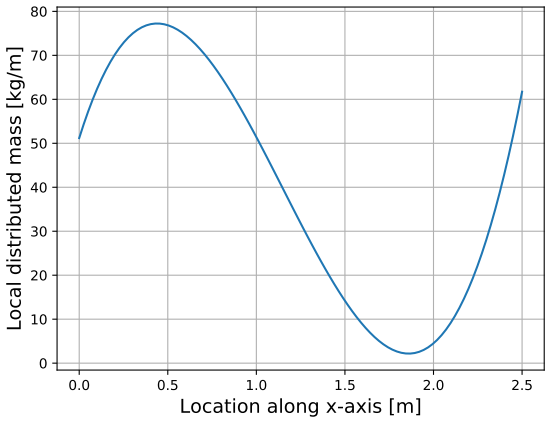

Figure 11.4: Estimated mass distribution of the spacecraft

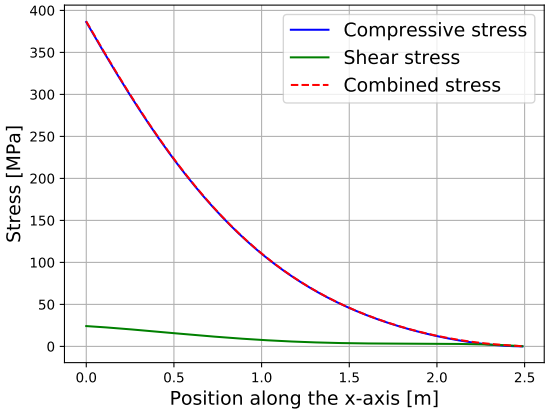

Figure 11.5: Stresses distribution for the composite shell

Finally, the stabilisation fins are analysed. The same safety factor of 1.5 on the natural frequency to account for inaccuracies in the boundary conditions is selected. The core and skin thickness of the sandwich panel were then chosen to be 1.4 cm and 0.48 mm respectively. The resulting total fin mass is 11.16 kg.

11.3.3. Sizing for the Quasi-Static Loads

After having sized the thickness for the vibration loads, the quasi-static loads are considered. These loads were presented in Table 11.3. However, using the thickness required for the vibration accelerations is sufficient for the structure to resist the quasi-static loads. The maximum stresses experienced are 46.3 MPa and 60 MPa for the aluminium and composite structure, respectively. These loads are evaluated for the quasi-static loads of the LauncherOne launch vehicle as these are more critical than the Electron loads.

11.3.4. Coating Selection

As the requirements for the coatings used depend highly on the location they are applied in, as described in section 11.2, the transparent coating will be considered separately. As the exposure to atomic oxygen is so significant for the mission, the resistance of the coatings to this exposure will be considered first.

Transparent Coating

Several parts of the satellite, such as the optics and the solar panels, require a transparent coating to function. For these part a Hollow silica nanosphere/polyimide composite film was selected as a coating [128]. This coating boasts an excellent transparency of over 92% [128]. Moreover the erosion yield of 4.67×10^{-26} cm^3/atoms is also of sufficient quality to function in the erosive environment. Another important quality of the tested films is that no optical degradation was observed after exposure to atomic oxygen [6]. This coating will be applied using a sol-gel method [129]. Another important aspect to note is that all surfaces this coating is applied to are not perpendicular to the on-coming flow of particles. Therefore, as was discussed in section 11.2, these surfaces experience a reduced fluence and suffer mostly from indirect attack. Therefore, the expected fluence on these surfaces can be halved [116]. Based on the erosion yield and the expected fluence, a thickness of about about 5 µm is strictly required. A safety factor of 1.5 is applied to account for any uncertainties in the prediction of the fluence. As a result, the optics and solar panels will be coated in a layer of 7.5 µm of composite film. This film will be applied using a sol-gel method.

Body Coating

The other exposed areas of the spacecraft have less strict requirements on the transparency of the applied coating. Therefore, the main concern when selecting a coating for these areas is the erosion yield. To maximise the performance a coating with a small erosion yield was selected. The coating that was selected is a

perhydropolysilazane derived silica coating [118]. This coating was selected for its extremely high erosion yield of 6×10^{-27} cm^3/atoms. Therefore, including the same safety factor of 1.5, a thickness of only 1.17 µm is required for this coating. The same sol-gel application method is used for applying this coating.

UV Exposure

The two selected coatings are both exceptionally resistant against atomic oxygen exposure. However, as discussed in section 11.2, UV induced erosion also plays a major role. As the transparent coating is facing the sun throughout the lifetime of the mission, it is critical that this coating is able to maintain its performance. The transparent coating selected has been developed recently and therefore has not been tested for UV resistance yet [129]. However based on the composition, an estimation can be made of the behaviour of the material when exposed to UV radiation. The inorganic silica component of the coating is expected to show good UV resistance as is the case in most metallic coatings [130]. Organic materials tend to have a significantly lower resistance to UV exposure [116]. However, due to the aromatic structures present in the polyimide, this group of polymers can be created such that they exhibit significantly increased UV resistance [131] and it is expected that a combination of these materials will also possess a good resistance against UV radiation exposure. This claim will have to be validated in future research.

11.3.5. Re-Entry Analysis

To model the re-entry of the spacecraft, the structure of the spacecraft was modelled in the SARA program [123]. Apart from the structure some other elements were included that could potentially survive re-entry. These elements were the mirrors and their support structure, which are described in chapter 9. Moreover, a thruster was included as the materials used in the thruster exhibit excellent resistance to high temperature. This configuration was in accordance with the design presented in chapter 2.

As the structure and the mirrors are made out of composites and the standard values for composites present in DRAMA are not applicable to the used material, the properties of this material had to input manually. The changed properties are presented in Table 11.5. Some other values also had to be added to the simulation, these are also presented in Table 11.5.

Table 11.5: Input values SARA simulation

Property	Value
Fibre reaction probability [-]	0.25 [132]
Heat capacity gas [J/K/kg]	0.844[2]
Activation temperature [K]	550 [127]
Reaction rate polymer [1/s]	0.01 [133]
Fatal collision energy [J]	80 [134]

The connection between parts was set to dissolve at 800 K. This temperature was chosen as it is significantly above the activation temperature of the used resin [127]. The structural shell was modelled as having a 2 mm thickness as the model requires a minimum thickness. Finally the orbital parameters as described in chapter 5 were entered into the model. The resulting trajectories are presented in Figure 11.6. The objects that reach the ground are the mirrors, the thruster and the composite shell.

The computed fatality probability computed by the programme is 1.19×10^{-4} using the parameters presented. This probability is above the acceptable value presented in section 11.2. However the structural shell was modelled as having an increased thickness of 2 mm, due to limitations of the simulation. The mass lost in the bottom panel of the structural shell during re-entry is more than the mass of the panel with the actual thickness. Thus this panel can be excluded from the fatality risk. The resulting fatality probability is 9.5×10^{-5}, which is below the maximum allowable risk. Therefore the re-entry can be classified as safe, despite being close to the maximum value. This is deemed acceptable as the increased thickness of the shells already causes an increased probability.

[2] http://catalog.conveyorspneumatic.com/Asset/FLS%20Specific%20Heat%20Capacities%20of%20Gases.pdf [Cited on 20 June 2019]

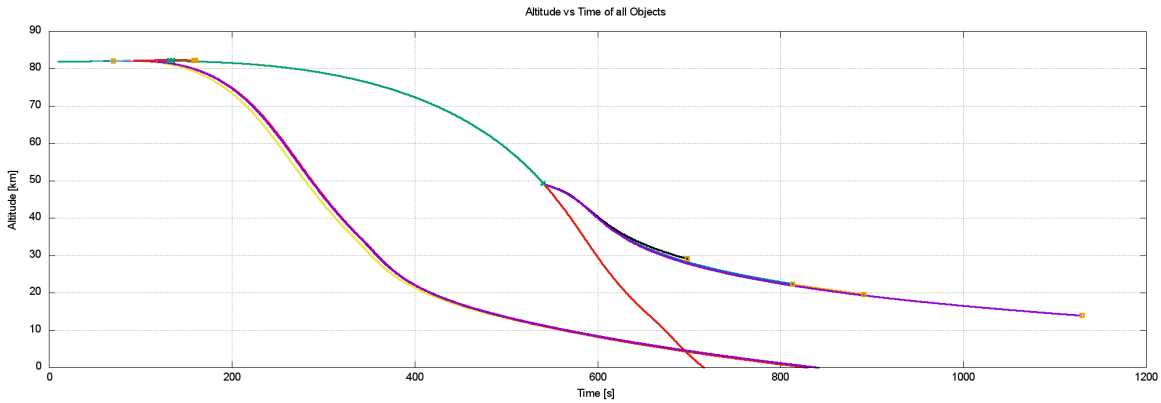

Figure 11.6: Re-entry of components of the RAMSES spacecraft

11.4. Verification & Validation

To prove the validity of the results presented in the previous section, the models used need to be verified and validated. The main verification and validation (V&V) efforts will be focused on the models that were developed for the vibration and quasi-static loading analysis.

11.4.1. Vibration Analysis

To test the method used for computing the natural frequency, the solution provided by the developed model will be compared to the analytical solution of an Euler-Bernoulli beam [135]. To do this the mass and stiffness distributions are set to a constant value and the compressive force is eliminated, as the Euler-Bernoulli solution is only valid in this case. As the first natural frequency is the most interesting while sizing for the launch loads, only the values of this frequency will be compared.

For length of 2.5 m, a moment of inertia of 2.067×10^{-4} m^4, an elastic modulus of 71.58 MPa and distributed mass of 60 kg/m the natural frequency found using the Euler-Bernoulli beam theory is 44.46 Hz [107]. The developed model produces a natural frequency of 44.20 Hz. The results of the two models are very similar, with a difference of less than 1%.

In order to validate the developed vibrations model it should also be proven that the results correspond with reality. The results from Euler-Bernoulli beam theory have already been proven to correspond quite closely to results obtained in experiments [135]. Therefore the model can be considered valid for a constant mass and stiffness distribution and lack of a compressive force.

However, the model is applied for a varying mass distribution combined with a non-zero compressive force. The effect of the compression force due to the acceleration is expected to lower the natural frequency [136]. This behaviour is observed for the model. For example if an acceleration of 10g is assumed in the axial direction, the natural frequency reduces to 44.18 Hz. This is a very minimal decrease in natural frequency. However, for a proper comparison the magnitude of the compressive load should be considered. This magnitude is significantly smaller when compared to the values considered in theoretical solutions [137]. For comparison, the magnitude of the presented F_r parameter, $\frac{PL^2}{\pi^2 EI}$, is 0.00063 if the maximum compression load at the root is considered for P. Therefore it can be concluded that the observed change in natural frequency is of an expected magnitude.

The effect of the mass distribution will also be qualitatively compared to literature. It has been observed that the natural frequency of a beam increases if the centre of mass is shifted closer to the root [138]. In the results of the model a very similar effect is observed. This effect is quantified by changing the mass distribution from uniform to triangular, such that the centre of mass moved from the mid-point to a third of the length of the structure. This shift is done such that the total mass remains unchanged, while using the same cross-sectional properties as defined earlier in this section. As a result of this shift the natural frequency shifts for 42.2 Hz to 72.2 Hz. The ratio between these two frequencies is 0.61. This is reasonable change when considering the effects observed in analytical methods [138]. The found frequency ratios of a system with the centre of gravity located at a third of the length and halfway along the length are 0.525 and 0.825 respectively [138]. Therefore the resulting fraction between the two frequencies is 0.636, which closely corresponds to the fraction found by the developed model.

11.4.2. Quasi-Static Analysis

For the V&V procedures of the quasi-static analysis a comparison to Euler-Bernoulli beam theory is made again. Firstly the results will be compared to beam with uniform mass and stiffness distributions as standard solutions are available for this type of problem. As the loads are introduced at the root of the structure, the resulting loading distributions are triangular for both the axial and transverse loads. The standard solution of the deflection due to a transverse acceleration of 2g, which corresponds to a shear force of 2.9 kN, gives a maximum deflection of 0.26 mm [107]. This value is found using $\delta_{\max} = \frac{w_0 L^4}{30EI}$. Where w_0 is the shear force at the root and the elastic modulus and moment of inertia are the same as in the previous section.

The maximum deflection found using the developed model is 0.3395 mm, which is 31% larger than the Euler-Bernoulli result. However it is known that the Euler-Bernoulli result underestimates the deflections for thick beams [139]. Moreover it is also found that the deformations found using Euler-Bernoulli theory are also lower than experiments [140]. The deflection is also found using the Timoshenko beam theory using Equation 11.16 [139]. In this equation the moment at the tip of the beam, M^E, is equal to zero. The moment at the root, M_0^E and Ω are found from Equation 11.17. Where G is the shear coefficient of 3 GPa [141], A is the enclosed area of 0.4 m^2 and K_s is the shear correction coefficient of 0.2412 [142]. However the resulting change in deflection is so small that the difference remains unchanged.

$$w_{\text{Timoshenko}} = w_{\text{Euler-Bernoulli}} + \frac{M^E - M_0^E}{EI} \cdot L^2 \cdot \Omega \tag{11.16}$$

$$M_0^E = -w_0 \cdot \frac{L^2}{6} \qquad \Omega = \frac{E}{GK_s}\frac{I}{AL^2} \tag{11.17}$$

Comparing the analytical results of Timoshenko beam theory to numerical simulation a trend of underestimating the deformations is observed [143]. It can be observed that a difference of as much as 22% is possible [143]. Therefore it is concluded, despite the higher resulting value of the model, that the model developed is of sufficient quality to estimate the loads experienced during launch.

11.4.3. Re-Entry Analysis

As the model used has not been developed internally the validation has already been done by the producer of the model [123]. Moreover, the re-entry analysis has been performed at a late stage of the design. Therefore the model made as an input for the SARA simulation corresponds closely to the actual satellite geometry. As a result, no further V&V activities have been performed on the re-entry model.

11.5. Sensitivity Analysis

To see how some of the input parameters affect the results their sensitivity is studied. The parameters chosen are the cross-sectional area, the thickness of the plates and the accelerations experienced. The first two influence the stiffness of the structure and thus its resistance to the same loading. The last changes the loading experienced. The sensitivity of each of these parameters is examined by varying them by 25% and computing the maximum stress experienced in the structure. The results are presented in Figure 11.7.

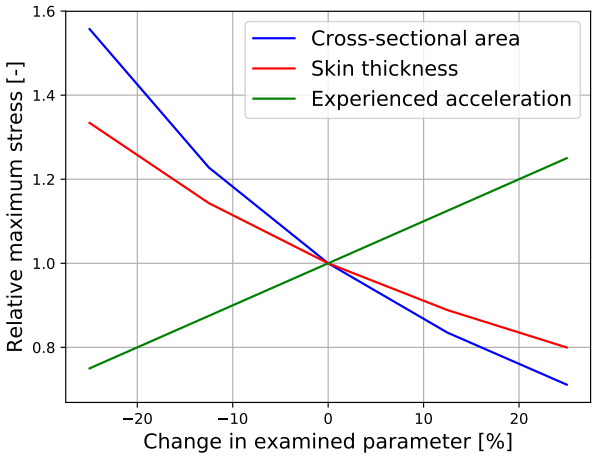

Figure 11.7: Sensitivity structural parameters

From Figure 11.7 it can be concluded that the cross-sectional area is the most sensitive parameter and a larger cross-section would be preferred. However this is not possible due to the constraints imposed by the integration into the fairing of the launcher.

For re-entry some parameters are also analysed, using the Monte Carlo simulation functionality of the SARA module. Some of the material parameters for the composite structure are varied as this structure is responsible for most of the material that survives re-entry. The first parameter is the reaction probability of the carbon fibres, this value was varied from 0.1 to 0.9. Secondly, the reaction rate of the resin was varied from 0.01 / sec to 1 / sec. Finally the temperature at which connections failed was varied from 700 K to 1200 K. As a result of these variations the fatality probability varies from 9.53×10^{-5} to 1.256×10^{-4}. So the exact behaviour of the selected composite can be of significant importance for the re-entry. Therefore this should be studied in more detail at a later stage. The dimensions of the shell were also analysed. This was done by varying the width of all panels in the shell by 25% in both directions. As a result the fatality probability varied from 1.01×10^{-4} to 1.348×10^{-4}. Therefore it can be concluded that the dimensions of the spacecraft also influence the risk associated with re-entry significantly.

11.6. Risk & RAMS Analysis

Despite the efforts made to make the structure of RAMSES as safe as possible, some risks are still present in the design. These risks and the efforts required to mitigate them are outlined in this section. Moreover the RAS analysis is also presented.

11.6.1. Identified Risks

For some of the risks associated with the structure efforts have already been made to mitigate them. These risks and their mitigation strategy are presented first.

RSK-STR-01 **Event:** Resonance occurs at a different frequency.
Risk: Due to the resonance at a different frequency, different accelerations will be experienced by the structure, as shown in Figure 11.3. These accelerations might lead to failure as they were not designed for. Therefore this risk is classified as catastrophic and likely. It as qualified as likely due to the inaccuracy in the mass distribution.
Mitigation: A safety factor of 1.5 was applied on the value of the computed natural frequency to ensure the experienced accelerations can be resisted.

RSK-STR-02 **Event:** Structure fails at different stress than predicted.
Risk: Failure occurs at a stress lower than expected, which is classified as catastrophic and possible.
Mitigation: Ensure that composite production is of high quality. Moreover a safety factor of 1.6 was applied for the stresses experienced.

Some other risks for the structural performance have to be mitigated in future steps. To do this a mitigation strategy is outlined for each of the identified risks.

RSK-STR-03 **Event:** Transparent coating degrades due to UV exposure.
Risk: UV exposure causes the coating applied to erode before the end of life, exposing the material below and compromising performance. This risk is classified as critical and possible as failure would not directly occur after the coating is eroded.
Mitigation: Test the selected coating in a combined UV and atomic oxygen environment. Moreover a safety factor of 1.5 was used for the thickness of the coating.

RSK-STR-04 **Event:** Coatings show non-linear behaviour at higher fluences.
Risk: The material in the coating erodes more quickly exposing the material below. This risk is determined to be critical and possible.
Mitigation: Test the selected coating for larger fluences to build confidence in the performance over the lifetime. Moreover a safety factor of 1.5 was used for the thickness of the coating.

RSK-STR-05 **Event:** Debris resulting from re-entry hits individual on the ground.
Risk: Civilian casualty, which is obviously classified as catastrophic. However due to the low likelihood associated with this event, as described in section 11.3, this risk is also classified as rare.
Mitigation: No mitigation possible without major design changes.

The risks identified and mitigated above are presented in Table 11.6.

Table 11.6: Risk map showing the severity and likelihood of the risks before and after mitigation

Severity \ Likelihood	Almost Certain	Likely	Possible	Rare
Catastrophic		RSK-STR-1 ←	RSK-STR-2 →	RSK-STR-5
Critical			RSK-STR-3, RSK-STR-4 →	
Marginal				
Negligible				

11.6.2. RAS Analysis

The first section of the RAS analysis to be discussed is the reliability. To maximise the reliability safety factors were included at every location they were deemed required. These section were the thickness of the coating, the natural frequency and the experienced stress. Moreover, the material that is used has been tested extensively [127] and therefore has well documented properties.

In terms of availability the launch vehicle is the only uncertainty of the subjects discussed in this chapter. The launch vehicle chosen is currently under development. However the first launches are already scheduled in 2019[3]. Therefore the expectations are that the chosen launch vehicle will be available when RAMSES is ready for launch.

The safety of the structure of RAMSES is assessed through the risk associated with the re-entry as no other manned mission are present in the orbit that is selected. This risk was computed after the design was completed and is presented in section 11.3. Therefore the safety of the re-entry of the system was assessed to be sufficient. Another section of the mission profile where safety could be an issue is the launch of RAMSES. However as Virgin Orbit would conduct the required analysis to ensure a safe launch [14], this section is also deemed to be safe. Finally, it should be noted that the materials used are also safe for use [144, 145].

11.7. Cost Analysis

To analyse the cost of the structure a parametric approximation was used [31]. The cost is separated into research development test and evaluation (RDT&E) and unit costs. The parametric equations are shown in Equation 11.18 and Equation 11.19. To account for the increased cost of producing composites an increase of 25% was applied for the RDT&E cost. For the unit cost an increase of 100% was applied.

$$Cost_{RDT\&E}[92\text{dollars}] = 2640000 + 416000 \cdot mass^{0.66} \tag{11.18}$$

$$Cost_{unit}[92\text{dollars}] = 86000 \cdot mass^{0.65} \tag{11.19}$$

The resulting cost for both a aluminium structure and a composite structure are shown in Table 11.7. It should be noted that the mass used to compute the cost also contained some additional masses. These are masses for the fins (11.136 kg), the fasteners (3.5 kg) and the adapter for the launcher (5 kg). The mass of the fasteners and adapter are described in chapter 14. The lower TRL and higher risk of the composite structure is due to the required coatings. These have not been used on an actual mission as of yet and were not explicitly taken into account for the cost.

Table 11.7: Cost of the structure

Material	RDT&E cost [2019€]	Unit cost [2019€]	Total cost [2019€]	Estimate Methodology	TRL	Technical risk
Aluminium	13178932	1785731	14964663	Parametric	9	Low
Composite	13511585	2641916	16153501	Parametric	6	Medium

[3] https://virginorbit.com/gomspace-signs-contract-for-low-inclination-launch-on-virgin-orbits-launcherone/ [Cited on 16 June 2019]

12. Thermal Control

In order to have a comfortable working environment for all of the components of the satellite, a thermal control subsystem must be designed for. The driving functions and requirements of this subsystem is given in section 12.1. The methods of how the subsystem is designed is discussed in section 12.2. section 12.3 shows the architecture of the subsystem and its resultant performance, while section 12.4 presents the verification and validation of the model created to design the subsystem. The model is further analysed for its sensitivity in section 12.5. Finally, the risks associated with this subsystem are shown in section 12.6 and the estimated costs are presented in section 12.7.

12.1. Functions & Requirements

The thermal control subsystem regulates the temperature of the satellite and is thus a critical subsystem. Its required actions are very brief and are listed in Table 12.1. The subsystem is driven by the required operating temperatures from relevant critical components. The temperature ranges each component can operate at is summarised in Table 12.2.

Table 12.1: Subsystem requirements on the thermal control subsystem

ID	Requirement	Notes	Met [✓/✗]	Section
THM-001	The thermal control system of RAMSES shall maintain the temperature of the various components of all subsystems of the spacecraft within their operating temperature boundaries	Table 12.5 for details regarding temperature boundaries	✓	section 12.3
THM-002	The thermal control system of RAMSES shall cope with the space environment it must go through its mission		✓	section 12.3

Table 12.2: Operating temperature for critical components

Component	Min Temperature [°C]	Max Temperature [°C]
Star sensor	-40	35
Sun sensor	-30	65
Magnetometer	-30	60
IMU	-40	75
Payload	-30	70
Communication	-80	40
PV cells	-170	150
On-board computer	-40	60
Batteries	-20	60
PCU & IPPCU	-25	60

12.2. Methodology

The temperature experienced by the spacecraft must be computed such that the compliance with the required operating temperature can be verified. Therefore, the heat received externally must first be consid-

ered, as explained in subsection 12.2.1, then a thermal analysis model is proposed to compute the temperature evolution.

12.2.1. Thermal Environment

In order to set up a thermal balance for the satellite, the heat source received from external sources must be identified. First, aerodynamic heating is considered for this mission. At altitudes above 100 km, with rarefied flow, there is free-molecular flow heating [146, 147]. However as seen in [148], this should be neglected above 180 km. With RAMSES flying above 214 km, aerodynamic heating is thus not included as an external heat source. Therefore, heat transfer from the environment only occurs by radiation.

The first heat source comes from solar radiation. The heat received by a spacecraft from solar radiation is given by $Q_{\text{solar}} = J_s \alpha A_{\text{solar}} cos(\theta)$, where J_s is the solar radiation intensity, α the absorptivity of the exposed surface, A_{solar} is the area of the satellite exposed the sun rays, and θ the angle of incidence of the solar vector with the plane of the area that is facing the sun. J_s is a value that varies throughout the year, the value used is set for the worst hot and cold conditions which will be further explained later in this section.

Next is the planetary albedo radiation which accounts for the incident solar radiation reflected off a planet, Earth in this case. The albedo radiation can be computed with the following equation, $Q_{\text{albedo}} = J_s \alpha A_{\text{albedo}} F K_a a$, where similarly, A_{albedo} is the area of the satellite exposed to the albedo radiation, F the view factor, a is the albedo factor and K_a the degree of collimated incoming solar energy off a spherical Earth. The factor K_a can be calculated using [31], $K_a = 0.664 + 0.521\rho - 0.203\rho^2$, where ρ, angle of Earth in the celestial sphere with respect to the satellite,

$$\rho = arcsin\left(\frac{R_e}{h + R_e}\right) \tag{12.1}$$

with h as the altitude of the satellite and R_e the radius of Earth. This term reappears in the computation of the view factor F, $F = sin^2(\rho)$. The view factor is relevant when the plane of the satellite facing the Earth is parallel to the surface of the Earth. For the faces that is perpendicular to this face the view factor is derived in [149] as,

$$F_\perp = \frac{1}{2\pi}\left(\pi - arcsin\left(\sqrt{1-F}\right) - sin\left(2arcsin\left(\sqrt{1-F}\right)\right)\right) \tag{12.2}$$

Lastly, the environmental heat flux that needs to be considered is planetary radiation which is given as, $Q_{\text{IR}} = J_{\text{IR}} \epsilon A_{\text{IR}} F$, with J_{IR} the flux intensity from Earth radiation, ϵ the emissivity factor, and again, A_{IR} the area of satellite exposed to Earth.

The total environmental heat contribution is then the summation of the above three heat sources, $Q_{env} = Q_{solar} + Q_{albedo} + Q_{IR}$.

12.2.2. Steady-State Thermal Analysis

For a preliminary analysis where the feasibility of the system is examined, the radiation equilibrium temperature must first be found. This is computed by finding a thermal balance where an equilibrium is achieved when the energy received is equal to the emitted energy from the spacecraft. In addition to the environmental heat received, there is heat generated within the system itself. Multiple components of the satellite have a certain efficiency and all the energy lost is dissipated as heat. This is denoted as Q_{int} in the thermal equilibrium of Equation 12.3 and its contribution from each component is summarised in Table 12.3.

$$Q_{\text{env}} + Q_{\text{int}} = A_{\text{surface}} \sigma T^4 \epsilon \tag{12.3}$$

In the above equation, σ is the Stefan-Boltzmann constant, ϵ is the emissivity of the satellite, A_{surface} is the surface area of the satellite that radiates, and T is the steady-state radiation temperature. Therefore for this feasibility analysis, the satellite is assumed of having one uniform equilibrium temperature.

Two steady-state temperatures are computed for worst hot and cold conditions. RAMSES experience a portion of eclipse in its orbit. During eclipse, the cold case, both solar and albedo radiation are omitted from the environmental heat input. For the hot case, the maximum values of J_s, J_{IR}, and albedo, a, are used. The first differ throughout the year due to changing Earth-sun orientation. Albedo technically changes over different parts of the Earth as for example, areas of clouds or forests will have very different values. The values used in the two cases are presented in Table 12.4.

As outlined in [31], for preliminary thermal analysis, the spacecraft is usually first assumed to be a sphere with an equivalent surface area. However, to replicate reality better, the shape of the spacecraft is main-

Table 12.3: Heat generated internally from various components

Component	Power dissipated W	Comment
PCU & IPCU	35	Efficiency of component
ADCS	10	Efficiency of component
On-board computer	2	Efficiency of component
Engine	115	Efficiency of component see Equation 7.4
Communications	5	Statistical relation from [150]
Payload	6	Mostly from sensors, only during daytime

Table 12.4: Worst hot and cold cases for environmental parameters

Parameter	Hot Case	Cold Case
Solar flux, J_s [W/m^2]	1420	0
Albedo factor, a []	0.46	0
Earth flux, J_{IR} [W/m^2]	274	198

tained. The satellite has six different faces which throughout its orbit will be oriented relatively the same way with respect to Earth as the camera must always face Earth directly. What each side of the spacecraft sees is recorded in Table 12.5.

Table 12.5: Environmental heat input on different sides of RAMSES

Side	Node	Heat Input	Description	Allowed Temperature [°C]
Main body				
1	Inlet	Albedo, Earth radiation	Parallel to velocity vector	-
2	Outlet	Albedo, Earth radiation	Opposite to inlet side	-40 to 60
3	Top	Solar radiation	Where the solar panels are mounted	-25 to 60
4	Bottom	Albedo, Earth radiation	Opposite to top side	-25 to 60
5	Nadir	Albedo, Earth radiation	Where the imaging payload is mounted, always directed towards Earth	-25 to 55
6	Zenith	Deep space	Opposite to nadir side	-15 to 30
7	Internal	-		-15 to 30
Fins				
1	Cells	Solar radiation	Where the solar panels are mounted on fins	-
2	Bottom	Albedo, Earth radiation	Opposite side of cells	-

For each side in Table 12.5, the heat input received is calculated, proportional to the area of the relevant side. Out of all the sides, only the 'internal' side is not included in the steady-state computation. Only the Nadir side has a view factor of F while the rest sees Earth with $F_\perp$ factor. The environmental heat inputs

for all sides and the values in Table 12.3 are summed. Using Equation 12.3, the steady-state temperature for each case can thus be calculated. The results are shown in Table 12.6.

Table 12.6: Hot and cold case

T_{hot}	70.7 °C	Solar, albedo, and planetary radiation included
T_{cold}	−88.1 °C	Only albedo radiation considered
T_{avg}	16.7 °C	ecl·T_{cold} + (1-ecl)·T_{hot}

The computed hottest and coldest temperatures show a very wide range of temperature and these extremes are hardly feasible. However, due to the tight constraint with regards to mass and power, it is very much preferred to use a passive thermal control system. Since these two steady-state temperatures will theoretically never be reached and are grossly an overestimation, they are used as a stepping stone to an increased accuracy of the model. The average temperature in one orbit is computed where in Table 12.6, ecl is the portion of time the satellite is in eclipse. This average temperature is used in the next model.

12.2.3. Transient Thermal Analysis

A thermal mathematical model (TMM) has been made to accommodate different nodal temperatures that varies through time. This would simulate reality closer. The satellite is then discretised into multiple nodes and for each node, Equation 12.4 [44] is applied.

$$m_i C_i \frac{dT_i}{dt} = Q_{\text{env},i} + Q_{\text{int},i} - \sigma \epsilon_i A_{\text{space},i} {T_i}^4 - \sigma \sum_{j=1}^{m} A_i F_{ij} \epsilon_{ij} (T_i^4 - T_j^4) - \sum_{j=1}^{m} h_{ij} (T_i - T_j) \tag{12.4}$$

The first three terms of the right hand side of Equation 12.4 are similar to Equation 12.3 where the subscript i denotes the node the equation is being computed for. The last two terms consider the heat transfer interaction of each node to its neighbouring nodes through radiation and conduction respectively. F_{ij} represents the view factor between the ith and the jth node, where a catalog of values of view factors for various geometries can be found in [151], h_{ij} is the thermal conductance and ϵ_{ij} the effective emittance which can be calculated with, $\epsilon_{ij} = \frac{\epsilon_i \epsilon_j}{\epsilon_i + \epsilon_j - \epsilon_i \epsilon_j}$. The thermal conductance h is given by, $h = \frac{\lambda A_{\text{cond}}}{l_{\text{cond}}}$, where λ is the thermal conductivity, A_{cond} the cross-sectional area of conduction and l_{cond} the length of conduction path. The thermal conductivity is assumed to be that of carbon fibre reinforced polymer. The two latter elements would depend on the conduction points of each node.

The left hand side of Equation 12.4 gives the thermal inertia of each node with m_i being the mass of node i and C_i the specific heat capacity of node i.

To finally calculate the temperature of each node at each point in time, a time-stepping method is implemented. Forward Euler is chosen to simplify the non-linearity in Equation 12.4. Computing for the temperature of the next time-step only requires the temperatures of the previous time-step which are already known and thus the right hand side of the transient equation reduces to a column vector, $\mathbf{q}$, with as many rows as the number of nodes. This way, the fourth power terms do not need to be linearised. A system of linear equations of m nodes is set up as in Equation 12.5.

$$\mathbf{T}^{n+1} = \mathbf{T}^n + dt \cdot \mathbf{dT}^n = \mathbf{T}^n + dt \cdot [M]^{-1} \mathbf{q}^n \tag{12.5}$$

In this equation $\mathbf{T}^{n+1}$ is the time vector of the nodes at time $n+1$, while $\mathbf{T}^n$ is that at time n, dt is the time step, M a diagonal matrix of the thermal inertia of the system of nodes, and $\mathbf{q}$ the net flux vector. As mentioned previously, the initial temperature for all of the nodes is assumed to be the average temperature of the satellite as calculated in the steady-state calculations.

Theoretically, the model can be applied to any spacecraft application with infinitely number of nodes for a higher temperature resolution. However, for this project, the number of nodes is constrained for simplicity. Six different nodes are created for each six different faces of the satellite, and a seventh node is included to consider the internal part as a lumped mass. The internal part will not receive any external heat fluxes nor will it emit radiation to space. The heat flux experienced by each face of the satellite follows the assumptions used to compute the steady-state temperatures as shown in Table 12.5. Furthermore, the fins of RAMSES are treated as an independent system from the main satellite body.

12.2.4. Hardware Sizing

Once the thermal analysis has been conducted, the resultant thermal performance can be adjusted with various thermal control systems such that the temperature ranges of the satellite fall under the requirement. Various thermal control systems have been examined. A lot of thermal control hardware is available for the conventional-sized spacecrafts but less hardware is developed for small satellites. It can be seen that small satellites mostly use passive control systems and occasionally, heaters [152]. The passive control includes multi-layer blankets for insulation, radiating surfaces and finishing and heat conductive lines. The more active systems most often only uses heaters, while louvers and thermoelectric coolers are used less.

Therefore, the first remedy tried to control the temperature range is the use of various surface finishes. A list of the surface finishes and their respective absorptivity and emissivity coefficients considered for this mission is compiled in Table 12.7. The absorptance and emittance values of the bare structure are also included for completion. Another layer of transparent coating is be placed on top of these paints for shielding against the toxic environment. Therefore, the transmissivity of the transparent coating must be included.

Table 12.7: Various surfaces and finishes absorptivity and emissivity

Surface	Absorptance(α)	Emittance(ϵ)	α/ϵ
Black paint	0.95	0.85	1.12
White paint	0.15	0.90	0.167
White paint: Chemglaze A276	0.28	0.88	0.318
Aluminized kapton (5 mil)	0.14	0.05	2.80
Electroplated gold	0.25	0.04	6.25
Photovoltaic cells	0.80	0.78	1.03
CFRP	0.80	0.80	1.00
Aluminium	0.24	0.08	3.00

It has been found after the thermal analysis, which is later shown in section 12.3, that the use of surface finish is not enough to regulate the thermal environment of the satellite. Some of the side still gets too cold during eclipse periods while other sides are too hot. This discrepancy can be minimised by transferring the heat from the hotter sides to the colder sides. This is done by utilising conductive lines. Therefore, the inclusion of heat pipes must be modelled. They are included in the thermal mathematical model in the conduction term as suggested in [44]. A schematic of a heat pipe can be seen in Figure 12.1

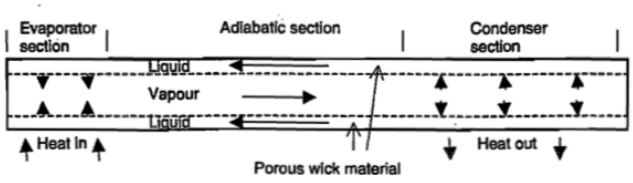

Figure 12.1: Simple schematic of a heat pipe [44]

It can be observed from the schematic that the mechanism of a heat pipe is straightforward. A difference in temperature between the evaporator section and the pipe triggers an energy exchange in which heat enters the pipe, vaporising the liquid within. This vapour travels to a region of lower pressure where the difference in temperature in the end of the pipe condenses the vapour to liquid. At this end, the heat is emitted out. The liquid then returns to the evaporator section through capillary motion with the help of the wick material. For the model, it is assumed that the temperature at the evaporator section is equal to the temperature at the condenser section of the previous time step. The heat conducted out is computed using the equation, $Q = h(T_i - T_j)$, a basis of the heat equation derived from Fourier's law.

Any further excess heat that is in the system can be emitted out using radiators. From [153], it was found that for range of radiating temperature of 20°C to 40°C, a radiator is capable of emitting up to 600 W/m^2.

Nevertheless, information on off-the-shelf radiators is found which are capable of performing heat rejection of > 370 W/m^2 [154]. This film radiator is thus used to size the area and mass of radiators needed for the spacecraft. The radiators are placed at sides which do not face the sun as to maximise their efficiency [155].

12.3. Architecture & Performance

Once the model is set up, the thermal behaviour of the satellite can immediately be studied. As mentioned in section 12.2, the thermal performance of the fin structure is analysed independently from the main body. The performance of the main body will first be discussed and the fins after. For all the simulations, the results are going to be shown for the conditions at an altitude of 214 km and eclipse period of 31% of the total orbital period.

12.3.1. Main Body Structure

Initially, the spacecraft as it is without any surface finish is simulated. The first run was conducted on the two options of materials as established in section 11.3: aluminium and carbon fibre. During the trade-off of the two materials, both materials are checked for feasibility, of whether any coating will suffice in passively controlling the temperature of the satellite. The results of the thermal analysis help in the choice of the material.

The simulation is ran for when the satellite is already in the middle of daylight conditions. Both Figure 12.3 and Figure 12.2 show the temperature variations in five orbits. The temperature evaluation for aluminium diverges quicker and for the internal node, is still increasing in the period of five orbits.

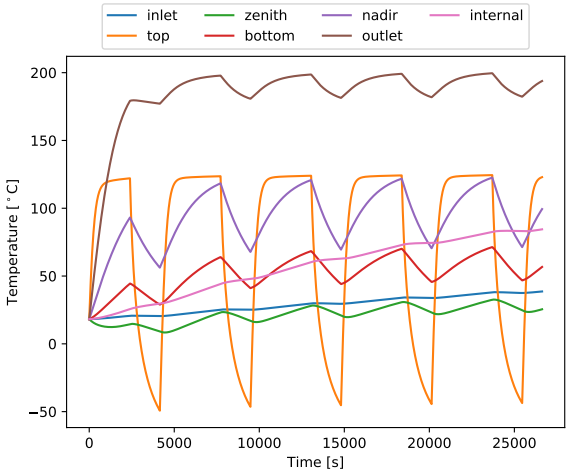

Figure 12.2: Thermal performance with full body aluminium

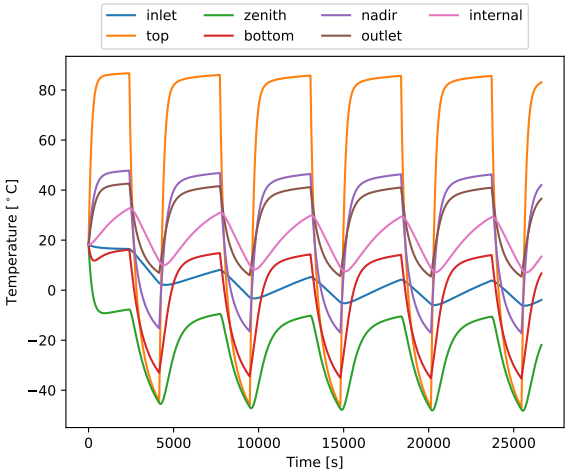

Figure 12.3: Thermal performance with full body composite

It can be seen from the two graphs that without any surface finish, using composite is already more beneficial for lowering the maximum temperature. The temperature of the solar arrays which are placed on the 'top' side, reaches over 100°C when aluminium is used. Moreover, it can be seen that the power dissipated from the thruster greatly increases the temperature of the 'outlet' side considerably with aluminium. When composite is used, the higher temperature can be compensated during eclipse periods. The significant difference in performance can be explained by the distinction in their α/ϵ ratio. Aluminium has a higher α/ϵ than CFRP thus there is not enough time during eclipse to reduce the temperature and emit excess heat. However with CFRP, as most heat absorbed is also emitted, most of its nodes get colder. Especially for its side that is not exposed to any external heat source, the temperature after eclipse period does not recover to its daylight condition. In conclusion, for both materials, different coatings and radiator sizes are to be designed. However, with both materials, passive thermal control are deemed possible. Therefore, with regards to thermal control, both materials are supported. As the design process is done concurrently with the other subsystems, while both aluminium and composites are considered in structures, the surface finish needed for both are also configured in the thermal subsystem. However in this report, only the result for a composite structure is shown as this is the final material chosen.

Taking in mind the temperature evolution seen in Figure 12.3, the main problem lies with regards to the temperature of most nodes lowering too much. Particularly for the zenith side, this will not be sufficient

for some of the components that need to be placed there. The zenith needs to have a coldest temperature of −20°C and a hottest temperature of 30°C. However the zenith faces deep space and is assumed to not received any external heat input. Therefore a heat source must come internally. Furthermore, as seen in section 8.2, a larger deviation from the base temperature leads to a higher degradation of the solar cells. The fluctuations in the temperature in the 'top' side must then be minimised. These two issues may be mitigated by the use of conductive lines between the different nodes. The use of heat pipes will not only minimise the temperature variation of the solar cells but also of the overall spacecraft.

Several different coatings and their combinations must be tried on the various sides of RAMSES in order to achieve the most ideal temperature ranges. Therefore, an optimisation procedure is enforced. The most potential candidate for the the sides that get too cold during eclipse is aluminium kapton as it has a relatively higher α/ϵ ratio while still having a low value of absorptance. This film is then applied on the zenith and outlet sides. For the nadir facing side, the most optimum solution is found to be the white paint Chemglaze A276. This side faces the Earth and receives considerable amount of albedo and planetary radiation compared to the perpendicular sides. Using white paint will reflect the heat while still having high emissivity. The resulting temperature variation is shown in Figure 12.4. Again, it is run for 5 orbits.

Figure 12.4 shows that the zenith side and inlet still depresses through time, it does not converge to steady state. The top panel also still has a high fluctuation. However, the inside of the top panel cannot be arbitrarily covered by an insulator as this will furthermore increase its own temperature, further elevating the degradation of the cells. Therefore, heat pipes must be sized such that the heat from the solar panels can be transferred to the other panels, especially to the colder ones. This way, the entire satellite can have a more uniform temperature. It has been decided that there is enough area on the outlet side for a radiator to emit the power dissipated from the engine. Although, not all of the heat will be rejected to still elevate the temperature of the satellite. With 50 W of heat dissipated off, the required radiator size at the outlet is 0.14 m^2. With the combination of the heat pipes, still 500 W of heat need to be radiated off. A panel area of 1.35 m^2 is needed to radiate this much heat. These panels will be partially placed on the zenith side and the bottom side. The final temperature evolution of the main body of RAMSES is shown in Figure 12.5 full with its thermal control hardware configured. The plot is shown for one orbit at the time when the system has gone steady and no longer diverges which occurs after three oscillations. It is cut to this interval to show clarity to the reader. The first 2000 s is daylight period, then the eclipse period starts, and after 4000 s, the daylight period starts again until it comes back to its starting position. Figure 12.5 shows that for each side, the temperature experienced is well within the required temperature boundaries. Therefore, with the use of surface coating, heat pipes, and radiators, the thermal environment of RAMSES has been successfully managed passively.

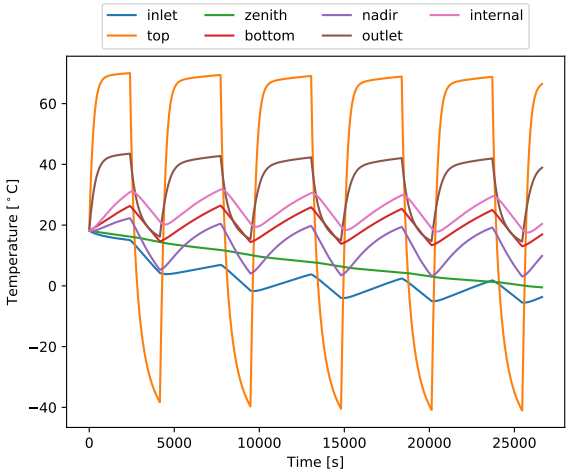

Figure 12.4: Main body analysis only with surface finish applied, for five orbits

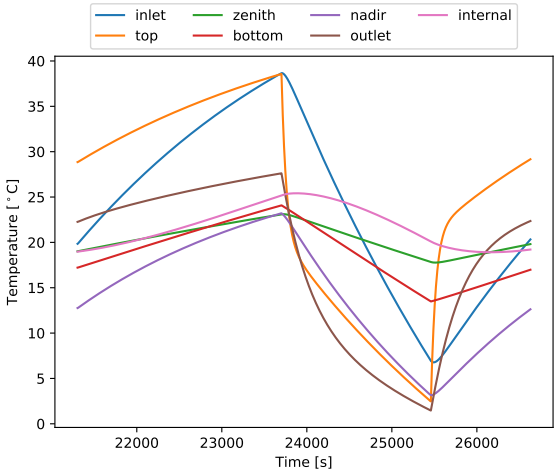

Figure 12.5: Body analysis with coating, radiators, and heat pipes, for one orbit after reaching periodic steady-state

12.3.2. Fins Structure

As mentioned in section 12.2, the transient analysis of the fin structure has been conducted independently of the main body. The same issue as the main body prevails. As seen in Figure 12.6, the variation in the temperature of the solar panels induce degradation that leads to excessive sizing of arrays. Here, the mitigation is more straightforward. There is no body-structure that houses the working components on the other side of the solar panel on the fins. Therefore, the back side of the panels can be coated with a surface finish enough to radiate the excessive heat. White paint is used to coat this side. The resultant temperature variation is shown in Figure 12.7. No heat pipes are required for the fins.

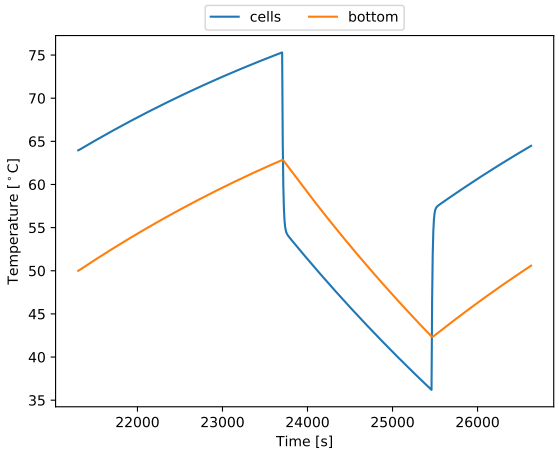

Figure 12.6: Fins without coating on back side, for one orbit after reaching periodic steady-state

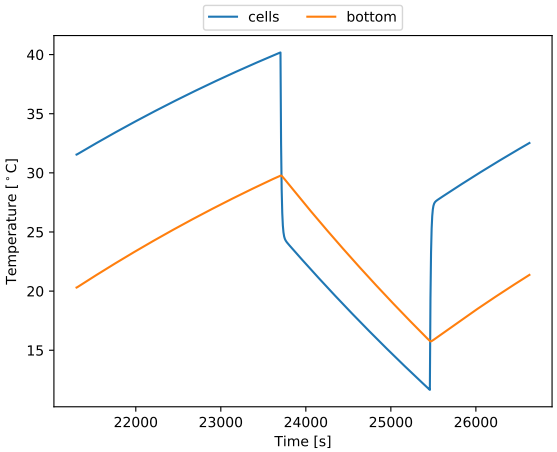

Figure 12.7: Fins with coating on back side, for one orbit after reaching periodic steady-state

12.3.3. Conclusion

The selected thermal control hardware is a passive system. Two types of coatings are used on the entire spacecraft. For the main body structure, aluminium kapton is applied on the zenith and bottom sides, and white paint is applied on the nadir side. For the fins, the bottom side is painted with white paint. Three radiator panels are sized. One in outlet of size 0.14 m^2 and each one in the zenith and bottom sides of in total 1.35 m^2. With a panel density of 2.4 kg/m^2[154], the masses of each panel is in total given to be, 3.6 kg. No concrete weight estimation is available for the heat pipes, but they are in magnitude of hundreds of grams. Due to the inaccuracy of the estimation, a margin is given to the weight of the heat pipes and cumulatively with the coatings, given to be less than 1 kilograms.

12.3.4. Further Considerations

The effect of variations of temperature in the structure itself has not been considered in this project. Further research can be conducted on the thermal stresses and the deformations of the spacecraft due to the differences in temperatures on its different sides. The issue of the optics being affected by fluctuations has been expressed during the design. A consideration to isolate the imaging payload from the rest of the spacecraft components is suggested in order to more closely regulate its thermal environment. Nevertheless, it was decided that such a thing shall not be necessary for two reasons. The first, being that the material chosen for the mirrors, carbon fibre reinforced silicon carbide, has a low coefficient of thermal expansion. The temperature variation on which this mirror is mounted is also narrow. Second, the other critical component of the payload is the chip(s). These are assumed to be part of the internal node due to its more inward position, and with the given temperature evolution, is still very much within its operating conditions.

12.4. Verification & Validation

This section discusses the verification and validation of the model. Also, a method of how the requirement can be verified is suggested.

12.4.1. Model Verification & Validation

Verification: There are no readily available analytical solution to compare with the model. The preliminary thermal analysis computation is verified with the method outlined in [44]. Here, the spacecraft is assumed to be spherical with an equivalent surface area. For the simple model created and the spherical analytical solution, the same input is used for solar flux intensity, albedo factor, Earth planetary radiation and α/ϵ ratio. The two values are compared and shows that the average temperatures are **1%** off from one another. Since the spherical model is often used in various literature such as [31, 156], this verification has been deemed sufficient for the model.

No analytical model can be found for the transient analysis as most thermal modelling, if not based on the most basic assumptions, requires numerical methods. Due to time constraints, no inspection with the use of numerical software has been conducted. Therefore, the verification of the transient model has receded to investigating the code written. Inputs are changed and the outputs are verified. This includes changing the solar or planetary heat input and albedo factor, increasing these generate higher temperatures, as expected. Several other similar tests are done such as: examining eclipse periods (the longer, the colder), examining α/ϵ ratios, changing internal heat values. Various others of these perceptive tests are done to ensure that the program is working as intended.

Validation: The result of the model is validated with comparison to the result of another thermal mathematical model performed in [44]. However, due to the lack of documentation on the conditions applied to the model, a face validation is done instead on the behaviour and trend of the result. Figure 12.8 shows that similarly, the temperature evolution of the nodes follow a sinusoidal oscillation. The nodes that are exposed to the environment are relatively close to one another and have the same phase. The node that is internal, the batteries, has less variation in temperatures. These trends can also be seen in the result of the TMM developed in section 12.2. Thus, it is deemed that the model has been validated.

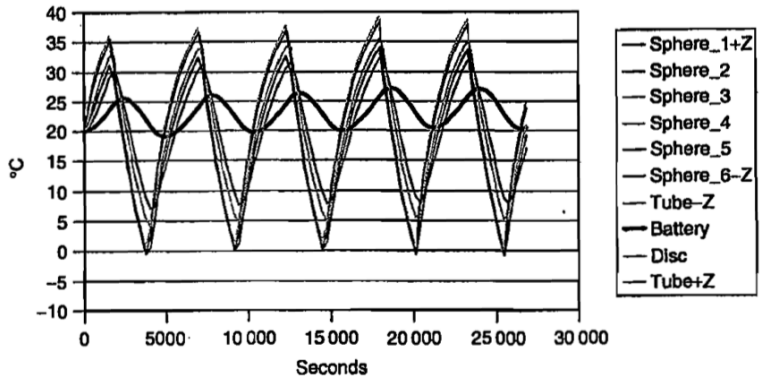

Figure 12.8: Temperature evolution of a spherical spacecraft in sunlit orbit. Where only the 'battery' node is encapsulated internally [44]

12.4.2. Requirement Verification

As to confirm the estimated temperature from the thermal mathematical model and verify that the requirement imposed on the thermal subsystem is complied, tests can be performed. As described in [44, 157], there are two verification by tests that should be done. The first is to demonstrate the compliance of the requirement on the control system which is called the 'thermal balance test'. The second is called the 'thermal vacuum test' where the requirement of the behaviour of the spacecraft is demonstrated. For both of the tests, the space conditions required to imitate the reality of the mission are tedious to achieve. It requires a heat sink to model the heat inputs from the external environment and also high vacuum to diminish conduction or convection by air. The test conditions must be fabricated such that worst conditions for the thermal environment are taken into account. To compare the resulting data with the thermal mathematical model, the same conditions must be imposed on the simulation.

12.5. Sensitivity Analysis

A sensitivity analysis is conducted on the transient model where the ranges in altitude and eclipse periods, as given in subsection 5.2.3, is used as an input. The maximum and minimum temperatures once a steady oscillation has been reached are recorded for each node. The percentage increase or decrease in temperature with respect to the temperature variation in section 12.3 is tabulated below. Table 12.8 shows the result for the nodes on the main body structure and the fin nodes. They are separated by a vertical line.

Table 12.8: Maximum and minimum temperatures of main body and fin nodes for various cases of orbit during mission

	Orbit	Inlet	Top	Zenith	Bottom	Nadir	Outlet	Internal	$Cells_{fin}$	$Bottom_{fin}$
T_{max}[°C]	h = 214 km	36.3	35.8	17.3	20.2	21.4	26.4	22.0	37.1	26.4
T_{min}[°C]	ecl = 37.6%	2.12	-1.68	11.7	9.10	0.131	-0.495	14.8	7.62	11.4
T_{max}[°C]	h = 240 km	39.0	39.1	24.7	24.3	23.3	27.2	26.0	41.3	31.1
T_{min}[°C]	ecl = 31.7%	7.67	3.35	19.4	14.0	3.58	1.60	19.5	12.9	17.2
T_{max}[°C]	h = 240 km	36.0	35.8	17.9	19.6	21.2	25.7	21.8	37.3	26.7
T_{min}[°C]	ecl = 36.7%	2.28	-1.44	12.4	8.78	0.109	-0.697	14.6	7.96	11.8

From Table 12.8, it is determined that for the extreme cases during orbit, there no temperature is exceeded in any nodes. This shows the system is robust enough for the experienced variation.

12.6. Risk & RAMS Analysis

However safe any subsystem can be, risks would still exist. In a good design, risks should be identified such that they can be mitigated. This section discusses the risk and the RAMS analysis.

12.6.1. Risk Identification and Mitigation

The risks for the thermal control system have been identified, analysed, and mitigated. Their severity levels are allocated in accordance to the definitions given in section 6.6.

RSK-THR-1 **Event**: Leakage in the heat pipes.
Risk: The pipes can get fractured such that the ammonia inside leaks. This may contaminate its surrounding. With malfunctioning heat pipes, the thermal environment becomes less regulated. This is thus a critical risk however rare as heat pipes are quite well developed with current technology.
Mitigation: Quality control of the heat pipes must be thoroughly performed before the satellite integration phase. Attention must also be paid towards sealants or welds in the pipe connections.

RSK-THR-2 **Event**: Heat that needs to be transferred through heat pipe is over its capacity.
Risk: This risk is a design flaw, as inaccuracies are present in the simplified model of the heat pipe. This is a critical risk as the degradation of the solar panels will be increased and the temperatures at the other nodes lowered. It is a rare event as heat pipes are as previously mentioned, well developed.
Mitigation: Developing a more detailed model of the heat pipe can be done. On top of this, a system hardware test can be performed to ensure that the heat pipes work as designed.

RSK-THR-3 **Event**: The coating paint erodes over time reducing the effectiveness of its insulating properties.
Risk: The satellite will be more exposed to the external heat inputs, leading to higher or lower temperatures. The direct consequence of this risk is critical. The paint itself will almost certainly degrade.
Mitigation: During the design of the thermal control system, the above effect must be taken into consideration. Additionally, a transparent coating is placed on top of the paint for the general protection of the spacecraft with the environment. This greatly reduces the likelihood of the degradation.

RSK-THR-4 **Event**: Radiator failure.
Risk: The radiator may be undersized for the mission especially in the occasion of the radiators being faced towards the sun. The spacecraft will heat up and this is critical. However in none of the mission trajectory will the radiators be facing the sun. Therefore, this risk is set to be rare.
Mitigation: A margin has been imposed on the operating temperatures and the controlled temperature variation of the spacecraft. Therefore, if it does get hotter, the components can still work before going to normal attitudes. The time period where radiators face the sun should also be very short

such that the effects are not long-lasting.

Table 12.9: Risk matrix showing the severity and likelihood of the risks before mitigation.

Severity \ Likelihood	Almost Certain	Likely	Possible	Rare
Catastrophic				
Critical		RSK-THR-3	RSK-THR2 →	RSK-THR-1, RSK-THR-4
Marginal				
Negligible				

12.6.2. RAS Analysis

The reliability of the thermal subsystem is mostly governed by the technology readiness level of its hardware. The coatings used are at TRL 9 and is often used in most missions, which prove to be successful. The limiting factor for the coating can only come from a design flaw and degradation. However, during the design, margins in the allowable temperatures have been allocated. Therefore, the reliability of the design of the coating shall be increased. In terms of degradation, as mentioned in section 12.2, on top of the paint, the spacecraft will be coated with transparent coating. This coating shall protect the spacecraft against atomic oxygen thus also hindering the degradation of the coating. The radiator is also a staple in many spacecraft missions. Its behaviour and performance have been well studied. Thus it also has high reliability. Similarly, the heat pipes are also well developed thermal hardware. However, it does have a lower TRL for applications in small satellites albeit still being matured.

The safety of the thermal subsystem can be addressed with regards to the manufacturing procedure. The white paint chosen, Chemglaze A276, contains aliphatic isocyanate monomer. Therefore, application must be done in properly ventilated areas with the proper respiratory protection.

12.7. Cost Analysis

The cost of the thermal subsystem has been estimated parametrically using the equations presented in section 11.7. This cost is estimated for the entire thermal control subsystem. The surface finish, radiators and heat pipes are already accounted for.

Table 12.10: Cost of thermal hardware

Component	RDT&E Cost [2019€]	Component Cost [2019€]	Total Cost [2019€]	Estimate Method-ology	Estimate Accuracy	Technical Risk	Notes
Thermal hardware	604,308.35	118,736.79	723,045.14	Parametric	Medium	Low	[31]

13. Command & Data Handling

The main functions of Command & Data Handling Subsystem are internal communications between the different subsystems and on-board operations. These tasks are undertaken mainly by the OBC. In the following sections, both the C&DH functionalities and OBC design are described. The subsystem main requirements are discussed in section 13.1. In light of these constraints, the approach to the design follows in section 13.2. The system performance and its architecture are illustrated in section 13.3. The design is verified and validated in section 13.4. Analysis of the systems' risks and its variables sensitivity are described in section 13.6 and section 13.5. Finally, an overview of the communications cost is provided in section 13.7.

13.1. Functions & Requirements

The functions of C&DH are vital for the satellite's operations and mainly are performing decision making, commanding actions, handling data, both from payload and on-board sensors, tracking time and acting as a memory [158]. RAMSES' C&DH main requirements are listed in chapter 13. Mind that these are strictly related to the On Board Computer (OBC) requirements.

Table 13.1: CDH requirements overview

ID	Requirement	Met [✓/✗]	Section
C&DH-01	The data handling subsystem shall support continuous uplink and downlink.	✓	subsection 13.2.1 and chapter 6
C&DH-002	The data handling subsystem shall support at least 400 KIPS (handling speed/throughput).	✓	section 13.3
C&DH-003	The command and data handling subsystem shall be capable of sustaining the maximum possible data rate from the payload (24.2 Mbps)	✓	section 13.3 and chapter 6
C&DH-003	The OBC shall have a file storage of at least 64 Gb.	✓	section 13.3
C&DH-004	The OBC shall be provided with radiation shielding.	✓	section 13.6
C&DH-005	The OBC shall provide enough interfaces to have a federated bus hardware.	✓	section 13.3

13.2. Methodology

The approach to the design of C&DH subsystem encompasses both the investigation of the general key characteristics and the system components.

13.2.1. C&DH Key Features

The key characteristics of the C&DH subsystem for the present design can be categorised in the following way: memory size and handling speed.

Memory Size

The required memory on board can be retrieved from the information given in Table 6.2 about imaging payload data rate. As discussed in chapter 6, the downlink of payload data has to be continuous; nonetheless the downlink rate is smaller than the number of bits the payload generates each second. The reason for this lies in the limited amount of data that can be transmitted in Ka-band, though the latter offers one of the highest frequencies available from ITU.

The housekeeping data is continuously sent once its processing in the OBC had been concluded: 10 kbps are extremely small compared with the images data rate, therefore issues with transmission's continu-

ity do not arise. As far as the payload data is concerned, during the time the camera is operative (17.5% of the orbital period) the images are immediately processed and compressed (the hardware components involved are visible in Figure 6.3); parts of it is downlinked, the rest is temporarily stored. The storage receives the data after being compressed (for CR see section 6.2). Moreover, although the camera is provided with three sensors (red, green, blue), the processed images would be a high resolution colour image: one sensor's pixels from each frame are combined with the other sensors' respective pixels such that the processed image would account for the same number of pixels generated from a single sensor. In Figure 6.3, it is possible to see that while pictures are taken, 67.2 Mbps enter the flash module. By multiplying this data rate with the amount of time allocated for payload operations, the storage needed results 62.4 Gb. As the storage size is expressed in Bytes (1 B = 8 b), it amounts to 7.8 GB.

Handling speed

The handling or processing speed, also referred to as throughput, can be estimated by defining typical thousands instruction per second (KIPS). This is done for each of the on-board functions, by confronting them with typical values from literature [17, 31]. Different margins have been taken into account for varying complexity of RAMSES subsystems, when comparing with typical throughput values. The RAMSES on-board functionalities are listed with the respective KIPS in Figure 13.1. The total amount of instruction per second adds up to 936 KIPS, including a safety margin of 1.5. In Figure 13.1, each coloured block represents a

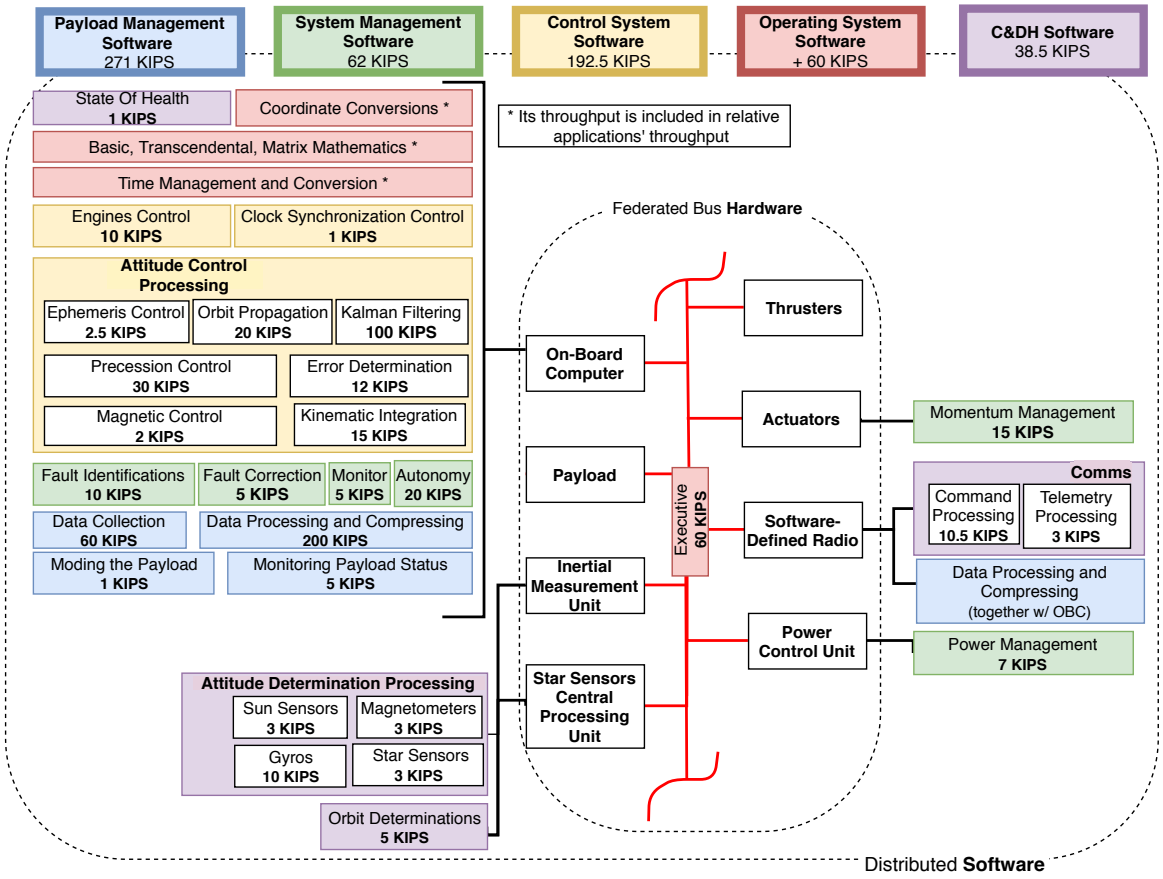

Figure 13.1: Hardware and Software block diagram

Computer Software Component (CSC) corresponding to all functions that take place on board of RAMSES. The colours groups separate the CSC in 5 distinguishable software groups: payload management, system management, control system, operating system and C&DH, specifically. Moreover, from Figure 13.1 the hardware component responsible for a certain CSC is visible via the connecting black lines. The red links, on the other hand, represent the internal structure of the federated bus hardware. It should be noted that all of the on-board hardware units share a common data bus. The choice of this architecture lies in its high level of reliability: even though a specific physical and electrical interface must be installed for each on-board component, the deterministic nature of the data transmission allows for a reduction in test and trouble shooting time [31].

13.3. Architecture & Performance

An overview of the C&DH performance is provided in Figure 13.2.

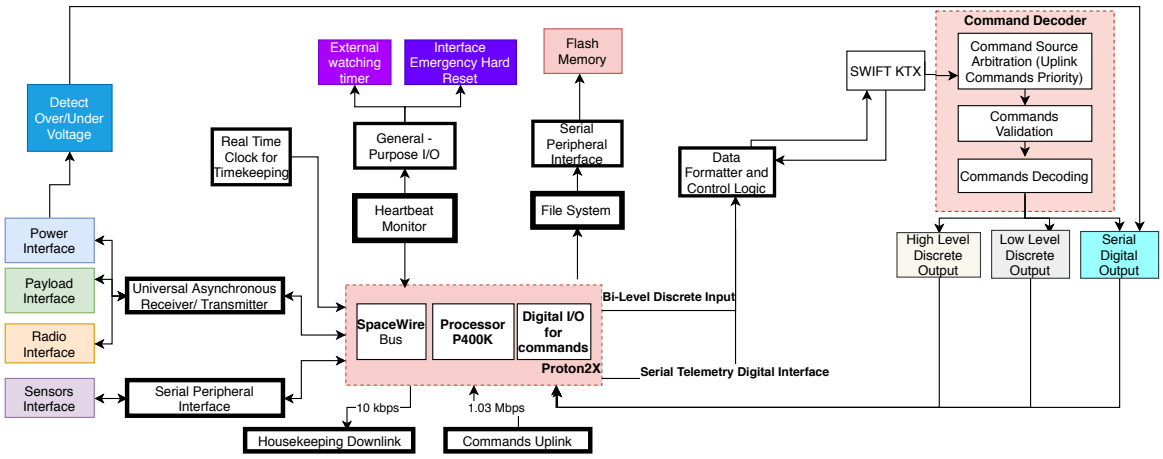

Figure 13.2: Command and Data Handling block diagram

The crucial constraint about reliability drives the design choices toward COTS items. Although, strictly speaking, C&DH has been allocated a specific software (see Figure 13.1), in theory all the other CSC are still related to commands and data to be handled; from the hardware point of view, OBC, IMU, Star Sensors CPU, PCU, SDR and actuators are, to different extent, involved. IMU, Star sensors and actuators are discussed in chapter 10, PCU in chapter 8 and SDR in chapter 6 (SWIFT KTX).

Starting from the foregoing memory size and the throughput estimation, a modular and customizable design has been selected: Proton2X-Box by SpaceMicro[159]. An Aluminium 6061-T651, high strength and radiation shielding frame and caps accommodate the "slices"[159] required for RAMSES. Three double-sided wide Print Circuit Boards (PCB) have been selected and their respective block diagrams are shown in Figure 13.3,13.4,13.5. Additionally, in Figure 13.1, the hardware configuration selected necessitates a common bus that can be shared by the entire system, namely, in this case, High Speed Parallel Bus and PCI 104S bus, visible in each of the OBC block diagrams. The colour allocation for each bus and their distribution over the three diagrams indicates the federated nature of the bus hardware.

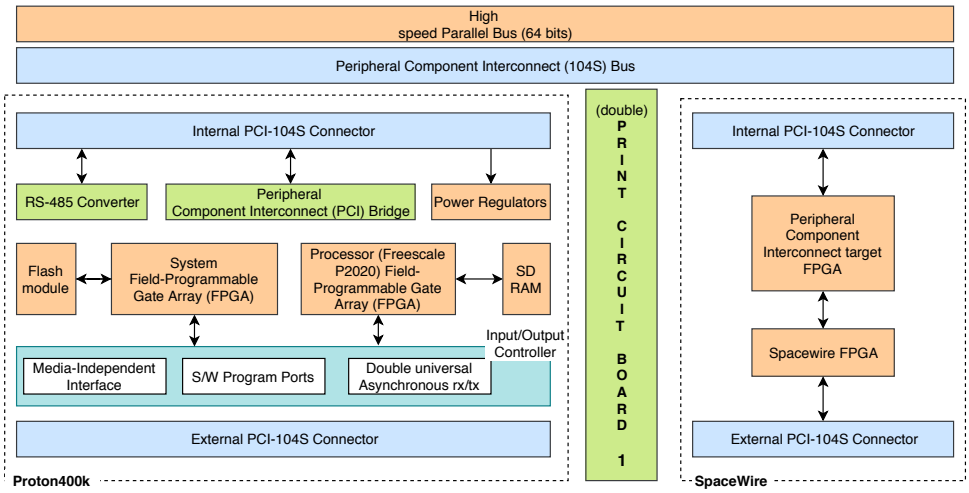

Figure 13.3: Hardware block diagram of the OBC's first slice: the processor P400k and SpaceWire [159]

The first slice, schematised in Figure 13.3, comprises the main processor (Proton400K) and the SpaceWire interface. The processor can handle $5.76 \cdot 10^9$ IPS which is way above the throughput estimated in section 13.2. Moreover, there is a double universal asynchronous transceiver whose involvement i the C&DH is shown in Figure 13.2. The operating system can be chosen to be Linux, which is free. On top of this, SpaceWire provides the interface for SWIFT KTX and has three ports for communications. The SD RAM is used for short storage of housekeeping in the processing-downlinking phase. The second slice, Figure 13.4,

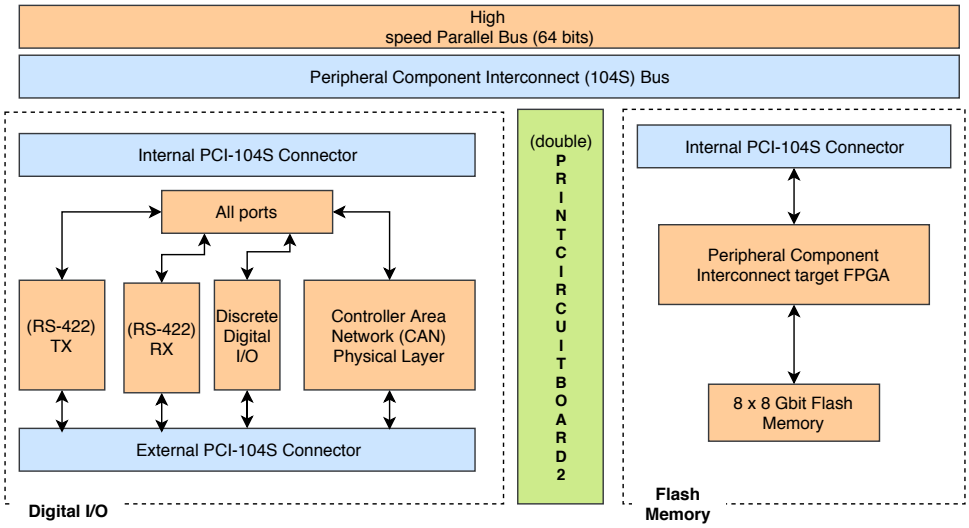

Figure 13.4: Hardware block diagram of the customised OBC: second slice with the digital input/output and the flash memory [159]

consists in the Digital I/O card and, above all, the flash memory. The latter has 64 Gb of storage which is slightly more than needed. Extra storage is also available in the processor and, if even more storage is needed, the flash memory can be extended up to 256 Gb. This might be the case when a customer requires a video from the imaging payload. Therefore, the number of IPS and the storage required are augmented. Having chosen a federated bus hardware, ports for interconnections are needed to link all hardware components: these are visible in the Digital I/O slice Figure 13.4. Lastly, the power supply and power switch

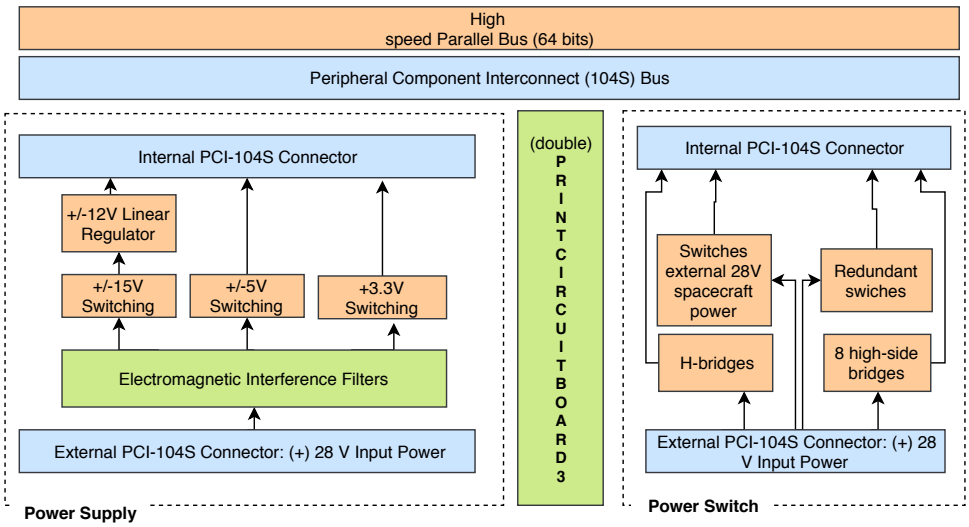

Figure 13.5: Hardware block diagram of the customised OBC: third slice with power supply and switches [159]

constitute the third slice of the OBC (see Figure 13.5. This is directly linked to the PCU and collaborates in distributing the power over the different subsystems. The functions undertaken by this slide are explicitly mentioned in the diagram. Additionally, from Figure 8.2 it is evident the shared nature of the hardware: a main 28 V bus is mentioned which, hereby, interfaces with the third slide of the OBC. The non-uniformity of voltages needed by the different systems requires all the switches visible in Figure 13.5.

The three PCBs are integrated in a 22.48 by 17.15 by 5.72 cm suite, with a total mass of 1.1 kg. It contains radiation hardened electronics and has a TRL of 9; it can be utilised for C&DH, payload control electronics, power allocation, sensor/data processing and transmitting. In spite of all of this, for redundancy, and considering the minute mass, a second unit is brought on board.

13.4. Verification & Validation

The approach for the design of C&DH described so far is fairly straightforward. The verification has only been performed for the memory size computations. Due to the ease of the operations undertaken, an analytical check is deemed sufficient. The throughput values have been validated, as mentioned already, with literature data [17]. Finally, the OBC has been verified, validated and used already. As it has a TRL of 9, no verification and validation are done thereof.

13.5. Sensitivity Analysis

The use of COTS OBC makes an extensive sensitivity study superfluous. It is only worth noticing that an increase in data rate and required memory storage would not require a redesign of the system: as mentioned in section 13.3, the memory size can be increased up to 256 Gb and 3 ports that can sustain 200 Mbps are present in SpaceWire. If this is not enough, RAMSES has already a second equal OBC for extreme redundancy that might be used for operation, if need be. Finally, even though an augment in IPS is experienced, the standard MIPS that the processor can handle is many orders of magnitude higher than the expected.

13.6. Risk & RAS Analysis

Since the architecture is mainly constituted by an OBC with TRL 9, it is possible to define its risk as low. The Proton2X failure is rare, yet, catastrophic. To account for this, a redundant unit is installed on board.

Commercial-off-the-shelf (COTS) processing components are typically used for mission lifetimes of less than one year [58], though the company Space Macro has looked into radiation hardened versions [58]. Since this mission is designed for a 10 years mission in VLEO, the use of radiation hardened processing components, or at least radiation tolerant components, is required. Also, in order to shield the electronics from magnetic field, and to help with radiation shielding, these electronics should be enclosed in a metal casing [160]. Proton2X complies with all of these requirements: its box is configurable and provides conductive cooling, high strength and radiation shielding. In addition to the high reliability of the unit, its performance availability is also guaranteed by the exceptional specifications of the component. On top of this, the selection of a federated bus hardware system allows for a level of independence of each interface (both within and outside the OBC), such that a failure or simply issues in one component would not delay or compromise the performance of the entire remaining architecture.

As discussed for SWIFT KTX in section 6.6, the OBC does not represent a major danger. The product is delivered in its entirety and personnel would receive clear, verified instruction on how to handle and assemble the component to the integrated system. Furthermore, the OBC is made out of aluminium that does not represent a toxic material for the personnel. Furthermore, as far as the environment is concerned, the Proton2X "suite" is inside the satellite, therefore its single failure could not directly generate by itself debris and endanger the external environment. Lastly, the spacecraft's safety might be severely compromised in case of the OBC failure nonetheless, the high reliability of the component makes this possibility highly unlikely.

13.7. Cost Analysis

The cost analysis mainly regards the price of the OBC. By comparing costs of similar missions' On-Board Computer the price has been estimated to be 4500 € each unit (two are installed for redundancy)[1].

[1] `https://www.cubesatshop.com/product/isis-on-board-computer/` [cited on 21 June 2019]

14. Integration and Development

Integration is the last stage of the spacecraft life cycle before it enters the operational phase to serve its purpose. In the following chapter, the requirements and functions of integration will be given first in section 14.1, followed by the approach to integration in section 14.2. The final system layout and the design budgets will be described in section 14.3. The production plan is outlined in section 14.4, followed by a brief overview of the project design and development logic in section 14.5 and a description of operations and logistics in section 14.6. Finally, some system integration risks are given in section 14.7.

14.1. Requirements & Functions

The main function of system integration is the consideration and design of the interfaces between all subsystems and between subsystems and the environment, ultimately leading to the overall system layout. In addition to that, the planning of testing activities required for product verification and validation form an essential part of integration.

Table 14.1: Requirements on system integration

ID	Requirement	Met [✓/✗]	Section
INT-001	The system shall integrate all subsystems and their respective components.	✓	section 14.3
INT-002	The system shall integrate the thruster with a resulting disturbance torque below 1e-4 Nm.	✓	subsection 14.2.2
INT-003	The system main body shall have a maximum longitudinal centre of gravity location of maximum 1.6 m from the front face.	✓	subsection 14.2.2
INT-004	The system shall integrate each sun sensor on a different body panel.	✓	section 14.3
INT-005	The system shall integrate the star sensors such that they are oriented 25 deg off of nadir and 30 deg off of sun pointing when used.	✓	section 14.3
INT-006	The system shall integrate the magnetorquers in an orthogonal configuration.	✓	section 14.3

14.2. Methodology

This section describes the methodology used to perform the subsystem integration. The system interfaces, its balance and interference will be discussed

14.2.1. Interfaces

The internal and external interfaces of the spacecraft can be distinguished into the following categories: mechanical, thermal, electrical, propellant and data [161]. The thermal interfaces are described in detail in chapter 12, the electrical interfaces in chapter 8, the propellant interfaces in chapter 7 and the data interfaces in chapter 6. The detailed design of the mechanical interfaces was deemed outside of the scope of the project, thus only some general considerations were taken. The following subsection will describe system level insights that impacted the final configuration of the spacecraft.

Mechanical: Mechanical interfaces serve to maintain the structural integrity of the spacecraft throughout the pre-launch, launch and operational phase of the mission. As described in chapter 11, erosion due to atomic oxygen is a critical risk for the spacecraft structure and components. While the main structure can be protected using an appropriate coating, not every component is compatible with it. It is thus advised to

make practically air-tight mechanical interfaces such that indirect attacks are avoided. Another consideration is the reversibility of main assembly interfaces, such that issues discovered during testing can easily be addressed. Note that, depending on the materials used, any mechanical interface can be an (unwanted) thermal or electrical interface.

Thermal: The function of thermal interfaces is to transmit the right amount of heat between components, to ensure acceptable maximum and minimum temperatures for all components under the constraint of the operating environment. Thermal interfaces pose a special case, as theoretically an interface exists between two components as soon as there is a direct line of sight between them. To achieve a comprehensive analysis, the components were grouped in thermal nodes, and only interactions between nodes and with the environment were considered. The fins were treated as thermally decoupled from the rest of the system. From a thermal control point of view, the top body surface is unfavourable for mounting components due to two reasons: As it is oriented towards the sun it reaches higher than average temperatures which can damage the attached components. Resolving this issue by putting an insulation layer between the component and the top surface will increase the temperature of the top panel even more, as less area is available to radiate heat away.

Electrical: All components that consume power naturally require an electrical interface. Apart from that, there are many electrical interfaces within the power subsystem itself. Each of these interfaces transmits power under different conditions, and the design of electrical interfaces forms an essential part of the power subsystem. From a systems point of view, the location of the PCUs can be optimised with respect to the required cabling and a sufficient area for solar arrays needs to be provided. It was also decided to use a dedicated PCU for the engine, the main reasons being the vastly different power needs and system reliability.

Propellant: Propellant interfaces can stem from both the propulsion subsystem and the ADCS. RAMSES does not store any propellant on-board and does not perform propellant flow control, which means that there are significantly fewer interfaces to consider. Nevertheless, the propellant feed system is largely unexplored and will be the first of its kind, meaning a lot of the component and interface performance is based on estimations at this point. Regarding integration, an important aspect is that the engine thrust vector shall be aligned with the centre of gravity. As any bends in the propellant feed line are disadvantageous to mass flow, this implies that the propellant feed line axis needs to coincide with the centre of gravity as well.

Data: The spacecraft not only collects data with its payload and then transmits it, but also uses data internally to maintain operations. To ensure that this is done in a reliable way, the data interfaces of the system need to be properly engineered. The on-board computer is the central element of the data handling activities and shall thus be positioned close to the payload, sensors and communication system.

14.2.2. Balance

Due to the unusually high drag forces, the relative position of centre of gravity and centre of pressure is of great importance to the design. If the spacecraft is not carefully trimmed, a continuous aerodynamic disturbance torque will need to be counteracted. This would increase the power consumption of the magnetorquers or lead to a different equilibrium attitude of RAMSES, unavoidably leading to a higher total drag.

The centre of gravity location needs to be controlled along all three axes of the body fixed coordinate frame: along x (longitudinal), along y (horizontal) and along z (vertical). The required horizontal and vertical location follows from the main body and fin geometry. When the spacecraft is perfectly aligned with the flow, the drag force on each component will be proportional to its cross-sectional area. Therefore, the horizontal and vertical position of the centre of gravity can be derived from the centre of area of the cross-section. As the external geometry of the satellite is symmetric about the xz-plane, the horizontal centre of area is in the centre. The vertical position can simply be obtained by taking a weighted average as shown in Equation 14.1. Note that the part of the fins which is parallel to the sides of the spacecraft is behind the main body and thus not taken into account. The bottom side of the spacecraft serves as the datum feature for this calculation.

$$z_{CoA} = \frac{A_{Trapezoid} \cdot z_{Trapezoid} + A_{Fin,horizontal} \cdot z_{Fin,horizontal} + A_{Fin,lip} \cdot z_{Fin,lip}}{A_{Trapezoid} + A_{Fin,horizontal} + A_{Fin,lip}} = 295 \text{ mm} \tag{14.1}$$

Longitudinally, the centre of pressure should generally be aft of the centre of gravity to guarantee stabil-

ity. This however is not feasible for the flight situation where the spacecraft is perfectly aligned with the flow, as most of the drag acts at the collimator while all other subsystems are integrated aft of the collimator. To mitigate this, it was decided to size the fins such that a small misalignment will move the centre of pressure behind the centre of gravity. Therefore, the longitudinal centre of gravity location directly drives the fin's geometry, with a centre of gravity further forward resulting in smaller fins.

The centre of gravity of the spacecraft was determined and trimmed using CATIA. To do this in an accurate and robust way, all components need to be modelled and integrated. While no masses were neglected, assumptions were taken on the centre of gravity locations of the cabling, fasteners, mechanisms and the launcher adaptor. This was necessary as the detailed allocation of these masses was out of scope of the project. Concerning cabling and fasteners, it is assumed that the mass distribution is driven by the distribution of the other components. The 5 kg for cabling and 3.5 kg for fasteners were thus modelled as point masses, vertically and horizontally centred within the trapezoid. It is generally favourable to align the launcher adaptor with the centre of gravity of the spacecraft, thus it is assumed that the mass of the adaptor is laterally coincidental with the centre of gravity and longitudinally at the end of the spacecraft.

By carefully arranging the components, it was demonstrated that it is possible to steer the centre of gravity of the spacecraft with great accuracy. The final misalignment was 0.5 mm in z and 0.9 mm in y, as can be seen in Figure 14.1. Both are significantly smaller than the estimated uncertainty in the process. Note that not only the distributed masses of the cables and fasteners introduce uncertainty, but also the fact that the component-internal location of its centre of gravity is not considered. The compatibility with requirement INT-003 can be verified by calculating the resulting disturbance according to Equation 14.2:

$$T = \sqrt{0.005^2 + 0.009^2} * 0.0058 = 5.97e-5 \text{ Nm} \tag{14.2}$$

While the requirement is met with a sufficient margin, the calculation also shows that even sub-millimetre misalignments can lead to significant disturbance torques which might impose a challenge on the ADCS. It is thus strongly encouraged to consider the centre of gravity steering early in the design cycle, in order to obtain detailed component specifications and plan thorough testing activities. It is also recommended to designate several components as trimming masses, and not fixing them permanently until the last wire and screw are installed.

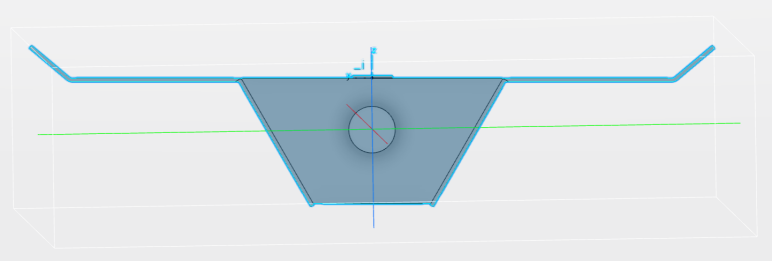

Figure 14.1: Final cross-sectional centre of gravity location of RAMSES, coincidental with the centre of pressure

14.2.3. Interference

One concern for system integration is interference between components aboard the spacecraft. Above all, the magnetorquers and the engine will induce strong electromagnetic fields, however the power control units can also contribute. Interference is especially critical for the on-board computer and the magnetometers, as it can lead to bit errors and false measurements. To mitigate this, the power control units and the OBCs will be shielded with a metal casing which serves as a faraday cage and should shield against most of the radiation.

14.3. System Layout

Driven by the integration requirements and the additional considerations as outlined above, the final spacecraft configuration was determined and will be presented subsequently. Most of the components are attached to one of the two side panels, with the zenith panel taking the star sensors and their associated electronics, one star sensor, the general power control unit, two magnetometers, the main on-board computer and the batteries. The nadir panel accommodates the payload, the ion propulsion power control unit,

two inertial measurement units, a sun sensor and a magnetorquer which needs to be integrated vertically and is therefore attached to the payload casing. The top panel carries the remaining two magnetorquers, the two antennas and a sun sensor. The bottom panel only carries the backup on-board computer and a sun sensor.

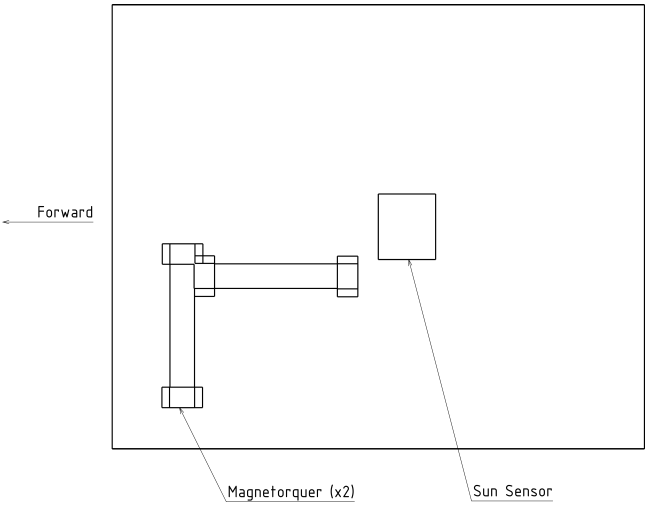

Figure 14.2: Layout of the top panel, sub-assembly E

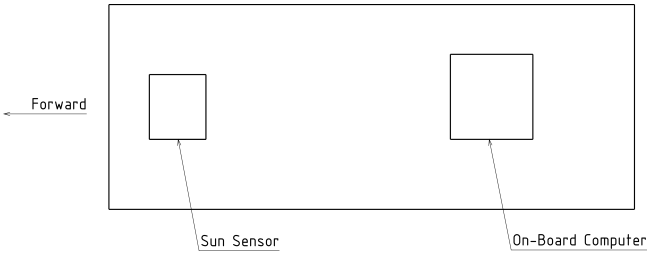

Figure 14.3: Layout of the bottom panel, sub-assembly C

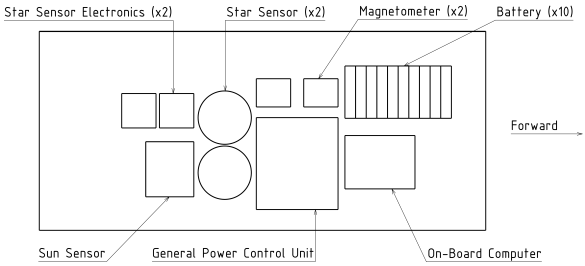

Figure 14.4: Layout of the zenith (left) panel, sub-assembly B

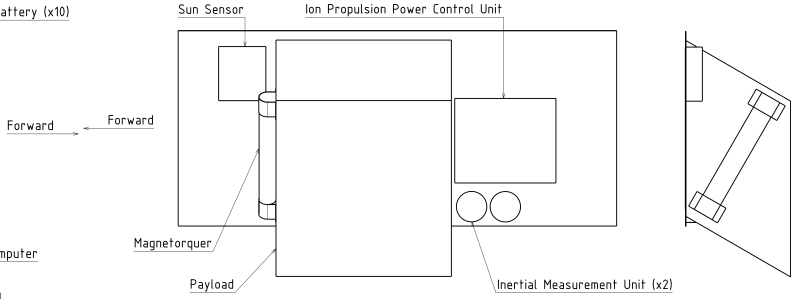

Figure 14.5: Layout of the nadir (right) panel, sub-assembly D

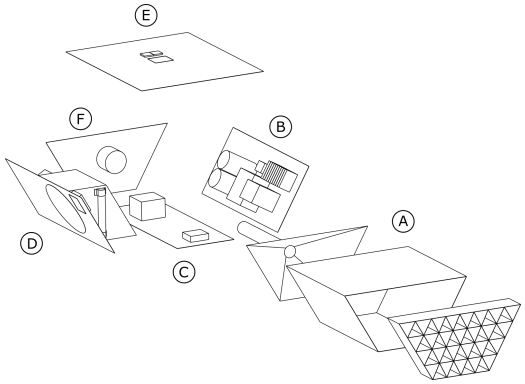

Figure 14.6: Exploded view of RAMSES excluding fins, radiators and solar arrays

14.3.1. Design Budgets

To achieve the best possible design, valuable resources like mass and power need to be appropriately allocated to the subsystems. For a detailed power budget the reader is referred to Table 8.1, the mass budget can be found in Table 14.2. In the latter table, two contingency values are provided. Firstly, the 15.5% mass increase to arrive at 150 kg total mass was uniformly applied to all subsystems, this is labelled 'Uniform Contingency'. Secondly, extra mass was primarily allocated to subsystems with high uncertainty such that future developments are less constrained. This approach led to higher than average contingencies for propulsion,

intake, fins and communication. Power and payload have lower than average contingency, as the former is a well established subsystem and the latter already includes contingency in the 30 kg mass estimation (see section 9.3).

Table 14.2: Final RAMSES mass budgets and contingencies

Subsystem	Mass [kg]	Uniform Contingency [kg]	Custom Contingency [kg]
Communication	2.55	0.40	1
Propulsion	1.8	0.28	1
Power	35.23	5.48	2
Payload	30	4.66	3
ADCS	11.94	1.86	1.5
Structures	21.66	3.37	2.18
Thermal	4.6	0.72	0.5
Command & Data Handling	2.2	0.34	0.5
Intake	8.68	1.35	5
Fins	11.16	1.73	3.5
Total	129.82	20.18	20.18

14.4. Production Plan

The layout of RAMSES allows for simple production with several independent sub-assemblies that facilitate integration and testing.

14.4.1. Manufacturing

Most of the flight hardware of the spacecraft is bought directly from private entities, meaning the manufacturing of these components does not have to be considered. However, the delivery times of space-grade components can be significant and can delay the production phase if not accounted for [17].

Nevertheless, there are several parts of the assembly that will be custom designed and manufactured. The most important ones are the intake grid, the collimator, the main structure, the fins and the imaging payload. While the material of the main structure was chosen carefully, no material study was performed for the intake grid and collimator. Both of these parts are non-essential to the structural integrity of the satellite and will be covered in an erosion-resistant coating. Thus it was decided to use the same material as for the trapezoid skin, the carbon fiber composite.

The intake grid can be manufactured from several 1 mm thick, 200 mm wide strips of carbon composite with varying lengths. It is designed to a high degree of symmetry such that several strips share the same geometry. By cutting out 1 mm wide, 100 mm long slits at the junctions of the strips, they can simply be slid into each other and then bonded to form the grid. As these joints do not carry significant loads, this method is deemed acceptable and simplifies the manufacturing of the grid.

In the current design stage, the collimator consists of four double-curved panels, which form a funnel-like interface from the trapezoidal intake to the smaller circular propellant feed line. While the side exposed to the flow should have a good surface finish, the other side of the panels is oriented towards the inside of the spacecraft and does not serve as a mounting point for other components. Thus these four panels can be manufactured using resin transfer moulding or vacuum assisted resin transfer moulding, which is relatively cheap even for double curved panels.

The main structure of RAMSES is composed of several flat, 1.35 mm thick panels of varying size. These panels can be provided by an external contractor, however the joints between the panels are crucial and need to be designed in detail. They should allow for easy disassembly to facilitate troubleshooting during the testing phase. The first 2 cm off of each edge are allocated to this joint and will be free of solar arrays or

other components.

The fins represent another part which could be manufactured to specification by an external contractor - sandwich panels are commonly used in aerospace applications. Nevertheless, the installation of cabling, mechanisms and solar arrays leads to a relatively complex assembly which might be easier to create in-house.

Due to the space constraints, regular off-the-shelf imaging payloads are not compatible to the system. The optics need to be developed and manufactured to strict specifications. To avoid misalignments, the payload should be constructed comparable to an optical bench, with low tolerances and a high stiffness.

14.4.2. Assembly

RAMSES is divided into eight major sub-assemblies to facilitate the installation of hardware and testing of individual components. These assemblies will be briefly discussed below.

As most components are mounted to one of the four skin panels, the general approach to assembly is to build each panel separately before integrating all four panels and the other two sub-assemblies into the final trapezoidal shape. With this approach, the panels can be prepared on a simple workbench and any work in confined spaces is avoided. This is beneficial to both the well-being of personnel as well as the quality of assembly. As shown in Figure 14.6, the skin panels are sub-assemblies B, C, D and E. The intake assembly, comprising the grid, thermolizer, collimator and feed line is denoted sub-assembly A. The rear bulkhead, including the engine and the payload adaptor forms sub-assembly F. Not shown in the figure is the assembly of the fins, which consists of two structural panels each and also approximately 2.5 m^2 of solar arrays. The left fin is sub-assembly G and the mirror version on the right side is sub-assembly H.

14.4.3. Integration

The integration phase of the production cycle is closely linked to testing and system validation. Following the general approach to perform verification and validation on all levels of the assembly, components are tested many times before flight certification is achieved. Figure 14.7 schematically shows these activities as proposed for RAMSES. In alignment with the approach to assembly, the first step of integration is dedicated to the separate testing of the four panels, followed by a comprehensive test. This test is performed to ensure full functionality after each test and consists of a number of predefined subroutines run by the subsystems. The spacecraft is carefully observed throughout and any unexpected behaviour is recorded and investigated. [17] Only after fundamental testing is done on a vehicle level the environmental testing phase begins, in which the spacecraft is subjected to a number of simulated launch and space environments.

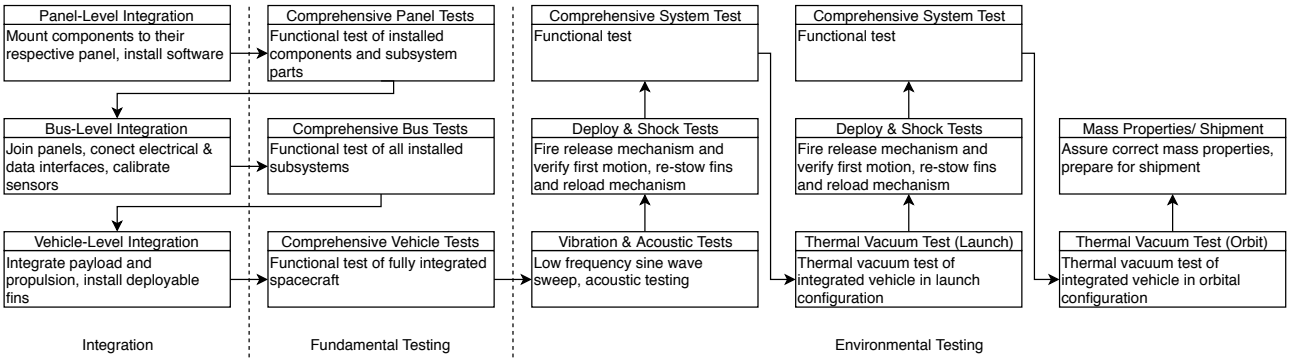

Figure 14.7: Outline of the proposed integration and testing procedures.

14.5. Project Design & Development Logic

In Figure 14.8 an outline of the activities to be performed after completion of this report is presented. A more detailed description is given in Figure 14.9. The Gantt chart shows the scheduled activities after the completion of the DSE. As the DSE comprises the concept and technology development phase, the design refinement in the chart includes the critical review and detailed design phases.

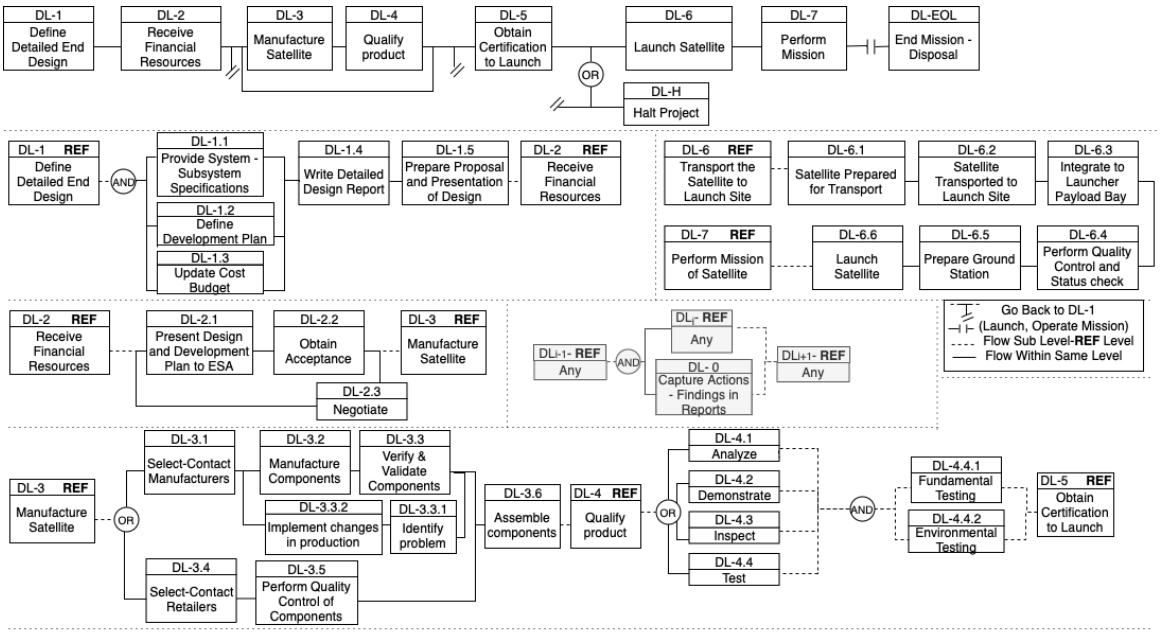

Figure 14.8: Design and development logic

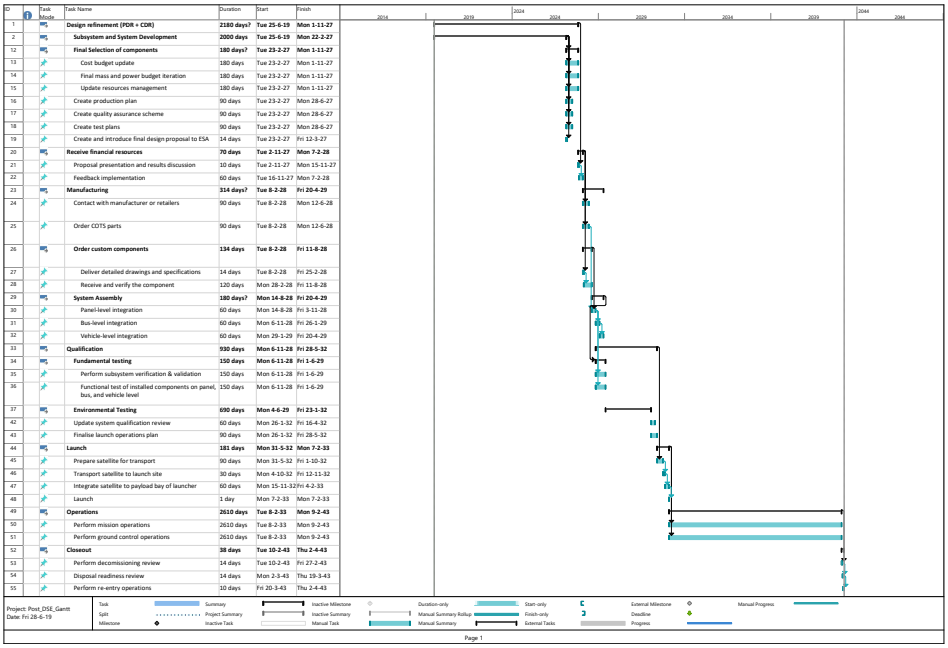

Figure 14.9: Gantt chart for post-DSE activity

14.6. Operations and Logistics

Operations and logistics of a spacecraft concern the functions to be performed during operation and the link between the payload data generation and the customer receiving the data. The operational aspects were already covered in the functional flow diagram in Figure 2.2. The logistics diagram is shown in Figure 14.10. It shows the (simplified) relation between the spacecraft, ground control and customer. In addition, some main processes that are performed internally are also shown in the diagram.

14.6.1. Deployment

As the principal approach of the Structures subsystem was to design for launch and to design for erosion, the mechanisms of the RAMSES were not analysed in detail. These concern the deployment of the fins, which

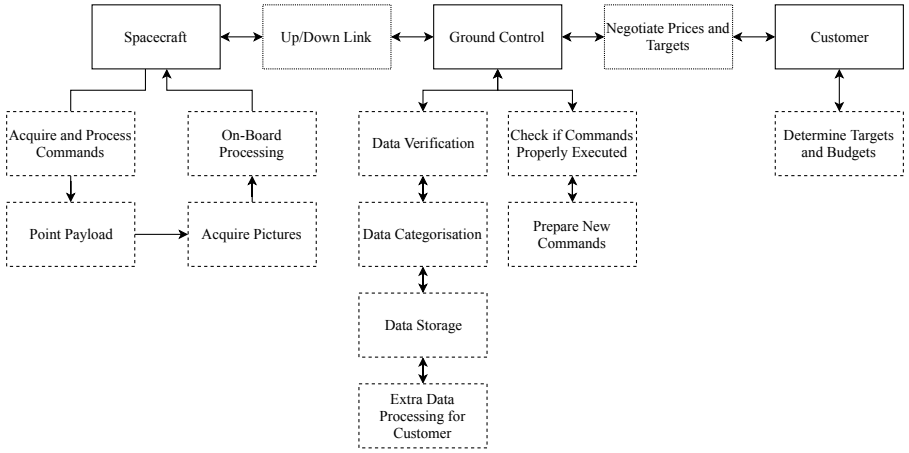

Figure 14.10: Logistics diagram of the payload operation

are stowed on the sides of the main body during launch. The deployment happens in two steps. Firstly, the panels fold backwards over a hinge aligned with the rear side edges of the satellite. Secondly, the horizontal fins fold out over the previously deployed angled parts. The winglets are fixed to the horizontal fin and are not mechanised. Note that the deployment of the left and right fin cannot happen simultaneously, as the horizontal panels would interfere.

14.7. Risks

As for any other part of the design and operation, there are also risks associated with integration.

RSK-INT-1 **Event**: Component is not to specification.
Risk: Any component ordered from an external contractor carries the risk of not fulfilling its specification. This will either necessitate a new component or adjustment work, causing delays either way.
Mitigation: Components which are present in higher numbers (e.g. the sun sensors) or are relatively cheap might be ordered as one too many to mitigate this.

RSK-INT-2 **Event**: Unexpected component interference.
Risk: There are several components on the spacecraft that generate electromagnetic fields when used. If this interference is not accounted for it can impact component performance or falsify data.
Mitigation: Next to the steps that were already taken to minimise and quantify interference, it is advised to evaluate past missions for unexpected interference. Sensors should be calibrated accordingly to account for the disturbances generated on-board.

RSK-INT-3 **Event**: Schedule delays due to component production times.
Risk: Some of the components used in RAMSES have high delivery times and can delay the program significantly if not ordered in time.
Mitigation: Lead times of all components should be evaluated and confirmed by the contractor early in the project development. Other contractors should be considered if the lead times are not compatible with the project schedule.

RSK-INT-4 **Event**: Spacecraft not balanced correctly.
Risk: If the spacecraft is not trimmed properly a continuous aerodynamic disturbance torque will be present. This leads to a sub-optimal performance when in orbit, endangering the lifetime requirement.
Mitigation: Detailed specification of centre of gravity locations of components and sub-assemblies should be provided such that the balance can be monitored throughout integration. Additionally a number of components should be identified that serve as trimming masses and will be mounted last.

RSK-INT-5 **Event**: Damaging a coating during production.
Risk: Due to the thinness of the applied anti-erosion coating it is very easy to scratch. Having defects in the coating will expose materials to atomic oxygen that cannot withstand the erosion for extended periods of time.
Mitigation: It is recommended to apply the coatings as late as possible during the integration phase. This will decrease the chance of defects significantly. In addition to that, a final surface coating in-

spection is recommended as it is possible to repair the coating when damage is detected in time.

Table 14.3: Risk map showing the severity and likelihood of the risks before and after mitigation

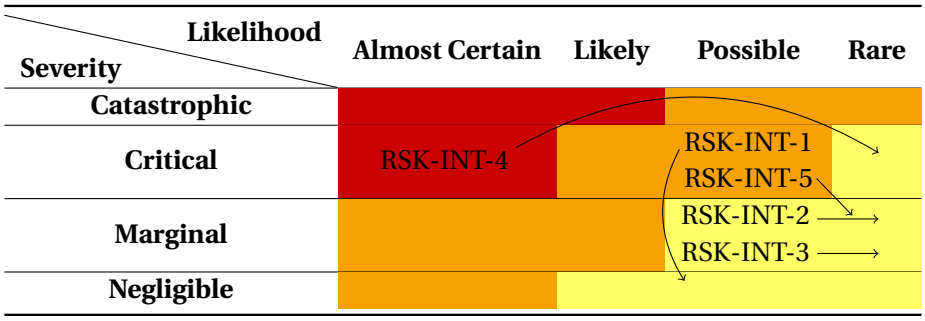

15. Sustainability Development Strategy

As is the case for any newly developed design, the sustainability of the presented design plays an important role. Due to the lack of propellant RAMSES has significant potential in terms of sustainability. In this chapter the performance of the current design is assessed first in section 15.1. Moreover, potential improvements in terms of sustainability are presented in section 15.2.

15.1. Assessment current design

To fully assess the proposed design of RAMSES, the impact can be assessed in two parts. Firstly, the direct impact of the design is presented using a MET matrix [162]. However, the proposed propulsion system allows for a different approach to space missions. Therefore, some potential impacts of the design on the industry are presented second.

15.1.1. Direct impact

In order to judge the direct impact on the environment, a MET matrix is used [162]. This matrix provides an overview of the materials and energy used throughout the lifetime of the product, as well as the emissions. In Table 15.1, all important impacts on the environment are presented, the most critical ones will be also be discussed in the following.

Table 15.1: MET matrix for RAMSES

Phase	Materials used	Energy used	(Toxic) Emissions
Obtainment of materials and technology	Carbon and epoxy for composites	High energy content materials (CFRP, copper, lithium)	Emisions for gathering lithium [163]
	Copper for the electronics.	Energy for engine testing	Emissions related to energy for engine testing
	Lithium for the batteries [163]		
	Gallium and Arsenide for solar panels[1]		
Production	Auxilary materials for connections, hinges	Energy used for curing composites	Wasted composite material
Distribution (launch)	Materials used in the launcher	Energy required launch	Emissions from the aircraft and rocket used during launch
		Energy required for transport	Emission of transport
Utilisation of the system	-	-	Charged particles
EOL operations	-	-	Disintegration & impact on ground

As much of the structure is made using a carbon fibre composite, the impact of this material is important to assess. The environmental impact of making products with carbon fibre reinforced composites (CFRP)

[1] https://www.ucsusa.org/clean_energy/our-energy-choices/renewable-energy/environmental-impacts-solar-power.html#bf-toc-2 [Cited on 22 June 2019]

is very significant [164]. Moreover, during the production of CFRP parts, much of the used materials is lost [165]. Therefore, the material used for the structure is a significant contributor to the sustainability.

The most significant impact in terms of energy used is expected to be the testing of the engine. As the TRL of the propulsion system is still very low, as discussed in chapter 7, testing will be required before RAMSES can be launched. This testing will require operation of the engine in a vacuum chamber for extended periods of time. The result of this method of testing is that a large amount of energy is required before the engine is operational. Depending on the power source for this energy, the emissions related to testing the engine could also create significant emissions.

The final impact that deserves a separate discussion is the launch of the satellite. As the emissions of launch vehicle can have a significant negative impact on the environment [166], a reduction in these emissions is an important consideration for a sustainable space mission.

15.1.2. Use in industry

Since the proposed propulsion system does not require any propellant, a different approach could be taken to satellite design. The lack of propellant storage, combined with the low operating altitude, would allow for a reduction in mass of spacecraft at launch. This would allow for smaller launchers to be used which could cause a reduction in the emissions related to the launch.

Another aspect of the RAMSES mission that could impact the design of satellites in future is the lifetime. The RAMSES mission is designed for a lifetime of 10 years, which is a relatively long lifetime compared to other satellites in LEO [167] and VLEO [114]. If other missions would also be capable of increasing their lifetime with the propulsion system proposed for RAMES, less launches would be required. This would clearly reduce the total emission produced by the space industry as launches can have a significant negative impact on the environment [166].

15.2. Potential improvements

In this section the areas that could potentially be improved on in terms of sustainability are outlined. An overview of these improvements and the current design performance is presented in Figure 15.1. In this plot, blue is the current design performance and red is the potential design performance. Not all potential improvements are implemented as they would either violate the requirements or be a significant design change that is beyond the scope of this report. The position of a category on the wheel is a qualitative assessment of its performance in terms of sustainability. The best possible performance is located at the outer part of the wheel and the worst in the centre.

15.2.1. Material selection and usage

The first category, material selection, assesses the impact of the materials selected and for example considers the energy needed and emissions produced when the material is gathered. As explained in section 15.1, the CFRP structure has a significant impact on the environment. Therefore, from a sustainability point of view, using a different material would greatly improve the sustainability[2]. An example of an alternative is aluminium. However as shown in section 11.3 the mass of the structure increase significantly when aluminium is used. It was found that this increase was so significant that the mass requirement could no longer be met. Therefore the material could only be changed if the design requirements were changed. The potential for improvement is visualised in Figure 15.1.

In the material usage category, the amount of material is judged. Using more material has a negative impact on the environment. As can be seen in Figure 15.1, the potential for improvement in terms of material usage is a lot more limited. The mass budget is definitely hard to decrease as many decisions already have been made to save mass. Some savings might be possible in the volume, this would allow for an easier transport of the final product. This could provide small savings in emissions. However, the performance in this area is still quite good as the total amount of material used is limited.

15.2.2. Production, distribution

The production branch of the design wheel assesses the amount of emissions and waste created during the production process. As has been discussed in section 3.1, a significant amount of waste is produced during

[2] http://www.welshcomposites.co.uk/downloads/environmental%20webinar.pdf [Cited on 21 June 2019]

CFRP part production. This waste could be captured and partially recycled. Although composites are not as easy or effectively recycled as other materials [168], this would still improve the sustainability of the design significantly.

In the distribution category, the emissions and material lost during launch are considered. For the launch, two options are selected in section 11.3. In terms of sustainability using the LauncherOne [14] launch vehicle improves the performance substantially. This launch vehicle uses an aircraft for the first section of the launch that can be reused after launch. Therefore the materials lost during launch are significantly reduced compared to another launch of similar size. Moreover, when launching two copies of RAMSES with this launcher, the capability of the launcher is closely matched [14]. Therefore, selecting this launch vehicle greatly improves sustainability.

15.2.3. Operations, lifetime and EOL

As seen in Figure 15.1, the potential for improvement for operations, lifetime and EOL is very limited. The operations and EOL branches consider the emissions produced and the materials lost during these phases. The EOL strategy can not be changed as the re-entry will always be uncontrolled due to the low thrust levels. Therefore no recovery of the materials is possible. Using the re-entry simulation from section 11.3 it was found that the temperature did not reach a high enough temperature to produce NO_x [169]. The emissions of CO_2 due to oxidation of the composite could be removed by selecting a different material but these emissions are limited anyways. Operations can also not be improved as currently the only emissions are charged particles coming from the engine. These particles will not have an extremely negative effect as such particles are already present in the environment [170]. Finally, the lifetime of RAMSES is already very long compared to other missions as discussed earlier. Therefore, the potential for improvement here is limited. Finally, the lifetime category simply assesses if the lifetime can be improved and thus if the materials used can be used more effectively. Increasing the lifetime is mainly limited by degradation caused by the extremely hostile environment [117], which will always have to be overcome.

15.2.4. Design changes

Optical imaging is not the only payload type that could benefit from the extremely low orbit RAMSES operates in. Some examples of these payloads are mentioned in chapter 16. If any of these payloads could be incorporated into the proposed design, this would allow for a reduction in the number of launches required. Therefore, the sustainability of the design would be improved. As this would require a very major design change, this strategy is not explored in the current report.

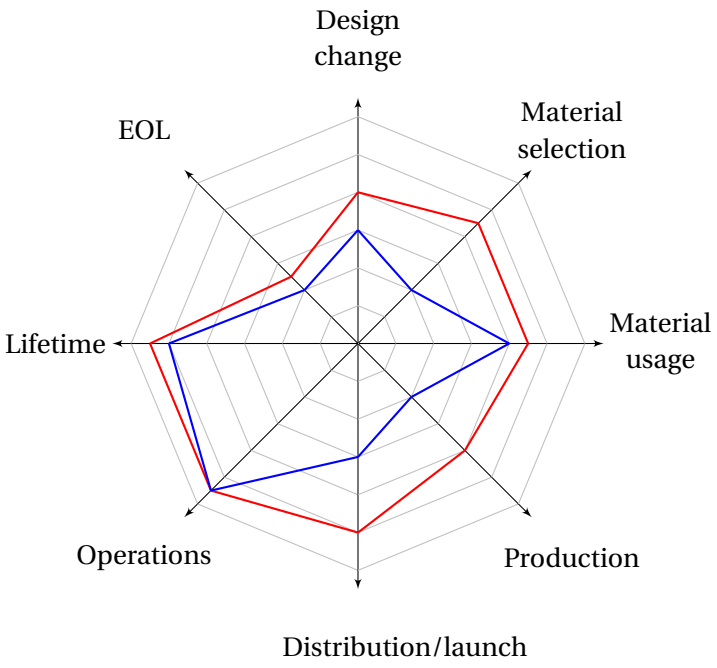

Figure 15.1: Ecodesign strategy wheel

16. Conclusion & Future Considerations

In this report, the design and analysis of a VLEO Earth-observation satellite using air-breathing electrostatic propulsion has been described. Air-breathing propulsion concepts for space applications are more versatile than the mission described in this report. In this chapter, the final conclusion on the RAMSES design is presented and some future considerations are outlined that can be beneficial to or benefit from air-breathing propulsion. Some aspects will require more research to achieve the required performances.

First, the compliance of the design with respect to the requirements is discussed in section 16.1. Areas where future improvements are possible are described in section 16.4. Additionally, some market considerations are described in section 16.5. Lastly, some alternative payload options and applications are mentioned in section 16.6.

16.1. Requirement Compliance Matrix & Feasibility Analysis

The compliance matrix provides an overview of the requirements met by the design, highlighting the original requirements, and, if those are not met, the update to the requirement such that compliance is achieved. To avoid repetitions, the compliance with the requirements was inserted inside requirement tables of the mission, system and subsystem requirements. These last requirements can be found at the beginning of each subsystem chapter. The green tick shows that the requirement is met, and the validation of compliance with the requirement is given in the sections cited next to the check marks. When a requirement is not met, a red cross is placed next to it, and the reason why is explained in the section mentioned.

The feasibility analysis discusses the requirements which are not met and in particular the possibility of improvement, which would allow RAMSES to meet the original requirements in a future design iteration.

For RAMSES, there are three requirements which are not met. These are the reliability requirement REQ-SYS-001, the system TRL requirement REQ-SYS-023 and the camera resolution requirement REQ-MIS-002.

Requirement REQ-SYS-001 is a follow up of REQ-SYS-023. The low TRL of the components used in the design influences the reliability of the system, discussed in section 16.2. Components with a low TRL are chosen in the design because of physical constraints. The design aims to minimise the area exposed to the flow in order to have a thrust ratio higher than 1, with the available air-breathing engine technologies. The camera payload requires a focal length of 2.02 m, and only fits in such a constrained space by a mirroring technique which has been studied but is not flight proven as mentioned in section 9.2. In order to meet the requirement, a lower thrust to drag margin could be considered for a future iteration, allowing for a larger frontal area and more space for the focal length.

As for requirement REQ-MIS-002, a lower spatial resolution of 34 cm × 34 cm was achieved, as explained in section 9.3. This constraint is due to the aperture of the camera, which would require a larger diameter to meet the original requirement, as explained in section 9.2. With a larger aperture, the camera would be able to get the required optical resolution. However, it would also require a larger and heavier spacecraft.

16.2. Reliability

The reliability of the S/C is assessed by looking at the TRL of the components included in the various subsystems. In each subsystem's section, the reliability is discussed as part of the RAMS analysis. The power, attitude determination & control, structures, thermal control, communication and command & data handling subsystems all use conventional architectures and components. For these subsystems, the reliability will be high, as all the components are chosen to comply with the reliability requirement REQ-SYS-001. On the other hand, the propulsion system and payload use non flight proven technology. The reliability of the engine is compromised by the low TRL of the engine and of the collimator, which has a TRL level of 1. The payload has a TRL of approximately 3. It is estimated that the system reliability, whose value is highly affected by these parameters, will therefore not meet the requirement.

16.3. Competitiveness

In chapter 3 the RAMSES satellite was found to be very competitive in terms of resolution and mass. Slightly less performance is achieved in terms of spectral range and the area that is imaged each day, which can be

attributed to the low mass and narrow field of view. The monetary performance is such that the break-even point of the mission is approximately 5 years, with two spacecraft.

16.4. Future Improvements

As mentioned in chapter 7, the propulsion system requires a collimator to redirect the particles into the feed line. Research into this component is still in the early stages. As this is a critical element of the propulsion system, extra research will be needed to verify its working principles and performance.

For the payload, the main future improvement can simplify the difficulties currently experienced in integrating the focal length (see section 9.3). Near future improvements are currently being research that would reduce the pixel size of the chip significantly [8].

For the communication system, especially for satellites that generate large amounts of data, the contact time to ground stations is very limited [11]. For the RAMSES mission, communication via relay satellites was therefore chosen (see chapter 6). For future mission, the availability of ground stations and/or relay satellites with sufficient data rates should be investigated and maintained.

Another area of research that is important for missions like RAMSES is the environmental research of VLEO, especially related to atomic oxygen. Since the detrimental effects of atomic oxygen are so severe and virtually no material is left untouched (see chapter 11), component and/or performance degradation could become the new limitation for mission lifetimes in VLEO.

16.5. Upcoming Markets

Market-wise, the current mission is mainly focused on the defence sector as that is the current largest sector (see chapter 3). The shift towards a more versatile market opens up new opportunities for this mission as well as other missions using air-breathing propulsion.

For the RAMSES mission the new markets lie mostly in the environment monitoring, infrastructure and natural resource markets (chapter 3). One good aspect of the RAMSES mission is its ability to provide data near real-time due to the use of a relay constellation, which is also beneficial for customers outside of the defence market. For more general air-breathing propulsion satellites, the market options are broad and depend on the payload that is taken (see section 16.6).

16.6. Alternative Options

The payload for the RAMSES mission is chosen because of the requirements to design a satellite that makes images in the visible spectrum. The low altitude is beneficial for cameras imaging at other wavelengths as well [11], mainly governed by the diffraction limit ($\Delta\theta h = \frac{1.22 \cdot \lambda \cdot h}{D}$, see chapter 9), reducing the aperture size for higher resolutions. However, the low altitudes that are achievable with air-breathing propulsion are not limited to imaging payloads. Other promising payloads that could be worth investigation are: (1) a communication payload (possibly with a constellation of satellites) [9], (2) LIDAR measurements [10], (3) (synthetic aperture) radar [11], (4) gravity field measurements [10–12], (5) electromagnetic field measurements [10] and (6) direct sensing of the atmosphere (density, chemical composition, etc.) [10]. All these alternative payloads can benefit from the lower altitude and the long mission lifetime.

Another benefit of air-breathing electrostatic propulsion is that it is not limited to Earth's atmosphere [13]. It can potentially be used on other planets with an atmosphere (such as Mars [13]) with similar payloads. Since Mars' atmosphere is significantly thinner than Earth's, the achievable altitudes are even lower, creating potentially more gains. To investigate such applications, the engine and intake systems will need to be tested with different densities and gas mixtures that mimic a non-Earth atmosphere.

References

[1] Adam, F., Aguado, M. V., Cravero, M., *et al.*, *Demonstrator for Air-Breathing Electrostatic Propulsion Earth Observation Satellite*, DSE Midterm Report version MD-1.1, Delft University of Technology, 2019, unpublished.

[2] Tremblay, E. J., Stack, R. A., Morrison, R. L., *et al.*, "Ultrathin Cameras using Annular Folded Optics," *Applied Optics*, vol. 46, no. 4, 2007, pp. 463–471, doi:10.1364/AO.46.000463.

[3] Richards, J. A. and Jia, X., *Remote Sensing Digital Image Analysis: An Introduction*, vol. 4, Springer, Cham, Switzerland, 2013, doi:10.1007/978-3-642-30062-2.

[4] Harnisch, B., Kunkel, B., Deyerler, M., *et al.*, *Ultra-lightweight C/SiC Mirrors and Structures*, Bulletin 95, European Space Agency, 1998.

[5] Mileti, S., Coluzzi, P., and Marchetti, M., "Degradation of Silicon Carbide Reflective Surfaces in the LEO Environment," in *AIP Conference Proceedings of the 9th International Conference: Protection of Materials and Structures from Space Environment*, vol. 1087, , 2008, pp. 67–74, doi:10.1063/1.3076885.

[6] Duo, S., Li, M., Zhu, M., *et al.*, "Resistance of Polyimide/Silica Hybrid Films to Atomic Oxygen Attack," *Surface and Coatings Technology*, vol. 200, no. 24, 2006, pp. 6671–6677, doi:10.1016/j.surfcoat.2005.09.028.

[7] Riley, D., Fuentes, I. P., Parigini, C., *et al.*, ""Design for Demise" Techniques to Reduce Re-Entry Casualty Risk," in *66th International Astronautical Congress*, Jerusalem, Isreal, 2015, pp. 1–9, iAC-15,A6,4,5,x30058.

[8] Beiley, Z. M., Cheung, R., Hanelt, E. F., *et al.*, "Device Design for Global Shutter Operation in a 1.1-um Pixel Sensor and its Application to Near-Infrared Sensing," in *Proceedings of SPIE, Physics and Simulation of Optoelectric Devices XXV*, vol. 10098, San Francisco, CA, USA, 2017, pp. 100981L–1 – 100981L–5, doi:10.1117/12.2253219.

[9] Nofal, M., "Engineering Aspects and Performance Evaluation of a Multi-Service Low Earth Orbit Mobile Satellite Communication System," in *Vehicular Technology Conference and 52nd Vehicular Technology Conference*, Boston, MA, USA, 2000, pp. 1879–1886, doi:10.1109/VETECF.2000.886143.

[10] Di Cara, D., Gonzalez del Amo, J., Santovincenzo, A., *et al.*, "RAM Electric Propulsion for Low Earth Orbit Operation: an ESA study," in *30th International Electric Propulsion Conference*, Florence, Italy, 2007, pp. 1–8, iEPC-2007-162.

[11] Llop, J. V., Roberts, P. C. E., Hao, Z., *et al.*, "Very Low Earth Orbit Mission Concepts for Earth Observation: Benefits and Challenges," in *Reinventing Space Conference*, London, UK, 2014, pp. 1–18, bIS-RS-2014-37.

[12] Rummel, R., Balmino, G., Johannessen, J., *et al.*, "Dedicated Gravity Field Missions — Principles and Aims," *Journal of Geodynamics*, vol. 33, no. 1-2, 2002, pp. 3–20, doi:10.1016/S0264-3707(01)00050-3.

[13] Romano, F., Binder, T., Herdrich, G., *et al.*, "Air-Intake Design Investigation for an Air-Breathing Electric Propulsion System," in *Joint Conference of 30th International Symposium on Space Technology and Science, 34th International Electric Propulsion Conference and 6th Nano-satellite Symposium*, Hyogo-Kobe, Japan, 2015, pp. 1–27, iEPC-2015-269/ISTS-2015-b-269.

[14] Virgin Orbit, *Launcher One*, Service Guide version 1.1, Virgin Orbit, August 2018.

[15] Fishman, S., *Earth Observation: State of Play and Future Prospects*, Presentation for the Advisory Committee On Commercial Remote Sensing Meeting 1, Euroconsult, 2018.

[16] Hatton, S., ed., *Proceedings of the 12th Reinventing Space Conference*, vol. 1, Springer, Cham, Switzerland, 2017, doi:10.1007/978-3-319-34024-1.

[17] Wertz, J. R., Everett, D. F., and Puschell, J. J., eds., *Space Mission Engineering: The New SMAD*, 2nd edition edition, Microcosm Press, Hawthorne, CA, USA, 2015, iSBN 978-1-881-883-15-9.

[18] Cook, G. E., "Satellite Drag Coefficients," *Planetary and Space Science*, vol. 13, no. 10, 1965, pp. 929–946, doi:10.1016/0032-0633(65)90150-9.

[19] Moe, M. M., Wallace, S. D., and Moe, K., "Recommended Drag Coefficients for Aeronomic Satellites," in *The Upper Mesosphere and Lower Thermosphere: A Review of Experiment and Theory*, edited by Johnson, R. M. and Killeen, T. L., vol. 87, American Geophysical Union, Washington, DC, USA, 1995, pp. 349–356, doi:10.1029/GM087p0349.

[20] de Jong, J. G. P., *Analytical Low-Thrust Trajectory Design*, Master's thesis, Delft University of Technology, 2018.

[21] Ruggiero, A., Pergola, P., Marcuccio, S., *et al.*, "Low-Thrust Maneuvers for the Efficient Correction of Orbital Elements," in *32nd International Electric Propulsion Conference*, Wiesbaden, Germany, 2011, pp. 1–12, iEPC-2011-102.

[22] Cao, J., Li, H., and Shen, H., "Orbital Plane Change Maneuver Strategy using Electric Propulsion," in *Proceedings of the Institution of Mechanical Engineers, Part G: Journal of Aerospace Engineering*, vol. 233, , 2018, pp. 2360–2367, doi:10.1177/0954410018779315.

[23] Capderou, M., *Handbook of Satellite Orbits*, vol. 1, Springer, Cham, Switzerland, 2014, doi:10.1007/978-3-319-03416-4.

[24] Ortiz Longo, C. R. and Rickman, S. L., *Method for the Calculation of Spacecraft Umbra and Penumbra Shadow Terminator Points*, NASA Technical Paper NASA-TP-3547, NASA Johnsen Space Center, 1995.

[25] Wertz, J. R., ed., *Orbit & Constellation Design & Management*, vol. 2 of *Space Technology Library*, Mircocosm Press and Springer, Hawthorne, CA, USA and New York, NY, USA, 2009, iSBN 978-1-881883-07-8.

[26] He, C., Yang, Y., Carter, B., *et al.*, "Review and Comparison of Empirical Thermospheric Mass Density Models," *Progress in Aerospace Sciences*, vol. 103, 2018, pp. 31–51, doi:10.1016/j.paerosci.2018.10.003.

[27] Shorshi, G. and Bar-Itzhack, I. Y., "Satellite Autonomous Navigation and Orbit Determination Using Magnetometers," in *Proceedings of the 31st IEEE Conference on Decision and Control*, , 1992, pp. 542–548, doi:10.1109/CDC.1992.371675.

[28] Psiaki, M. L., "Autonomous LEO Orbit Determination From Magnetometer and Sun Sensor Data," in *Guidance, Navigation and Control Conference and Exhibit*, Boston, MA, USA, 1998, pp. 1086–1096, aIAA-98-4308, doi:10.2514/6.1998-4308.

[29] Anigstein, P. A. and Pena, R. S. S., "Analysis of Solar Panel Orientation in Low Altitude Satellites," *IEEE Transactions on Aerospace and Electronic Systems*, vol. 34, no. 2, 1998, pp. 569–578, doi:10.1109/7.670337.

[30] ITU, *Characteristics of Data Relay Satellite Systems*, Recommendation ITU-R SA.1414-2, International Telecommunication Union, 2017.

[31] Larson, W. J. and Wertz, J. R., eds., *Space Mission Analysis and Design*, 2nd edition edition, Kluwer Academic Publishers, Dordrecht, the Netherlands, 1993.

[32] Sun, R., Maessen, D., Guo, J., *et al.*, "Enabling Inter-Satellite Communication and Ranging for Small Satellites," in *Symposium of Small Satellite Systems and Services (4S)*, Funchal, Portugal, 2010, pp. 1–15.

[33] Perea-Tamayo, R. G., Fuchs, C. M., Ergetu, E., *et al.*, "Design and Evaluation of a Low-Cost CubeSat Communication Relay Constellation," in *IEEE MTT-S Latin America Microwave Conference*, Arequipa, Peru, 2018, pp. 1–4, doi:10.1109/LAMC.2018.8699047.

[34] Bedon, H., Negron, C., Llantoy, J., *et al.*, "Preliminary Interworking Simulation of the QB50 CubeSate Constellation," in *IEEE Latin America Conference on Communications*, Bogota, Colombia, 2010, pp. 1–6, doi:10.1109/LATINCOM.2010.5640977.

[35] Campbell, J. B., *Introduction to Remote Sensing*, 3rd edition, The Guildford Press, New York, NY, USA, 2002.

[36] Helin, H., Tolonen, T., Ylinen, O., *et al.*, "Optimized JPEG 2000 Compression for Efficient Storage of Histopathological Whole-Slide Images," *Journal of Pathology Informatics*, vol. 9, no. 20, 2018, pp. 1–6, doi:10.4103/jpi.jpi_69_17.

[37] Jo, K. Y., *Satellite Communications Network Design and Analysis*, vol. 1, Artech House, Norwoord, MA, USA, 2011, iSBN 9781608071951.

[38] Orban Microwave, *Ka-Band Antenna Array*, Product Series Data Sheet 004-107-001, Orban Microwave, 2015.

[39] Buttazzoni, G., Comisso, M., Cuttin, A., *et al.*, "Reconfigurable Phased Antenna Array for Extending CubeSat Operations to Ka-band: Design and Feasibility," *Acta Astronautica*, vol. 137, 2017, pp. 144–121, doi:10.1016/j.actaastro.2017.04.012.

[40] NASA Goddard Space Flight Center, *Space Network Users' Guide (SNUG)*, Space Network Project 450-SNUG, NASA Goddard Space Flight Center, 2012.

[41] Tethers Unlimited, Inc., *SWIFT-KTX*, Product Data Sheet 001-100-004-A, Tethers Unlimited, 2017.

[42] Stock Wireless Components, *Signal Splitter*, Data Sheet and Technical Drawing GPS820, Stock Wireless Components, 2010.

[43] Bau, J. H., *Topologies for Satellite Constellatioins in a Cross-linked Space Backbone Network*, Master's thesis, Massachusetts Institute of Technology, 2000.

[44] Fortescue, P., Swinerd, G., and Stark, J., eds., *Spacecraft Systems Engineering*, Aerospace Series, 4th edition edition, John Wiley & Sons, Hoboken, NJ, USA, 2011, iSBN 978-0-470-75012-4.

[45] Mitsubishi Electric, "AESA Antennas for Ka Band Satellite Communication," Presentation, 2018.

[46] Romano, F., Binder, T., Boxberger, A., *et al.*, *Literature Review of ABEP Systems*, Horizon 2020 DISCOVERER D4.1, European Union, 2017.

[47] Bathgate, S. N., Bilek, M. M. M., and McKenzie, D. R., "Electrodeless plasma thrusters for spacecraft: A review," *Plasma Science and Technology*, vol. 19, 2017, p. 24, doi:10.1088/2058-6272/aa71fe.

[48] Kokan, T. and Joyner II, C. R., "Mission Comparison of Hall Effect and Gridded Ion Thrusters Utilizing Various Propellant Options," in *AIAA Space 2012 Conference & Exposition*, Pasadena, CA, USA, 2012, pp. 1–12, aIAA 2012-5237, doi:10.2514/6.2012-5237.

[49] Cifali, G., Misurei, T., Rossetti, P., *et al.*, "Experimental Characterization of HET and RIT with Atmospheric Propellants," in *32nd International Electric Propulsion Conference*, Wiesbaden, Germany, 2011, pp. 1–12, iEPC-2011-224.

[50] Cifali, G., Dignani, D., Misuri, T., *et al.*, "Completion of HET and RIT Characterization with Atmospheric Propellants," in *Proceedings of Space Propulsion*, Bordeaux, France, 2012, pp. 1–12.

[51] Goebel, D. M. and Katz, I., *Fundamentals of Electric Propulsion: Ion and Hall Thrusters*, JPL Space Science and Technology Series, John Wiley & Sons, Hoboken, NJ, USA, 2008, doi:10.1002/9780470436448.

[52] Lotz, B., *Plasma Physical and Material Physical Aspects of the Application of Atmospheric Gases as a Propellant for Ion-Thruster of the RIT-Type*, Ph.D. thesis, Justus-Liebig-University of Giessen, 2013.

[53] Barral, S., Cifali, G., Albertoni, R., *et al.*, "Conceptual Design of an Air-Breathing Electric Propulsion System," in *Joint Conf. of 30th Int. Symp. on Space Technology and Science, 34th Int. Electric Propulsion Conf. and 6th Nano-Satellite Symp*, Hyogo-Kobe, Japan, 2015, pp. 1–14, iEPC-2015-271/ISTS-2015-b-271.

[54] Binder, T., Boldini, P. C., Romano, F., *et al.*, "Transmission Probabilities of Rarefied Flows in the Application of Atmosphere-Breating Electric Propulsion," in *AIP Conference Proceedings*, vol. 1786, , 2016, pp. 190011–1 – 190011–8, doi:10.1063/1.4967689.

[55] Preukert, M., "OHB-System's View on Electric Propulsion Needs," EPIC Workshop Presentation, 2014.

[56] Drinkwater, M. R., Haagmans, D. M., Popescu, A., *et al.*, "The GOCE Gravity Mission: ESA's First Core Earth Explorer," in *Proceedings of the 3rd International GOCE User Workshop*, Frascati, Italy, 2007, pp. 1–8, eSA Special Publication, SP-627, ISBN 92-9092-938-3.

[57] Reichbach, J. G., Sedwick, R. J., and Martinex-Sanchez, M., "Micropropulsion System Selection for Precision Formation Flying Satellites," in *37th AIAA/ASME/SAE/ASEE Joint Propulsion Conference & Exhibit*, Salt Lake City, UT, USA, 2001, pp. 1–19, aIAA 2001-3646, doi:10.2514/6.2001-3646.

[58] Shimmin, R., *Small Spacecraft Technology State of the Art*, NASA Technical Report NASA/TP-2015-216648/REV1, NASA Ames Research Center, 2015.

[59] Hyder, A. K., Wiley, R. L., Halper, G., *et al.*, *Spacecraft Power Technologies*, vol. 1 of *Space Technology*, Imperial College Press, London, UK, 2003, iSBN 1-86094-117-6.

[60] Park, H. and Cha, H., "Electrical Design of a Solar Array for LEO Satellites," *International Journal of Aeronautical and Space Sciences*, vol. 17, no. 3, 2016, pp. 401–408, doi:10.5139/IJASS.2016.17.3.401.

[61] Chatwin, C. R., "Satellite & Space Systems - Electrical Power Systems," School of Engineering & Informatic Presentation, April 25 2017.

[62] ECSS, *Space Engineering: High Voltage Engineering and Design Handbook*, vol. 1, ESA Requirements and Standards Division, Noordwijk, the Netherlands, 2012, eCSS-E-HB-20-05A.

[63] Surampudi, R., Blosiu, J., Bugga, R., *et al.*, *Energy Storage Technologies for Future Planetary Science Missions*, Planetary Science Program Support Task Report JPL D-101146, NASA Jet Propulsion Laboratory, 2017.

[64] Arcis, N., Bulit, A., Gollor, M., *et al.*, *Database on EP (and EP-related) technologies and TRL*, Horizon 2020 DISCOVERER D2.1, Ares(2015)791364, European Union, 2014.

[65] Arcisto, S., Gambarara, M., Garutti, A., *et al.*, "Power Supply and Control Unit (PSCU) for Radiofrequency Ion Thrusters (RIT)," in *2nd European Spacecraft Propulsion Conference*, Noordwijk, the Netherlands, 1997, pp. 643–648, eSA SP-398.

[66] Tato, C., De la Cruz, F., and Palencia, "Power Control Unit for Ion Propulsion Assembly in GOCE Program," in *30th International Electric Propulsion Conference*, Florence, Italy, 2007, pp. 1–11, iEPC-2007-295.

[67] Mondt, J. and Halper, G., *Energy Storage Technologies for Future Space Science Missions*, Planetary Science Program Support Task Report JPL D-30268, NASA Jet Propulsion Laboratory, 2004.

[68] Peper, T., Schilling, Q., and Grein, S., *Handling, Storage and Processing of III/V Semiconductor Products*, Recommendations for handling, storage and processing of III/V multi-junction solar cells HNR 0064684-00, Azur Space, 2015.

[69] Fox, B., Brancato, K., and Alkire, B., *Guidance and Metrics for Assessing Space System Cost Estimates*, Project AIR FORCE Technical Report ISBN 978-0-8330-4023-7, RAND Corporation, 2008.

[70] Hecht, E., *Optics*, vol. 5, Pearson, Boston, MA, USA, 2017, iSBN 1-292-09693-4.

[71] Tempfli, K., Kerle, N., Huurneman, G. C., *et al.*, eds., *Principles of Remote Sensing*, vol. 4 of *ITC Educational Textbook Series*, International Institute for Geo-Information Science and Earth Observation (ITC), Enschede, the Netherlands, 2009, iSBN 978-90-6164-270-1.

[72] Picart, P., Mounier, D., and Desse, J. M., "High-Resolution Digital Two-Color Holographic Metrology," *Optics Letters*, vol. 33, no. 3, 2008, pp. 276–278, doi:10.1364/OL.33.000276.

[73] Fossum, E. R., "CMOS Image Sensors: Electronic Camera-On-A-Chip," *IEEE Transactions on Electron Devices*, vol. 44, no. 10, 1997, pp. 1689–1698, doi:10.1109/16.628824.

[74] Saint-Pé, O., Tuleta, M., Davancensa, R., *et al.*, "Space Optical Instruments Optimisation thanks to CMOS Image Sensor Technology," in *Proceedings of SPIE, Sensors, Systems, and Next-Generation Satellites IX*, vol. 5978, Bruges, Belgium, 2005, pp. 597811–1 – 597811–8, doi:10.1117/12.628113.

[75] Murthy, K., Shearn, M., Smiley, B. D., *et al.*, "SkySat-1: Very High-Resolution Imagery from a Small Satellite," in *Proceedings of SPIE Remote Sensing; Sensors, Systems and Next Generation Satellites*, vol. 9241, Amsterdam, Netherlands, 2014, pp. 1–12, doi:10.1117/12.2074163.

[76] Meynants, G., "Global Shutter Imagers for Industrial Applications," in *SPIE Photonics Europe*, vol. 9141, Brussels, Belgium, 2014, pp. 914108–1 – 914108–9, doi:10.1117/12.2060072.

[77] Van Putten, B. T., *Design of the Deployment Mechanism for the Primary Mirror Elements of a Deployable Space Telescope*, Master's thesis, Delft University of Technology, 2017.

[78] Champagne, J., Hansen, S., Newswander, T., *et al.*, "CubeSat Image Resolution Capabilities with Deployable Optics and Current Imaging Technology," in *28th Annual AIAA/USU Conference on Small Satellites*, Utah State University, Utah, USA, 2014, pp. 1–9.

[79] Schwartz, N., Pearson, D., Todd, S., *et al.*, "Laboratory Demonstration of an Active Optics System for High-Resolution Deployable CubeSat," in *4S Symposium*, Sorrento, Italy, 2018, pp. 1–15.

[80] Heshmat, B., Tancik, M., Satat, G., *et al.*, "Photography Optics in the Time Dimension," *Nature Photonics*, vol. 12, 2018, pp. 560–566, doi:10.1038/s41566-018-0234-0.

[81] Carlin, P. S., "Lightweight Mirror Systems for Spacecraft - an Overview of Materials and Manufacturing Needs," in *IEEE Aerospace Conference Proceedings*, Big Sky, MT, USA, 2000, pp. 169–181, doi:AERO.2000.878393.

[82] Deyerler, M., Pailer, N. M., Wagner, R., *et al.*, "Ultrlightweight mirrors: recent developments of C/SiC," in *Proceedings of SPIE, Optical Design, Materials, Fabrication, and Maintenance*, vol. 4003, Munich, Germany, 2002, pp. 73–79, doi:10.1117/12.391543.

[83] Zhou, H., Zhang, C., Cao, Y., *et al.*, "Lightweight C/SiC Mirrors for Space Application," in *Proceedings of SPIE, 2nd International Symposium on Advanced Optical Manufacturing and Testing Technologies: Large Mirrors and Telescopes*, vol. 6148, Xian, China, 2006, pp. 61480L–1 – 61480L–6, doi:10.1117/12.674096.

[84] Yui, Y. Y., Goto, K., Kaneda, H., *et al.*, "Performance of Lightweight Large C/SiC Mirror," in *Proceedings of SPIE, International Conference on Space Optics*, vol. 10566, Toulouse, France, 2008, pp. 105660M–1 – 105660M–8, doi:10.1117/12.2308191.

[85] Papenburg, U., Pfrang, W., Kutter, G. S., *et al.*, "Optical and Optomechanical Ultralightweight C/SiC Components," in *Proceedings of SPIE, Optical Manufacturing and Testing III*, Denver, CO, USA, 1999,

pp. 141–156, doi:10.1117/12.369180.

[86] Chang, Y. K., Hwang, K. L., and Kang, S. J., "SEDT (System Engineering Design Tool) Development and its Application to Small Satellite Conceptual Design," *Acta Astronautica*, vol. 61, no. 7-8, 2007, pp. 676–690, doi:10.1016/j.actaastro.2007.01.067.

[87] Topal, E., Akyilmaz, O., and Aslan, A. R., "Spaceborne Push-Broom Image Guidance, Attitude Realization Errors: A System Engineering Approach," *Arabian Journal for Science and Engineering*, vol. 41, no. 11, 2016, pp. 4477–4486, doi:10.1007/s13369-016-2141-3.

[88] Bougoin, M., "SiC Challenging Parts for GAIA," in *Proceedings of SPIE, International Conference on Space Optics*, vol. 10565, Rhodes Island, Greece, 2010, pp. 105652C–1 – 105652C–6, doi:10.1117/12.2309232.

[89] Broder, M. A., Mahr, E. M., Barkmeyer, D. E. F., *et al.*, "Review of Three Small-Satellite Cost Models," in *AIAA SPACE Conference & Exposition*, Pasadena, CA, USA, 2009, pp. 1–11, aIAA 2009-6689, doi:10.2514/6.2009-6689.

[90] Hsü, S. T., *Engineering Heat Transfer*, N. J. Van Nostrand, Princeton, NJ, USA, 1963.

[91] Hughes, P. C., *Spacecraft Attitude Dynamics*, John Wiley & Sons, New York, NY, USA, 1986, iSBN 0-471-81842-9.

[92] Eyerman, C. E., *A Systems Engineering Approach to Disturbance Minimization for Spacecraft Utilizing Controlled Structures Technology*, Master's thesis, Massachusetts Institute of Technology, 1990.

[93] Lassakeur, A. and Underwood, C., "Precision Attitude Determination and Control System of CubeSats by On-Orbit Determination of the Dynamic Magnetic Moment," in *10th International ESA Conference on Guidance, Navigation & Control Systems*, Salzburg, Austria, 2017, pp. 1–11.

[94] NASA, *Spacecraft Magnetic Torques*, Space Vehicle Design Criteria (Guidance and Control) NASA SP-8018, NASA, 1969.

[95] Ley, W., Wittmann, K., and Hallmann, W., *Handbook of Space Technology*, John Wiley & Sons, Hoboken, NJ, USA, 2009, doi:10.1002/9780470742433.

[96] de Ruiter, A. H., Damaran, C., and Forbes, J. R., *Spacecraft Dynamics and Control: An Introduction*, John Wiley & Sons, Hoboken, NJ, USA, 2013, iSBN 978-1-118-34236-7.

[97] Woo, P., Langelier, M. K., Hamel, J. F., *et al.*, "Performance Assessment of a Gyroless 3-Axis Stabilised Sun Pointing Mode on a Highly Elliptical Orbit," *IFAC-PapersOnLine*, vol. 49, no. 17, 2016, pp. 146–151, doi:10.1016/j.ifacol.2016.09.026.

[98] Avanzini, G. and Giulietti, F., "Magnetic Detumbling of a Rigid Spacecraft," *Journal of Guidance, Control, and Dynamics*, vol. 35, no. 4, 2012, pp. 1326–1334, doi:10.2514/1.53074.

[99] Leomanni, M., *Comparison of Control Laws for Magnetic Detumbling*, Technical report, University of Siena, 2012.

[100] Lovera, M., "Magnetic Satellite Detumbling: The B-dot Algorithm Revisited," in *American Control Conference*, Chicago, IL, USA, 2015, pp. 1867–1872, doi:10.1109/ACC.2015.7171005.

[101] Guerrant, D. V., *Design and Analysis of Fully Magnetic Control for Picosatellite Stabilization*, Master's thesis, California Polytechnic State University, 2005.

[102] Wood, M., Chen, W. H., and Fertin, D., "Model Predictive Control of Low Earth Orbiting Spacecraft with Magneto-Torquers," in *IEEE International Conference on Control Applications*, Munich, Germany, 2006, pp. 2908–2913, doi:10.1109/CACSD-CCA-ISIC.2006.4777100.

[103] Silani, E. and Lovera, M., "Magnetic Spacecraft Attitude Control: a Survey and Some New Result," *Control Engineering Practice*, vol. 13, no. 3, 2005, pp. 357–371, doi:10.1016/j.conengprac.2003.12.017.

[104] Tewari, A. and Renuganth, V., "Optimal Attitude Control Through Magnetic Torquers and Reaction Wheels," *IFAC Proceeings Volumes*, vol. 40, no. 7, 2007, pp. 19–24, doi:10.3182/20070625-5-FR-2916.00005.

[105] Psiaki, M. L., "Magnetic Torquer Attitude Control via Asymptotic Periodic Linear Quadratic Regulation," *Journal of Guidance, Control, and Dynamics*, vol. 24, no. 2, 2001, pp. 386–394, doi:10.2514/2.4723.

[106] Mazzini, L., *Flexible Spacecraft Dynamics, Control and Guidance*, vol. 1 of *Springer Aerospace Technology*, Springer, Cham, Switzerland, 2016, doi:10.1007/978-3-319-25540-8.

[107] Hibbeler, R. C., *Engineering Mechanics: Statics*, vol. 14, Pearson, London, UK, 2016, iSBN 9780133921564.

[108] Rao, S. S., *Vibration of Continuous Systems*, John Wiley & Sons, Hoboken, NJ, USA, 2006, doi:10.1002/9780470117866.

[109] Wijker, J., *Miles' Equation in Random Vibrations*, vol. 1 of *Solid Mechanics and Its Applications*, Springer, Cham, Switzerland, 2018, doi:10.1007/978-3-319-73114-8.

[110] Ben, B. S., Ben, B. A., Adarsh, K., *et al.*, "Damping Measurement in Composite Materials using Combined Finite Element and Frequency Response Method," *International Journal of Engineering Science Invention*, vol. 2, 2013, pp. 89–97.

[111] Mevada, H. and Patel, D., "Experimental Determination of Structural Damping of Different Materials," *Procedia Engineering*, vol. 144, 2016, pp. 110–115, doi:10.1016/j.proeng.2016.05.013.

[112] Levy, D., *Introduction to Numerical Analysis*, Report, University of Maryland, 2010.

[113] Reddy, M. R., "Effect of Low Earth Orbit Atomic Oxygen on Spacecraft Materials," *Journal of Materials Science*, vol. 30, no. 2, 1995, pp. 281–307, doi:10.1007/BF00354389.

[114] Shepherd, G. C. and Cho, Y. M., "Stationary Depletions in Thermospheric Atomic Oxygen Concentration and Mass Density Observed with WINDII, GUVI, GOCE and Simulated by NRLMSISE-00," *Journal of Atmospheric and Solar-Terrestrial Physics*, vol. 164, 2017, pp. 29–38, doi:10.1016/j.jastp.2017.07.016.

[115] Banks, B. A., Miller, S. K., and de Groh, K. K., "Low Earth Orbital Atomic Oxygen Interactions with Materials," in *2nd International Energy Conversion Engineering Conference*, Providence, RI, USA, 2004, pp. 1–19, aIAA 2004-5638, doi:10.2514/6.2004-5638.

[116] de Rooij, A., "Corrosion in Space," in *Encyclopedia of Aerospace Engineering*, edited by Blockley, R. and Shyy, W., vol. 9, John Wiley & Sons, Hoboken, NJ, USA, 2010, p. 209, doi:10.1002/9780470686652.eae242.

[117] Samwel, S. W., "Low Earth Orbital Atomic Oxygen Erosion Effect on Spacecraft Materials," *Space Research Journal*, vol. 7, no. 1, 2014, pp. 1–13, doi:10.3923/srj.2014.1.13.

[118] Hu, L., Li, M., Xu, C., *et al.*, "Perhydropolysilazane Derived Silica Coating Protecting Kapton from Atomic Oxygen Attack," *Thin Solid Films*, vol. 520, no. 3, 2011, pp. 1063–1068, doi:10.1016/j.tsf.2011.10.011.

[119] Waters, D. L., de Groh, K. K., Banks, B. A., *et al.*, "Changes in Optical and Thermal Properties of the MISSE 2 PEACE Polymers and Spacecraft Silicones," in *11th International Symposium on Materials in a Space Environment*, Aix-en-Provence, France, 2009, pp. 1–10.

[120] de Groh, K. K., Banks, B. A., and Smith, D. C., "Environmental Durability Issues for Solar Power Systems in Low Earth Orbit," in *International Solar Energy Conference*, Lahaina, Maui, Hawaii, 1995, pp. 1–13, nASA-TM-106775.

[121] Vest, C. E., "The Effects of the Space Environment on Spacecraft Surfaces," *John Hopkins APL Technical Digest*, vol. 12, no. 1, 1991, pp. 46–54.

[122] de Groh, K. K. and McCollum, T. A., "Low Earth Orbit Durability Evaluation of Protected Silicone for Advanced Refractive Photovoltaic Concentrator Arrays," in *AIAA 32nd Aerospace Sciences Meeting and Exhibit*, Reno, NV, USA, 1994, pp. 1–10, nASA-TM-106543, AIAA-94-0374.

[123] Braun, V., Gelhaus, J., Kebschull, C., *et al.*, "DRAMA 2.0 - ESA's Space Debris Risk Assessment and Mitifation Analysis Tool Suite," in *64th International Astronautical Congress*, Beijing, China, 2013, pp. 1–12, iAC-13,A6.4,4x18862.

[124] European Space Agency, *Debris Risk Assessment and Mitigation Analysis (DRAMA) Software User Manual*, User Manual 2, European Space Operations Centre, 2019.

[125] Rocket Lab, *Electron Payload User's Guide*, Payload User's Guide version 6.4, Rocket Lab, June 2019.

[126] Vector, *Vector H*, Payload User's Guide PUG-VECTOR-H-2019.4.18, Vector, April 2019.

[127] Rahmani, H., Najafi, S. H. M. N., and Ashori, A., "Mechanical Performance of Epoxy/Carbon Fiber Laminated Composites," *Journal of Reinforced Plastics & Composites*, vol. 33, no. 8, 2014, pp. 773–740, doi:10.1177/0731684413518255.

[128] Zhang, J., Ai, L., Li, X., *et al.*, "Hollow Silica Nanosphere/Polyimide Composite Films for Enhanced Transparency and Atomic Oxygen Resistance," *Materials Chemistry and Physics*, vol. 222, 2019, pp. 384–390, doi:10.1016/j.matchemphys.2018.10.022.

[129] Bahuguma, G., Mishra, N. K., Chaudhary, P., *et al.*, "Thin Film Coating through Sol-Gel Technique," *Research Journal of Chemical Sciences*, vol. 6, no. 7, 2016, pp. 65–72, e-ISSN 2231-606X.

[130] Qi, H., Qian, Y., Xu, J., *et al.*, "An AZ31 Magnesium Alloy Coating for Protecting Polyimide from

Erosion-Corrosion by Atomic Oxygen," *Corrosion Science*, vol. 138, no. 1, 2018, pp. 170–177, doi:10.1016/j.corsci.2018.04.013.

[131] Watson, K. A., Palmieri, F. L., and Connell, J. W., "Space Environmentally Stable Polyimides and Copolyimides Derived from [2,4-Bis(3-aminophenoxy)phenyl]diphenylphosphine Oxide," *Macromolecules*, vol. 35, no. 13, 2002, pp. 4968–4974, doi:10.1021/ma0201779.

[132] Rosner, D. E. and Allendorf, H. D., "High Temperature Oxidation of Carbon by Atomic Oxygen," *Carbon*, vol. 3, no. 2, 1965, pp. 153–156, doi:10.1016/0008-6223(65)90042-4.

[133] Snegirev, A., Talalov, V., Stepanov, V., *et al.*, "Formal Kinetics of Polymer Pyrolysis for Modeling of Ignition and Burning in Fire Tests," in *13th International Fire Science & Engineering Conference*, London, UK, 2013, pp. 755–767.

[134] Valsamos, G., Casadei, F., Larcher, M., *et al.*, *Implementation of Flying Debris Fatal Risk Calculation in EUROPLEXUS*, Scientific and Technical Research Reports EUR 27135, Publications Office of the European Union, 2015, doi:10.2788/058640.

[135] Kumar, P., Bhaduri, S., and Kumar, A., "Vibration Analysis of Cantilever Beam: An Experimental Study," *International Journal for Research in Applied Science & Engineering Technology*, vol. 4, no. 11, 2016, pp. 361–369, doi:10.1016/j.corsci.2018.04.013.

[136] Hosseini, H., Ganji, D. D., Abaspour, M., *et al.*, "Effect of Axial Force on Natural Frequency of Lateral Vibration of Flexible Rotating Shafts," *World Applied Sciences Journal*, vol. 15, no. 6, 2011, pp. 853–859.

[137] Sakar, G., "The Effect of Axial Force on the Free Vibration of an Euler-Bernoulli Beam carrying a number of various Concentrated Elements," *Shock and Vibrations*, vol. 20, no. 3, 2013, pp. 357–367, doi:10.3233/SAV-120750.

[138] Wang, X. Q. and Chan, K. T., "Free Vibration of a Cantilever Beam with a Partial Span of Distributed Mass," in *Fifth International Congress on Sound and Vibration*, Adelaide, South Australia, 1997, pp. 1–8.

[139] Wang, C. M., "Timoshenko Beam-Bending Solutions in Terms of Euler-Bernoulli Solutions," *Journal of Engineering Mechanics*, vol. 121, no. 6, 1995, pp. 763–765.

[140] Mahato, B., Anil, and Harish, H. V., "Experimental Verification of Deflection of Beam using Theoretical and Numerical Approach," *International Journal of Advance Research in Engineering, Science & Technology*, vol. 2, no. 3, 2015, pp. 2394–2444.

[141] Zhou, Z. Q., Liu, X. L., and Chiu, W. K., "In-Plane Mechanical Properties of a Carbon-Epoxy Composite Laminate at Elevated Temperatures," *Polymers & Polymer Composites*, vol. 15, no. 3, 2007, pp. 207–216.

[142] Bank, L. C., "Shear Coefficients for Thin-Walled Composite Beams," *Composite Structures*, vol. 8, no. 1, 1987, pp. 47–61, doi:10.1016/0263-8223(87)90015-8.

[143] Ključanin, D. and Manđuka, A., "The Cantilever Beams Analysis by the means of the First-Order Shear Deformation and the Euler-Bernoulli Theory," *Tehnički Glasnik*, vol. 13, no. 1, 2019, pp. 63–67, doi:10.31803/tg-20180802210608.

[144] TORAYCA, *Carbon Fiber TORAYCA Sizing Type 4*, Material Safety Data Sheet I2E-C004-1, TORAYCA, 2014.

[145] Agilent Technologies, *Compensated Epon*, Safety Data Sheet 29CFR1910.1200, Agilent Technologies, 2014.

[146] Romano, F., *System Analysis and Test Bed for an Air-Breathing Electric Propulsion System*, Master's thesis, University of Stuttgart, 2014.

[147] McGuire, T. J., *Aero-Assisted Orbital Transfer Vehicles Utilizing Atmosphere Ingestion*, Master's thesis, Massachusetts Institute of Technology, 2001.

[148] Caruso Jr., P. S. and Naegeli, C. R., *Low-Perigee Aerodynamic Heating during Orbital Flight of an Atmosphere Explorer*, NASA Technical Report NASA-TN-D-8308, NASA Goddard Space Flight Center, 1976.

[149] Rickman, S. L., "Introduction to On-Orbit Thermal Environments," Thermal and Fluids Analysis Workshop, 2014.

[150] Van Weeren, H., Ter Brake, H. J. M., Holl, G., *et al.*, "Thermal Aspects of Satellite Downscaling," *Journal of Thermophysics and Heat Transfer*, vol. 23, no. 3, 2009, pp. 592–600, doi:10.2514/1.41857.

[151] Howell, J. R., *A Catalog of Radiation Heat Transfer Configuration Factors*, 3rd edition, University of Texas at Austin, Austin, TX, USA, 1982.

[152] Baturkin, V., "Micro-Satellites Thermal Control - Concepts and Components," *Acta Astronautica*, vol. 56, no. 1-2, 2005, pp. 161–170, doi:10.1016/j.actaastro.2004.09.003.

[153] Gilmore, D. G., ed., *Spacecraft Thermal Control Handbook: Fundamental Technologies*, vol. 1, Aerospace Press, Reston, VA, USA, 2002, doi:10.2514/4.989117.

[154] Benthem, B. and Mena, F., "Innovative new High Performance Radiators: Developing Heat Rejecting Systems with Flexible Film Technology," in *45th International Conference on Environmental Systems*, Bellevue, WA, USA, 2015, pp. 1–20, iCES-2015-180.

[155] Birur, G. C., Siebes, G., and Swanson, T., *Spacecraft Thermal Control*, Preprint 20010091676, NASA Goddard Space Flight Center, 2001.

[156] Sidi, M. J., *Spacecraft Dynamics and Control*, vol. 1 of *Cambridge Aerospace Series 7*, Cambridge University Press, Cambridge, UK, 1997, doi:10.1017/CBO9780511815652.

[157] JAXA, *Spacecraft Thermal Control System*, Design Standard JERG-2-310, Japan Aerospace Exploration Agency, 2009.

[158] Zandbergen, B. T. C., *AE1222-II Aerospace Design & Systems Engineering Elements 1: Spacecraft (bus) Design and Sizing*, TU Delft, Faculty of Aerospace Engineering, Delft, the Netherlands, 2015, internal publication.

[159] Space Micro, *Protonn2X-Box Suite*, Product Data Sheet 4, Space Micro, 2018.

[160] Eickhoff, J., *Onboard Computers, Onboard Software and Satellite Operations*, vol. 1 of *Springer Aerospace Technology*, Springer, Cham, Switzerland, 2012, doi:10.1007/978-3-642-25170-2.

[161] Hirshorn, S. R., *NASA Systems Engineering Handbook*, 2nd edition, NASA, Washington, DC, USA, 2016.

[162] Brezet, H. and van Hemel, C., *Ecodesign - A promising approach to sustainable production and consumption*, 6th international edition edition, UNEP, Paris, France, 1998.

[163] Peters, J. F., Baumann, M., Zimmermann, B., *et al.*, "The Environmental Impact of Li-Ion Batteries and the Role of Key Parameters – A Review," *Renewable and Sustainable Energy Reviews*, vol. 67, 2017, pp. 491–506, doi:10.1016/j.rser.2016.08.039.

[164] Al-Lami, A., Hilmer, P., and Sinapius, M., "Eco-Efficiency Assessment of Manufacturing Carbon Fiber Reinforced Polymers (CFRP) in Aerospace Industry," *Aerospace Science and Technology*, vol. 79, 2018, pp. 669–678, doi:10.1016/j.ast.2018.06.020.

[165] Shuaib, N. A., Mativenga, P. T., Kazie, J., *et al.*, "Resource Efficiency and Composite Waste in UK Supply Chain," *Procedia CIRP*, vol. 29, 2015, pp. 662–667, doi:10.1016/j.procir.2015.02.042.

[166] Ross, M. and Vedda, J. A., *The Policy and Science of Rocket Emissions*, Paper OTR2018-00493, The Center for Space Policy and Strategy, The Aerospace Corporation, 2018.

[167] Kramer, H. J. and Cracknell, A. P., "An Overview of Small Satellites in Remote Sensing," *International Journal of Remote Sensing*, vol. 29, no. 15, 2008, pp. 4285–4337, doi:10.1080/01431160801914952.

[168] Van Oudheusden, A. and Joustra, J., *Recycling of Composite Materials*, Student Thesis February, Delft University of Technology, 2019, `http://resolver.tudelft.nl/uuid:0749ed5c-7aeb-4275-abee-0f904a08ea4d`.

[169] Larson, E. J. L., Portmann, R. W., Rosenlof, K. H., *et al.*, "Global Atmospheric Response to Emissions from a Proposed Reusable Space Launch System," *Earth's Future*, vol. 5, no. 1, 2016, pp. 37–48, doi:10.1002/2016EF000399.

[170] Aerospace Medicine Office, "Space Operations: The Space Environment," in *Advanced Aerospace Medicine On-Line*, Federal Aviation Agency, Washington, DC, USA, 2018, pp. 4.1.2–1 – 4.1.2–26.